Study of Dy diffusion in sintered polycrystalline Nd2Fe14B magnets by electron microscopies

Abir Ismail

THÈSE

Pour obtenir le grade de

DOCTEUR DE L'UNIVERSITÉ GRENOBLE ALPES

École doctorale : PHYS - Physique
Spécialité : Physique des matériaux
Unité de recherche : Modélisation et Exploration des Matériaux

Etude de la diffusion du Dy dans les aimants polycristallins frittés Nd2Fe14B par microscopie électronique

Study of Dy diffusion in sintered polycrystalline Nd2Fe14B magnets by electron microscopies

Présentée par :

Abir ISMAIL

Direction de thèse :

Jean-Luc ROUVIERE DIRECTEUR DE RECHERCHE, CEA CENTRE DE GRENOBLE	Directeur de thèse
Laure GUETAZ INGENIEUR CHERCHEUR, Université Grenoble Alpes	Co-encadrante de thèse
Gérard DELETTE INGENIEUR CHERCHEUR, CEA CENTRE DE GRENOBLE	Co-encadrant de thèse

Rapporteurs :

DAMIEN JACOB
PROFESSEUR DES UNIVERSITES, UNIVERSITE DE LILLE
NIRINA RANDRIANANTOANDRO
PROFESSEUR DES UNIVERSITES, UNIVERSITE DU MANS

Thèse soutenue publiquement le **15 décembre 2023**, devant le jury composé de :

KARINE MASENELLI-VARLOT, PROFESSEURE DES UNIVERSITES, INSA LYON	Présidente
DAMIEN JACOB, PROFESSEUR DES UNIVERSITES, UNIVERSITE DE LILLE	Rapporteur
NIRINA RANDRIANANTOANDRO, PROFESSEUR DES UNIVERSITES, UNIVERSITE DU MANS	Rapporteur
VIRGINIE NACHBAUR, MAITRESSE DE CONFERENCES, UNIVERSITE DE ROUEN NORMANDIE	Examinatrice
EIRINI SARIGIANNIDOU, MAITRESSE DE CONFERENCES HDR, GRENOBLE INP	Examinatrice

Acknowledgements

Epigraphe

Epigraphe

Dédicace

Acronyms and abbreviations

ADF: Annular Dark Field

APT: Atom Probe Tomography

bcc: body-centered cubic

BF: Bright field

BSE: Backscattered Electrons

CALPHAD: CALculation of PHAse Diagrams

CILFM: Chemically Induced Liquid Film Migration

CIP: Cold Isostatic Pressing

CSP: Cross-Section Polisher

dhcp: double hexagonal close-packed

EBSD: Electron Backscatter Diffraction

EDS: Energy Dispersive X-ray Spectroscopy

EPMA: Electron Probe MicroAnalyzer

fcc: face-centered cubic

FE: Finite-Element

FEG: Field Emission Gun

FIB: Focus Ion Beam

GB phase: grain boundary phase

GB: Grain Boundaries

GBDP: Grain Boundary Diffusion Process

GIS: Gas Injecting System

HAADF: High-Angle Annular Dark Field

hcp: hexagonal close-packed

HD: Hydrogen Decrepitation

HREE: Heavy Rare-Earth Element

JM: Jet Mill

LPS: Liquid Phase Sintering

LREE: Light Rare-Earth Element

NPED: Nanobeam Precession Electron Diffraction

PDA: Post-Diffusion Annealing

PED: Precession Electron Diffraction

PIPS: Precision Ion Polishing System

PSA: Post-Sinter Annealing

REE: Rare-Earth Element

ROI: Region Of Interest

SAED: Selected Area Electron Diffraction

SC: Strip Casting

SDD: Silicon Drift Detector

SE: Secondary Electrons

SEM: Scanning Electron Microscope

STEM: scanning transmission electron microscope

TEM: transmission electron microscope

TJs: Triple Junctions

WD: Working Distance

WDS: Wavelength Dispersive X-ray Spectroscopy

Z: atomic number

Outline

Introduction

The global aim to reach carbon neutrality by 2050 requires decarbonization of all sectors, among others the transport sector. In France, for example, the greenhouse gas emissions from the transport sector are the highest compared to other economic sectors, and account for around 30% of total greenhouse gas emissions (see Figure 1).

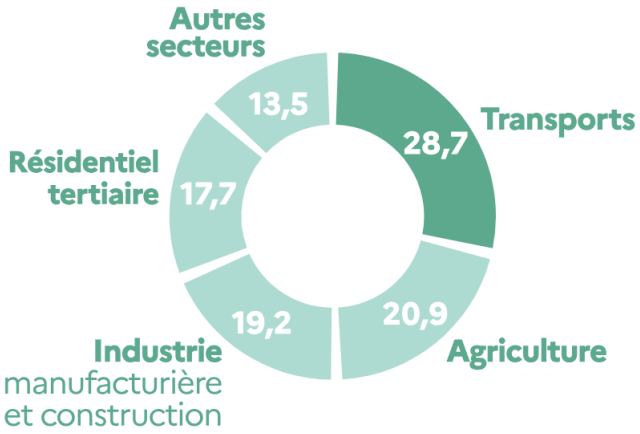

Figure 1: Greenhouse gas emissions (in %) from economic sectors in France for the year of 2020. Adapted from the website of the French ministry of ecological transition.

This has led to an accelerated shift to electric vehicles (EV). The latter play an important role in reducing greenhouse-gas emissions and dependence on fossil fuel. According to the International Energy Agency[1], EV sales accounted for 14% of total car sales worldwide in 2022 and are expected to raise up to 18% by the end of 2023. Today, about 80-90% of EV use rare-earth permanent magnets in their traction motors[2]. Among these rare-earth permanent magnets, sintered NdFeB magnets are the most used because they produce the highest energy density, enabling miniaturization of the EV motor while ensuring enhanced performance (see Figure 2).

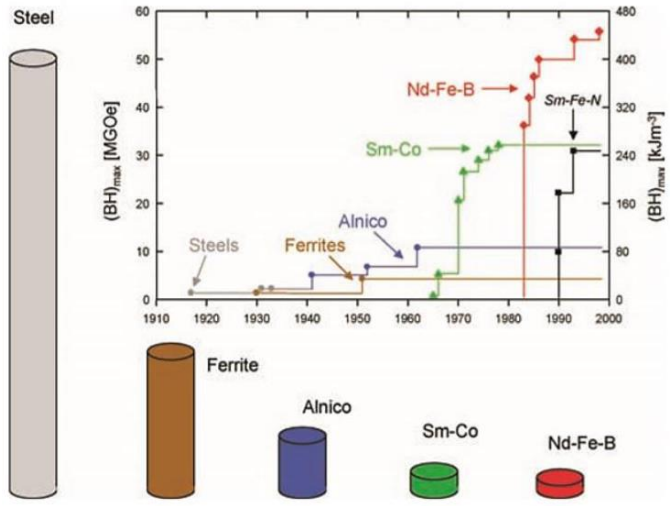

Figure 2: Evolution of $(BH)_{max}$ at room temperature for permanent magnets during the 20th century and their relative volume for the same energy density. Adapted from Gutfleisch et al[3].

Despite having the highest energy density, a main drawback of NdFeB magnets is their poor thermal stability. This leads to a considerable loss in their ability to resist demagnetization effects (characterized by a parameter called coercivity) at the operating temperature of traction motors (150°C-200°C). To overcome this problem, a part of Nd is substituted with heavy rare-earth elements (HREE) such as Dy.

As the sales of EV vehicles will continue to grow, this means that the demand for NdFeB magnets and HREE will increase. However, according to the EU's list for critical raw materials published in 2023[4], China is the only supplier of HREE (100%). This underlines the great vulnerability of HREE supply chain for European industry (see Figure 3).

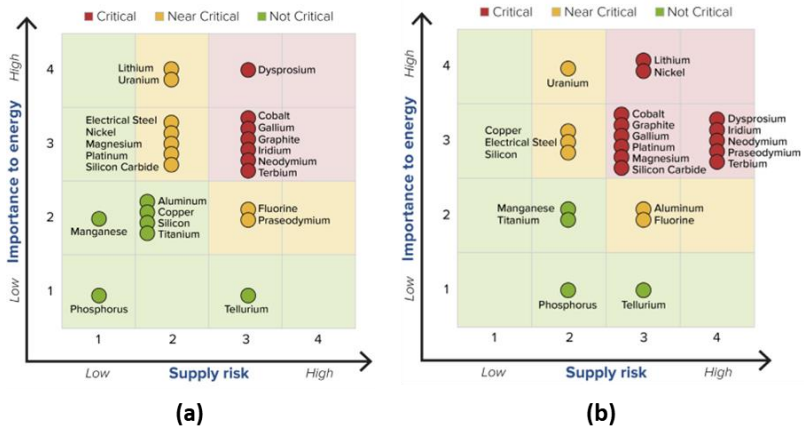

Figure 3: Criticality matrix for (a) the short term (2020 to 2025) and (b) the medium term (2025 to 2035). Adapted from the critical materials assessment issued in 2023 by the U.S department of energy[5].

In addition, it is important to note that when Dy substitutes Nd, its magnetic moments couple antiparallel with the Fe ones, leading to a decrease in the energy density of the sintered NdFeB magnet. As the operating temperature of the application using the NdFeB magnet increases, more Dy is required to increase the coercivity of the magnet so it can operate at this temperature. Simultaneously, the higher the amount of Dy, the lower the energy density. This can be seen in Figure 4.

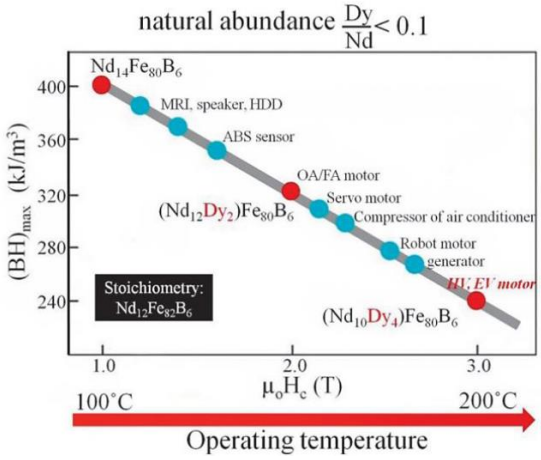

Figure 4: Maximum energy product (BH)max and coercivity H_c of commercial Nd-Fe-B sintered magnets according to their composition. Adapted from Sepehri-Amin et al[6].

Facing these limitations, the research around NdFeB magnets focuses on enhancing the magnetic properties of sintered NdFeB magnets with a reduced amount of Dy. These efforts have led to the development of the Grain boundary diffusion process (GBDP) in 2000. The latter enables to concentrate the Dy in the magnet "weak points" instead of being homogenously distributed, which allows reducing Dy usage and enhancing the magnet properties. Today, the GBDP remain the most efficient technique to produce NdFeB magnets with minimum Dy content for high-temperature applications. However, there are still some limitations regarding this process. These limitations detailed later in chapter I, are related to the lack of understanding of the mechanism(s) that controls the distribution of Dy inside the magnet during the GBDP.

In this work, sintered NdFeB magnets were fabricated at the pilot line of the CEA/LITEN. These magnets were annealed at different temperatures. Then, their magnetic properties were measured before and after annealing using the hysteresigraph system to determine the optimal annealing temperature. The microstructure of the optimally annealed sintered NdFeB magnet was then characterized using scanning (SEM) and transmission (TEM) electron microscopy techniques. Hereafter, the GBDP was applied to the optimally annealed NdFeB magnet, and the changes in the magnetic and microstructural properties that occurred were reported. Finally, the distribution of Dy inside the magnet was modeled by considering the experimental findings.

This manuscript is organized in five chapters.

Chapter I presents the state of art framing the thesis work. Thus, after recalling the magnetic properties of NdFeB magnets, their microstructure is presented in detail and the microstructure-coercivity relationship is clarified. Finally, the GBDP is defined, and the underlying mechanisms proposed in literature are stated.

Chapter II reports the material, instruments, and experimental procedures that were used in this study. First, the fabrication process of sintered NdFeB magnet and the GBDP protocol are described. Then, the challenges faced during sample preparation for microstructural characterization are highlighted. Finally, the magnetic and microstructural characterization methods are presented. A particular attention is given to the Energy dispersive X-ray spectroscopy (EDS) and Wavelength dispersive X-ray spectroscopy (WDS) techniques. The quantification techniques used in EDS to quantify the chemical composition of the materials are detailed.

Chapter III provides a detailed characterization of the microstructure of sintered NdFeB magnets prior to the last step (Dy diffusion) that is the subject of the next chapter. This characterization is mandatory to track the evolution of the microstructure due to Dy diffusion.

Chapter IV describes the magnetic properties and the structure of the polycrystalline NdFeB magnet after the diffusion of Dy in it. The diffusion of the Dy via the grain boundaries will be evidenced; this is the so-called Grain Boundary Diffusion Process (GBDP).

Chapter V presents simulations used to understand the underlying mechanism(s) that control the distribution of Dy inside the NdFeB magnet. The mechanisms proposed in literature are first tested one by one by using new hypotheses issued from the experimental findings of chapter IV. Finally,

new elements are proposed in this work to consider that better explain the microstructural changes occurring during the GBDP.

We conclude the manuscript by recalling the main results of this thesis work. The perspectives are also given.

1. Chapter I: State of the art

This chapter recapitulates the state of the art regarding sintered NdFeB permanent magnets, and reviews the research devoted to tailor their coercivity. It is divided into three sections:

- The first section discusses the origin of the outstanding magnetic properties of NdFeB magnets. After explaining how the performances of the magnets are characterized, the relation between the performances and the intrinsic magnetic properties is clarified. A particular attention is devoted for the concept of coercivity.
- The second section describes the microstructure of NdFeB magnets and the related properties. In particular, how the understanding of the role of secondary phases present in polycrystalline NdFeB magnets have helped to improve their coercivity via GB engineering.
- The third section is dedicated for the grain boundary diffusion process (GBDP), in which we explain how this process is used to further improve the coercivity of the NdFeB magnet and how it modifies its microstructure. In addition, the mechanisms proposed in literature to account for microstructural modifications induced by GBDP are reviewed.

1.1 Magnetic properties

1.1.1 Performances of magnets

The performances of magnets[7] are determined from the measurement of the so-called hysteresis loop. The latter is a 4-quadrant J-H or B-H loop that shows the variation of the polarization J (or the magnetic flux density B) of the magnet when varying the intensity of an external applied magnetic field H (Figure 5).

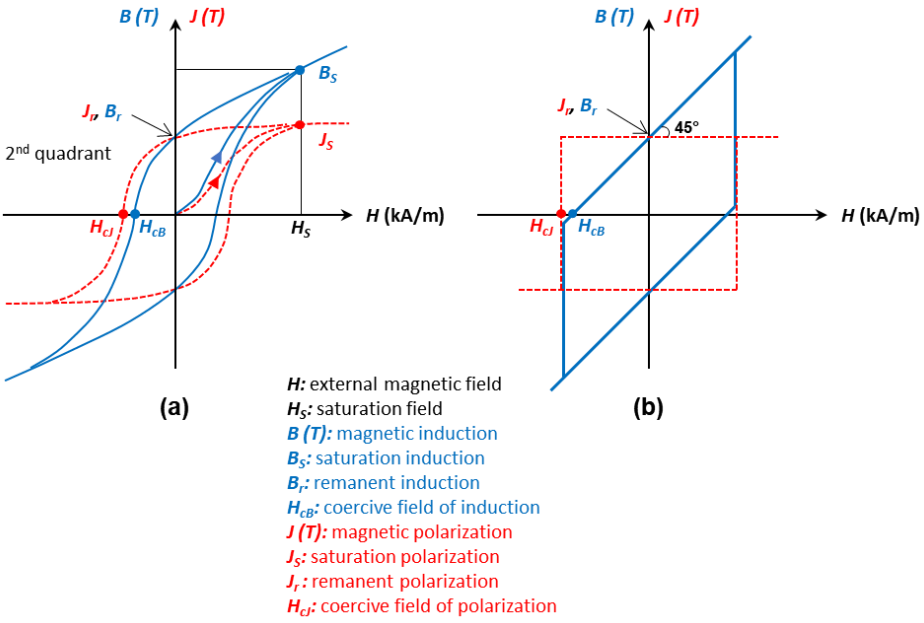

Figure 5: *J-H* and *B-H* hysteresis loops of (a) a real permanent magnet and (b) an ideal permanent magnet. *J-H* and *B-H* loops are related by Eq. (1.1). A permanent magnet has only one remanence (i.e., residual magnetization) but two definitions of coercivity (i.e., coercive fields). This is because $J_r = B_r$ while $H_{cJ} \neq H_{cB}$. H_{cJ} is the field required to reduce the polarization to zero while H_{cB} is the field required to reduce the magnetic induction to zero. It is necessarily that $H_{cJ} > H_{cB}$. Usually, *B-H* loop is used by engineers while *J-H* loop is more adapted by physicists. Adapted and modified from Degauque[8].

The physical quantity J (or M related to J as $J = \mu_0 M$, where $\mu_0 = 4\pi \times 10^{-7}$ Henry/meter is the vacuum permeability) reflects the density of magnetic moments developed into the materials whereas the amount B accounts for the total magnetic flux density into the material. Obviously, the magnetic induction occurring in the material, B, is the (vectorial) summation of the induced field, resulting from the magnetic moments M, and the external field H. The relation between J, B and H is given by Eq. (1.1):

$$\vec{B} = \mu_0 \left(\vec{H} + \vec{M}\right) = \mu_0 \vec{H} + \vec{J}, \qquad (1.1)$$

where $\vec{B}$ is the magnetic flux density in tesla (T), $\vec{H}$ is the external magnetic field in tesla (A/m), $\vec{M}$ is the magnetization in (A/m), and $\vec{J}$ is the polarization in (T).

In practice, the measure of the hysteresis loop starts by applying an external magnetic field H to a magnet in a demagnetized state. As a result, the polarization J of the latter will rapidly increase and reach an asymptotic value known as the saturation polarization J_S at an external field strength known as the saturation field H_S. At this state, all the magnetic moments are aligned parallel to the external applied field, hence further increasing the intensity of the applied external field will not increase the polarization. Then, when the intensity of H decreases, J decreases and reaches a non-zero value at $H = 0$ (1st quadrant). The polarization at $H = 0$ is known as the remanent polarization or remanence J_r. It represents the residual polarization stored inside the magnet in the absence of an external magnetic field. Further increase in the intensity of H in the negative values (i.e., in an opposite direction to the initial polarization) will decrease the polarization until it reaches zero at

H = -H_{cJ} (2nd quadrant). H_{cJ} is known as the coercive field of polarization or the coercivity (hereafter, it will be simply referred to by H_c). It represents the intensity of the external magnetic field at which the magnet is fully demagnetized. This parameter is particularly important since it translates the resistance of the magnet to the demagnetization in applications. Beyond H = -H_{cJ}, the polarization J continues to decrease (i.e., increases in the negative sense) until it reaches a value of -J_S. Finally, when H is again applied in the positive direction, J increases from -J_S to J_S and the hysteresis loop is closed.

Since magnets usually operate under a demagnetizing field, a particular interest is given to the 2nd quadrant of the hysteresis loop, known as the demagnetization curve. The latter helps explain the behavior of the magnet under a demagnetizing field by providing various indispensable magnetic properties. Besides revealing the J_r and H_{cJ} values, it also gives the maximum energy product $(BH)_{max}$ of the magnet and the squareness factor (SF) of the demagnetization curve. $(BH)_{max}$ represents a figure of merit of the hard magnet, i.e., it represents the maximum energy per volume unit that a magnet can deliver in a magnetic circuit. Schematically, $(BH)_{max}$ corresponds to the largest rectangle that can be fit under the demagnetization curve (B-H) and gives. The intrinsic limitation of the value of $(BH)_{max}$ is given by Eq. (1.2):

$$(BH)_{max} \leq \frac{\mu_0 \times M_r^2}{4} = \frac{J_r^2}{4\mu_0} = \frac{B_r^2}{4\mu_0} \tag{1.2}$$

SF is another parameter of great significance as it characterizes the stability of the magnets during the application. This parameter is calculated by determining the ratio of the knee field H_k and the coercive field H_{cJ} as shown in Eq. (1.3).

$$SF = \frac{H_k}{H_{cJ}}, \tag{1.3}$$

where H_k corresponds to the external magnetic field at which the polarization reduces to 90% of remanence J_r (see Figure 6). For an ideal magnet, the SF is equal to 1, which indicates that below the coercive field, there is no reversal of polarization. For real magnets, this is almost impossible to achieve due to the heterogeneity of the material and the presence of defects, however for sintered NdFeB magnets SF as high as 0.98 are obtained. If the SF is closer to unity, the value of is H_{cJ} can be considered as a limit for the application by the designers.

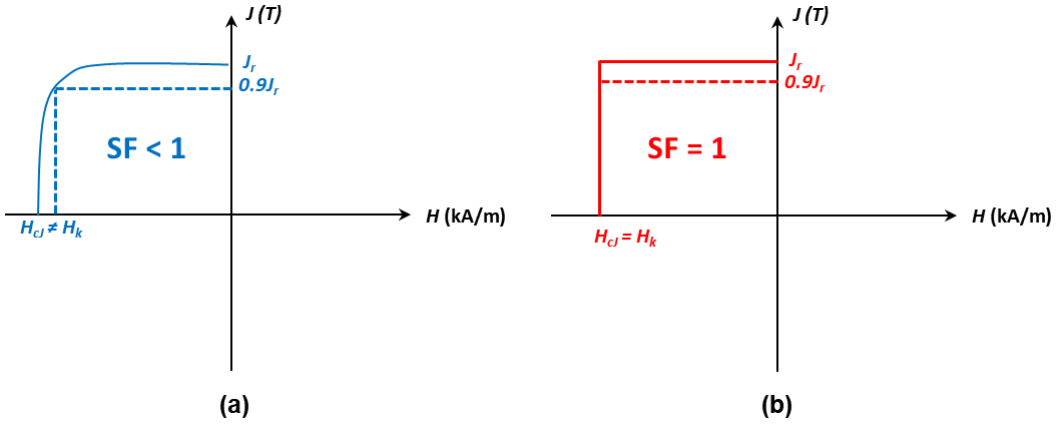

Figure 6: Schematic representation of the squareness of the demagnetization curve in the case of (a) real magnet and (b) ideal magnet.

Finally, the two independent values, namely the energy product $(BH)_{max}$ and coercivity H_{cJ} characterize together the performance of hard magnets. They are tabulated for commercial grades and widely considered by magnetic systems designers for the selection of magnetic materials. Obviously, the performances are related to the intrinsic magnetic properties of materials which will be detailed in the following. With an energy product that can exceeds 400 kJ/m^3 and a coercive field higher than 1500 kA/m (at room temperature), sintered NdFeB magnets are largely used in applications requiring high performances and compactness[3].

1.1.2 Atomic-scale magnetism

Magnetism in materials originates at the atomic level. The quantum theory states that an electron has two angular momenta: an orbital angular momentum $\vec{l}$ and a spin angular momentum $\vec{s}$. The first is a characteristic property of the orbital motion of the electron (similar to a classical angular momentum but with the difference that it is a quantized value) while the second is a quantum mechanical degree of freedom that has no classical analog.

In the case of an atom with n electrons, only the electrons in partially filled shells contribute to the total magnetic moment of the atom. These unpaired electrons combine to give non-zero total orbital angular momentum $\vec{L}$ and total spin angular momentum $\vec{S}$:

$$\vec{L} = \sum_{i=1}^{n} \vec{l}_i, \tag{1.4}$$

$$\vec{S} = \sum_{i=1}^{n} \vec{s}_i, \tag{1.5}$$

The above angular momenta give rise to two magnetic moments: an orbital magnetic moment m_L and a spin magnetic moment m_S. The relationship between each angular momentum and the associated magnetic moment is given by:

$$m_L(\mu_B) = -g_L L, \tag{1.6}$$

$$m_S(\mu_B) = -g_S S, \tag{1.7}$$

where $g_L = 1$ and $g_S = 2$ are the Landé g-factors and μ_B is the Bohr magneton. The negative sign is due to the electron negative charge.

From the periodic table, only the 3d-transition metals and the 4f-rare-earth metals exhibit magnetic properties. In the following, their magnetic moments in their pure metallic form are given.

3d-transition metals

The magnetic properties of the 3d-transition metals originate from the electrons that reside in the delocalized 3d shell. Table 1 provides the theoretical and experimental values of the spin and orbital magnetic moments of the 3d-transition metals (Fe, Co, and Ni).

Table 1: Spin and orbital magnetic moments of Fe, Co, and Ni at zero temperature and zero external magnetic field. Theoretical values are taken from Eriksson et al.[9] and experimental values are taken from Madelung[10].

	bcc-Fe		**hcp-Co**		**fcc-Ni**	
	$m_S(\mu_B)$	$m_L(\mu_B)$	$m_S(\mu_B)$	$m_L(\mu_B)$	$m_S(\mu_B)$	$m_L(\mu_B)$
Theory	2.21	0.06	1.57	0.14	0.61	0.07
Experimental	2.13	0.08	1.52	0.14	0.57	0.05

Table 1 shows that the total magnetic moment of the 3d-transition metals is largely given by the spin magnetic moment. Compared to the latter, the orbital magnetic moment is very small, typically of the order of 0.1 μ_B, and its contribution to the total magnetic moment is negligible. The orbital motion of electrons being "quenched" by the crystal field as explained in[11].

4f rare-earth metals[12]

The magnetic properties of the rare-earth (RE) metals originate from the electrons that reside in the strongly localized 4f shell. This shell is screened by the higher energy fully occupied 5s and 5d shells, hence the electrons of the 4f shell are not affected by their environment, which allow applying the Hund rules to calculate their magnetic moments as for single ions RE^{3+} (Table 2). In the case of single ions, an angular momentum J is defined which is equal to L – S for light rare-earth elements (e.g., Nd, Pr) and L + S for heavy rare-earth elements (e.g., Dy, Tb). Consequently, the magnetic moment is given by the following equation:

$$m_J^{theo}\ (\mu_B) = g_R J, \tag{1.8}$$

where g_R is the Landé g-factor defined by $g_R = 1 + \frac{J(J+1) + S(S+1) - L(L+1)}{2J(J+1)}$.

Table 2: Magnetic properties of some light trivalent rare-earth ions (Pr, Nd) and heavy trivalent rare-earth ions (Tb, Dy). n is the number of 4f electrons n = Z - 57, S is the total spin angular momentum: S is n/2 for n < 7 and (14 - n)/2 for n > 7, L is the total orbital angular momentum, J is the total angular momentum: J = L – S for n < 7, J = L + S for n > 7, g_R is the Landé g-factor given by $g_R = 1 + \frac{J(J+1)+S(S+1)-L(L+1)}{2J(J+1)}$, m_J^{theo} is the theoretical total magnetic moment and m_J^{exp} is the experimental total magnetic moment. Theoretical values are taken from Coey[13]. Experimental values for Tb and Dy are taken from Oudet[14].

	Z	n	S	L	J	g_R	m_J^{theo} (μ_B) = $g_R \times J$	m_J^{exp} (μ_B)
Pr^{3+}	59	2	1	5	4	4/5	3.2	-
Nd^{3+}	60	3	3/2	6	9/2	8/11	3.3	-
Tb^{3+}	65	8	3	3	6	3/2	9	9.28
Dy^{3+}	66	9	5/2	5	15/2	4/3	10	10.4

3d-4f intermetallic compounds: $Nd_2Fe_{14}B$

The combination of 3d and 4f metals is at the origin of designing many powerful permanent magnets. Of particular interest is the ternary $Nd_2Fe_{14}B$ intermetallic compound as it possesses the highest $(BH)_{max}$. $Nd_2Fe_{14}B$ has a tetragonal crystal symmetry as presented in Figure 7. The structure was first revealed by Herbst et al. (USA)[15,16] using neutron powder diffraction techniques and confirmed by Givord et al.[17] (France) and Shoemaker et al. (USA) who both used X-ray diffraction technique as well as Sagawa et al.[18] (Japan) by means of electron diffraction technique. They all revealed that $Nd_2Fe_{14}B$ crystallizes in an elegant yet quite complex tetragonal structure of space group $P4_2/mnm$ and lattice parameters a = 8.80 Å and c = 12.19 Å. The tetragonal structure contains 68 atoms in its unit cell (i.e., 4 formula units of $Nd_2Fe_{14}B$) distributed as follows: 4 atoms of boron, 8 atoms of neodymium and 56 atoms of iron.

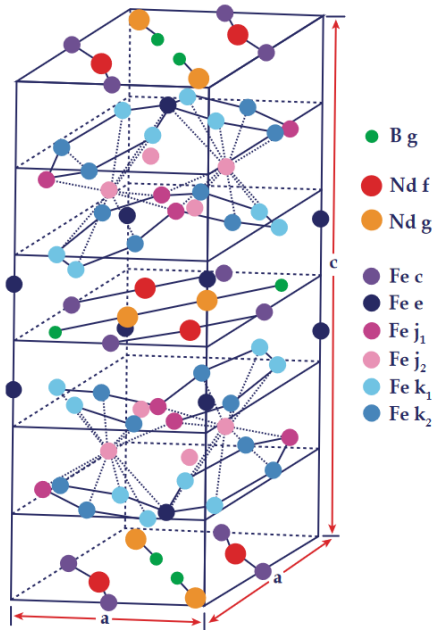

Figure 7: Schematic of the crystal structure of the $Nd_2Fe_{14}B$ phase. The c/a ratio is exaggerated to emphasize the puckering of the iron nets[15].

As shown in Figure 7, the $Nd_2Fe_{14}B$ unit cell is composed of 8 layers perpendicular to the c-axis. All the Nd and B atoms, but only 4 of the 56 Fe atoms, reside in planes z = 0 and z = $\frac{1}{2}$ c. The remaining Fe atoms are distributed between these 2 planes and form fully connected hexagonal nets. Depending on their local atomic environment (i.e., number of the nearest neighbors), the 68 atoms can be classified into crystallographic sites[1]: there are 6 inequivalent crystallographic sites for Fe ($16k_1$, $16k_2$, $8j_1$, $8j_2$, 4e and 4c), 2 inequivalent crystallographic sites for Nd (4f, 4g) and 1 crystallographic site for Boron (4g). These sites can be distinguished by their corresponding Weigner-Seitz atomic cell volume reported in Table 3 (except for Boron).

The magnetization of the $Nd_2Fe_{14}B$ phase comes mainly from the iron sublattice. Table 3 lists the contribution of each Fe atom according to its crystallographic site. At saturation, an $Nd_2Fe_{14}B$ compound has a magnetization of 37.7 μ_B/formula unit. The contribution of Nd is only 3.2 μ_B, or 6.4 μ_B/formula unit[16].

Table 3: Weigner-Seitz atomic cell volume of the Nd and Fe atoms at their various sites in the 2:14:1 unit cell taken from Isnard et al.[19] Theoretical and experimental values of the spin magnetic moments of the Fe atoms at their various sites in the 2:14:1 unit cell taken from Ching et al.[20] and Givord et al.[21] respectively.

Site	Nd (4f)	Nd (4g)	Fe (4e)	Fe (4c)	Fe ($8j_1$)	Fe ($8j_2$)	Fe ($16k_1$)	Fe ($16k_2$)
Weigner-Seitz atomic cell volume (Å^3)	31.40	32.24	11.83	12.30	12.11	12.70	11.75	11.55
m_S^{theo} (μ_B) (T = 0 K)			1.99	2.97	2.48	3.40	2.15	2.28
m_S^{exp} (μ_B) (T = 4.2 K)			2.10	2.75	2.30	2.85	2.60	2.60

1.1.3 Soft and hard ferromagnetism

Ferromagnetism is a form of magnetic order that arises in some substances. It is expressed by a temperature dependent spontaneous macroscopic magnetization M (T) allowing the ferromagnetic material to interact with external magnetic fields (e.g., attraction of Fe by a magnet). The magnetization originates from the spontaneous ordering of the individual microscopic magnetic moments for temperatures lower than a critical value, characteristic of the material and named the Curie temperature. Basically, magnetic moments are carried by neighboring atoms are coupled by short-range exchange interaction which tends to align them. This exchange interaction is in competition with the thermal agitation which tends to disrupt the magnetic ordering. Ferromagnetism occurs in few substances such as 3d-transition metals (iron, nickel, cobalt), their alloys, and some 4f-rare-earth elements (lanthanides). However, the magnetic character can depend on the crystallographic structure (e.g.: α-Fe is ferromagnetic while γ-Fe is antiferromagnetic). In

[1] We note that the site notation adopted here is the Wyckoff notation. There are other site notations given by Shoemaker et al. and Givord et al. The correspondences between notations can be found in the review of Herbst[16].

addition, it is possible for a material to display ferromagnetism even if its components are non-ferromagnetic in their pure state (e.g., alloys of manganese MnAl or MnAlC).

Ferromagnetic materials could be classified as soft, semi-hard or hard magnetic materials depending on the contribution of the magneto-crystalline energy in the total internal free energy upon the application of an external magnetic field. The underlying concept can be introduced in the frame of the coherent rotation of the magnetic moments (Stonner Wolfarth model) which is, however, a simplification of the magnetism of real materials. Let us first consider an ideal infinite ferromagnet at a given temperature such that M (T) = M = constant. Under an external magnetic field H_{ext} along the z-direction, the free energy E(θ) of the ferromagnet is given by Zeeman energy:

$$E(\theta) = \mu_0 \boldsymbol{M} \times \boldsymbol{H}_{ext} = \mu_0 M H_{ext} \cos(\theta) \quad (1.9)$$

where H_{ext} is the projection of the external field along +z and θ is the angle between M and +z.

Minimization of the above free energy with respect to θ results in θ = 0 for $H_{ext} > 0$ and θ = π for $H_{ext} < 0$. This means that the magnetization is aligned with the external magnetic field. If the isotropic ferromagnet is initially magnetized along +z, a small external magnetic field applied along -z suffices to flip the magnetization direction (and vice-versa). Such a ferromagnet for which all directions of magnetization are equivalent is described as a soft isotropic magnetic material. This behavior is shown in Figure 8(a).

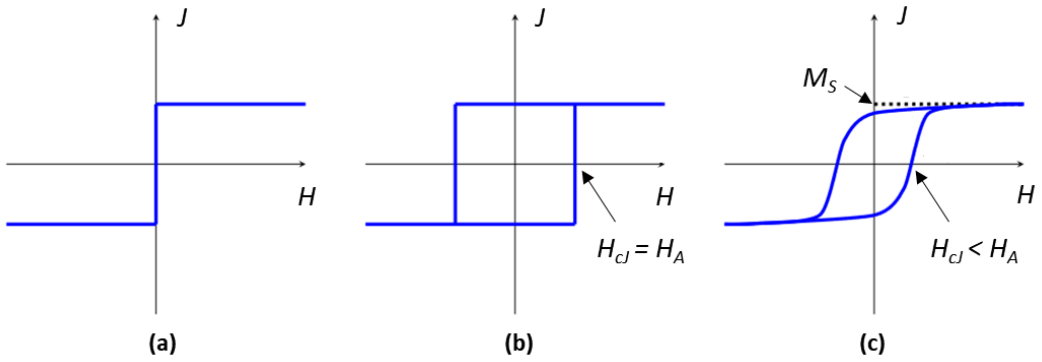

Figure 8: Variation of magnetization in a ferromagnetic system under an external applied field in the case of (a) Ideal isotropic (soft) ferromagnet, (b) Ideal anisotropic (hard) ferromagnet and (c) Real finite ferromagnet. Adapted and modified from Boust[22].

In some ferromagnets, notably NdFeB, the microscopic magnetic moments are preferentially oriented along a specific crystallographic direction known as easy axis of magnetization or simply easy axis. This results in a magnetic response driven by the so-called magneto-crystalline anisotropy rather than the sole Zeeman term. Compared to the isotropic ferromagnet, an additional work is required here to be able to change the direction of magnetization of the system, which is why an anisotropic ferromagnet is described as hard. This behavior is illustrated in Figure 8(b). The magneto-crystalline anisotropy can be accounted by adding a new term to the free energy. This term is given by the Stoner-Wohlfarth[23] model:

$$E_a(\theta) = K_1 sin^2(\theta) + K_2 sin^4(\theta) + K_3 sin^6(\theta) + \cdots + K_i sin^{2i}(\theta) \quad (1.10)$$

where $E_a\ (\theta)$ is the magneto-crystalline anisotropy energy, K_i is the i[th] order anisotropy constant expressed in MJ/m^3, and θ is the angle between M and the easy axis.

Generally, in the case of the NdFeB magnet, only the first term of $E_a\ (\theta)$ is considered. The latter becomes:

$$E_a\ (\theta) \approx\ K_1 sin^2(\theta) \tag{1.11}$$

In the absence of an external magnetic field, the energy of the ferromagnet is given by:

$$E\ (\theta) =\ E_a\ (\theta) \approx\ K_1 sin^2(\theta) \tag{1.12}$$

if $K_1 > 0$, the magneto-crystalline anisotropy favors alignment of the magnetization along the z-easy axis (uniaxial anisotropy); if $K_1 < 0$ the magnetization favorably lies in the basal plane perpendicular to the z-easy axis (planar anisotropy).

In the presence of an external magnetic field, the energy of the ferromagnet is given by:

$$E\ (\theta) =\ \mu_0 M H_{ext} \cos(\theta) +\ K_1 sin^2(\theta) \tag{1.13}$$

Considering the case of $K_1 > 0$ (case of NdFeB magnet at room temperature), the minimization of the above energy with respect to θ calculated by solving $\frac{dE(\theta)}{d\theta} = 0$ yields:

- θ = 0, M = +M_S. The system is stable for $H_{ext} > 0$ and locally stable for $H_{ext} \in]-\frac{2K_1}{\mu_0 M_S}, 0\ ]$,
- θ = π, M = -M_S. The system is stable for $H_{ext} < 0$ and locally stable for $H_{ext} \in [0, \frac{2K_1}{\mu_0 M_S}\ [$.

This means that if the anisotropic ferromagnet is initially magnetized along +z, it requires an external magnetic field of magnitude $\frac{2K_1}{\mu_0 M_S}$ to flip the magnetization direction (vs quasi zero in the case of the isotropic ferromagnet). A visual presentation is provided in Figure 9.

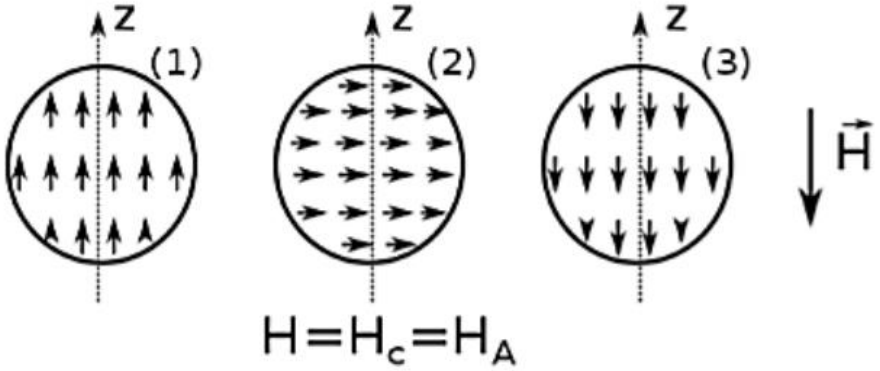

Figure 9: Magnetization reversal in ideal anisotropic ferromagnet according to the Stoner-Wohlfarth model also known as the coherent rotation of magnetization. (1) and (3) correspond to the energy minima configurations while (2) is the hard-axis magnetization configuration. Adapted from Ciuta[24].

The $\frac{2K_1}{\mu_0 M_S}$ value is known as the anisotropy field H_A; it represents the magnetic field required to change the magnetization direction M from an easy axis configuration to a hard axis configuration. Ideally (for a perfect system), H_A is a measure of the resilience of the anisotropic ferromagnet to external demagnetizing magnetic fields i.e., it would equate the coercivity defined earlier. Practically (for a real system), this is not quite the case. For instance, in the case of NdFeB magnets, the anisotropy field H_A is around 8 T at room temperature. However, the measured coercivity for these magnets is only about 20-30% of H_A. This discrepancy is known as Brown's paradox. The latter explains that the defects present in the microstructure locally lower the magneto-crystalline energy. As a result, the local magnetization carried out within the region around these defects requires a lower external magnetic field to reverse its direction. In this regard, the concept of the activation volume is introduced; it represents the smallest volume in which magnetization reversal occurs before macroscopic propagation. This will be further detailed in section 1.1.5. The takeaway message is that H_A should be regarded as the upper limit of coercivity.

Another anisotropy term to consider in real systems is the shape anisotropy. Except for specific shapes, the shape of a finite ferromagnet generates a magnetic field in its volume called the demagnetizing field H_d. As suggested by its name, H_d opposes the magnetization M and acts to reduce it; hence further lowering the resilience of the magnet to **external** demagnetizing magnetic fields (in other terms, the ferromagnet experiences a demagnetizing field $H = H_{ext} + H_d$). The behavior of real finite ferromagnets is illustrated in Figure 8(c).

The expression of the demagnetizing field vector H_d is given by:

$$H_d = -N \times M, \tag{1.14}$$

$$\text{with } N = \begin{bmatrix} n_{xx} & 0 & 0 \\ 0 & n_{yy} & 0 \\ 0 & 0 & n_{zz} \end{bmatrix}$$

where N is the demagnetizing tensor, a non-homogenous second order tensor whose coefficients verify $n_{xx} + n_{yy} + n_{zz} = 1$ and that depends solely on the magnet shape. The values of N corresponding to some classical magnet shapes are listed in Table 4.

Table 4: Values of the coefficients of the demagnetizing factor N for certain shapes of ferromagnet. Adapted from Hugonnet[25]

Shape	Values of coefficients of N
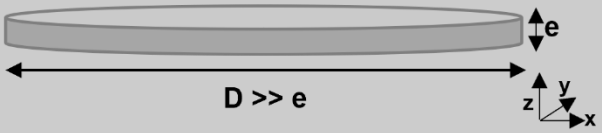	$n_{xx} = n_{yy} = 0$ and $n_{zz} = 1$
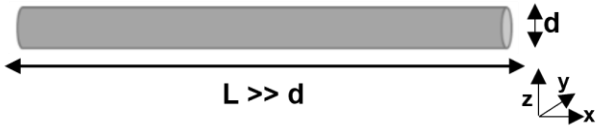	$n_{xx} = 0$ and $n_{yy} = n_{zz} = 1/2$
	$n_{xx} = n_{yy} = n_{zz} = 1/3$

In the case of a disk, the shape anisotropy favors alignment of the magnetization in the plane whereas in the case of a cylinder the shape anisotropy favors alignment of the magnetization along the axis of cylinder. As already said, the shape anisotropy negatively affects the magnetization of the ferromagnet. To avoid shape demagnetization, earlier ferromagnets had to be made in specific shapes such as elongated compass needles and classical horseshoes. This is no longer an issue nowadays, as the discovery of the rare earth – transition metal compounds allow us to prepare permanent magnet in any desired shape. In these compounds, the transition metals provide most of the saturation magnetization (37.7 μ_B/formula unit for Fe vs 6.4 μ_B/formula unit for Nd for example) and a high Curie temperature T_C (i.e., strong ferromagnetism); whereas the rare-earths highly increase the magnetic anisotropy K_1 due the spin-orbit coupling, favoring a [001] easy-axis alignment of the magnetization, and enhancing the stability of the magnet against demagnetizing fields (i.e., hard magnetism). These features make the rare earth – transition metal compounds excellent choice to design permanent magnets. In fact, for an intermetallic compound to be considered as a candidate for making practical permanent magnets it needs to satisfy the following requirements:

- Curie temperature $T_C > 500$ K,
- Low symmetry crystal structure, preferably uniaxial (tetragonal, rhombohedral, or hexagonal),
- $K_1 > 0$ so that the c-axis is the easy direction,
- Saturation magnetization $J_S = \mu_0 M_S > 1$ T.

These requirements are satisfied for the tetragonal $Nd_2Fe_{14}B$ and $Dy_2Fe_{14}B$ intermetallic compounds as it can be seen from Table 5. The difference between these compounds is that $Nd_2Fe_{14}B$ has a higher saturation polarization while $Dy_2Fe_{14}B$ has a higher anisotropy field.

Table 5: Magnetic properties of $Nd_2Fe_{14}B$ and $Dy_2Fe_{14}B$ compounds determined at room temperature. m_{tot} is the total magnetic moment per formula unit, K_1 is the anisotropy constant, J_S is the saturation polarization determined, $\mu_0 H_A$ is the anisotropy field and T_C is the Curie temperature. The values are taken from Coey[13].

	m_{tot} (μ_B/f.u.)	K_1 (kJ/m^3)	J_S (T)	$\mu_0 H_A$ (T)	T_C (K)
$Nd_2Fe_{14}B$	37.7 m_{tot}^{Nd}= 6.4; m_{tot}^{Fe}= 31.3	4900 K_1^{Nd}= 3800; K_1^{Fe}= 1100	1.61	7.7	588
$Dy_2Fe_{14}B$	11.4	4200	0.72	15	598

1.1.4 Role of magnetic domains

Besides the short-range exchange interaction, another form of interaction that occurs between the individual magnetic moments is the long-range dipolar (magnetostatic) interaction. The latter introduce a new form of energy, magnetostatic energy, to be added to the energy balance of the real ferromagnetic system (Eq. (1.13)). Minimization of this energy requires the system to split up in magnetic domains in which the magnitude of the magnetization $\boldsymbol{M}$, known as M_S, is uniform. The direction of magnetization varies from one domain to another and typically lies along a crystallographic axis. In equilibrium, the magnetization summed over the entire volume of the system is zero, and the ferromagnetic system is in unmagnetized state (see Figure 10 (a)). The magnetization can be restored by subjecting the ferromagnet system to an external magnetic field that acts to eliminate the magnetic domains in each crystallite (see Figure 10 (b)).

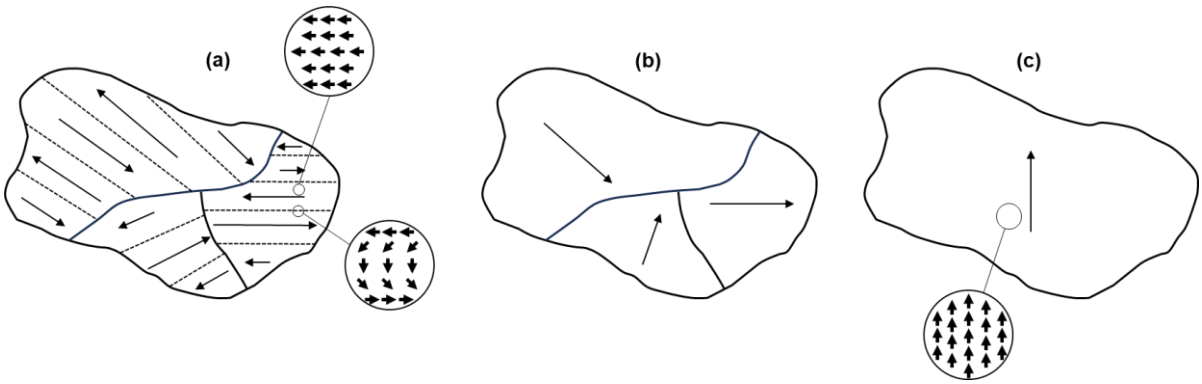

Figure 10: Schematic representation of the magnetic domains in a real NdFeB magnet in its (a) unmagnetized state (M_s = 0) and (b) remanent state (M_s = M_r ≠0). Grain boundaries and domain boundaries are represented by the solid and dotted lines respectively. Inserts are a magnified view showing the alignment of the atomic moments within the magnetic domains and in the domain boundaries. In (c) the case of an ideal homogenous NdFeB magnet is shown in which there is no occurrence of magnetic domains. Adapted and modified from Coey[13].

The boundary of the magnetic domains is not abrupt as clarified in the magnified insert taken at the magnetic domain boundary in Figure 10 (a). If the boundary is abrupt, atoms on either side of the boundary will interact via the powerful exchange interaction consequently increasing the energy of the system. To avoid this configuration, the reversal of the magnetization from one magnetic

domain to another is spread over many atomic planes. The length of these planes defines the domain wall width denoted by δ_w (in nm). A particular type of a domain wall is the Bloch domain wall for which the magnetization rotates in the plane of the domain wall as illustrated in Figure 11 taken from Coey[13].

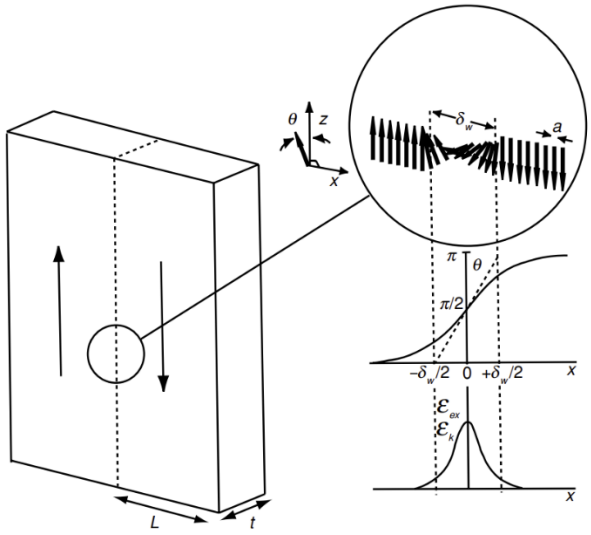

Figure 11: Two dimensional Bloch-type domain wall where δ_w indicates the domain wall width. Adapted from Coey[13].

The width of a Bloch-type domain wall is given by:

$$\delta_w = \pi \left(\frac{A_{ex}}{K1}\right)^{1/2} \times 10^9, \tag{1.15}$$

where δ_w is the domain wall width in nm, A_{ex} is the exchange stiffness in J.m^{-1} and K_1 is the magnetocrystalline anisotropy constant in J.m^{-3}.

Moreover, the energy associated to the formation of the domain wall is given by:

$$\gamma_w = 4(A_{ex} \times K_1)^{1/2}, \tag{1.16}$$

where γ_w is the domain wall energy expressed in J.m^{-2}.

Another important length scale is the exchange length l_{ex} below which atomic exchange interactions dominate dipolar interactions. l_{ex} is given by:

$$l_{ex} = (A_{ex}/\mu_0 M_S^2)^{1/2}, \tag{1.17}$$

Finally, another important length scale to be considered in a magnet is the critical single-domain particle size d_c. The latter is the largest crystallite that the system can create below which the formation of a domain wall is energetically unfavorable and above which a multi-domain configuration is stable. Keep in mind that the formation of crystallites is dictated by the competition between the short-range exchange interaction and the long-range dipolar interaction. The system

cannot split itself infinitely into crystallites because the energy needed to create domain walls will exceed the exchange energy which will defy the initial goal of minimization of energy.

$$d_c = 18\gamma_w/\mu_0 M_S^2, \tag{1.18}$$

In Table 6, the values of all the above defined parameters for both $Nd_2Fe_{14}B$ and $Dy_2Fe_{14}B$ compounds are reported.

Table 6: Micromagnetic properties of $Nd_2Fe_{14}B$ and $Dy_2Fe_{14}B$ compounds. All values are taken from Coey[13] except for the value of A_{ex} of $Dy_2Fe_{14}B$ taken from Zickler[26].

	A_{ex} ($J.m^{-1}$)	K_1 ($J.m^{-3}$)	M_S (A/m)	δ_w (nm)	γ_w ($J.m^{-2}$)	l_{ex} (nm)	d_c (µm)
$Nd_2Fe_{14}B$	8×10^{-12}	4.9×10^{6}	1.28×10^{6}	4.0	25×10^{-3}	2.0	0.22
$Dy_2Fe_{14}B$	7.7×10^{-12}	4.2×10^{6}	0.57×10^{6}	4.3	23×10^{-3}	4.3	1.01

The above defined parameters are of a great importance since the practical extrinsic magnetic properties (coercivity, remanence and $(BH)_{max}$) determined from the hysteresis loop of the magnet greatly depend on them. In fact, the hysteresis loop of a permanent magnet is a direct result of nucleation, propagation, and annihilation of domain walls.

1.1.5 Magnetization reversal in hard magnets

As already explained in section 1.1.3, the Stoner-Wohlfarth model, in which the mechanism of magnetization reversal of magnetic moments is described by a coherent rotation, does not apply for real NdFeB magnet as witnessed by the discrepancy between the coercivity of the magnet and its anisotropy field. This is because a real NdFeB magnet inevitably includes inhomogeneities in its microstructure that give rise to the smaller coercivity observed in practice. Namely, there exist defects with lower magneto-crystalline anisotropy, non-magnetic secondary phases that generate stray fields, and surface irregularities (i.e., grains with sharp corners) with large demagnetizing factors N. These inhomogeneities constitute the "weak points" of a real NdFeB magnet at which the magnetization reversal occurs in two stages: first, reversed magnetic domains start to nucleate in regions around the "weak points", and then the reversed magnetic domains propagate within the entire microstructure as the intensity of the external demagnetizing field increases. The intensity of H_{ext} at which the NdFeB magnet is fully demagnetized corresponds to the coercivity H_{cJ} of the magnet. This mechanism of magnetization reversal is a nucleation-type and is illustrated in Figure 12.

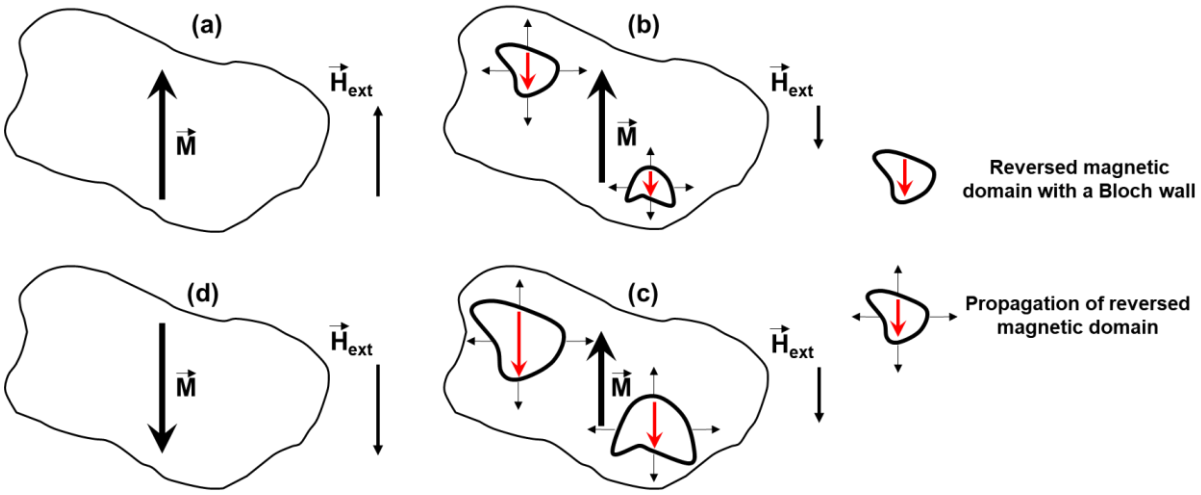

Figure 12: Nucleation-type magnetization reversal mechanism. (a) NdFeB magnet in its saturation state after being subjected to a magnetizing magnetic field, (b) formation of reversed magnetic domains with a Bloch-type domain wall after reversing the direction of the external demagnetizing field, (c) Expansion of the reversed magnetic domains when further increasing the intensity of the external demagnetizing field, and (d) NdFeB magnet in its demagnetized state for $H_{ext} = H_{cJ}$. Adapted and modified from Coey[13].

An empirical equation that takes into account the dependence between the coercivity of the magnet and its microstructure is proposed by Kronmüller[27]:

$$H_{cJ} = \alpha_K^{nuc} \alpha_\psi H_A - N_{eff} M_S, \tag{1.19}$$

where α_K^{nuc} accounts for the effect of the inhomogeneity of the magneto-crystalline anisotropy in regions such as grain boundaries whose anisotropy is lower than the 2:14:1, and α_ψ accounts for misalignment between 2:14:1 grains. N_{eff} is the averaged local effective demagnetization factor that depends on the morphology of the 2:14:1 grains and the secondary phases.

Equation (1.19) clearly shows the intimate relation between the coercivity and the microstructure. An optimized microstructure with refined and smooth $Nd_2Fe_{14}B$ grains[28], minimized amount of secondary phases, and a thin, smooth and defect free GB layer is crucial to increase the coercivity of the magnet. Of particular interest is the defect free GB layer as it contributes the most in enhancing the coercivity. It is well documented in literature that subjecting a NdFeB magnet to a heat treatment, called aging or annealing, leads to microstructural modifications along its grain boundaries giving rise to coercivity improvement. To understand these microstructural modifications and how they increase the coercivity, the microstructure of the NdFeB magnet is first introduced. This is treated in the following section.

1.2 Microstructure of sintered NdFeB magnets

Today, NdFeB magnets are mostly manufactured by the powder metallurgy process involving pressing and sintering steps to obtain the highest magnetic performances of the market. The

coercivity is however still lower than the one expected from the intrinsic properties due to the role of defects acting as nucleation sites for the magnetization reversal (Brown's paradox). Since the discovery of the hard magnetic phase $Nd_2Fe_{14}B$ in 1983, there have been constant efforts in the magnet industry to improve the coercivity. Significant progress has been achieved by a better understanding of the role of secondary phases present in polycrystalline NdFeB magnets. A brief overview of this approach is detailed hereafter.

1.2.1 Role of the manufacturing process

The main steps of the conventional powder metallurgy route used to manufacture anisotropic sintered NdFeB magnets are recapitulated in Figure 13.

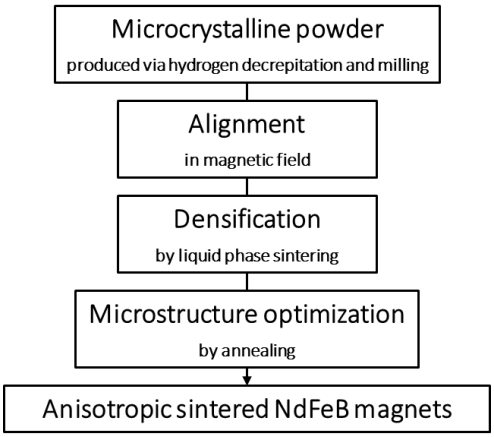

Figure 13: Flow chart illustrating the main steps of the conventional powder metallurgy process used to manufacture anisotropic sintered NdFeB magnets.

The starting alloy (contains the following main elements Nd, Fe, B, and additive elements Al, Cu, Co, Ga, Zr, Nb, Ti) is first pulverized into a coarse powder by hydrogen decrepitation and then transformed into a fine microcrystalline powder by jet milling. Hereafter, the resulting powder is aligned in a magnetic field so that the easy axis of magnetization of its particles (i.e., the c-axis of the $Nd_2Fe_{14}B$ tetragonal phase) are aligned in the same direction, leading to a textured NdFeB powder. The latter is then fully densified into a fully dense anisotropic sintered NdFeB magnet by liquid phase sintering by the Nd-rich phases that are liquid at the sintering temperature. Finally, the sintered magnet is annealed to optimize its microstructure. A detailed description of each step of the manufacturing process is provided later in chapter II.

As a result of the manufacturing process, fully dense anisotropic sintered NdFeB magnets with a relatively complex multiphase microstructure that contains the following: $Nd_2Fe_{14}B$ phase, Nd-rich phases (metallic and oxides) and $NdFe_4B_4$ phase are obtained. The typical microstructure of an anisotropic sintered NdFeB is illustrated in Figure 14.

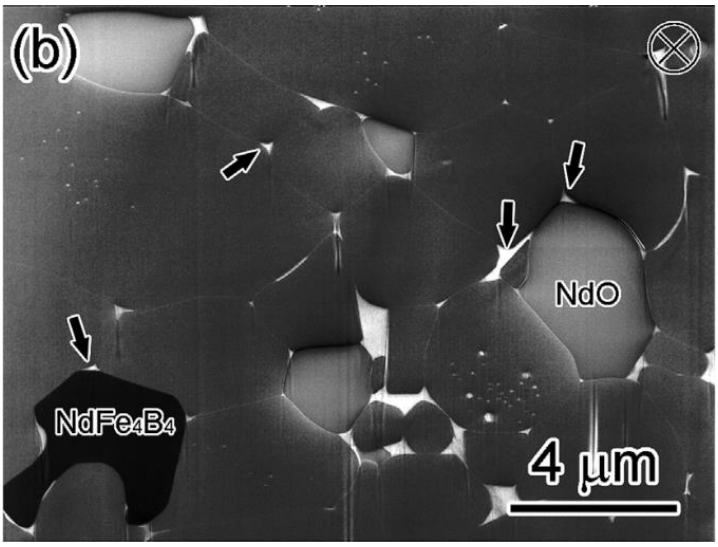

Figure 14: In-Lens secondary electron SEM image showing the typical microstructure of sintered NdFeB magnet.[29]

$Nd_2Fe_{14}B$ phase is seen in uniform grey contrast in Figure 14. $Nd_2Fe_{14}B$ grains have a typical size of 3-10 µm, are highly oriented and constitutes more than 90% of the microstructure of the sintered NdFeB magnet. It is the main magnetic phase in the sintered NdFeB magnet and is the origin of its remarkable extrinsic magnetic properties.

$NdFe_4B_4$ phase seen in black in Figure 14 is the Nd-boride phase. This phase is non-ferromagnetic and constitutes less than 1% of the microstructure of the sintered NdFeB magnet, which is why little interest has been shown in studying this phase.

Nd-rich phases can be seen in bright inhomogeneous contrast and are located at the triple/multiple junctions as well at the grain boundaries. These phases are of major importance in polycrystalline sintered magnets since the coercivity is driven by nanoscale defects of main phase, mainly located near the GBs. Several approaches categorized under the term of Grain Boundary Engineering have been deployed to improve the magnet performances, they involve some composition adjustments and thermal treatment optimization during the process:

- Alloy with excess Nd: An alloy with a composition with an excess Nd content with respect to the stoichiometry of $Nd_2Fe_{14}B$ phase is required. A typical alloy composition would be $Nd_{14}Fe_{80}B_6$ (at%) with respect to $Nd_{11.8}Fe_{82.3}B_{5.9}$ (at%) (i.e., $Nd_2Fe_{14}B$ phase). The excess Nd content leads to the formation of secondary non-magnetic Nd-rich phases (see Figure 15). The importance of these Nd-rich phases stems from the fact that they have a lower melting point with respect to the $Nd_2Fe_{14}B$ phase (the ternary eutectic temperature of L ↔ $Nd_2Fe_{14}B$ + Nd-rich + $NdFe_4B_4$ is 682.2 °C). Hence, they enable liquid phase sintering at relatively low temperature. This densifies the NdFeB magnet while preventing grain growth. In addition, by selecting a composition with an excess Nd content, the precipitation

of bcc-Fe phase could be avoided during the alloy synthesis. The latter is a soft magnetic phase and is highly detrimental for coercivity.

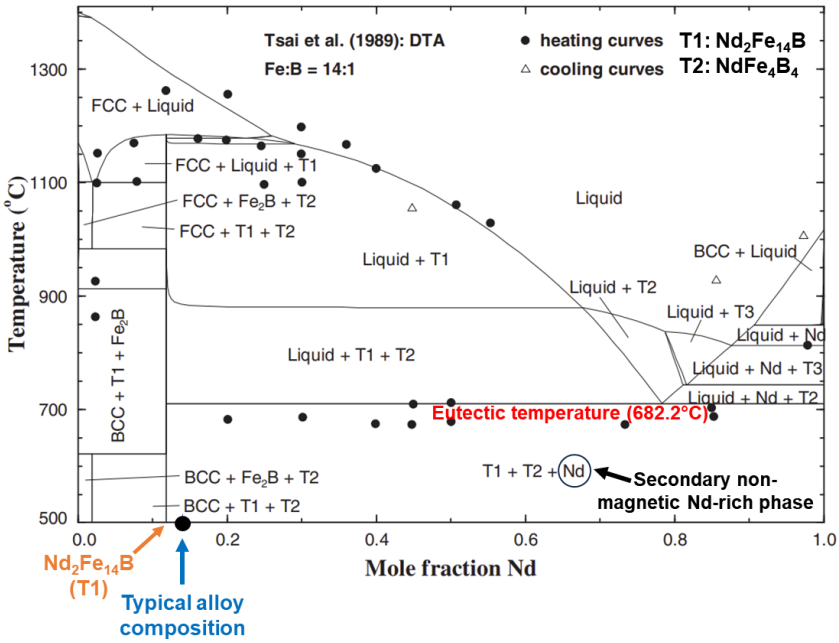

Figure 15: Pseudo binary phase diagram of the Nd-Fe-B system at Fe/B ratio of 14. The $Nd_2Fe_{14}B$ phase (with 11.8 at% of Nd) is indicated by the arrow in orange and the typical alloy composition (with 14 at% of Nd) used for practical magnets is indicated by the arrow in blue. The eutectic temperature corresponding to the reaction L → T1 + hcp Nd is determined to be 682.2°C. Adapted from Van Ende et al.[30]

- Additive elements: In addition to the basic elements (Nd, Fe and B) that make up the NdFeB magnet, and among the wide range of possible additive elements, at least the three following additive elements are often added: Cu, Co and Al These elements favor the sintering process, promote the effect of annealing and lead to the formation of new intergranular phases that affect the magnetic properties.

- Addition of heavy-rare earth elements (namely Dy) via grain boundary diffusion process (GBDP): The most effective technique to enhance the coercivity of the magnet and is especially adopted when designing permanent magnets for high temperature applications.

In the following section, the state of the art regarding the characterization of the Nd-rich secondary phases located at triple/multiple junctions in a sintered NdFeB magnet with an excess Nd content and no additive elements is summarized in (1.2.2.1). For that, the case of metallic Nd-rich phases (section A) and Nd-oxides (section B) are considered. Then, the effect of additive elements on the microstructure in general, and on the formation of new secondary phases in particular (1.2.2.1C) is discussed. Hereafter, the state of the art concerning the characterization of the Nd-rich secondary phases located at the grain boundaries (referred to by the GB phase, 1.2.2.2) is presented. Finally, this section is concluded by a summary of the effect of the Nd-rich secondary phases on the coercivity of sintered NdFeB magnet (1.2.3). The GBDP is treated separately in section 1.2.3.

1.2.2 Nd-rich secondary phases

According to the excess Nd content, Nd-rich secondary phases constitute between 3-6% of the microstructure of the NdFeB magnet and are generally considered to be non-magnetic. They are located at the triple/multiple junctions as well at the grain boundaries and are either metallic or oxide phases.

1.2.2.1 Triple/multiple junction phases

A. Metallic Nd-rich phases

Starting with the simple case of a NdFeB alloy with no additive elements, the Nd-Fe-B phase diagram (Figure 15) indicates that the Nd-rich phases are composed of 100 at% of Nd. However, little amount of dissolved Fe and traces of B are also found inside the Nd-rich phases. The chemical composition of the latter was examined by Sagawa et al.[18] using quantitative electron probe microanalyzer (EPMA), and they revealed that the Nd-rich phases consist of 95 at% of Nd, 3-5 at% of Fe and trace amount of B. In the same publication, Sagawa et al. reported that the Nd-rich phases have a face centered cubic (fcc) crystal structure with lattice parameter a ≈ 0.52 nm as revealed by selected area electron diffraction (SAED). This was surprising since pristine metallic Nd crystallizes in double hexagonal close packed [2](dhcp) structure[31] and there is no fcc structure in the Nd-rich side of the Nd-Fe phase diagram (Figure 16).

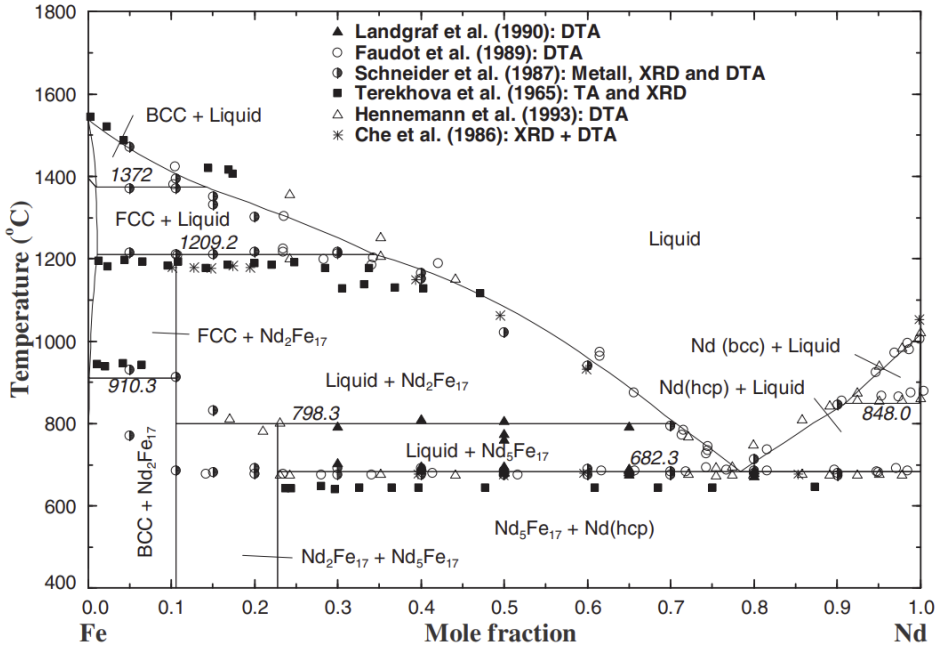

Figure 16: Binary phase diagram of the Fe-Nd system showing that the Nd-rich phase crystallizes in hcp structure. Adapted from Van Ende et al.[30]

[2] The dhcp crystal structure is similar to fcc or bcc crystal structures, but it uses a 4-layer stacking pattern ABAC-ABAC, instead of FCC's ABC-ABC or HCP's AB-AB stacking pattern.

The fcc crystal structure was also reported by several other researchers[32–37], however they all noted the presence of oxygen in the Nd-rich phases in contrast to Sagawa's finding. Several authors have reported that oxygen is soluble in metallic Nd-rich phase. Stadelmaier and ElMasry[38] suggested that the fcc structure might be stabilized by the presence of O in the Nd-rich phase. To test this hypothesis, Tang et al.[35] measured the overall O content of the ingot and the as-sintered sample and found that the O content increases from 0.017 wt.% in the former to 0.63 wt.% in the latter. This confirmed the introduction of O into the alloy when it is sintered at high temperatures. Since the O content (0.63 wt.%) was found to be comparable to the B content (0.98 wt.%) of the starting alloy, the authors pointed out that the initially ternary Nd-Fe-B system must be regarded as a quaternary Nd-Fe-B-O system. They proceeded to compare the X-ray diffraction curves of both the ingot and the as-sintered sample and showed that the dhcp-Nd-rich phase present in the former is largely replaced by fcc-Nd-rich phase in the latter. Finally, using EDS-TEM and Auger spectroscopy techniques, they determined the composition of the fcc-Nd phase as follows: 70% of Nd, 15% of Fe and 15% of O. **Consequently, they concluded that dhcp-Nd largely transforms into fcc-Nd during sintering due to the introduction of O.**

Recently, Abe et al.[39] compared the stability of dhcp-Nd structure against fcc-Nd structure when O is introduced by calculating their formation energies. Their results can be seen in the Figure 17 below.

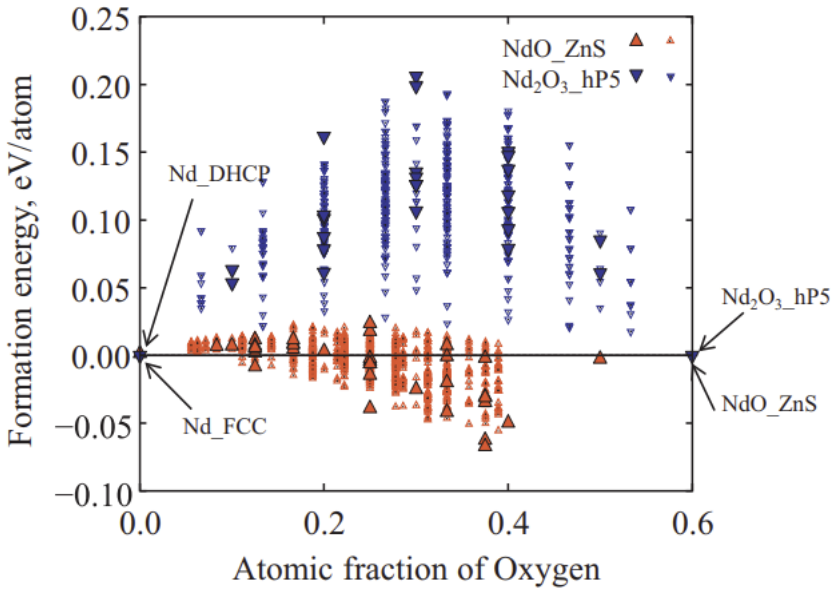

Figure 17: Comparisons of stabilities of O-vacancy doped structures for ZnS and hP5 series. The segregation limits of two series as the reference of terminal phases are marked at the plots, they are Nd-fcc and NdO-ZnS for ZnS series, Nd-dhcp and Nd_2O_3-hP5 for Nd_2O_3-hP5 series. Adapted from Abe et al.[39]

The graph shows that when O is added to pure Nd, the formation energy of dhcp lattice increases while that of fcc lattice decreases. This means that when O penetrates inside a metallic Nd-rich phase, it is more energetically favorable for the system to form fcc-Nd instead of dhcp-Nd. Their work provides a theoretical confirmation of Tang's conclusion.

However, other crystal structures were reported for the Nd-rich phases. Fidler et Knoch[40] carried out an extensive study of the microstructure of sintered NdFeB magnet and revealed the presence of two types of Nd-rich phases: (i) the above mentioned fcc-Nd-rich phase (a = 0.52 nm) with a high dislocation density and (ii) a new Nd-rich phase with hcp crystal structure (a = 0.39 nm and c = 0.61 nm) and only individual dislocations. In another study, Fidler[41] reported the presence of a Nd-rich phase with a dhcp crystal structure (a = 0.37 nm and c = 1.18 nm). Furthermore, a complex cubic phase (i.e. a superlattice) with a space group Ia3 and a doubled lattice parameter compared to the fcc-structure (a = 1.108 nm) is reported[42,43]. This evidenced the need to further elucidate the relationship between Nd crystal structure and O content in the magnet.

Motivated by this, Mo et al.[44] conducted a detailed study by means of TEM and EDX measurements and succeeded to establish the relationship between the O content of the Nd-rich phases and their crystal structure. This can be seen in Figure 18.

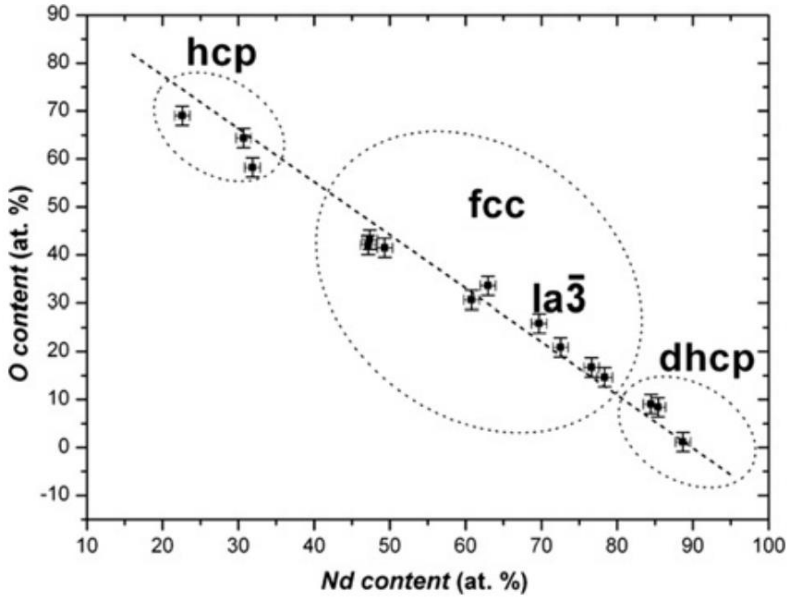

Figure 18: Crystal structure as a function of O and Nd content of Nd-rich phase in sintered Nd-Fe-B magnet. Adapted from Mo et al.[44]

Their results show that with increasing O content, the Nd-rich phases follow the structural sequence dhcp → fcc → hcp. For the specific case of O = 25 at%, the Nd-rich phase is a superlattice with Ia3 symmetry and lattice constant a = 1.108 nm. The dhcp-Nd-rich phase is the stable room temperature phase in which pristine metallic Nd is known to crystallize. This phase is stable in the sintered NdFeB magnet up until an O level of 9 at%. When the O content inside the Nd-rich phase further increases, the metallic dhcp-Nd-rich phase transforms into metallic fcc-Nd-rich phase as proposed by Tang[35] and confirmed theoretically by Abe[39]. As shown in Figure 18, the fcc-Nd has a large O range (11% < O < 45%) which explains why this phase is frequently reported in literature. Beyond O > 55 at%, fcc-Nd transforms into hcp-Nd.

In Table 7 the metallic-Nd rich phases detected in the sintered NdFeB magnet are summarized as reported in literature and compared to the stable phases of pristine metallic Nd.

Table 7: Comparison between the crystal structures and lattice constants of pristine metallic Nd and the metallic Nd-rich phases found in sintered NdFeB magnets. The reported values are taken from Fidler et al.[45] and Fukagawa et al.[46]

	Hexagonal	Cubic
Pristine metallic-Nd	• Space group: P63/mmc, • α-Nd • Symmetry: dhcp, • Lattice parameters: a = 0.366 nm and c = 1.180 nm, • Room temperature stable phase (T < 860°C). This phase is also detected in the sintered NdFeB magnets by electron diffraction.	• Space group: Im3m, • β-Nd • Symmetry: bcc, • Lattice parameter: a = 0.413 nm, • High temperature stable phase (T > 860°C).
Metallic Nd-rich phases	• α'-Nd • Symmetry: hcp, • Lattice parameters: a = 0.39 nm and c = 0.61 nm, • Room temperature phase found by electron diffraction in sintered NdFeB magnets.	• β'-Nd • Symmetry: fcc, • Lattice parameter: a = 0.52 nm, • Room temperature phase found by electron diffraction in sintered NdFeB magnets

B. Nd-oxides

Besides metallic Nd-rich phases, the following Nd-oxides are also reported to be present in the microstructure of NdFeB magnet: NdO[33], NdO_2[47], a-type Nd_2O_3[12,18] and c-type Nd_2O_3[43]. The crystallographic information of each phase is summarized in Table 8.

Table 8: The crystal structures and lattice parameters of all reported Nd-oxides in sintered NdFeB magnets.

Crystal system	Space group	Prototype	Lattice parameters
NdO	$Fm\bar{3}m$	NaCl type	a = 0.509 nm
NdO_2	$Fm\bar{3}m$	CaF_2 type	a ≈ 0.52 nm
c-type Nd_2O_3	$Ia\bar{3}$	Mn_2O_3 type	a = 1.108 nm
a-type Nd_2O_3 (could be referred also by h-Nd_2O_3)	$P\bar{3}m1$	La_2O_3 type	a = 0.382 nm and c = 0.598 nm

While a-type Nd_2O_3 is a stable oxide, the others aren't as it can be seen when comparing their formation energies calculated by Chen et al.[48] (Figure 19). The Nd_2O_3 has the lowest formation energy which is why it is a very stable oxide phase. Since the formation energy of the NaCl-type NdO and CaF_2-type NdO_2 is slightly above the ground state, they can possibly be formed as

metastable phases if the processing temperature is lower than the temperature needed to form the Nd_2O_3 phase. This explains why these oxides have been reported in literature.

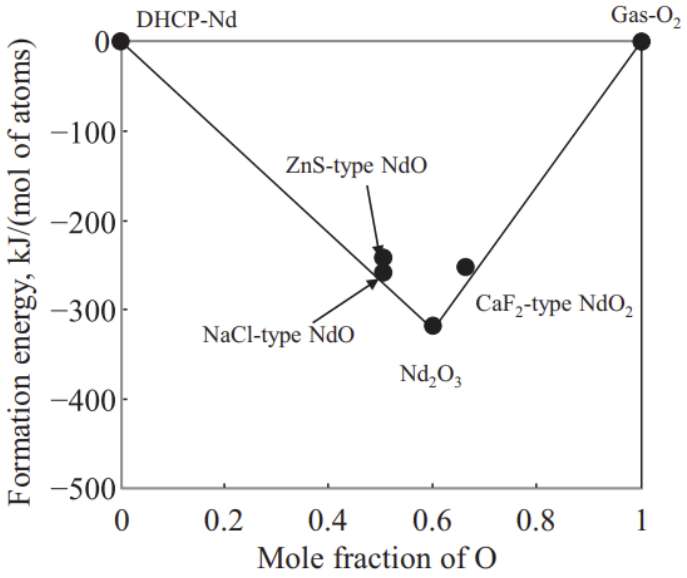

Figure 19: Calculated formation energies of several ordered phases in the Nd-O binary system with respect to the ground state structures of dhcp-Nd and oxygen at T = 0K. Adapted from Chen et al.[48]

Since fcc-NdO, NdO_2 and c-type Nd_2O_3 are metastable phases, none of them exist on the Nd-O binary phase diagram where only stable phases are included. Abe et al. proceeded to calculate the Gibbs energy functions to be able to cover the metastable range and carried out the assessment of Nd-O binary phase diagram using the CALPHAD approach, but only fcc-NdO was included in their work. The calculated Nd-O metastable binary phase diagram can be seen in Figure 20.

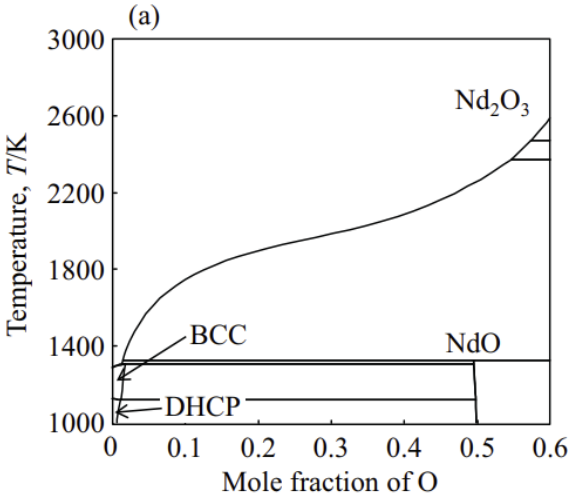

Figure 20: Calculated metastable Nd-O binary phase diagram. Adapted from Abe et al.[39]

Their results show that oxygen forms fcc-NdO type oxides at temperatures below T ≈ 1330 K, while it changes to Nd_2O_3 at higher temperatures. Since sintering temperature ranges between 1320 K - 1340 K, the fcc-NdO phase could be stabilized during sintering.

C. Additive elements

Let us now consider the case of a NdFeB magnet with additive elements. As mentioned earlier, three elements are frequently added to the typical alloy magnet: Cu, Al and Co. Since the system was already considered a quaternary alloy before adding these elements, one can imagine the complexity of the now 7-component system. Although the additive elements are added in small amounts, they tend to concentrate at the Nd-rich phases. Hence, they cannot be neglected when considering the phase equilibria between the $Nd_2Fe_{14}B$ phase and the Nd-rich phases. There are many advantages for adding the above elements: (i) they favor the sintering process during manufacturing (enable densification while preventing grain growth), (ii) they improve the wetting behavior of the liquid Nd-rich phase, and (iii) they recover the crystallinity at the surface of the $Nd_2Fe_{14}B$ phase. All these advantages were shown to improve the magnet coercivity.

First, Cu is one of the most researched additive elements since it enhances the coercivity even in small amounts (0.2 at%). It has been shown that Cu doesn't penetrate the $Nd_2Fe_{14}B$ phase but is only found in the Nd-rich phases[49]. Adding Cu lowers the melting temperature of the metallic Nd-rich phase from 682.2 °C (corresponding to the $Nd_2Fe_{14}B$/Nd-rich eutectic reaction temperature) to ≈ 505°C (corresponding to the Nd/Nd-Cu eutectic reaction temperature).

Kim et al.[50] convincingly showed that the L ↔ Nd + NdCu decomposition leads to the formation of Cu^{high} Nd-rich phase (30-45 at% of Cu) and Cu^{low} Nd-rich phase (5-15 at% of Cu). In fact, starting from a magnet of composition $Fe_{(76.7-x)}Nd_{12.0}Dy_{2.7}B_{6.0}Cu_x(Al, Co, Nb)_{2.6}$ (at%) and by varying the Cu content (from x = 0.2 up to x = 0.5), both phases were systematically present in the magnet's microstructure as illustrated in Figure 21.

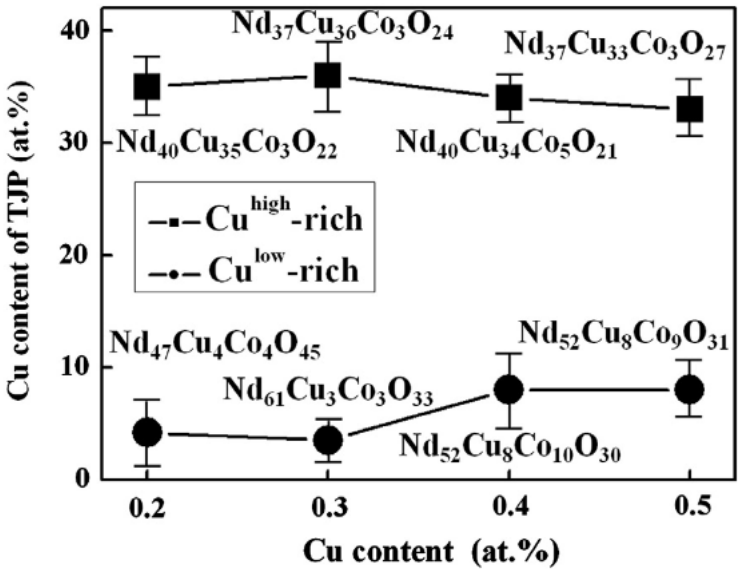

Figure 21: Compositional changes of the Cu^{low} Nd-rich and Cu^{high} Nd-rich TJP as a function of Cu content. The chemical compositions are determined by EDS, WDS and EPMA. Adapted from Kim et al.[50]

According to their results, the Cu content of the Cu^{high} Nd-rich phase ranges between 30-45 at% while that of the Cu^{low} Nd-rich phase ranges between 5-15 at%. The Cu content of both phases is unaffected by the increase in the initial Cu content of the magnet.

The distinction between these two phases is important as each has different crystallographic structure and contributes differently to the coercivity. The Cu^{high} Nd-rich phase has the same crystal structure as the metastable c-Nd_2O_3 phase while the Cu^{low} Nd-rich phase has the same structure as the stable h-Nd_2O_3. This is in line with earlier reports where it was revealed that Cu segregation in the Nd-rich phases stabilizes the metastable c-Nd_2O_3 phase[51,52]. Earlier, we noted that the c-Nd_2O_3 phase, in contrast to h-Nd_2O_3 phase, produces the smallest distortions at the $Nd_2Fe_{14}B$/Nd-rich interface. This shows that the Cu^{high} Nd-rich is beneficial for coercivity while the Cu^{low} Nd-rich phase is not. Since the formation of the Cu^{low} Nd-rich phase is unavoidable, it is important to modify its structure and composition in such a way to stabilize the c-Nd_2O_3 phase. Kim et al. showed that this is possible through selective dissolution of other additive elements such as Al and Co in the Cu^{low} Nd-rich phase[53].

Mottram et al.[54] showed that the addition of Al up to 2 at% increases the coercivity of the magnet but decreases its remanence. Unlike Cu, Al can be found in both the $Nd_2Fe_{14}B$ phase and the Nd-rich phases. It partially substitutes the Fe in the former and dissolves inside the latter (3-8 at.% Al). By partially substituting the Fe in the $Nd_2Fe_{14}B$ phase, Al slightly lowers its magneto-crystalline anisotropy and its saturation polarization[55]. The decrease in the saturation polarization explains the decrease in the remanence of the magnet. However, the decrease in the magneto-crystalline anisotropy should have yielded a decrease in the coercivity of the magnet which is not the case. This implies that the coercivity enhancement is attributed to microstructural modifications. In fact, dissolution of Al inside the Nd-rich phase enhances its wetting behavior during sintering. Namely, Knoch et al.[56] showed that Al decreases the dihedral angle between the $Nd_2Fe_{14}B$ phase and the liquid Nd-rich phase during sintering. This helps effectively coating the grains by the non-magnetic Nd-rich phase leading to better magnetic isolation, hence the increase in the coercivity of the magnet.

Two new secondary phases have been reported to occur at the triple junctions of an Al containing NdFeB magnet: $Nd(Fe,Al)_2$ phase[40,56,57] with the following compositional range $Nd_{29.5\text{-}39.5}Fe_{51.9\text{-}63.6}Al_{5.2\text{-}7.9}$ and a lamellar morphology μ-phase[58,59] ($Nd_{36.5}Fe_{(63.5\text{-}x)}Al_x$ with x = 2.5-5). The former is a paramagnetic phase while the latter is a ferromagnetic phase[58] whose anisotropy field $\mu_0 H_A$ and saturation polarization J_S are 10.7 T and 0.85 T respectively (vs $\mu_0 H_A$ = 7.7 T and J_S = 1.61 T for the $Nd_2Fe_{14}B$ phase). Both phases increase the coercivity of the magnet and decrease its remanence: (i) $Nd(Fe,Al)_2$ increases the coercivity since it decouples the $Nd_2Fe_{14}B$ grains; but decreases the remanence since it dilutes the volume fraction of the ferromagnetic phase and (ii) μ-phase increases the coercivity since it has a higher anisotropy field than the $Nd_2Fe_{14}B$ phase; but decreases the remanence since its saturation polarization is lower than the $Nd_2Fe_{14}B$ phase.

Lastly, addition of Co increases the thermal stability and the remanence of the magnet but decreases its coercivity[60–62]. The increase in thermal stability is related to the increase in the Curie temperature. Co substitutes Fe in the $Nd_2Fe_{14}B$ phase and linearly increases its Curie temperature by a rate 10.9°C/at% in the range of 0-10 at% of Co.[60] In addition, by substituting Fe, Co decreases the

anisotropy field of the $Nd_2Fe_{14}B$ phase[63]; which is a factor contributing to the decrease of the coercivity of the magnet. One can think that Co, very similar to Fe, will only be found in the matrix phase, however Sepehri-Amin et al.[64] showed that the distribution of Co and Fe is not always the same. In fact, Co concentration is rather higher in the Nd-rich phases compared to the $Nd_2Fe_{14}B$ phase.

Two new secondary phases have been reported to occur at the triple junctions of a Co containing NdFeB magnet: $Nd_3(Fe,Co)$[60] phase with an approximate composition of $Nd_{75}Fe_5Co_{20}$ (at%) and the cubic Laves-type $Nd(Fe,Co)_2$ phase[41,60,65] with an approximate composition of $Nd_{35}Fe_{50}Co_{15}$ (at%). The $Nd_3(Fe,Co)$ phase is nonmagnetic at room temperature[66], however the $Nd(Fe,Co)_2$ phase is ferromagnetic[67] and is the main factor behind the decrease in the coercivity of the magnet. Mottram et al. showed that the decrease in coercivity can be overcome by adding simultaneously Co and Al to the NdFeB magnet[54]. In this case, Al promotes the formation of $Nd(Fe,Al)_2$ phase instead of the ferromagnetic $Nd(Fe,Co)_2$ phase, and the coercivity of the magnet is restored while keeping the high Curie temperature provided by Co. In another study, Mottram et al.[68] examined the effect of adding Co and Cu simultaneously. They found that combining Cu and Co helps to better enhance the Curie temperature compared to Co solely. In conclusion, it is quite interesting to carefully combine Al, Cu and Co to design NdFeB magnets with better magnetic properties.

All the above information regarding the effect of the additive elements is recapitulated in Table 9.

Table 9: Effects of Cu, Co and Al additive elements on the microstructure and magnetic properties of NdFeB magnets.

Additive elements	Location in the microstructure	Effect on the microstructure	Effect on the magnetic properties
Cu	Grain boundaries	• Modifies the crystallographic structure of the triple/multiple junction phases. • Improves the wetting behavior by lowering the melting temperature of the triple/multiple junction phases. • Leads to the formation of: Cu^{high} Nd-rich and Cu^{low} Nd-rich phases.	• Increases the coercivity of the magnet due to better magnetic isolation. • Doesn't affect the remanence of the magnet.
Al	Matrix and grain boundaries	• Substitutes Fe in the $Nd_2Fe_{14}B$ phase. • Improves wetting of the triple/multiple junction phases during sintering. • Leads to the formation of new triple/multiple junction phases: **$Nd(Fe,Al)_2$** and **$Nd_{36.5}Fe_{(63.5-x)}Al_x$** with x = 2.5-5.	• Slightly lowers the magnetocrystalline anisotropy and saturation polarization of the $Nd_2Fe_{14}B$ phase. • Increases the coercivity of the magnet due to better magnetic isolation. • Lowers the remanence of the magnet due to the formation of new secondary triple/multiple junction phases.
Co	Matrix and grain boundaries	• Substitutes Fe in the $Nd_2Fe_{14}B$ phase. • Leads to the formation of new triple/multiple junction phases: **$Nd_3(Fe,Co)$** and **$Nd(Fe,Co)_2$.**	• Increase the Curie temperature of the $Nd_2Fe_{14}B$ phase. • Decreases the coercivity of the magnet. • Increases the remanence of the magnet.

It is important to note that it is mainly the secondary phases with Cu that will melt during annealing to form a thin layer along the Nd2Fe14B grain boundaries (referred to by the grain boundary phase) and consequently improving the overall magnetic properties of the magnet.

1.2.2.2 Grain boundary phase

After annealing, several studies[43,64,69] reported the formation of a thin Nd-rich layer at the $Nd_2Fe_{14}B$ grain boundaries (i.e. $Nd_2Fe_{14}B/Nd_2Fe_{14}B$ interfaces). This Nd-rich layer known as the grain boundary (GB) phase plays a key role in enhancing the coercivity of NdFeB magnets. In the case of a NdFeB alloy with no additive elements, the formation of this phase is explained by the

eutectic reaction between the Nd-rich phase and the $Nd_2Fe_{14}B$ phase that occurs at 950 K[18,70]. Hereafter, the liquid infiltrates along the grain boundaries driven by capillary pressure and surface tension[40]. Good wetting between the Nd-rich phase and the $Nd_2Fe_{14}B$ phase (i.e., small dihedral angle) is required to allow the liquid phase to penetrate into the grain boundaries. If not, the liquid becomes isolated at the triple/multiple junctions.

In the case of a NdFeB alloy with Cu additive element, the annealing temperature is lowered from 950 K (677°C) to 793 K (520°C). Sepehri-Amin et al.[64] showed that the decrease in the annealing temperature is due to the binary eutectic Nd/NdCu. In the as-sintered magnet, NdCu precipitates are found to be formed within the metallic Nd-rich phase grains in the as-sintered sample as showed by the 3D atom probe tomography (APT) maps displayed in Figure 22.

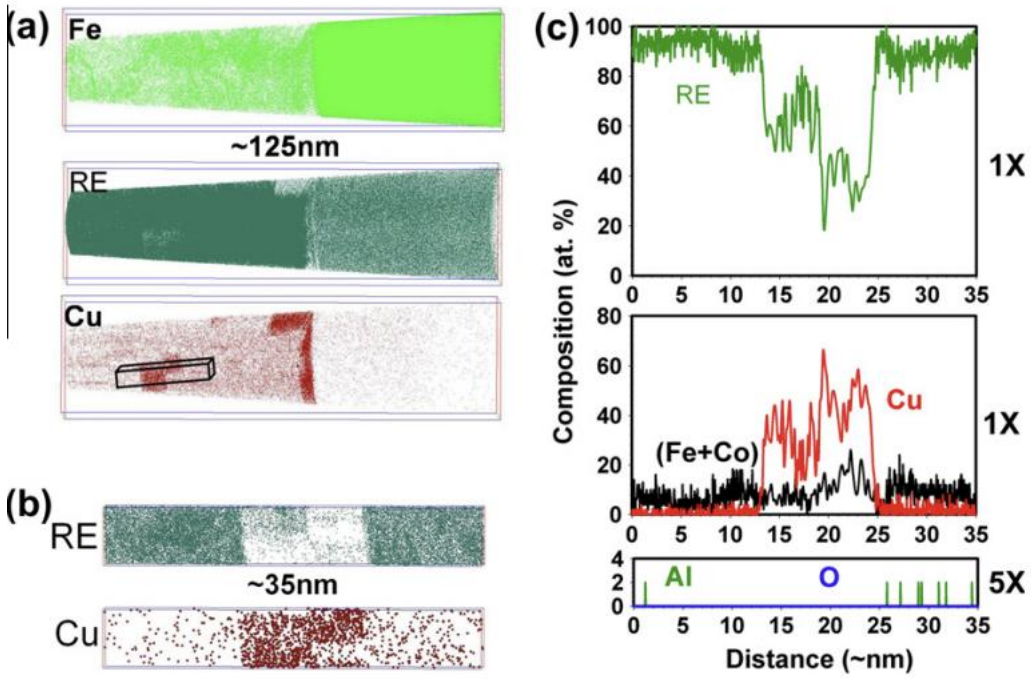

Figure 22: (a) 3D-APT map of Fe, RE = (Nd + Pr), and Cu atoms obtained from the Nd-rich grains in the as-sintered sample; (b) atom probe maps of Nd and Cu of the selected volume from Cu-rich precipitates in (a); (c) concentration depth profiles for RE, Fe + Co, Cu, O and Al determined from the 3DAP analysis shown in (b). Adapted from Sepehri-Amin et al.[64]

However, no Cu was detected in the GB of the as-sintered sample as showed by the 3D-APT maps displayed in Figure 23 . The chemical composition of the GB phase is approximately $(Nd + Pr)_{21}(Fe + Co)_{71}B_8$ (at%).

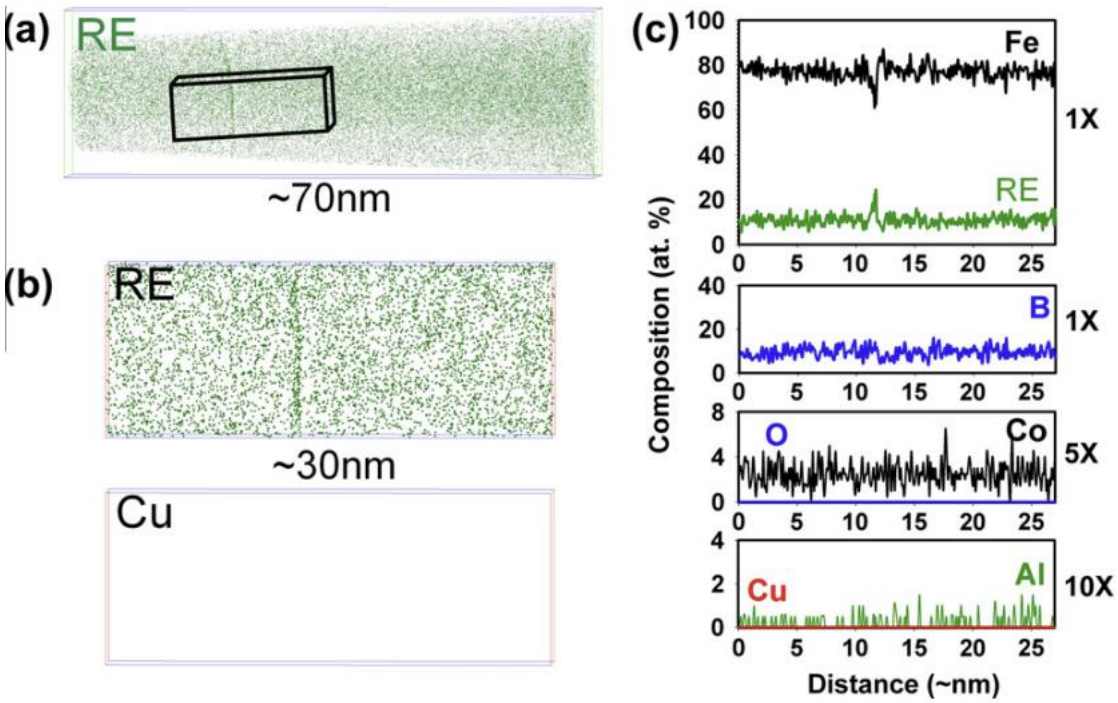

Figure 23: (a) 3D-APT maps of RE = (Nd + Pr) of the as-sintered sample; (b) atom probe maps of RE, and Cu of the selected volume perpendicular to the grain boundary; (c) concentration depth profiles for Fe, RE, B, Co, O, Cu, and Al determined from the 3DAP analysis shown in (b). Cu and O were not detected in this analysis. Adapted from Sepehri-Amin et al.[64]

After annealing, the NdCu precipitates are not found anymore. However, Cu was clearly detected to segregate at the GB phase/$Nd_2Fe_{14}B$ interfaces as opposed to the as-sintered state (see Figure 24). The chemical composition of the GB phase is approximately $(Nd + Pr)_{33}(Fe + Co)_{64}B_3$ (at%). One side of the GB phase contains ≈ 1.8 at.% Cu and the other side contains ≈ 1.0 at.% Cu. Sepehri-Amin et al. explained that the NdCu precipitates melt by the Nd + NdCu eutectic reaction, and that the melts are believed to impenetrate into the GBs to form the GB phase.

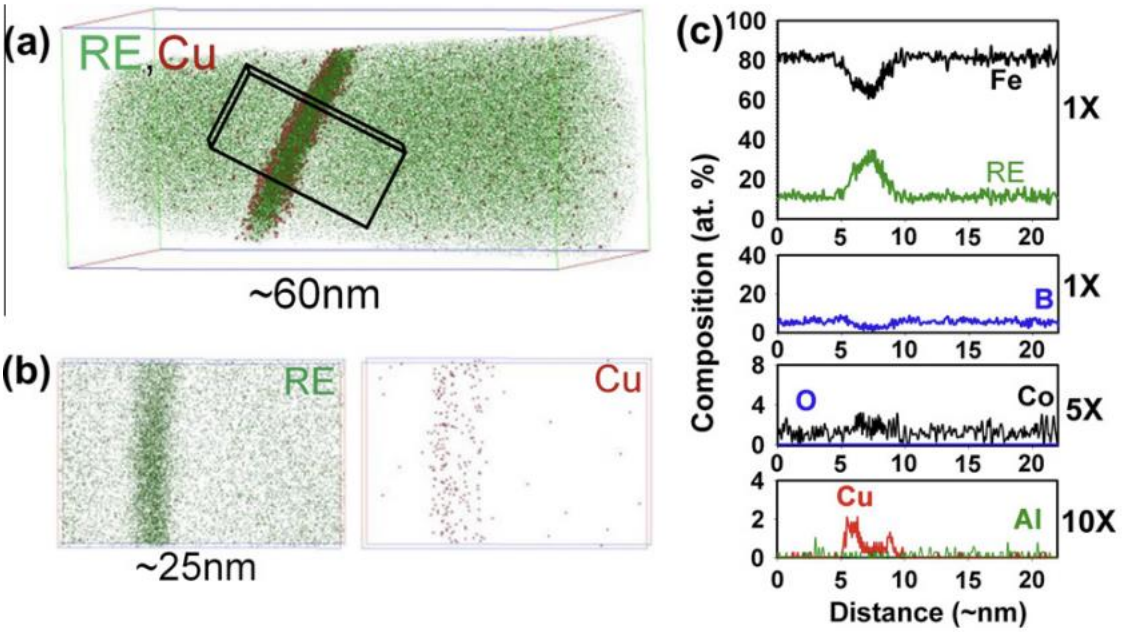

Figure 24: (a) 3D-APT maps of RE = (Nd + Pr) (green atoms) and Cu (red atoms) of the post-sinter annealed sample; (b) atom probe maps of RE, and Cu of the selected volume perpendicular to the grain boundary; (c) concentration depth profiles for Fe, RE, B, Co, O, Al, and Cu determined from the 3DAP analysis shown in (b). Adapted from Sepehri-Amin et al.[64]

One can think that the GB phase is simply an extension of the triple/multiple junction phase especially since earlier works reported that both have the same chemical composition and crystal structure. However, recent works showed that this is not quite the case. In fact, the chemical composition and the crystal structure of the GB phase were found to be dependent on the orientation of the GB with respect to the c-axis of the $Nd_2Fe_{14}B$ grain. Namely, Sasaki et al.[29] showed the presence of two types of GB phases: crystalline GB phase perpendicular to the c-axis of the $Nd_2Fe_{14}B$ phase and with more than 60 at% of Nd and amorphous GB phase parallel to the c-axis of the $Nd_2Fe_{14}B$ phase and with less than 35 at% of Nd. This can be seen in Figure 25.

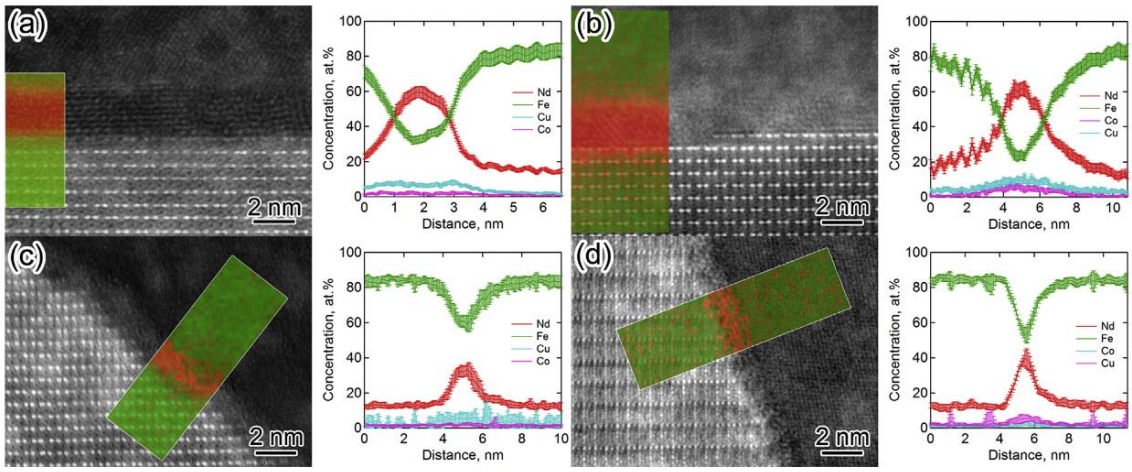

Figure 25: HAADF- STEM images and EDS concentration profiles taken from the insets area containing a thin Nd-rich GB phase (a) parallel to (001) plane, (b) 7° tilted from the (001) plane, 45° tilted from the (001) plane and (d) 70° tilted from the (001) plane of a $Nd_2Fe_{14}B$ grain. Adapted from Sasaki et al.[29]

The amorphous GB phase with less than 35 at% of Nd is thought to be ferromagnetic. It is worth noting that Sasaki et al did not include O in the analysis of the chemical composition of the GB phase. They justified that by the fact that previous atom probe work showed that this phase does not contain O[64]. From their work it can be concluded that the Nd-rich GB phase is not always rich in Nd and that both paramagnetic and ferromagnetic GB phase can exist in a sintered NdFeB magnet resulting in an anisotropic inter-grain exchange coupling.

Furthermore, Sakuma et al.[71] studied the magnetic properties of Nd_xFe_{1-x} film to clarify the magnetism of the GB phase. They found that for Nd content less than 70 at% (i.e., $x<70$), the model film exhibit ferromagnetism at room temperature. For Nd content of 30 at% (same as determined by Sasaki et al.[29]), the magnetization is about 0.8 T corroborating the ferromagnetism hypothesis proposed by Sasaki et al.[29] This work shows that the Nd content in the GB phase must be higher than 70 at% to decouple inter-grain exchange inside the NdFeB magnet.

1.2.3 Microstructure-coercivity relationship

The variety of the Nd-rich phases crystal structure implies a variety of $Nd_2Fe_{14}B$/Nd-rich interfaces, which raise the question as to the impact of the latter on the coercivity of the NdFeB magnet. This can be treated by considering two aspects: (i) whether the Nd-rich phases are magnetic or non-magnetic and (ii) the lattice mismatch between the $Nd_2Fe_{14}B$ phase and the Nd-rich phases.

First, it is important to ensure the formation of low melting non-magnetic secondary Nd-rich phases instead of magnetic ones. These non-magnetic phases distribute along the grain boundaries after annealing and ensure the magnetic decoupling of the $Nd_2Fe_{14}B$ grains[69,72]. In this case, if the polarization of a $Nd_2Fe_{14}B$ grain is reversed under an external demagnetizing field, it doesn't impact the $Nd_2Fe_{14}B$ grains next to it, hence increasing the overall coercivity of the magnet.

The second important aspect is the lattice mismatch between the $Nd_2Fe_{14}B$ phase and the Nd-rich phases. This was evaluated by Hrkac et al.[73] who predicted using atomistic models the presence of distorted layers at these interfaces. The thickness of the distorted layers was found to be dependent on the crystal structure of the Nd-rich phase: metallic dhcp Nd produces the largest distortions in $Nd_2Fe_{14}B$, then a-type Nd_2O_3 and finally cubic structures Nd-rich phases (metallic fcc-Nd, fcc-NdO and c-type Nd_2O_3) produce the smallest distortions. These distorted layers have lower magneto-crystalline anisotropy than the $Nd_2Fe_{14}B$ phase, hence they act as sites of nucleation of reversed magnetic domains which is detrimental to the coercivity of the magnet. It can be concluded that removal of metallic dhcp Nd-rich phases is important to avoid lowering the coercivity. Consequently, the introduction of Oxygen in a control quantity is beneficial to minimize the distortions at the interface. However, excess O should be avoided since Nd-oxides do not contribute in liquid phase sintering[74].

1.3 Grain boundary diffusion process

Despite the beneficial effect of the secondary phases at GBs, Heavy Rare Earth Elements (HREE) are still used in magnet industry, as a partial substitution of Nd, owing to the higher magneto-crystalline anisotropy of Dy or Tb, especially for high temperature applications.

Traditionally, the addition of HREE was performed using conventional binary alloy method, a process in which the main alloy powder (NdFeB powder) and the HRE alloy powder (Dy or Tb-rich powder) are mixed then sintered. However, the understanding of the role of the defects in the main phase, located near GBs, has stimulated to investigate some process adjustments that lead to segregation of HREE at GBs providing a beneficial effect on the coercivity with low amounts of added HREE. This process is called the grain boundary diffusion process (GBDP) and was first proposed by Park et al. in 2000. In their study, Park et al. coated sintered NdFeB magnets by Dy metal using the sputtering technique. The coated magnets were then heat-treated at T = 1073 K followed by subsequent aging to allow Dy diffusion. They found that Dy diffused mainly over the grain boundaries and formed thin Dy-rich shells around the $Nd_2Fe_{14}B$ grains, and that the magnets had very high coercivities without a reduction in their remanence. Compared to the conventional binary alloy method, the GBDP allows the formation of thinner Dy-rich shells with higher Dy concentrations[75]. Therefore, the GBD processed magnets have higher coercivities while maintaining the remanence of the sintered NdFeB magnet without Dy. In addition, GBDP uses considerably less amounts of HREE to increase the coercivity of sintered NdFeB magnets as clearly seen in Figure 26.

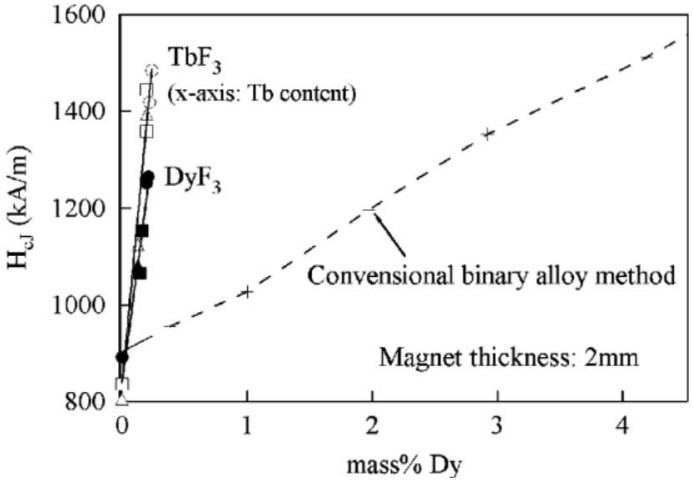

Figure 26: Coercivity plotted against Dy or Tb contents in (a) HREE-GBD processed sintered NdFeB magnets and (b) conventional binary alloyed sintered NdFeB magnets. Adapted from Hirota[76].

In particular, Sepehri-Amin[77] showed that the coercivity of GBD processed magnet containing 1.0 wt.% of Dy is comparable to commercial $N_{dDy}FeB$ sintered magnet containing 2.5 wt.% of Dy. This means that around 60% of Dy is saved by the GBDP. Consequently, the GBDP was quickly industrialized aiming to reduce the cost of HRE containing magnets by efficiently utilizing critical HREE.

Several studies extended this technique by using various diffusion sources (such as oxides, fluorides, alloys and hydrides) and diffusion coating techniques (such as adhesive coating, electrodeposition and vapor deposition)[78], and so far the GBDP remains the most efficient method to introduce Dy in the NdFeB magnets.

The aim of the following section is to explain the microstructural modifications induced by the GBDP, and the mechanisms proposed in literature to account for these microstructural modifications.

1.3.1 Microstructure of HREE-GBD processed sintered NdFeB magnet.

The schematic illustration of the HREE-GBDP applied to sintered NdFeB magnets is shown in Figure 27.

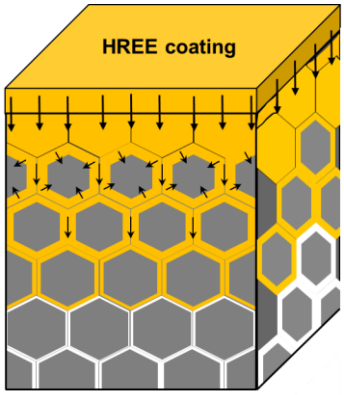

Figure 27: Schematic illustration of the HREE-GBDP.

After coating the surface of the sintered NdFeB magnet with HREE, it undergoes a heat treatment at around 900 °C. At this temperature, the intergranular Nd-rich phases with low melting point are in liquid state. Consequently, HREE atoms penetrate from the surface to the inside of the magnet through the liquid Nd-rich grain boundary phase. This result in a gradient distribution of the HREE concentration along the magnet depth (i.e., high Dy concentration near the magnet surface and low Dy concentration far from the magnet surface) as reported by several authors, for example in Loewe's work[79] (see Figure 28).

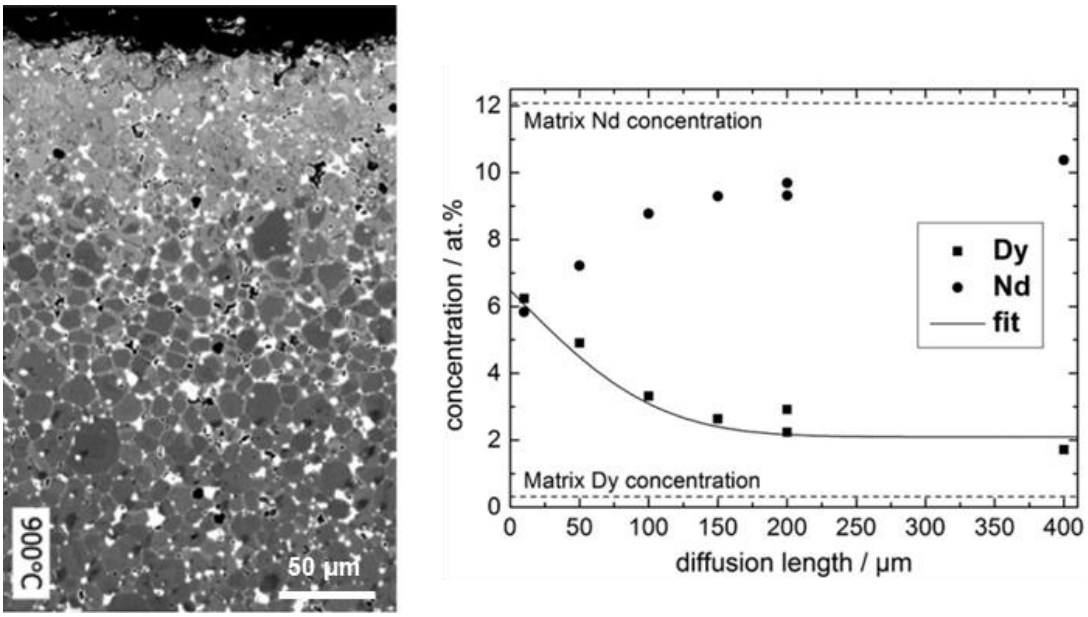

Figure 28: left: BSE-SEM image of near surface cross-section of HREE-GBDP sample at 900 °C for 6 h, right: Depth profiles of the Nd and HREE (Dy) concentration after HREE (Dy) diffusion treatment at 900 °C for 6 h. Each data point was obtained from a WDS measurement in a HRE (Dy)-rich shell. Adapted from Loewe[79].

Compared to the microstructure of a typical sintered NdFeB magnet that consists of $Nd_2Fe_{14}B$ grains surrounded by Nd-rich secondary phases, the microstructure of a typical HREE-GBDP sintered NdFeB magnet displayed in Figure 28 (left) exhibits distinct features according to which it can be described in terms of zones:

- The first zone consists of the $Nd_2Fe_{14}B$ grains just below the surface of the magnet (up to a depth of ≈ 90 µm in Loewe's example): these grains are considerably brighter than the ones further apart from the coated surface. Since the image is recorded using the BSE signal, this indicates that the surface grains have a higher average atomic weight compared to the volume grains. The increase in the average atomic weight is induced by the HREE substitution of Nd as verified by Loewe using energy dispersive X-ray spectroscopy (EDS) technique. It is worth to note that this zone is not beneficial for practical applications. In fact, the high amount of HREE present in the surface grains decrease their saturation polarization compared to their initial state prior the GBDP. Hence, the need to remove this zone to avoid the loss in remanence, which leads to wasting HREE.

- The second zone is adjacent to the first one and extends up to a few hundred microns within the depth of the magnet (up to a depth of ≈ 500 µm in Loewe's example): in this region, only the outer part of the $Nd_2Fe_{14}B$ grains (i.e., shell) appear in a bright contrast while their interior (i.e., core) remains unchanged (gray); consequently the grains in this region are said to have a core-shell structure. Here again, the bright shell is induced by the HREE substitution of the Nd atoms as revealed by EDS. It is important to note that the (i) HREE substitution of Nd takes place without changing the crystallographic structure of the 2:14:1 phase as proven by electron backscattered diffraction EBSD (see Figure 29) and (ii) the thickness of the HRE-rich shells decreases with increasing magnet depth, for

instance in Loewe's example it decreases from 1 μm at the start of the second zone and is no longer visible by SEM at the end of this zone.

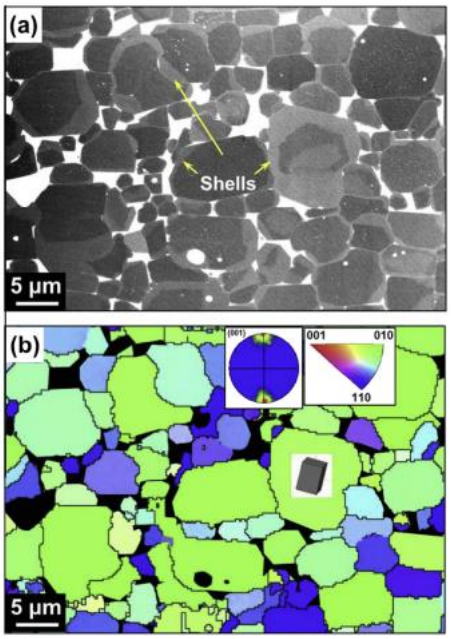

Figure 29: (a) BSE-SEM image of HREE-GBDP sintered Nd–Fe–B magnet (c-axis in-plane); this image highlights the core/shell structure (b) EBSD grain mapping from the same region; Nd-rich phases are marked black color. EBSD mapping shows that both the core and the shell have the same crystallographic structure. Adapted from Seelam[80].

- The third zone is just below the core-shell zone and extends up to the magnet center: this zone shows no difference to the microstructure prior to the HREE GBDP when observed by SEM. However, advanced characterization techniques (such as Transmission electron microscopy/TEM and three-dimensional atom probe tomography/3D-APT) showed the existence of thin HRE-rich shells (with a few to several nm thickness) in this region.

Furthermore, Loewe[79] studied quantitatively the HREE concentration gradient along the magnet depth using wavelength dispersive X-ray spectroscopy (WDS) technique (Figure 28, left). He showed that the HREE concentration rapidly decreases from 6 at.% near the surface to below 2 at.% at depths greater than 400 μm.

In literature, the coercivity enhancement post GBDP is mainly attributed to the formation of the HRE-rich shells, which is why a particular attention is paid to studying them. First, Loewe[79] studied the local HREE concentration gradient across the core-shell structure near the magnet surface by means of wavelength dispersive X-ray spectroscopy (WDS) technique. Remarkably, the local HREE concentration profile displayed a plateau (see Figure 30) indicating a uniform distribution of HREE across the thickness of the HRE-rich shell, strikingly different from the rapidly decreasing HREE concentration profile along the magnet depth seen in Figure 28 (right).

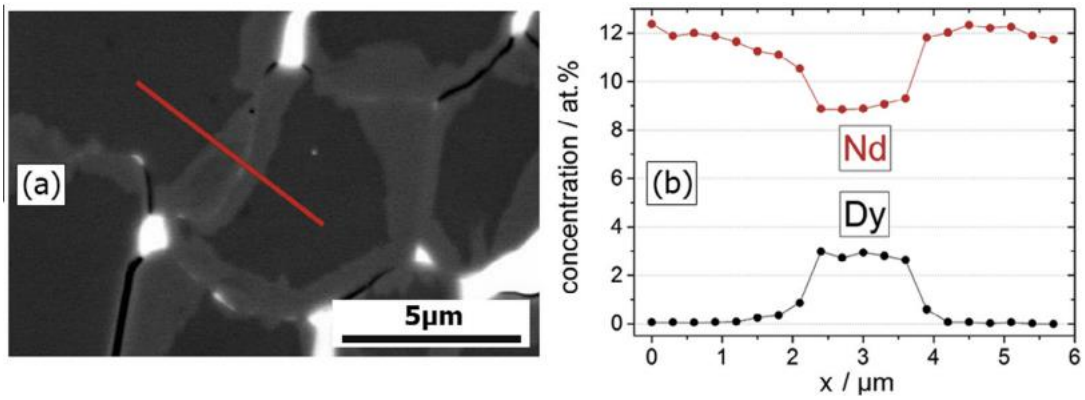

Figure 30: (a) BSE-SEM image of the cross-section of a HREE (Dy)-coated magnet showing a core-shell structure and (b) corresponding WDS line scan showing the Dy and Nd concentration. The analyzed area was at a distance of ≈110 µm from the coated surface. Adapted from Loewe[79].

Second, both thickness and HREE content of the HRE-rich shell were reported to decrease with increasing distance from the magnet surface. For instance, Loewe[79] found that the thickness of the HRE-rich shell decreases from 1 µm at a depth of ≈110 µm from the magnet surface to 20-30 nm at the center of the magnet (1500 µm). Similarly, the Dy content was found to decrease from ≈3 at.% at 110 µm to 0.4 at.% at 1500 µm as determined by EDS-SEM and EDS-TEM respectively. Sepehri-Amin[77] also determined the HREE content across HRE-rich shells located at 400 µm from the magnet surface as well at the center of the magnet (2700 µm) by means of three-dimensional atom probe (3DAP) analysis. The HREE content was determined to be 3.3 at.% at 400 µm and 1.4 at.% at 2700 µm.

It is interesting to compare the **thick** HRE-rich shells at the surface of the magnet and **thin** HRE-rich shells in the volume of the magnet in terms of their effect on the overall magnetic properties post GBDP. This has been done by Soderžnik et al.[81] who compared the coercivity and the remanence at the surface and in the volume parts of the GBDP magnet with respect to the non-GBDP magnet. For that, they cut both the GBDP and non-GBDP magnets into 5 slices perpendicular to the magnet surface, which is the direction of HREE-GBDP. Hereafter, they measured the coercivity and the remanence of each slice. Their results can be seen in Figure 31. Note that the 1st and 5th slices represent the surface slices where the HREE were deposited while the 3rd slice is the volume slice of the magnet.

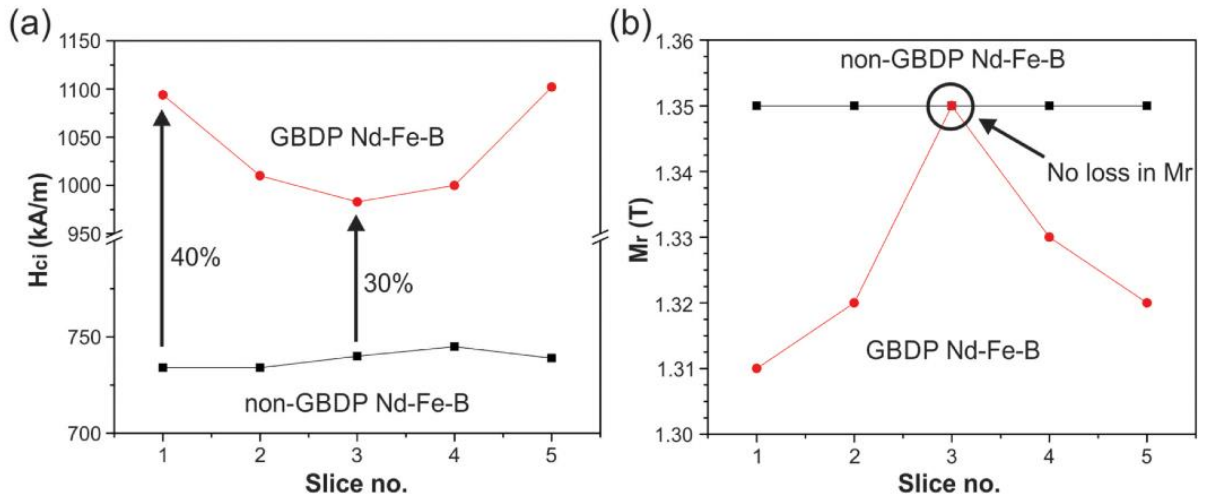

Figure 31: Lateral profiles of (a) coercivity (Hci) and (b) remanent magnetization (Mr) at 70 °C. Black curve represents non-GBDP Nd-Fe-B magnet, red curve represents GBDP Nd-Fe-B magnet. Adapted from Soderžnik[81].

Compared to the non-GBDP magnet, both the surface and the volume slices of the GBDP magnet have higher coercivities. The coercivity of the surface slices (i.e., 1st and 5th slices where thick HRE-rich shells are formed) is only 10% higher than the coercivity of the volume slice (i.e., 3rd slice where thin HRE-rich shells are formed). On the other hand, the remanence magnetization of the surface slices of the GBDP magnet is slightly lower than the non-GBDP magnet, while that of the volume slice of the GBDP magnet is identical to the non-GBDP magnet. This shows that thick HRE-rich shells are not essential for coercivity enhancement and that thin HRE-rich shells are a better compromise to increase coercivity and avoid loss in remanence simultaneously.

In conclusion, despite the GBDP being currently the most economically effective technique to introduce HREE into NdFeB magnets, it is still not the ideal technique due to the following limitations[82]:

- A part of the HREE is being wasted in the first zone just below the surface of the magnet. As explained earlier, this zone should be removed by polishing the GBDP magnet to recover the remanence prior to the GBDP. This result in an unnecessary wastage of HRE resources[79].

- Formation of unnecessary micrometer-thick HRE-rich shells: as already seen, **thick** HRE-rich shells are not necessary for coercivity improvement as they slightly increase the coercivity at the expense of loss in remanence. According to micromagnetic calculation performed by Suss[83], a 15-20 nm thick HRE-rich shell is sufficient to inhibit nucleation of reversed magnetic domains and improve the coercivity of the magnet. This implies that the formation of thick HRE-rich shells that extends up to several hundreds of microns of the magnet depth is wasting HRE resources and limiting the penetration depth of HREE. A limited penetration depth produces a coercivity gradient where the coercivity is improved only up to the penetration depth.

- Limitation of the GBDP to magnets with thickness < 5 mm: since the amount of HREE deposited at the magnet surface is limited, the effect of coercivity enhancement via GBDP decreases for thicker magnets[76]. Although it is possible to increase the amount of HREE supplied from the magnet surface, this however goes against the principle of the GBDP of using the bare minimum of HREE. More importantly, Zhou[84] showed that the gain in coercivity does not increase linearly with the increase in the amount of HREE. In particular, Zhou[84] showed that the coercivity increment rate per 1 wt.% Dy decreased from 2330 kA/m/wt.% to 1550 kA/m/wt.% when Dy amount increased from 0.1 wt.% to 0.3 wt.%.

To overcome these limitations, it is important to understand the formation mechanism of the HRE-rich shell to propose levers that help to homogenously distribute the Dy inside the NdFeB magnet. Several mechanisms have been proposed to explain the formation of HRE-rich shell, however there is still no consensus on the predominant mechanisms. In the following, we will explain how each mechanism accounts for the microstructural observations post GBDP.

1.3.2 Mechanisms of Dy-rich shell formation

In this section, the different models proposed in literature to explain the microstructural modifications induced by GBDP are reviewed, namely the homogeneous HREE-shell whose thickness varies with depth. All the models agree that, at the GBDP temperature, a liquid Nd-rich phase forms at the GBs. To support this point, the isopleth at 80 wt.% Fe extracted from the Nd-Fe-B ternary phase diagram is displayed in Figure 32.

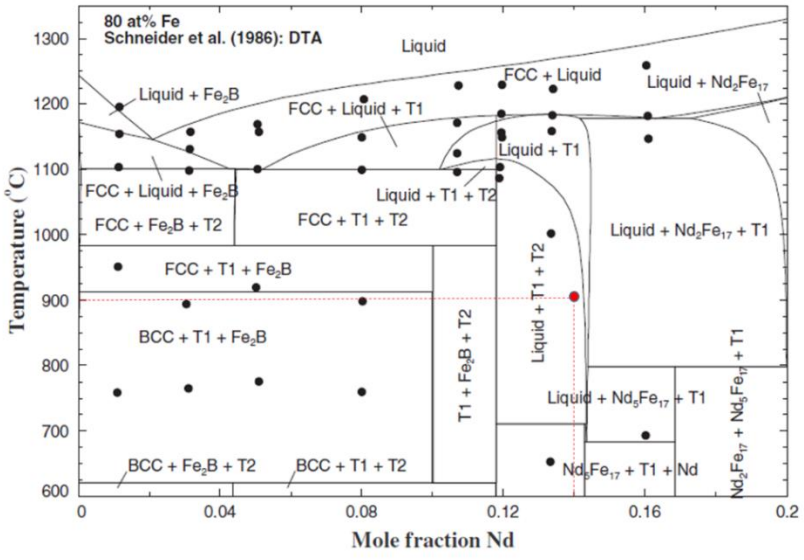

Figure 32: Isopleth at 80 wt.% Fe extracted from the ternary phase diagram Nd-Fe-B. Adapted from Van Ende et al., 2013[30].

This figure shows that for the ternary $Nd_{14}Fe_{80}B_6$, the phases formed at 20°C are $Nd_2Fe_{14}B$ (T1), $Nd_{1.11}Fe_4B_4$ (T2) and α-Nd whereas at 900°C (the GBDP temperature) the phases T1 and T2 coexist with a liquid phase made of Nd, Fe and B. In the different proposed models, the authors suppose that HREE (hereafter Dy) penetrates the magnet through this liquid phase and comes into

contact with the surface of the $Nd_2Fe_{14}B$ grains inside the magnet. However, these models disagree on the driving force by which Dy penetrates the $Nd_2Fe_{14}B$ grains. Understanding the underlying mechanism of Dy-rich shell formation is fundamental to propose levers for optimizing the grain boundary diffusion process by tailoring Dy distribution within the thickness of the magnet.

1.3.2.1 Solidification of a Dy-rich liquid phase

This model, proposed by Seelam et al.[80], explain the Dy-rich shell thickness as a result of the solidification of liquid phase from the GBDP. In their study, the authors found that the surface fraction of the Nd-rich phases increases after the GBDP. Accordingly, they assumed that Dy enters the liquid Nd-rich phase and increases the total amount of liquid phase.

The increase in the liquid phase fraction implies a compositional shift of the overall alloy towards the RE-rich side as illustrated in Figure 33. It is worth noting that the authors reason with the Nd-Fe-B ternary phase diagram assuming that Dy behaves like Nd. This is because the quaternary Nd-Dy-Fe-B phase diagram is incomplete due to the lack of thermodynamic data.

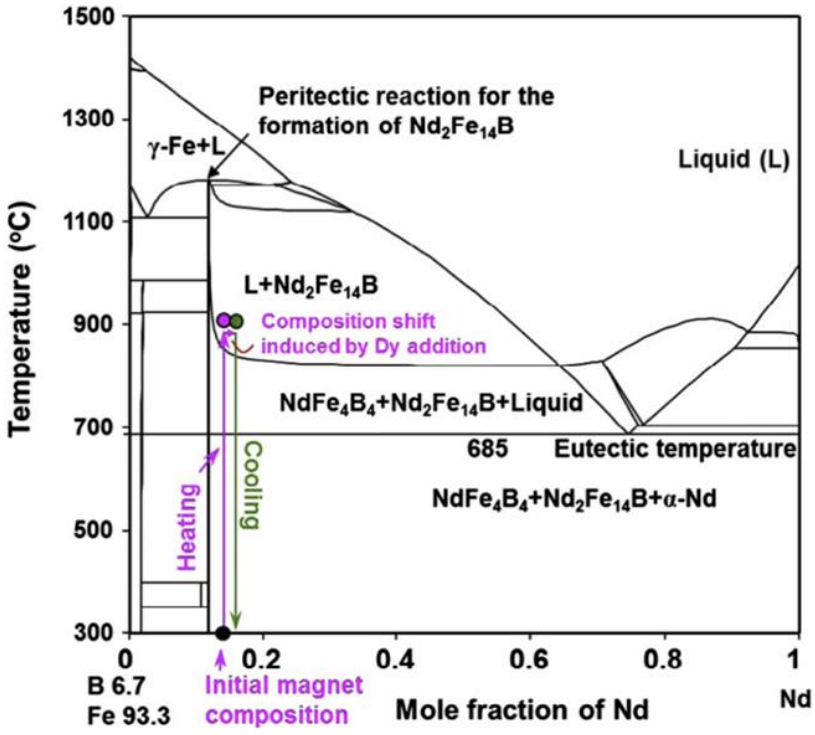

Figure 33: Calculated pseudo-binary phase diagram of Nd–Fe–B at Fe/B ratio of 14. The initial composition of the total rare-earth is 14.20% and after diffusion process, it is increased to about 14.69%. This is due to the addition of Dy as indicated by the horizontal arrow at 900°C. Adapted from Seelam et al.[80]

According to the lever rule, this shift increases the quantity of the liquid phase by further melting the T1 phase (here T2 phase in neglected since it has a very low volume fraction).

The second step of their model consider that during the cooling down from the GBDP temperature to the RT, the Dy-rich liquid phase undergoes partial solidification into $(Nd,Dy)_2Fe_{14}B$

shell. The latter nucleate at the surface of the non-melted $Nd_2Fe_{14}B$ grains forming coherent but chemically abrupt interface.

The advantage of this model is that is allows to explain the Dy concentration profile in the form of plateau observed systematically across the core-shell interface. However, its major limitation stems from the discrepancy between the expected area fraction of the Dy-rich shells and the observed one. Namely, by using the phase diagram, Seelam et al.[80] calculated the expected area fraction of the Dy-rich shell to be around 3.1 %. This value is much lower than the area fraction of shells they observed on the micrographs which was about 6-15%.

1.3.2.2 Solid-state diffusion

Another model proposed to explain the Dy-rich shell formation is the solid-state diffusion. As for the previous model, the source of Dy comes from the liquid phase at the GBs, but in this case Dy diffuses during the GBDP into the solid $Nd_2Fe_{14}B$ grain, and the Dy-rich shell forms during the high GBDP temperature.

Loewe et al.[79] attempted to link the variation of the Dy-rich shell thickness to the Dy concentration profile resulting from GB diffusion. He assumed that the evolution of the Dy content in the solid shells C_{shell}^{Dy}, as measured at RT, reflects the Dy diffusion profile along the liquid phase formed during the thermal treatment at 900°C. Therefore, he measured the concentration of the Dy-shells located at different depths and traced the concentration profile displayed in Figure 28. By fitting the concentration profile, he extracted the GB diffusion coefficient D_{GB}^{Dy}. The value given by Loewe is $D_{GB}^{Dy} = (2.5 \pm 0.5) \times 10^{-13}$ m²/s.

Fliegans et al.[85] implemented the Fisher model to account for both the grain boundary and intragranular diffusions to simulate distribution of Dy in the magnet. The Fisher model depicts the diffusion along one grain boundary considered as a linear channel oriented along a direction normal to the surface and separating two lateral semi-infinite media representing the grain solid phase (see Figure 34). The diffusion coefficient in both media, grain boundary and grain bulk, are assumed to be independent of the concentration.

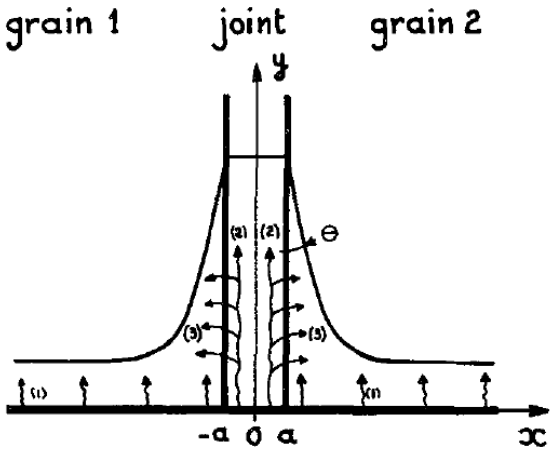

Figure 34: Geometrical representation of the bi-crystal model considered by Fischer. Three diffusion paths are considered: (1) direct bulk diffusion from the surface, (2) diffusion along the grain boundary of width 2a and (3) lateral diffusion into the grain from the grain boundary. Adapted from Martin et Perraillon[86].

The authors found that the shape of the Dy-concentration profile observed across the Dy-rich shell differs strongly from the calculated one using Fisher model as seen in Figure 35.

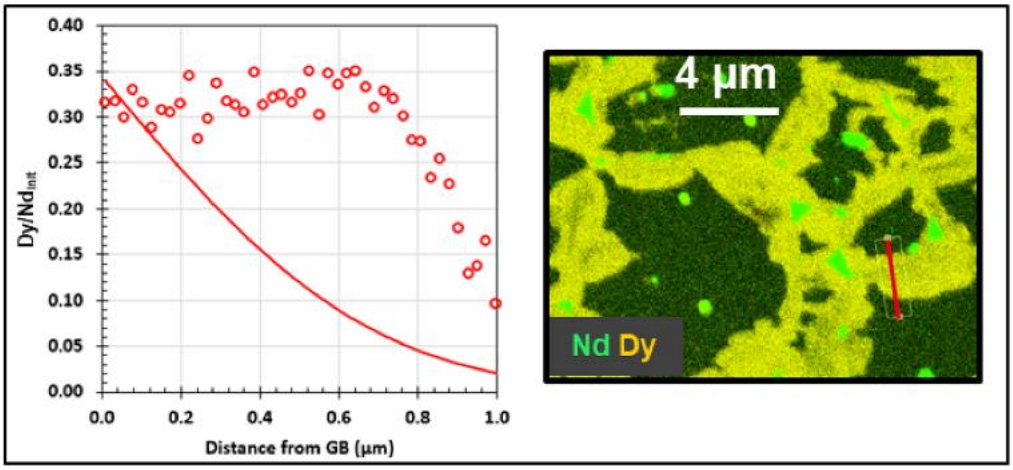

Figure 35: Nd and Dy elemental maps (right) and Dy/Nd$_{init}$ profiles (left) obtained by SEM/X-EDS analysis for a GBDP magnet at a depth z = 100 µm. Dy/Nd$_{init}$ values (open red symbols) are determined along the half red lines crossing GBs, indicated on the SEM images, and are compared to calculated profiles obtained with the Fisher model (solid lines). Adapted from Fliegans et al.[85]

It can be concluded that the solid-state diffusion mechanism fails to explain the plateau of the Dy concentration profile observed along the Dy-rich shell.

1.3.2.3 Chemically induced liquid film migration (CILFM)

Recently, an alternative model is proposed by Kim el al.[87] to explain the Dy-rich shell formation is the chemically induced liquid film migration (CILFM). According to Kim et al, CILFM accounts for several microstructural features observed on Dy diffused magnets that could hardly be described by the solidification of a Dy-rich liquid phase or by the intragranular solid diffusion

namely the large grain area covered by the shell (50 %), the abrupt fall in the Dy concentration at the core-shell interface and the quasi-constant Dy profile measured in solid shells. It is worth noting that Kim et al. correlated the formation of the shells by CILFM with the grain growth phenomenon, which was actually noticed in their samples, near the magnet surface after GBDP. In this mechanism, the shell would result from the migration of the grain boundaries that pushes the GB liquid phase outward at the expense of neighboring smaller grains that would tend to disappear (see Figure 36).

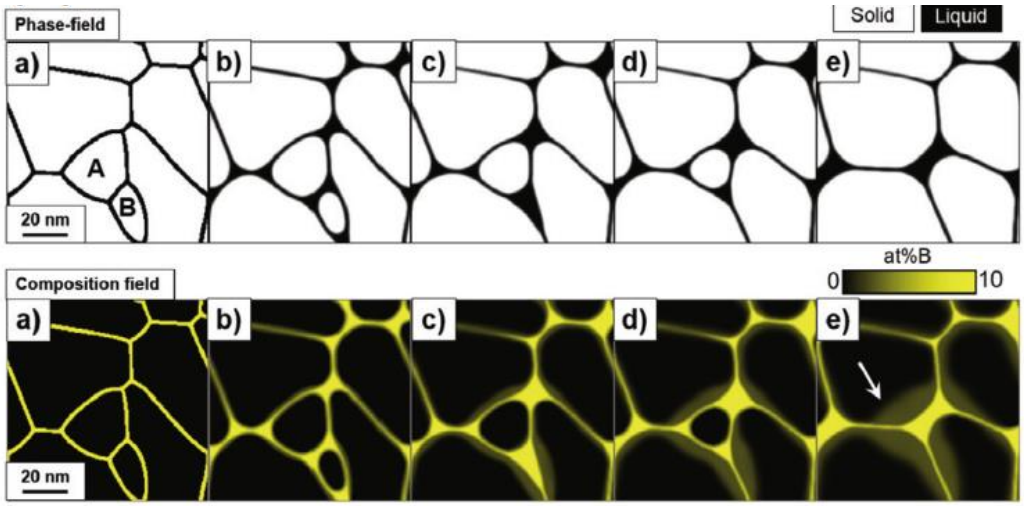

Figure 36: The steps of the grain coarsening simulated by Kim et al. (2020) to account for the core-shell formation in NdFeB magnets after GBDP. The small grains marked A and B present in the initial microstructure (a) disappear due to the migration of GBs (b, c, d) leaving in their tracks the shells pointed by the white arrow (e). Adapted from Kim et al.[87]

Besides the grain coarsening, another driving force in LFM[88] process has been identified as the coherence strain energy for various systems such as Mo-Ni (see Figure 37). The coherence strain energy is linked to the insertion of an atom in the crystalline lattice, which generates thermodynamical stress. The relaxation of the stress causes the film to propagate with a constant concentration in the solid formed behind the film (Baik et al.[89]). The associated Gibbs energy and velocity expressions for the coherence strain approach has been clarified by Song et al.[90]

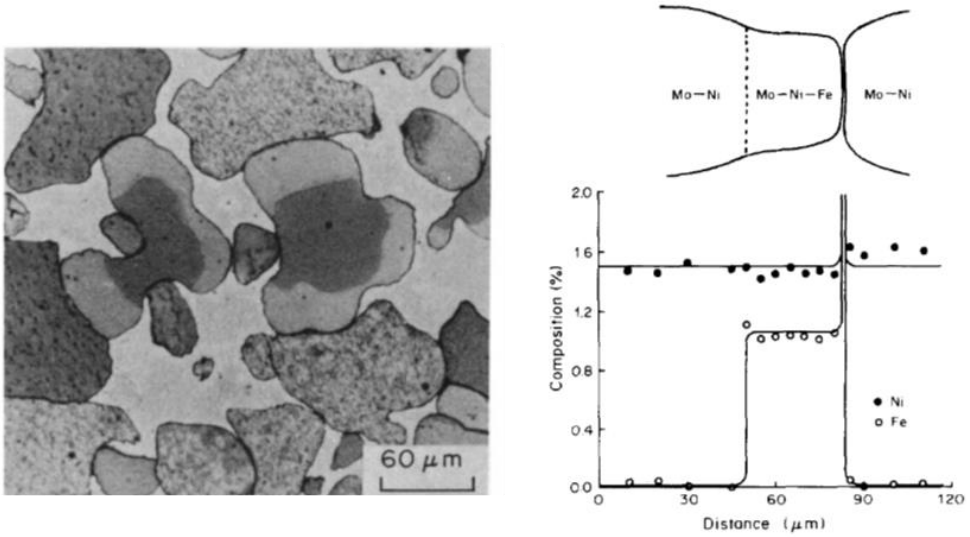

Figure 37: Observation of Liquid Film Migration in the Mo-Ni binary alloy after addition of Fe, from Baik et al.[89] (1986). On the left, The microstructure of 90Mo-10Ni alloy sintered at 1400°C for 20h and heat-treated at 1400°V for 1h after adding 2.8 at.% Fe to the matrix. On the right, The composition profile along the direction of LFM in the 2.8 Fe specimen.

The advantage of this model is that it accounts for the Dy plateau observed at the level of the shell and the Dy-rich shell thickness. However, the correlation between grain coarsening and the thickness of Dy-rich shells is not clearly established in literature. In addition, if we consider the coherence strain energy as a possible driving force in the NdFeB system, up to date, there is no data in literature to support or evidence the consistency of this approach.

1.4 Motivation of the thesis

The GBDP is an efficient process to improve the coercivity of sintered NdFeB magnets. It localizes Dy in the regions of the magnet where nucleation of reversed magnetic domains occurs. Due to the high magneto-crystalline anisotropy of Dy, the GBDP acts as a magnetic hardening technique. However, the process still requires to optimization Dy distribution in order to use less amount of this critical element. This needs to have a better understanding of the underlying mechanisms of Dy distribution induced by GBDP. Nowadays, there is a lack of general agreement on the model of Dy-rich shell formation.

This thesis aims to clarify the influence of GB phases on the diffusion of Dy. It is worth to note that in literature little to no attention is given to the evolution of the secondary phases during the GBDP. We believe that characterizing these phases is important namely because Dy penetrates the magnet through these intergranular phases. For that, we precisely characterize the microstructure of the sintered NdFeB magnet before and after GBDP by analyzing all the phases present in the magnet (main and secondary Nd-rich phases). For that purpose, we rely on electron microscopy techniques, in particular energy dispersive X-ray spectroscopy to quantify the chemical compositions of the various phases present in the magnet before and after GBDP. This global view will provide a comprehensive understanding of the microstructural evolutions during GBDP.

2. Chapter II: Materials and methods

This chapter reports the material, instruments, and experimental procedures that were used in this thesis. It is divided into three parts: in the first part, the different steps of the fabrication process of sintered NdFeB magnets, and the protocol used for the grain boundary diffusion process (GBDP) are given. Both are based on the previous work of Hugonnet[91] and Fliegeans[92] respectively. In the second part, sample preparation techniques for microstructural characterizations are presented, and the challenges encountered are highlighted. In the final part, the characterization methods used to analyze sintered and GBDP NdFeB magnets are described. Among these, a particular attention is paid to the energy dispersive X-ray spectroscopy (EDS) technique in both scanning electron microscopy (SEM) and transmission electron microscopy (TEM). This technique is described in detail, and the associated quantification methods are presented and compared.

2.1 Material: Sintered NdFeB magnet

2.1.1 Fabrication process

Sintered NdFeB magnet samples used in this work are fabricated using the traditional powder metallurgy technique, involving liquid phase sintering (LPS), that is illustrated in Figure 38.

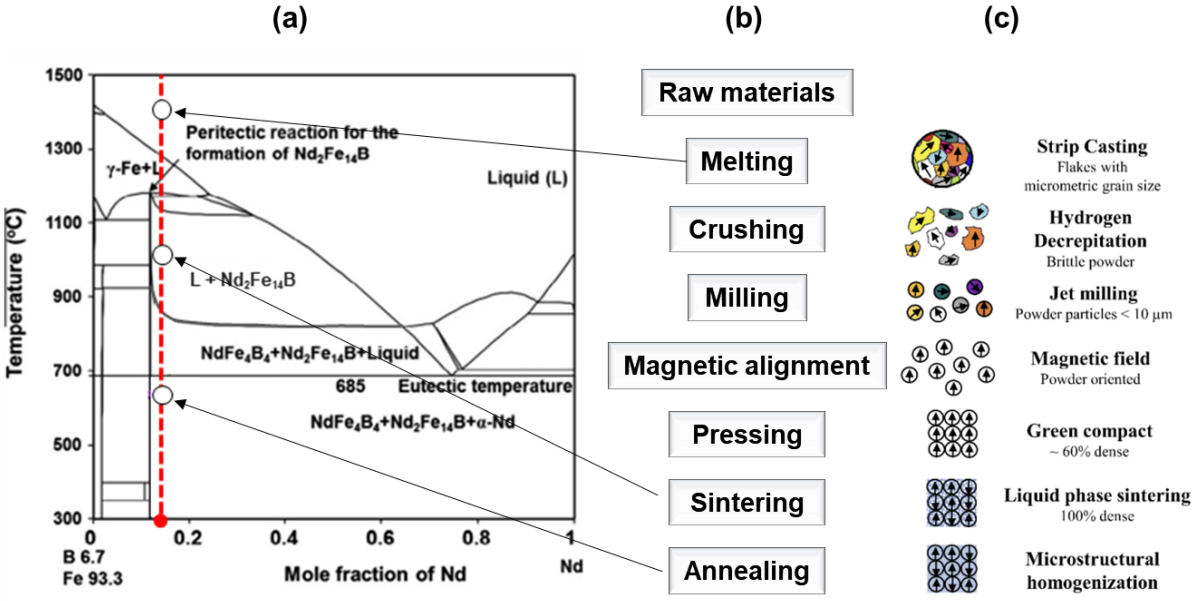

Figure 38: Industrial production route of Nd-Fe-B sintered magnets: (a) Calculated pseudo-binary phase diagram of Nd-Fe-B at Fe/B ratio of 14 taken from Seelam[80] and showing the temperature range at which melting, sintering and annealing should occur, (b) Flow chart of sintering NdFeB magnets, and (c) Schematic representation of the evolution of the microstructure with each step of the sintering process taken from Sarriegui-Estupiñan [93].

After melting the raw materials, the starting alloy for the magnet manufacturing is produced via a rapid solidification technique, called strip-casting (SC). The latter is a rapid quenching method that consists of rapidly cooling a molten NdFeB alloy by ejecting a sheet of the molten alloy onto the surface of a water-cooled metallic roll as illustrated in Figure 39.

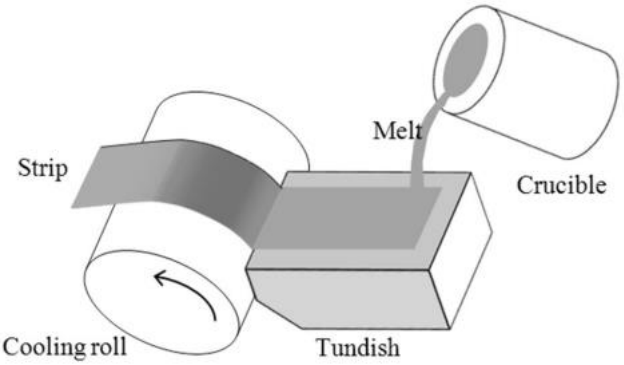

Figure 39: Schematic illustration of the strip casting method. Adapted from Yamamato[94].

The ejected molten alloy cools down in the form of SC ribbons/flakes. The SC ribbons are less sensitive to oxidation than the alloy in the powder form, so it's mainly in this form that the NdFeB alloy is commercially sold. To obtain the alloy in the powder form, the SC ribbons undergo hydrogen decrepitation and jet milling. These steps are detailed in sections 2.1.1.1 and 2.1.1.2 respectively. For the fabrication of the magnets used in this work, five SC ribbons were purchased and transformed into powders. The powders were then mixed together to form the desired NdFeB alloy composition which is as follows: $(Nd,Pr,Dy)_{31}Fe_{67.1}Co_{0.5}Cu_{0.1}Al_{0.3}B_1$ (in wt.%) with 0.5 wt.% of Dy or $(Nd,Pr,Dy)_{14.1}Fe_{78.6}Co_{0.6}Cu_{0.1}Al_{0.7}B_{5.9}$ (in at.%) with 0.2 at% of Dy. The advantage of the powder blend technique is that the overall chemical composition and the amounts of additive elements can be varied by simply varying the ratio of the mixed powders. The chemical composition of each SC ribbon is given in Table 10.

Table 10 : Chemical composition (in wt.%) of the SC ribbons used in this thesis (as determined by Inductively coupled Plasma ICP). RE denotes rare-earth.

	Nd+Pr	Dy	Fe	Co	Cu	Al	B
RE30	29.5	0.5	Bal.	0	0	0	1
RE32	31.5	0.5	Bal.	0	0	0	1
RE31Al2	30.5	0.5	Bal.	0	0	2	1
RE31Co4	30.5	0.5	Bal.	4	0	0	1
RE31Cu0.4	30.5	0.5	Bal.	0	0.4	0	1

Hereafter, the fine jet milled powder is filled in a mold, aligned under an external magnetic field, and pressed to obtain a green compact (i.e., a partially dense magnet). The latter is then subjected to LPS at a relatively high temperature to form dense blocks. Finally, the blocks are cut into the desired shape (here cylindrical shape) and annealed at a relatively lower temperature to optimize their microstructure. As a result, a fully dense NdFeB magnet is obtained with high energy product $(BH)_{max}$ and a relatively simple shape. In the following, each step of the process is detailed.

2.1.1.1 Hydrogen decrepitation (crushing the SC ribbon into a coarse powder)

After SC, the SC ribbons undergo hydrogen decrepitation (HD). The latter is a pre-milling step that is composed of two stages: (i) hydrogen absorption to crush the SC ribbons into a coarse powder, and (ii) partial hydrogen desorption to remove the hydrogen from the coarse powder. During the absorption process, the hydrogen is absorbed by the phases present in the SC ribbons: first, Nd-rich phases preferentially absorb hydrogen[95] and form neodymium hydride NdH_3 via an exothermic reaction[96], and then the heat released from the exothermic reaction allows the $Nd_2Fe_{14}B$ phase to absorb hydrogen and form interstitial solution hydride $Nd_2Fe_{14}BH_x$ with $0 \leq x \leq 5$[16,97]. The exact amount of absorbed hydrogen depends on the temperature, Nd content, and the hydrogen pressure[96]. Due to the hydrogen absorption, both phases expand, and cracks appear at the grain boundaries and to some extent across the grains. The cracks greatly improve the efficiency of subsequent milling process performed by jet milling. The process is illustrated in Figure 40.

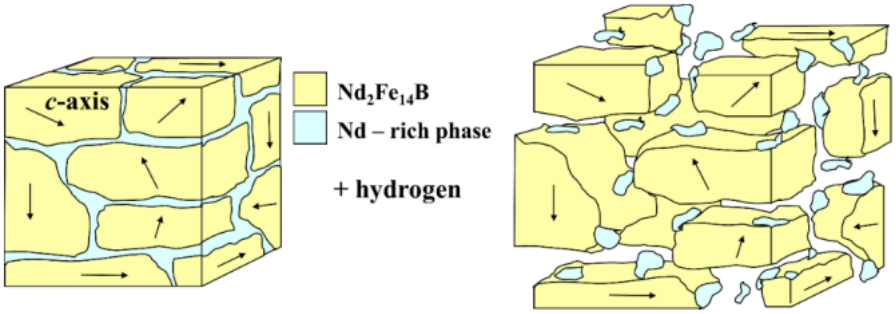

Figure 40: Bursting of the SC ribbons following hydrogen absorption. Adapted from Sarriegui-Estupiñan[93].

The problem with hydrogen absorption alone is that the NdH_3 phase is easily oxidized[98] and the hydrogen present in the $Nd_2Fe_{14}B$ phase lowers its anisotropy field H_A[16]. This is why hydrogen desorption is necessary. The latter is performed in three steps[99]: (i) desorption from the $Nd_2Fe_{14}B$ phase by heating the HD coarse powder at 200°C under vacuum, (ii) partial desorption from Nd-rich phases (i.e., transformation of NdH_3 into NdH_2 which is less susceptible to oxidation) by an additional heat treatment at 400-500°C under vacuum, and (iii) complete desorption from the Nd-rich phase (i.e., decomposition of NdH_2 into Nd and H_2) which, unlike the previous desorption processes, is performed later during sintering. Hereafter, the HD coarse powder is ready for jet milling.

2.1.1.2 Jet milling (obtaining a fine powder)

Jet Milling (JM) consists of mechanically crushing the HD coarse powder into a fine powder. To do so, the particles of the HD powder are entered to the Jet mill, picked up by several opposing gas streams (3 in our case fed by nitrogen gas), and ground by colliding the streams with each other as seen in Figure 41.

Figure 41 : Nitrogen jet milling device used at CEA/LITEN. Adapted from Fliegans[92].

Compared to ball milling, JM is a faster process. In addition, the milling gas is inert which lowers the risk of powder contamination. JM is a low energy milling process; hence it maintains the adhesion of the Nd-rich phases at the surface of the $Nd_2Fe_{14}B$ grains. This ensures an optimal distribution of the Nd-rich phases which is crucial to achieve homogenous LPS. As the JM process progresses, the grain size is continuously adjusted until reaching the desired grain size. The typical grain size after JM is around 5 μm. The smallest grain size achieved by nitrogen jet milling is 3 μm[100]. Ultrafine grain size of ≈ 1 μm can be achieved by using the higher energy helium jet milling[101].

After obtaining the refined jet milled powder, the next step is to consolidate it into a green compact. For that, the NdFeB powder is first transferred into a glove box under nitrogen atmosphere to minimize the risk of oxidation during powder handling. Then, the powder is put inside a cylindrical shaped silicon mold with a diameter of 14 mm and a height of 25 mm. The latter is finally sealed inside a plastic bag and taken outside the glove box to carry on with the alignment and pressing steps.

2.1.1.3 Magnetic alignment

Magnetic alignment consists of applying an external magnetic field to rotate and align the monocrystalline $Nd_2Fe_{14}B$ grains so that their easy axis (i.e., the c-axis) are parallel. For that, the system (silicon mold + plastic bag) is put inside a Bitter coil as displayed in Figure 42.

Figure 42: Bitter coil used for magnetic alignment.

The Bitter coil produces strong pulsed magnetic fields that can reach 8 T. Such strong magnetic fields are necessary to obtain sufficiently high torques to rotate and align the $Nd_2Fe_{14}B$ grains into the direction of the external magnetic field.

Inside the Bitter coil, the powder undergoes an alignment cycle composed of a succession of alternate pulsed magnetic fields of opposite direction (along +z or -z) and decreasing intensity. The use of an "alternate" pulsed magnetic fields instead of a conventional "positive" magnetic field has many advantages: (i) compacts with higher $(BH)_{max}$ are obtained[102] and (ii) the process has a better repeatability[102]. The direction, intensity and duration of each pulse field are given in Table 11.

Table 11: The succession of pulsed fields used for magnetic alignment of the NdFeB powder.

Pulse number	Magnetization/ Demagnetization	Pulse direction	Pulse intensity (T)	Pulse duration (ms)
1	Magnetization	+	7	5
2	Magnetization	-	6	5
3	Magnetization	+	4	5
4	Magnetization	-	0.5	5
5	Demagnetization	+	6	5

At the end of magnetic alignment, the aligned powder is demagnetized by applying a reverse magnetic field. If not, the interaction between the magnetized $Nd_2Fe_{14}B$ grains will make the compact too brittle and the cold isostatic pressing less effective.

2.1.1.4 Cold isostatic pressing

After magnetic alignment, the aligned powder is pressed into a partially dense magnet (usually called a green compact) inside a cold isostatic pressing (CIP) machine. The CIP machine is displayed in Figure 43.

Figure 43: Cold isostatic pressing system used at CEA/LITEN for compressing powders.

The principle of CIP is to apply pressure to the aligned powder evenly from all directions. The pressure is applied via a liquid medium, which in our case is water, and the pressure is P = 1500 bars. The even pressure application allows to maintain powder alignment while pressing the aligned powder. The final product is a green compact whose degree of alignment ranges between 86-93%[103].

2.1.1.5 Sintering

The sintering process consists of two main steps: (i) complete hydrogen desorption from the Nd-rich phases, and (ii) densification of the green compact into a fully dense magnet via liquid phase sintering (LPS). Hydrogen desorption is carried out at 600-800 °C under vacuum[75], during which NdH_2 decomposes into Nd and H_2. LPS is then carried out at 1000-1100 °C under vacuum[75]. Liquid formation starts by the melting of the Nd-rich phases via the ternary eutectic reaction L ↔ $Nd_2Fe_{14}B$ + Nd-rich + $NdFe_4B_4$ at 682.2 °C. As the temperature increases, the amount of liquid phase increases. The optimal temperature for LPS depends on several factors such as the magnet composition and grain size. The temperature should be high enough to obtain sufficient liquid phase to completely wet the grain boundaries and ensure a full densification; and low enough to prevent abnormal grain growth. Straumal et al.[104] showed that the liquid phase completely wets the grain boundaries at 1150 °C; whilst only 10% of the grain boundaries are wet at 700 °C.

In our work, sintering and all other heat treatments are performed in the Lilliput sintering furnace from ECM Technologies that is shown in Figure 44.

Figure 44: Furnace used at CEA-LITEN for sintering, annealing and diffusion heat treatments. Taken from Fliegans[92].

This furnace is equipped with a home-made glove box to minimize the contamination of the green compact. Inside the furnace, there is a secondary vacuum atmosphere, and heat treatments start when a pressure of 9×10^{-5} is reached.

For the magnets used in this work, complete hydrogen desorption is performed at 750 °C for 4h, and LPS is performed at 1032 °C for 4h. The thermal cycle used for sintering is illustrated in Figure 45.

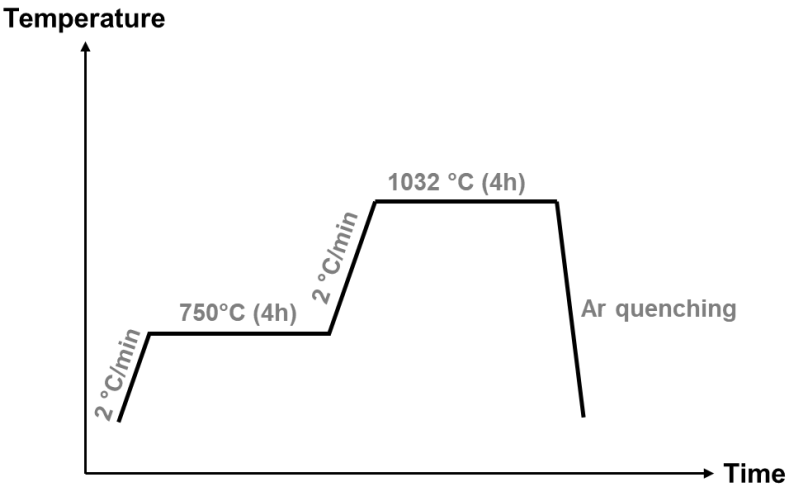

Figure 45: Thermal cycle used for sintering.

After sintering, the magnets were cut into a cylindrical shape of diameter (ϕ) of about 10 mm and a thickness of about 5 mm. The average density of the NdFeB magnets was calculated using Archimedes' principle and determined to be 7.57 g/cm^3.

2.1.1.6 Post-sinter annealing

Hereafter, the sintered magnets are subjected to an additional heat treatment, called post-sinter annealing (PSA). The latter aims to enhance the coercivity of the magnets by optimizing their microstructure. Annealing consists of two heat treatments: The first one is performed at 800 °C such that the Nd-rich phase is in liquid state, and the second one is performed at a variable temperature ranging between 500°C-550°C (the temperature of the second heat treatment will be determined in chapter III). The thermal cycle used for annealing is illustrated in Figure 46.

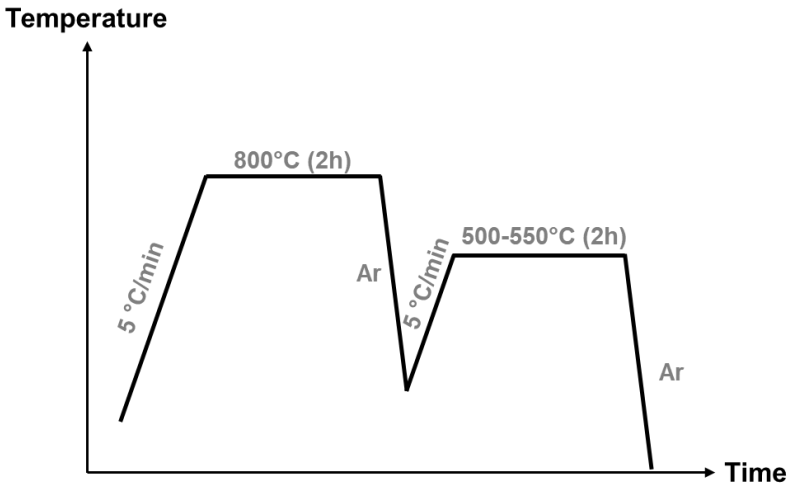

Figure 46: Thermal cycle used for annealing.

2.1.2 Grain boundary diffusion process (GBDP) protocol

2.1.2.1 Sample preparation for the GBDP

In this work, GBDP is performed using $Dy_{63}Co_{37}$ (at.%) intermetallic compound. The choice of $Dy_{63}Co_{37}$ is based on the previous work of Fliegans[92]. As it can be seen in Figure 47, $Dy_{63}Co_{37}$ has a low melting point (melting temperature T_M = 734 °C) which is crucial to achieve efficient diffusion.

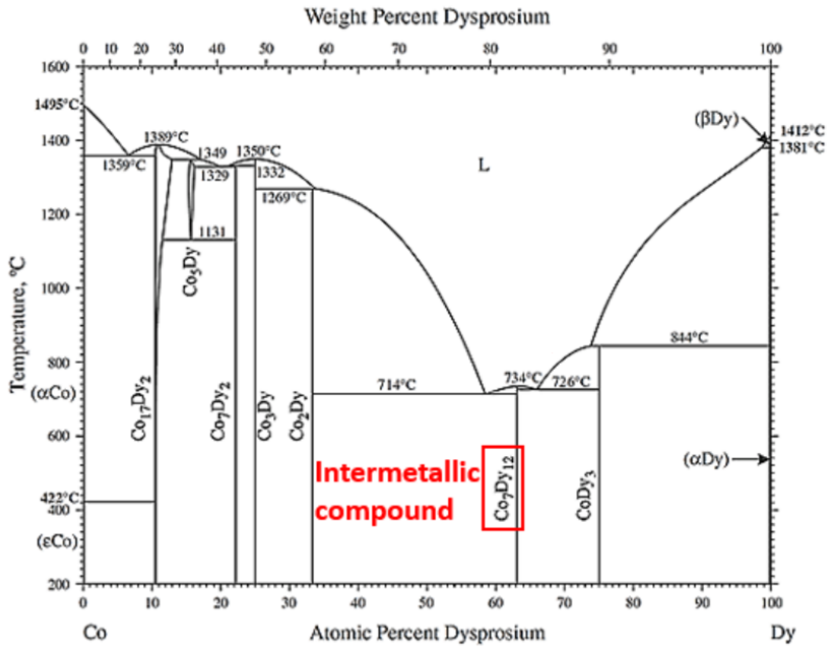

Figure 47: Dy-Co binary phase diagram. Adapted from Fliegans[92].

Before diffusion, the cylindrical shaped NdFeB magnets ($\phi 10 \times 5$ mm²) are chemically cleaned using a diluted nitric acid solution. This ensures the removal of surface oxidation. Then, the GBDP source is prepared. The latter is an ink prepared by mixing the DyCo powder with a lubricant (Terpineol). The ink contains 65 wt.% of Dy-Co for optimal viscosity. Finally, the Dy-Co ink is painted using a brush on both the upper and lower surfaces of the magnet (see Figure 48). The amount of ink used for each magnet is calculated so that it is coated by 0.7 wt.% of Dy.

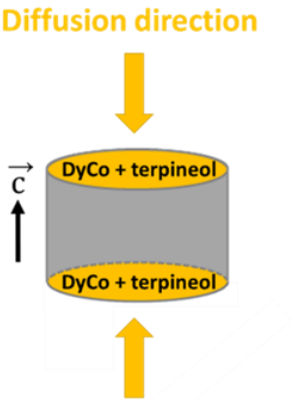

Figure 48: Schematic representation of sample preparation for the GBDP.

2.1.2.2 Diffusion heat treatment

Diffusion heat treatment consists of a two-step heat treatment. The first step is performed at 250°C and aims at removing the residual Terpineol at the surface of the magnet; while the second step is the actual diffusion heat treatment that enables the penetration of DyCo inside the magnet. This step is carried out at 920°C for 3h, or 920°C for 1h, or 870°C for 3h to investigate the effect of the

GBDP temperature and time on the magnetic and microstructural properties. The thermal cycle used for GBDP is illustrated in Figure 49.

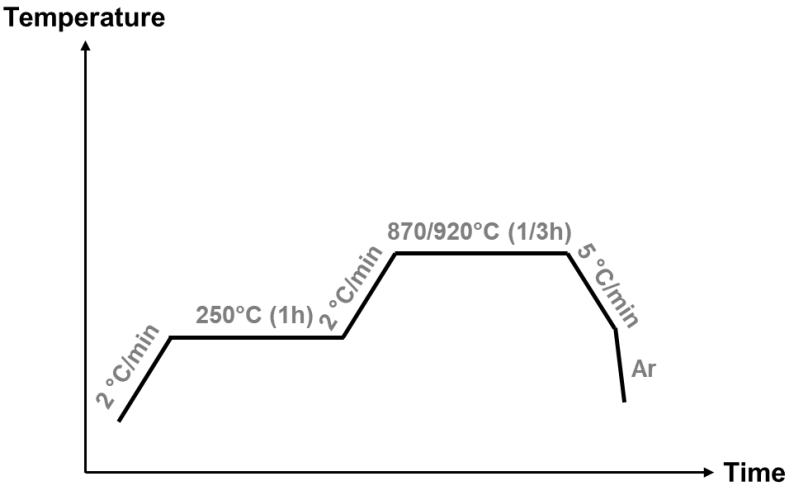

Figure 49: Thermal cycle used for GBDP.

After the diffusion treatment, the GBDP magnets are subjected to an annealing heat treatment named post-diffusion annealing (PDA). The latter follows the exact thermal cycle of the annealing treatment displayed in Figure 46. This enables to compare the PDA magnet to the PSA state.

2.2 Sample preparation

2.2.1 Metallography (cross-section polishing)

To be able to perform microstructural analysis (SEM observations, EDS-SEM analysis, and EBSD analysis), the samples are embedded in Epoxy or Carbon resin and subsequently polished. Polishing is done using the equipment "Mecatech 300" by PRESI shown in Figure 50.

Figure 50: Equipment « Mecatech 300 » by PRESI used for polishing.

The advantage of the "Mecatech 300" is that it allows to automate the polishing process, hence ensuring its repeatability. The polishing steps are detailed in Table 12.

Table 12: Polishing steps used during sample preparation for microstructural analysis.

Polishing step	Polishing disk	Lubricant	Duration (sec)	Rotation speed of the head (rpm)	Rotation speed of the plateau (rpm)	Applied force (daN)
1	SiC 1200	Water	120	135	150	2
2	SiC 2400	Water	120	135	150	2
3	PAD TOP 9 µm	Ethanol	180	135	150	1
4	PAD RAM 3 µm	Ethanol	240	135	150	1
5	PAD NT 1 µm	Ethanol	360	135	150	1
6	PAD NT 1/4 µm	Ethanol	360	135	150	1

It is important to note that the surface oxidation of the sample is the most challenging part of this sample preparation procedure. Surface oxidation is evidenced by the detection of O inside the $Nd_2Fe_{14}B$ phase as determined by the EDS-SEM analysis. This is problematic since it affects the amount of O determined in the Nd-rich phases and probably their crystallographic structure. In addition, surface oxidation suppresses EBSD signal leading to unsuccessful EBSD analysis (only one EBSD experiment was done successfully during the thesis). A cross-section polisher (CSP) and a proper transfer box are therefore indispensable for preparing this kind of samples.

After polishing, the samples are coated with a 5 nm layer of carbon using the "safematic" equipment displayed in Figure 51.

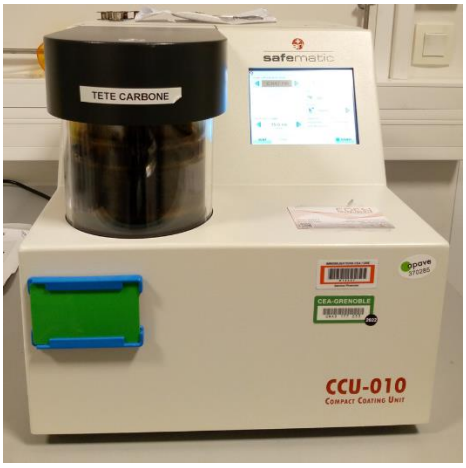

Figure 51: Safematic equipment used for carbon coating.

2.2.2 Focus ion beam (FIB)

Focus Ion Beam (FIB) is a lift out technique used to prepare lamellae for transmission electron microscopy (TEM) characterizations. Among other TEM lamellae preparation techniques (such as tripod polishing or ionic thinning using Precision Ion Polishing System PIPS), FIB has the advantage of precisely choosing the location from where to lift out the lamella and to execute the entire process under vacuum to avoid oxidation. On the other side, the main drawback is that the TEM lamellae have small dimensions (here 15×3 μm^2). Therefore, several TEM lamellae should be prepared and characterized to be able to draw sustainable conclusions.

A FIB is usually paired with an electron column used for imaging and to supervise the entire process of TEM lamella preparation. The electron column lies vertically, and the FIB column is tilted at T=45° from it. In addition, a Gas Injecting System (GIS) is also found inside a FIB-SEM chamber. The GIS is used to deposit a protective layer on the region of interest (ROI).

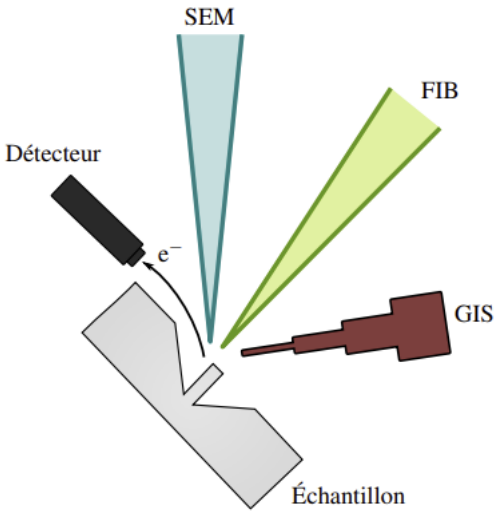

Figure 52: Schematic representation of the different parts found in a FIB-SEM.

FIB is a technique that focalizes ions extracted from a liquid metal ion source (here gallium) to produce an accelerated ionic beam. After locating and protecting the ROI with platinum (here a 1300 nm layer of Pt is deposited), the ionic beam is accelerated, and the high mass accelerated ions pulverizes the sample and get rids of the material near the ROI leaving behind a chunk. The chunk is then extracted, glued on a molybdenum (Mo) grid in a flag geometry, and subsequently thinned to be transparent to electrons (≈ 100 nm). The Mo grid is chosen instead of a Cu grid due to the presence of Cu inside the samples. This process is illustrated in Figure 53.

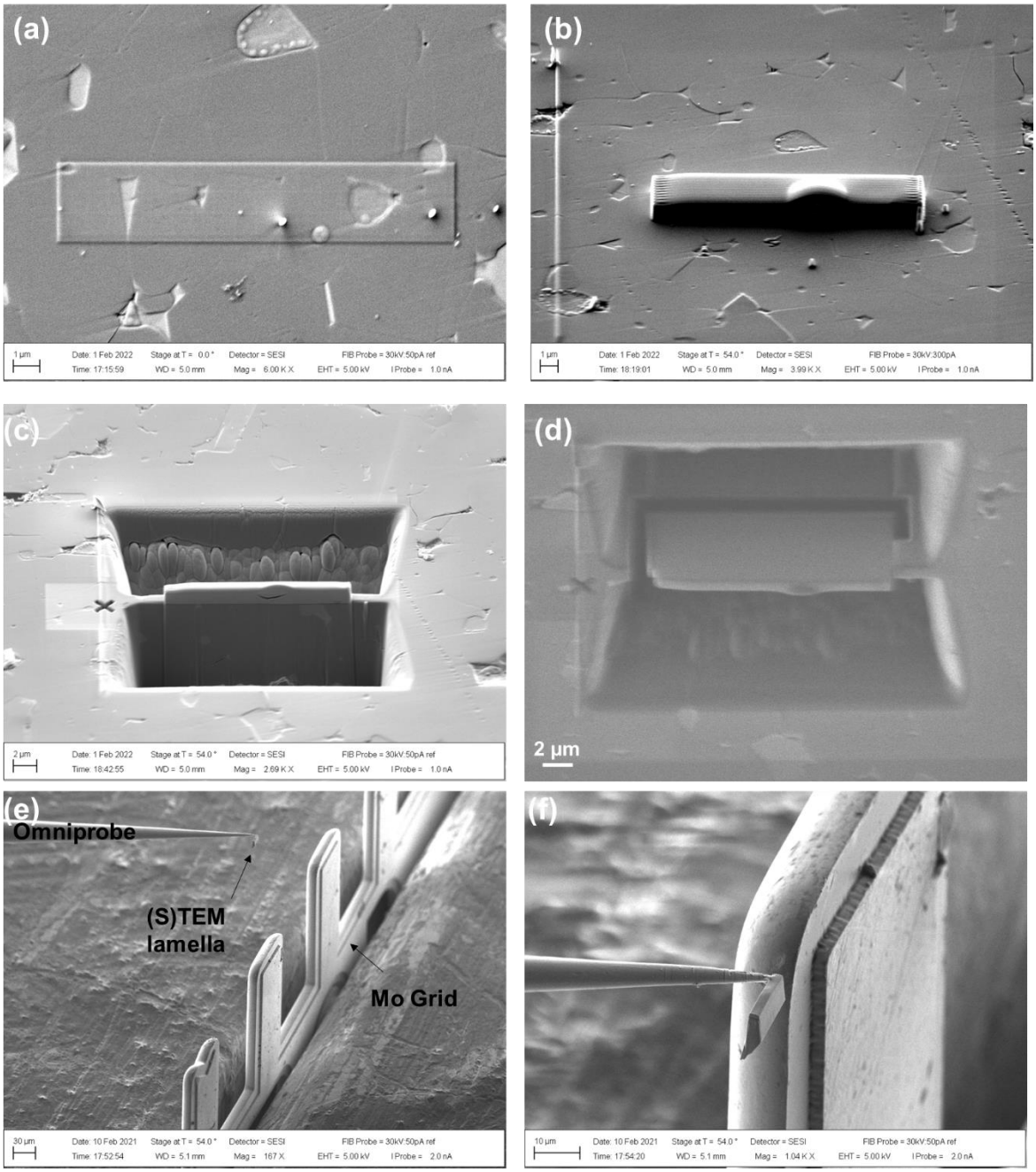

Figure 53: Steps of (S)TEM lamellae fabrication using FIB-SEM: (a) deposition of Platinum protective layer of 200 nm on the ROI using the e-beam, (b) deposition of second Platinum protective layer of 1 µm on top of the first protective layer using the Ga ionic beam, (c) pulverization of the material surrounding the ROI to define the chunk to extract, (d) U shape cut to be able to detach the chunk from the sample, (e) extraction of the chunk using the Omniprobe, and (f) Gluing the chunk on the molybdenum (Mo) grid in a flag geometry.

In this work, the main objective of TEM characterizations is to study the phase at the grain boundaries. However, it is not evident to prepare lamellae for this purpose. In fact, it seems that there are strong internal stresses in the bulk magnet that are released during the lamellae thinning. As a result, the lamellae end up by bending (see Figure 54). In addition, grain boundaries are often found cracked and/or cracks appear during thinning. As a result, we have had numerous failures during the preparation of FIB lamellae.

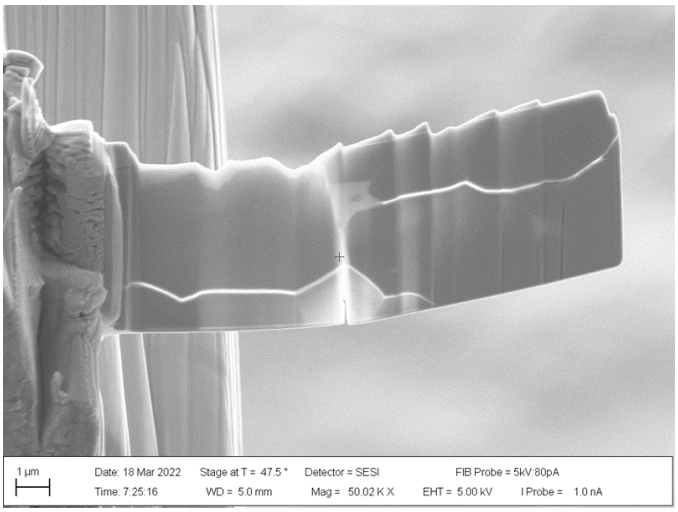

Figure 54: Image of a TEM lamellae bent during thinning and showing the cracks at the grain boundaries.

To prevent the distortion of the TEM lamellae, it is recommended to switch from gluing it in a flag geometry to gluing it in a M shape as illustrated in Figure 55. However, this technique does not prevent the occurrence of cracking at the grain boundaries.

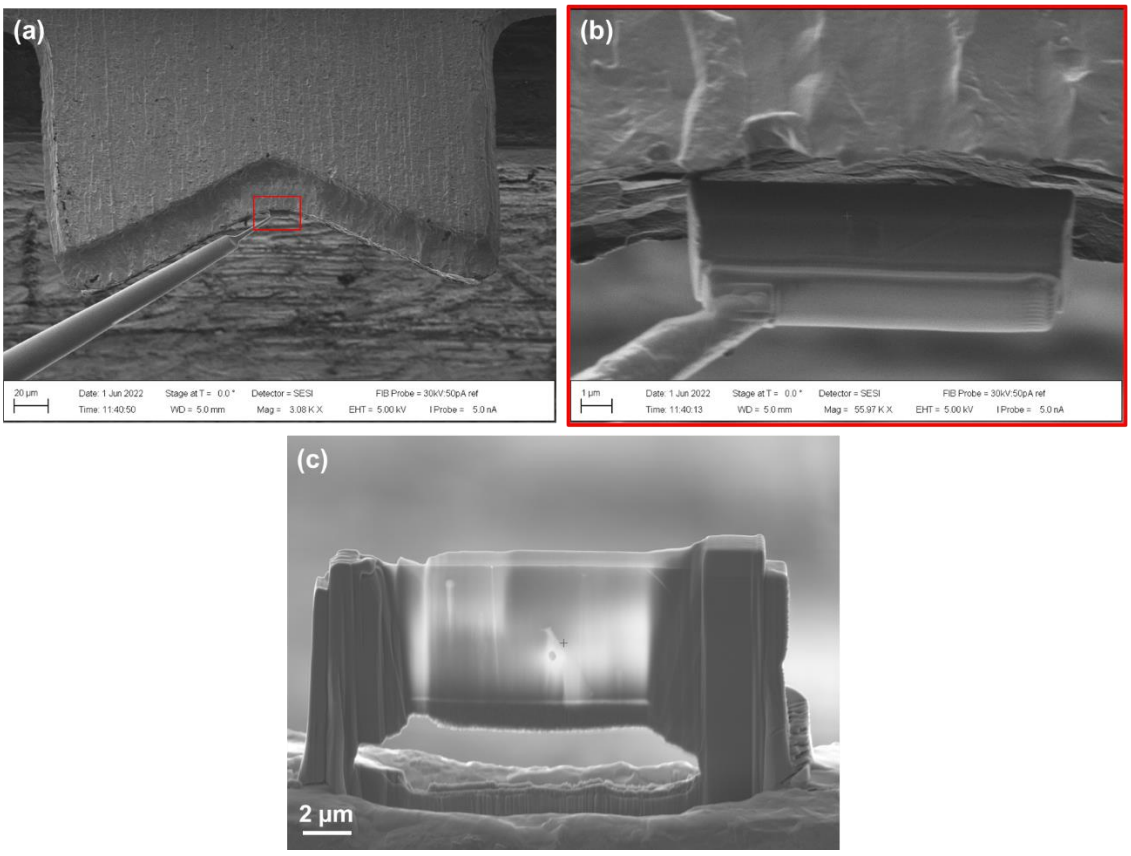

Figure 55: (a) Gluing of the chunk in an M geometry, (b) zoomed in image to better show the M geometry, and (c) thinning of the lamella in the M geometry without distortions.

All the TEM lamellae studied in this thesis are prepared using the FIB-SEM ZEISS Crossbeam 550 shown below.

2.3 Characterization techniques

2.3.1 Hysteresigraph

Magnetic measurements are performed using the AMH-300-P hysteresigraph system of Laboratorio Elettrofisico shown in Figure 56.

Figure 56 : Hysteresigraph system used at CEA-LITEN for magnetic characterization. Adapted from Fliegans [92].

This method is used to determine the magnetic properties of the materials and to construct their demagnetization curve. First, the sample is machined to ensure it has plane surfaces. This is done to avoid air gap and mechanical stress during magnetic measurements as it can affect the measured remanence[105]. Then, the sample is magnetized in a large magnetic field (in our case 6 Tesla) produced by a bitter coil, so it reaches its saturation value. Afterwards, it is inserted within the airgap of the magnetic circuit in the hysteresigraph system (see Figure 57).

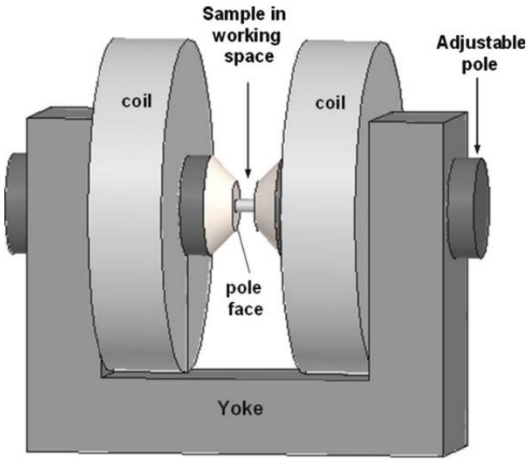

Figure 57: Sketch of the magnetic circuit in the hysteresigraph system. Adapted from Chen[106].

The magnetic circuit itself presented in Figure 57 is composed of two poles made of Fe-Co (the upper pole is adjustable to be able to adjust the air gap), two electromagnetic (winding) coils, and

a large yoke structure in the form of a horseshoe. The magnetic field inside the magnetic circuit is generated by an electric current circulating in the winding coils. The large yoke structure plays a crucial role in guiding and shaping the magnetic field so that a uniform and controlled magnetic field pass through the sample. This is essential to ensure accurate measurements of the sample's magnetic properties and the construction of its demagnetization curve. The polarization of the sample is then determined using a pick-up probe composed of three concentric coils (an inner coil that measures the polarization and two other coils for compensation purposes) that allows accurate flux measurements. For that, the sample is inserted in the hole of the probe. It is not mandatory that the sample fits exactly inside the hole of the probe, namely in our work, the LJT-10 probe presented in Figure 58 was used. The latter has a 10 mm diameter hole and can accommodate samples with a minimal thickness of 2.5 mm. All the characterized samples are cylindrical shaped samples of dimensions 5 (thickness) × 10 (diameter) mm^2.

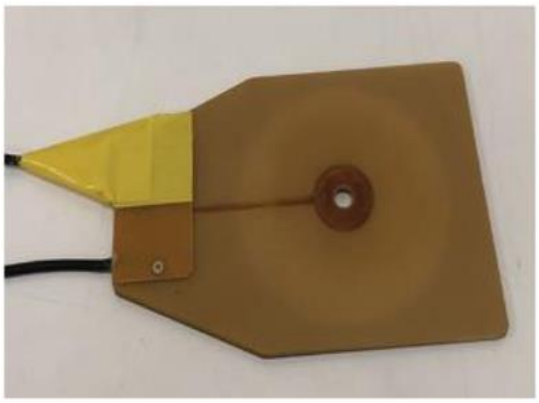

Figure 58: LJT-10 pick-up probe used for magnetic measurements. Adapted from Fliegans [92].

As the sample is subjected to the applied magnetic field, its polarization changes in response. This change in polarization induces an electromotive force in the pick-up coil that is proportional to the rate of change of polarization due to Faraday's law of electromagnetic induction. The signal from the pick-up coil is then amplified, filtered, and integrated over time to calculate the flux values Φ. Hence, the pick-up probe measures the magnetic flux and not directly the polarization. The latter can be determined from the former using Eq. (2.1):

$$\Phi = NAJ, \tag{2.1}$$

where N is the number of turns of the inner coil, A is the geometrical section of the sample and J is the polarization of the sample.

As it can be seen from (2.1), the determination of the polarization from the measured flux requires a prior knowledge of the geometrical section of the sample. This is why the sample thickness, diameter, weight, and density (which is determined using Archimedes method) are given as input parameter. The measurement process is automatically managed by the Xenon-1.0 software associated with the AMH-300-P hysteresigraph instrument. In addition, the Xenon-1.0 software offers several additional options, one of which is to complete the demagnetization curve for high

coercive magnets (such as NdFeB magnets) by extrapolation since the hysteresigraph system is not capable to fully demagnetize these magnets[3].

Following the magnetic measurements (all performed at room temperature), the following typical demagnetization curve characteristic of sintered NdFeB magnets is obtained.

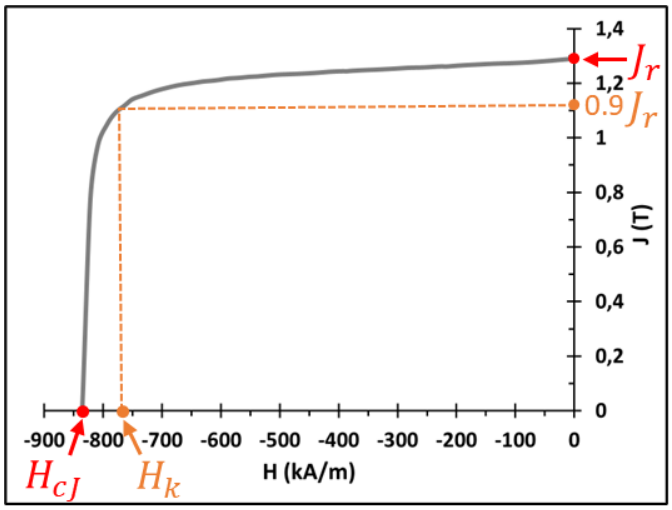

Figure 59: Demagnetization curve of a sintered NdFeB magnet manufactured in the CEA-LMCM laboratory and measured at room temperature using the hysteresigraph system on site.

From this curve, important magnetic properties can be extracted such as the remanence J_r, the coercivity H_{cJ}, the maximum energy product $(BH)_{max}$, and the knee field H_k from which the squareness factor of the demagnetization curve can be evaluated.

2.3.2 Scanning electron microscopy (SEM)

Scanning electron microscope is one of the most versatile instruments used by researchers to examine and analyze the microstructural features of a solid object. Besides its higher resolution (compared to optical microscopy), SEM is equipped with detectors that record signals revealing topographical (with a high depth of field), chemical compositions, and structural details (e.g., texture, crystallographic structure) of the sample under examination. Compared to TEM, SEM requires less sample preparation (samples should be polished and coated with a conductive coating such as carbon or platinum in case they are non-conductive).

The working principle of an SEM is the following: electrons are first extracted from a source present in upper part of the SEM column, beam shaped and then accelerated using a set of electromagnetic lenses. Hereafter, the resulting electron beam is scanned on the sample surface where it interacts with the sample atoms. The electron beam has a spot size of a few nanometers and interacts with several atomic layers inside the sample, creating a complex interaction volume. The interaction volume consists of various signals resulting from the electron beam-sample

[3] To fully demagnetize the NdFeB magnets prior to the microstructural observations, they are heated for 30 min above their Curie temperature inside the Lilliput furnace from ECM Technologies located at CEA-LMCM.

interaction (see Figure 60), of which the most important are primary backscattered electrons (BSE), secondary electrons (SE), and X-rays. Each signal originates from a different mechanism, is recorded by a specific detector, and reveals different information about the sample. For instance, BSE unveil information regarding the atomic number, SE disclose topographical information and X-rays serves to determine the chemical composition of the phases inside a sample. These signals are detailed below.

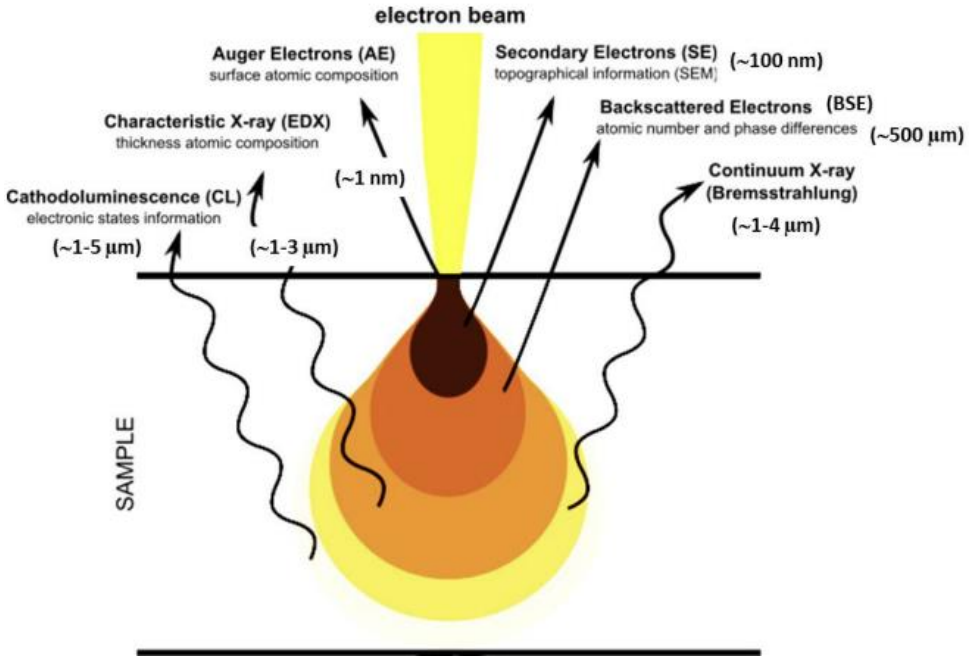

Figure 60: Signals emitted from the different parts of the interaction volume. Adapted from Chauhan[107].

2.3.2.1 Secondary and backscattered electrons

A visual representation comparing SE and BSE is provided in Figure 61.

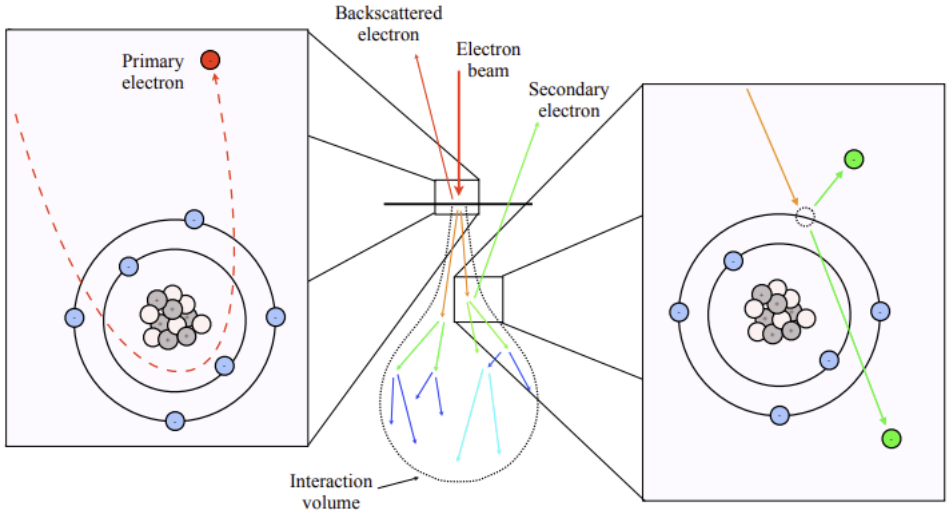

Figure 61: Schematic illustration of backscattered and secondary electrons resulting from the electron beam-specimen interaction in SEM. Adapted from Gaudenzei de faria[108].

SE are so called because they are generated from a secondary source (the sample). SE are electrons that are weakly bonded to atoms and knocked out due to inelastic scattering between the energetic electron beam and these atoms. Since the scattering is inelastic, SE ejected from atoms deeper inside the sample propagate in the interaction volume in a cascade effect and quickly lose their energies (i.e., they are not detected). However, SE from atoms at the sample surface (few nm) are emitted (can escape from the sample) before losing their energies and detected with the appropriate detectors. All electrons emitted from the sample with a kinetic energy less than 50 eV (arbitrary choice) are considered SE. SE images are usually used for topographical information.

BSE are primary electrons (i.e., electrons of the electron beam) whose trajectory is deviated by elastic scattering produced by the atomic nuclei. Since the scattering is elastic, electrons don't lose their energies, and undergo multiple scattering events that alter their trajectories until they are sent back to the same hemisphere containing the electron beam (hence the term backscattered). Consequently, BSE have considerably higher energies than SE and emerge from deeper locations in the interaction volume resulting in lower resolution of BSE images compared to SE images. BSE increase with increasing atomic number Z, as heavier atoms have more positive charges and scatter electrons more intensely than lighter atoms. Hence, when imaging a sample with BSE, light elements will appear darker than heavy elements. This is called the Z contrast.

In this work, the BSE were used for imaging the sample to reveal Z contrast information. The BSE images were recorded using an insertable 4 quadrant BSE detector mounted on a MERLIN Gemini scanning electron microscope from ZEISS. Figure 62 shows a BSE-SEM image acquired from a NdFeB magnet, in which the gray contrast corresponds to the matrix and the bright contrast correspond to the Nd-rich phases of higher atomic number. A SE-SEM image is shown in comparison.

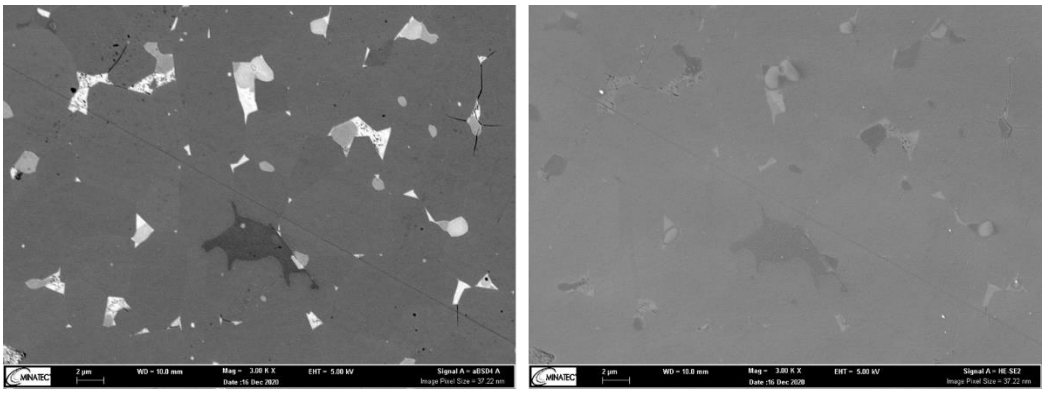

Figure 62: (a) BSE-SEM and (b) SE-SEM images acquired from a sintered NdFeB magnet.

The spatial resolution of SE images is directly related to the size of the electron beam, whereas for BSE images and EDX analysis it is related to the electron beam energy and sample density. Figure 63 illustrates the effect of varying the electron beam energy on the interaction volume for NdFeB.

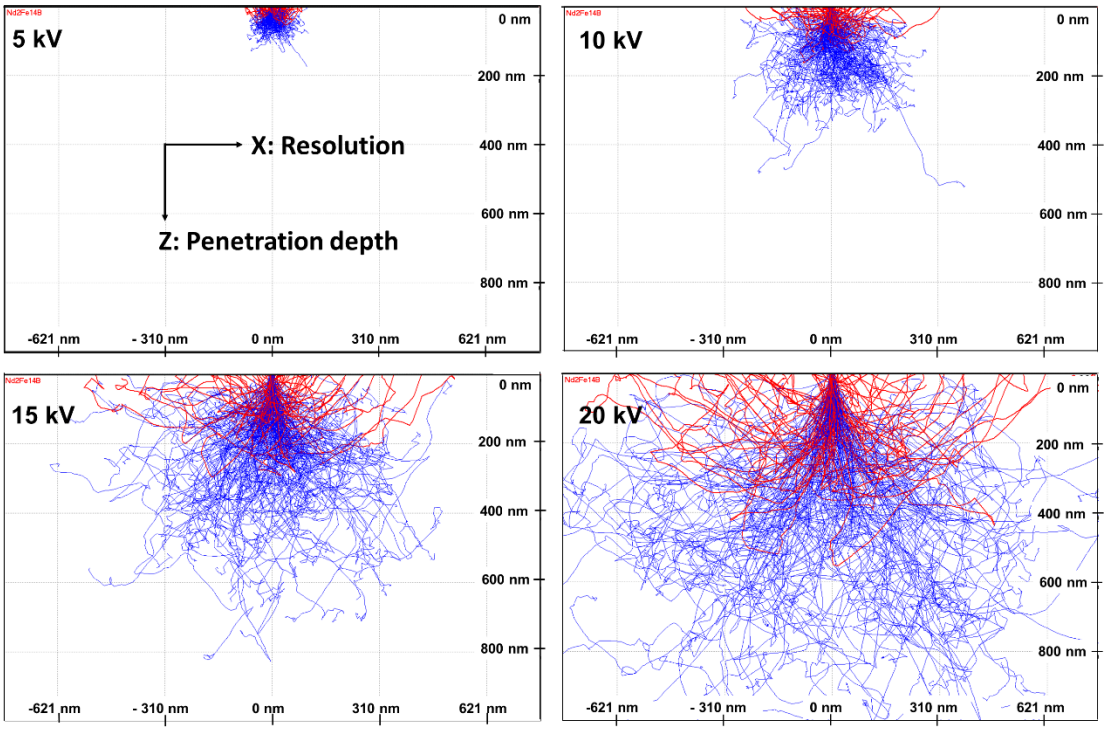

Figure 63: Variation of the interaction volume for NdFeB at (a) V_{acc}= 5 keV at (b) V_{acc}= 10 keV, (c) V_{acc}= 15 keV and (b) V_{acc}= 20 keV. Trajectories in red correspond to the BSE and in blue to the X-rays. The simulation is performed using Casino software.

Depending on the beam energy, the resolution is as follows: 116 nm at 5 keV, 300 nm at 10 keV, 580 nm at 15 keV, and 840 nm at 20 keV. In our study, the electron beam energies used when examining the NdFeB sample inside the SEM are 5 kV for imaging and EDS analysis, 10 kV for WDS analysis and 20 kV for EBSD analysis.

2.3.2.2 Energy dispersive X-ray spectroscopy (EDS)

In our work, EDS technique is used to analyze the elemental composition of the phases present in both sintered and Dy-GBD processed NdFeB magnets. In the following, the underlying principle of EDS is explained as well as the quantitative procedure by which concentration of elements can be obtained. This section is concluded by listing the steps and parameters used to acquire and analyze the EDS data for our NdFeB samples.

A. Principle

When an energetic electron beam interacts with the atoms of a sample, its electrons are scattered elastically or inelastically. During inelastic scattering, electrons of the electron beam transfer energy to the inner shell electrons of the atoms. If the transferred energy is high enough[4], inner-shell ionization can occur which means that inner shell electrons can be ejected from the atoms leaving inner shell vacancies and putting the atoms in a higher energy excited state. As a result, outer shell

[4] The minimum energy required to remove an electron from a specific shell is equal to the *critical ionization energy* of the shell. It is defined as the energy needed to remove an electron from a bound state in a shell to an effective infinity outside the atom.

electrons fall to fill the inner shell vacancies by releasing a specific amount of energy in the form of characteristic X-rays or characteristic electrons (Auger electrons). The energy of the characteristic X-rays is equivalent to the energy difference between the energy levels involved in the electronic transition. Each atom has its specific energy levels, consequently the released energy is characteristic of the atom. Since an atom has multiple energy levels, multiple electronic transitions can take place giving rise to multiple X-ray energies or X-ray lines. These X-ray lines are characteristic of the atoms that released them and are used to identify the elements present in the sample, and to quantify their concentrations.

The generated X-rays are detected by an EDS detector (the most typically used is a Silicon Drift Detector SDD) that measures their energies, sort them into channels according to their energies, and records their intensities. As a result, an EDS spectrum is obtained, where the X-ray energy (expressed in kilo-electron volts keV) is displayed on the x-axis and the X-ray intensity (expressed in counts per second cps) is displayed on the y-axis. The peaks in the EDS spectrum correspond to the characteristic X-rays generated by the elements present in the sample. These peaks are always accompanied by a band of continuous X-ray radiation (also known as Bremsstrahlung radiation) that is observed as an EDS spectrum background. The continuous X-ray radiation arises from the deceleration of the primary electrons by the electric field close to atomic nucleus.

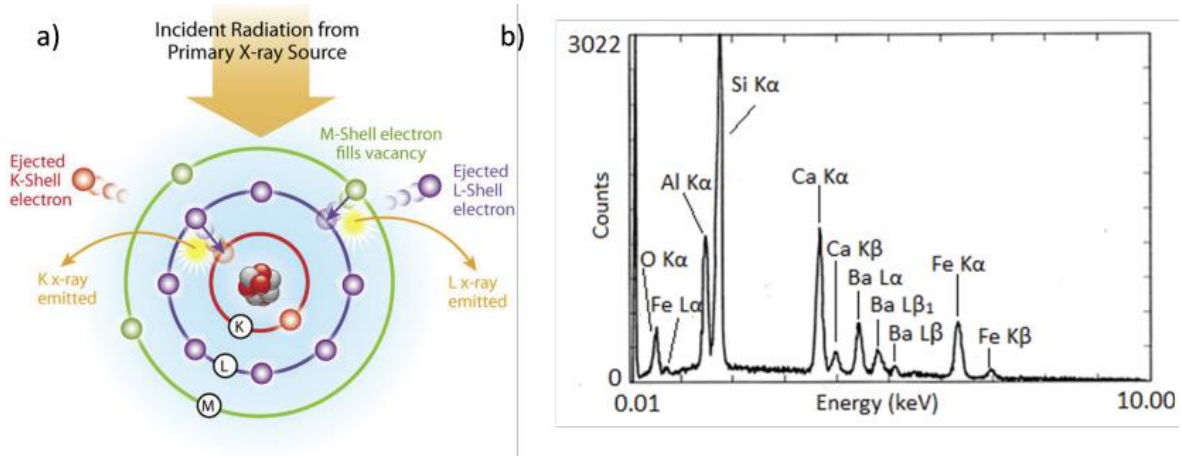

Figure 64: (a) X-ray generation mechanism in the electron microscope and (b) an example of an EDS spectrum. Adapted from Agnese[109].

In the EDS spectrum, the characteristic X-ray lines are labeled according to the Siegbahn notation widely used in X-ray spectroscopy. The Labelling is based on the relative intensity of the X-ray lines arising from different ionized shells and is as follows: first, the chemical symbol of the element emitting the X-ray is indicated followed by the ionized shell (K, L, M…). Since the transition to fill the vacancy in the ionized shell can occur from several higher energy outer shells, multiple X-rays with different energies are released. It follows that each ionized shell has multiple X-ray lines. To distinguish these X-ray lines, Greek letters[5] (α, β, γ…) are used. For example, for the K-shell, Kα and Kβ X-ray lines are possible. The first corresponds to the transition from the L shell to the K shell, while the latter corresponds to the transition from the M shell to the K shell. Greek letters are assigned based on the general order of observed intensity, this means that the intensity of Kα

[5] Not all X-ray lines have a Greek designation, for example there is a Ll transition.

is higher than Kβ and so on. Furthermore, we know that the shells may be divided into subshells. Hence, a subscript number is used to precise the subshell from which the transition took place, with number 1 indicating the highest relative intensity. For example, Fe $K\alpha_1$ corresponds to the X-ray line that is released from the transition of an electron from the subshell III of the L shell to the vacancy in the ionized K shell. Fe $K\alpha_1$ is the most intense X-ray line in the EDS spectrum of iron. An example of electronic transitions and corresponding X-ray lines is illustrated in Figure 65. It should be noted that not all electronic transitions are allowed (X-ray emission follow selection rules).

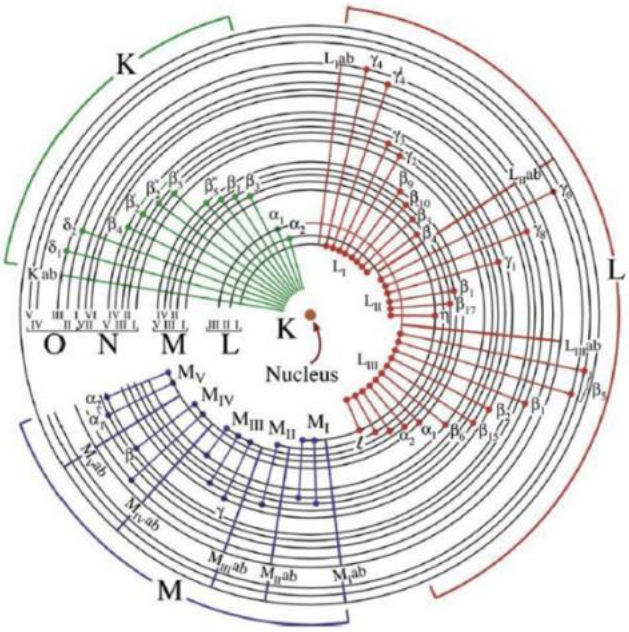

Figure 65: Diagram showing possible electronic transitions and the corresponding X-ray lines (labelled according to the Siegbahn notation). Adapted from Williams and Carter[110].

Generally, K-lines are more intense than L-lines, which are also more intense than M-lines, and so on. $K\alpha_1$ and $L\alpha_1$ lines are of particular interest since usually they are the most intense and have minimum overlap with other X-ray lines. This is why these peaks are usually chosen by the analyst to proceed with quantitative analysis. In the following, we detail the procedure by which the selected measured characteristic X-ray lines can be used to quantitatively analyze the concentrations of the elements present in the sample. Much of the formalism that will be presented is taken from the work of Goldstein[111].

B. Quantitative X-ray analysis for bulk[6] specimen: from k-ratio to composition

The intensity of a particular X-ray peak primarily depends on the concentration of the element emitting the X-ray. Higher concentration elements emit higher intensity peaks while lower concentration elements emit lower intensity peaks. However, various physical effects related to the sample, experimental conditions, geometry, and the detection system impact the intensity of the

[6] In the context of EDS, a bulk sample is a sample that is opaque to the electron beam.

X-ray peaks. These effects should be taken into consideration to be able to determine the concentration of an element from the intensity of its characteristic X-ray peak selected by the analyst for the quantitative analysis. The work of Castaing and many other researchers in this field have led to the establishment of a rigorous protocol that can be followed to obtain quantitative results with high accuracy. This protocol deals with the appropriate experimental setup and correction procedures that can be used to obtain accurate quantitative results. Today, these correction procedures are almost always implemented in commercial programs for quantitative EDS analysis, with which the analyst interacts as a user. However, it is extremely important to understand the underlying physics incorporated into the algorithm of these programs, especially when analyzing complex materials. In addition, the EDS software often asks the user to choose the correction procedure to apply. An optimal choice requires a proper knowledge of the relative merits of each correction procedure. Hence, we aim in the following part to provide a comprehensive overview of the different available correction procedures that are commonly used for EDS quantitative analysis in SEM.

k-ratio and matrix correction factors (effects)

In his thesis, Castaing[112] developed a k-ratio measurement protocol with which the k-ratio for each element present in the sample can be determined by measuring, under the **same** experimental conditions (beam current, acceleration voltage and detector settings), the intensity of an X-ray characteristic of an element in the sample and the intensity of the same X-ray characteristic of that element in a standard of known composition:

$$k_i = \frac{I_i}{I_{(i)}}, \tag{2.2}$$

where I_i and $I_{(i)}$ are the X-ray intensities of the element i in the sample and in the standard respectively.

By using the k-ratios, instrumental factors affecting the measured intensities cancel out. In other terms, we ensure that the X-ray measurements acquired from the unknown sample are properly normalized and corrected for instrument specific variations (e.g., variation of the detector efficiency as a function of the X-ray energy). Determination of k-ratios is the basic experimental measurement that underlies all quantitative X-ray analysis. Nowadays, a database of standards spectra recorded for the dedicated SEM-EDS is often included in the associated commercial EDS software, and readily available for quantitative analysis. However, the experimental conditions used to acquire these spectra are not known, nor the quality of the standards used by the manufacturer. Hence, using standards of known and uniform composition is a mandatory step to ensure a robust and reliable quantitative analysis in which we account for our specific experimental conditions.

While k-ratios account for the variations in the measured X-ray intensities caused by instrumental factors, they don't consider the effect of the sample itself on the measured intensities. These effects, termed matrix effects, are divided (for conceptual and computational reasons) into three factors Z, A, and F defined as follows:

- Z is the "atomic number factor", which accounts for the differences between the sample and the standard in terms of X-ray generation.
- A is the "absorption factor", which accounts for the differences in absorption of generated X-rays within the sample and the standard.
- F is the "characteristic fluorescence factor", which accounts for the differences in secondary X-ray emission due to self-absorption of characteristic X-rays in the sample and the standard.

Once Z, A, and F factors are determined for each element, they are applied to the k-ratios to convert them into mass concentrations. Consequently, the relative concentration can be determined by the following equation:

$$\frac{C_i}{C_{(i)}} = k_i \, [Z.A.F]_i, \qquad (2.3)$$

where C_i and $C_{(i)}$ are the concentrations of the element i in the sample and the standard respectively.

There exist several techniques currently in use to calculate the matrix correction factors. The most generally applicable and capable of producing accurate results are the ZAF and PhiroZ techniques. These techniques are commercially available, for instance they are implemented in the Quantax Esprit software from Bruker available in our laboratory. Another technique called IZAC and developed by Robin[113] at CEA can be also used (not commercially available). In the following, each technique is presented together with its limitations. But first, the concept of $\Phi(\rho z)$ function is introduced.

Distribution in depth of the primary generated X-ray intensity: $\Phi(\rho z)$ functions

The distribution in depth of the generated intensity plays a critical role in developing quantitative EDS procedures. This is because, when the X-rays are generated below the surface, they need to travel through the atoms of the sample to exit its surface and be collected by the detector. During their travel, some of the X-rays can be absorbed. It follows that the intensity of the X-rays collected at the detector is different than the intensity generated inside the sample. This difference should be accounted in order to perform accurate elemental quantification.

Castaing[112] noted the difficulty of measuring or calculating an absolute value for the X-ray intensity generated with depth. To overcome this limitation, he proposed to use instead a normalized intensity which varies with depth, that he called $\Phi(\rho z)$. The term ρz is called mass depth and is the product of the density of the sample by its depth. The $\Phi(\rho z)$ curve is normalized by the X-ray intensity generated in the free-standing thin film (thin enough to ensure that no elastic scattering occurs, e.g., < 10 nm). $\Phi(\rho z)$ can be either simulated or measured using a tracer method as proposed by Castaing.

The general shape of $\Phi(\rho z)$ is shown in Figure 66.

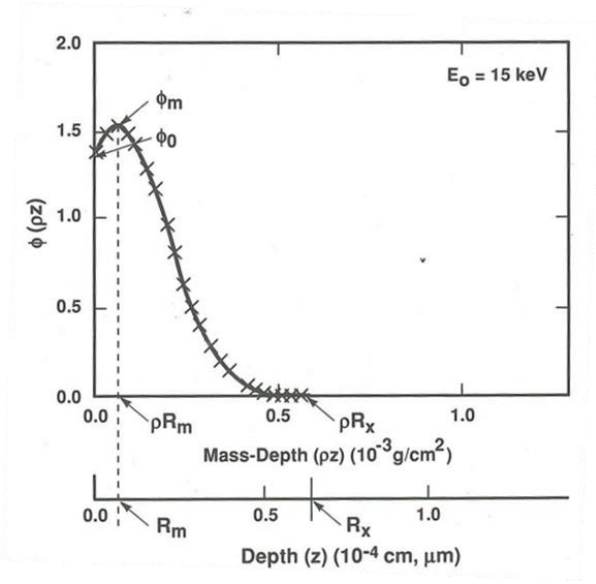

Figure 66: Schematic for the measurement of a $\Phi(\rho z)$ curve. Adapted from Goldstein[111].

From Figure 66 we can see that the X-ray generation increases with depth from the sample surface $(\rho z = 0)$ and goes through a peak at a certain depth ρR_m, after which X-ray generation begins to decrease with depth and finally it goes to zero at a depth ρR_x. This can be explained as follows:

- As the electron beam penetrates the layers of the sample in depth, elastic scattering deflects the electrons out of the normal straight line along which the beam is penetrating the sample. This leads to increase the length of the electron trajectory in each successive layer. In addition, backscattering results in electrons lying deeper in the sample to cross the sample in the opposite direction. In both cases (scattering out of the normal path, backscattering), the electron trajectory inside the sample is increased, causing the X-ray generation to increase. It is worth to note that $\Phi_0 > 1.0$ because backscattered electrons excite X-rays as they exit the sample.

- After depth ρR_m, the decrease in X-ray generation with depth is related to the loss in beam electron (due to the backscattering) and the loss in energy (therefore in ionization power) of the remaining electrons (due to the multiple scattering events).

- At depth ρR_x, there is no X-ray generation because the energy of the electrons is less than E_c.

The shape of $\Phi(\rho z)$ function varies considerably with the atomic number Z and the beam energy. The importance of the $\Phi(\rho z)$ curve is that it can be used to calculate the generated intensity of each X-ray line in the sample, simply by taking the area under the $\Phi(\rho z)$ curve and multiplying it by the X-ray intensity generated in the free-standing thin film.

Now that the concept of $\Phi(\rho z)$ is clarified, we carry on discussing the quantitative EDS techniques (i.e., the correction procedures).

ZAF technique:

The ZAF approach was first introduced by Castaing[112] in 1952, and further developed thanks to substantial contributions made by many researchers (namely Wittry in 1963[114], Philibert in 1963[115], Duncumb and Shields[116] in 1966). It consists of calculating the matrix correction factors **Z**, **A** and **F independently** and successively. In the following, only the expression of **A** is given. This is because its expression is the key difference between the ZAF and PhiroZ techniques. The reader interested in the detailed theory and the equations to calculate the other correction factor is referred to this work[111].

As explained above, the X-rays generated upon interaction with the electron beam are created at a non-zero depth in the sample. Therefore, these X-rays must pass through the sample to be collected by the detector. During their travel, some of these X-rays can be absorbed by the atoms of the various elements present in the sample. This implies that the intensity of X-rays generated by the electron beam is different than the intensity emitted by the sample and detected by the detector. This difference should be evaluated and corrected to ensure appropriate quantification of the X-ray peaks. For that absorption correction factors should be calculated.

In the absence of absorption, the intensity of the characteristic X-ray generated by an element i in a layer of thickness dz and density ρ at a depth z below the sample is given by:

$$I_{i,generated} = I_i(\Delta\rho z) \int_0^{\infty} \Phi_i(\rho z)\, d(\rho z), \tag{2.4}$$

where $I_i(\Delta\rho z)$ is the X-ray intensity of an isolated thin film and $\Phi_i(\rho z)$ is the ionization cross-section.

Considering absorption of the generated X-rays, the intensity emitted by the sample is:

$$I_{i,emitted} = I_i(\Delta\rho z) \int_0^{\infty} \Phi_i(\rho z) \exp^{-\left[(\mu/\rho)_i^{sample}\ cosec\ \psi\ (\rho z)\right]} d(\rho z), \tag{2.5}$$

where $(\mu/\rho)_i^{sample}$ is the mass absorption coefficient of the characteristic X-ray line of element i in the sample and ψ is the take-off angle, the angle between the direction of the measured X-ray and the sample surface. The product $(\mu/\rho)_i^{sample}\ cosec\ \psi$ is called χ.

The standard absorption term, which accounts for the absorption of generated X-rays occurring in a target (sample or standard), is defined as the ratio $I_{i,emitted}/I_{i,generated}$:

$$f(\chi) = \frac{\int_0^{\infty} \Phi_i(\rho z) \exp^{-(\chi)} d(\rho z)}{\int_0^{\infty} \Phi_i(\rho z)\, d(\rho z)}, \tag{2.6}$$

The absorption correction factor A_i, which accounts for the differences in absorption of generated X-rays for an element i within the sample and the standard, is defined by:

$$A_i = \frac{f(\chi)_{standard}}{f(\chi)_{sample}}. \tag{2.7}$$

The key difference between ZAF and PhiroZ is the way $f(\chi)$, and subsequently A_i, are evaluated. In the ZAF approach, an analytical expression of $f(\chi)$ was derived by Philibert[115] and further

developed by Duncumb[116] and Heinrich[117]. The expression is based on an empirical equation that was used to fit the experimental $\Phi(\rho z)$ curves available at that time, which were very limited in number. In his expression, Philibert assumed a null surface ionization, and derived the following expression for $f(\chi)$:

$$\frac{1}{f(\chi)} = \left(1 + \frac{\chi}{\sigma}\right)\left(1 + \frac{h}{1+h}\frac{\chi}{\sigma}\right), \tag{2.8}$$

with:

$$\chi = (\mu/\rho)\,\mathrm{cosec}\,\psi, \qquad \sigma = \frac{4.5 \times 10^5}{E_0^{1.65} - E_c^{1.65}}, \qquad h = 1.2\frac{M}{Z^2}, \tag{2.9}$$

where σ is the Lenard coefficient which accounts for the voltage dependence of the absorption or loss of the primary electrons, E_0 is the beam energy, E_c is the critical energy, M is the atomic weight, and Z is the atomic number.

The problem with the PDH absorption correction is that it is particularly prone to errors when the absorption is high (light elements, low energy X-rays) and/or most of the X-ray signals are emitted from regions near the surface of the sample. This is due to the crude approximations made by Philibert to derive an analytical expression for $f(\chi)$ which he pointed out himself. For instance, he considered a null surface ionization while in reality Φ_0 is always >1.0 as discussed above.

Recognition of the limitations of the ZAF approach had led to the development of the PhiroZ technique, that takes explicit consideration to operation at low beam energies and with low-energy X-rays.

PhiroZ ($\Phi(\rho z)$) technique: Distribution in depth of the primary generated X-ray intensity

Compared to ZAF, PhiroZ is a newer approach introduced by Packwood and Brown in 1981[118]. It also consists of applying matrix correction factors, however the PhiroZ approach does not dissociate Z and A as in the ZAF approach (F remains calculated separately).

PhiroZ is a mathematical model that uses a database of several hundred experimentally determined $\Phi(\rho z)$ curves to develop generalized equations that describe $\Phi(\rho z)$ curves for various elements, X-ray lines, and beam energies. These equations allow the PhiroZ approach to predict the generated $\Phi(\rho z)$ curve for a selected sample composition and beam energy. Therefore, the absorption correction factor and atomic number correction factor can be obtained directly from the generated $\Phi(\rho z)$ curve (the equations can be found in the work of Goldstein[111]). Since no approximations were considered in its formulation, and due to the large number of accessible $\Phi(\rho z)$ curves determined at different beam energies (which guarantees that the method is unbiased), the PhiroZ method extend quantitative analysis to light elements, low energy X-ray peaks and low beam energy.

Today, the ZAF procedure remains the most frequently used EDS quantitative technique for routine analysis owing to its effectiveness, accuracy, and widespread acceptance. However, it is important to keep in mind that this technique uses crude approximations to compute the absorption correction factor. These approximations have been shown to not hold when analyzing

light elements or X-ray lines with strong mass absorption coefficient in general and when most of the X-rays are emitted near the sample surface. In these specific cases, the use of the PhiroZ technique is advised since it incorporates a more advanced absorption correction.

ζ^+ technique (IZAC code):

ζ^+ technique, developed by Robin[119] at CEA, is a $\phi(\rho z)$-corrected version of the ζ-factors used for EDS quantification in TEM (defined later in 2.3.3.4). Therefore, it is the only technique so far that can be applied in both SEM and TEM. This technique is based on the following terms:

- $\overline{\Theta}$: incidence correction term that accounts for the angle of incidence of the electron beam.
- $\bar{\theta}_i$: incidence correction term of the element i.
- $\bar{\phi}_i$: atomic number correction term of the element i used to determine the $\phi(\rho z)$ function defined earlier.
- $\bar{\chi}_i$: absorption correction term of the chemical element i based on $\overline{\Theta}$ and $\bar{\phi}_i$.

$\overline{\Theta}$ and $\bar{\phi}_i$ are calculated using Monte Carlo simulations in Casino software. $\bar{\chi}_i$ is computed based on a modified version of the quadrilateral model described by Scott and Love[120] to depict the depth distribution of X-rays inside the sample.

The technique is implemented in a code called IZAC which allow the determination of both the chemical composition and the mass-depth (ρz) of the analyzed region. First, the intensity of the X-ray peaks, determined after the deconvolution and subtraction of the continuum background of the acquired EDS spectrum, are given as input parameter. Then, an initialization step is performed during which the algorithm calculates initial values of the chemical composition and the ρz by assuming that the measured intensities (given as input parameter) are equal to the generated intensities. Hereafter, an iterative cycle of calculation is performed as follows:

- Calculation of $\overline{\Theta}$ and $\bar{\theta}_i$ for the different elements present in the sample
- Calculation of $\bar{\phi}_i$ using $\overline{\Theta}$ and $\bar{\theta}_i$.
- Calculation of $\bar{\chi}_i$ using $\overline{\Theta}$, $\bar{\theta}_i$, and $\bar{\phi}_i$.
- Modification of initial values of the concentration and ρz.

The cycle continues until the difference between the concentration and ρz between two iterations is below a limit defined by the user.

C. Case of Dy-GBD processed NdFeB magnet: protocol and challenges.

Figure 67 displays a typical spectrum acquired from a sintered NdFeB magnet at 20 keV. The spectrum can be seen as composed of two parts: a lower energy part where mostly L and M X-ray lines are present and a higher energy part where mostly K and L X-ray lines are present. Not surprisingly, the EDS spectrum of the seven-component system is quite complex and contains a lot of peaks of different intensities and with severe interferences. Although K and L lines are usually preferred for quantitative analysis, this is not applicable in our samples due to the overlapping between Fe K (6.401 keV) and Dy L (6.494 keV) peaks, which are the main elements of interest in our study. Consequently, the peaks selected for our quantitative analysis are the low energy peaks Fe Lα (0.692 keV), Co Lα (0.764 keV), Nd Mα (0.989 keV), Dy Mα (1.303 keV), Cu Lα (0.923 keV), Al Kα (1.487 keV), and O Kα (0.525 keV). Considering that the beam energy should be 2× higher than the highest energy X-ray peak (which is Al Kα in our case), an acceleration voltage of 5 keV is selected. Although a lower acceleration voltage can be taken and is preferable in terms of spatial resolution, we preferred not to use it to avoid the signal from surface contamination and oxidation. Also, when lowering the acceleration voltage, we lose X-ray signal. Consequently, a longer acquisition time is needed to improve the signal to noise ratio.

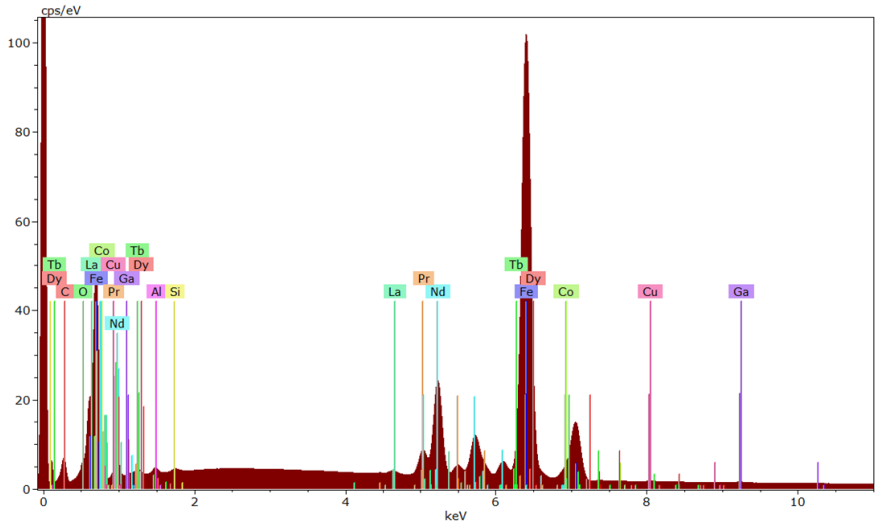

Figure 67: EDS-SEM spectrum of a sintered NdFeB magnet acquired at 20 kV using Quantax Esprit software from Bruker.

In our work, all the EDS experiments were performed in the MERLIN Gemini field-emission gun SEM from Zeiss. The EDS detector used is the XFlash 6|60 with a resolution 127.40 eV at Mn Kα and a take-off angle $\psi = 35°$. The spectra of the samples and standards were all performed under the same experimental conditions: beam energy (i.e., V_{acc}) 5 keV, beam current 1.5 nA, maximum pulse throughput 30 kcps, and working distance (WD) 10 mm. We note that all the EDS quantitative analyses were performed either in spectrum mode or line-scan mode. In these modes, the entire 4096 channels of the EDS analyzer are used to record the spectra, hence ensuring maximum spectral resolution.

The protocol we used for the acquisition of EDS spectra is the following:

1) Energy calibration of the detector: the theoretical position of the X-rays must be matched with the actual position in the multi-channel analyzer to avoid peaks misidentification. For

that, a spectrum with a very well separated X-ray peaks is needed. In our case, we have used a Cu sample which has a very well separated low energy Lα peak and a high energy Kα peak.

2) Creation of standards spectra database: after calibrating the detector, we proceed to acquire the spectra of the standards to use for determination of ratios. The following standards were used for this database Fe, Co, NdF_3, DyF_3, Al_2O_3, Cu, LaB_6.

3) Acquisition of the sample's spectra: hereafter, spectra or line scans from regions of interest can be acquired for quantitative analysis.

4) Quantification method: finally, the EDS data are treated to extract the chemical composition of the regions of interest. Since the X-ray peaks that are selected for quantitative analysis are low energy peaks, and since the analysis is performed at a low beam energy, and since our samples are composed of both light and heavy elements, ZAF technique is not adapted to choose. Both PhiroZ and IZAC techniques can be used to quantify our data, and we have chosen the IZAC code.

Once the standards spectra database is created, only steps 1, 3 and 4 from the above protocol should be repeated for subsequent EDS analysis.

2.3.2.3 Wavelength dispersive X-ray spectroscopy (WDS)

As seen above, there are many challenges for chemical analysis in Dy-GBD processed NdFeB magnets. Of particular concern is the overlap between Fe (Lα) and Co (Lα) peaks from one side and Dy (Mα) and Nd (Mg) peaks from the other side. To overcome this problem, we opted to use WDS technique. Compared to EDS, this technique has a better spectral resolution allowing to properly measure the intensity of the peaks. In addition, WDS has a higher sensitivity which make it more adapted to measure minor elements (such as Cu, Co and Al in our samples) and allow to measure light elements such as Boron which is inaccessible when using the EDS technique. However, WDS is time consuming as only one element can be analyzed at a time (time acquisition of a complete WD spectrum took around 30 min) as opposed to EDS where all elements are analyzed at the same time. In addition, WDS requires a higher beam current compared to EDS to increase the number of generated X-rays.

Both EDS and WDS techniques analyze characteristic X-rays emitted from the sample after being exposed to the electron beam, the difference relies in the detection system (i.e., the spectrometer used to detect the characteristic X-rays). First generation WD spectrometers are conventionally installed in electron probe microanalyzers (EPMAs) and not in SEMs. They consist of three main components: a curved analyzer crystal with a well-defined interplanar spacing (d-spacing), a detector, and a detector electronics. The curved analyzer crystal acts as a filter and a diffractor; it receives the X-rays generated from the interaction between the electron beam and the sample and diffracts towards the detector only the ones whose wavelength satisfy the Bragg's law (i.e., it filters the X-rays according to their wavelengths and allows only X-rays emitted at a single wavelength corresponding to one element to be sent to the detector). Since the X-rays received by the analyzer

crystal are of a divergent nature, the use of a **flat** analyzer will lead to a divergent diffracted X-rays and a low X-ray count at the detector. This is why a **curved** analyzer crystal is used instead so it can converge and focus the diffracted X-rays onto the detector and maximize the signal at the latter (see Figure 68). The detector itself is a gas-filled proportional counter, in which diffracted X-rays enter through a slit and a window (the window is used to isolate the gas inside the detector from the vacuum inside the microscope) and are absorbed by the atoms of the gas inside the detector. Consequently, each atom that have absorbed an X-ray emits a photoelectron. The photoelectrons are then processed by the detector electronics: amplified by the pre-amplifier and amplifier, converted into a standard electric pulse whose amplitude is proportional to the energy of the absorbed X-rays by a single-channel analyzer, and counted by a scalar. As a result, an X-ray spectrum composed of a single X-ray peak is displayed on the computer connected to the station (equipment). Finally, a WDS spectrum is displayed on the computer connected to the equipment in which X-rays with an intensity proportional to the number of atoms in the interaction volume.

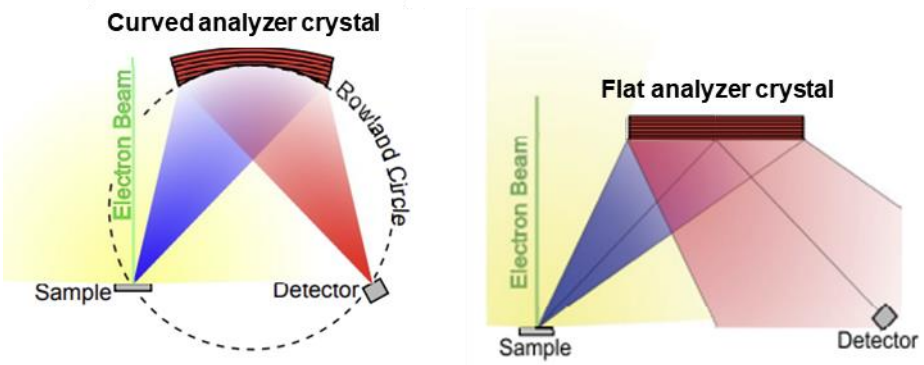

Figure 68: Schematic diagrams showing the difference between a WD spectrometer with a curved analyzer crystal (diffractor size is greatly exaggerated) versus a flat analyzer crystal. The yellow area represents all the diverging X-rays emitted from the sample by the interaction of the electron beam with the sample. The blue area represents the subset of X-rays that will collide with the diffractor. The red area represents the X-rays that are reflected by the diffractor. When diverging X-rays contact a curved analyzer crystal (left), they reflect and converge yielding a high-count rate at the detector. When they contact a flat diffractor (right), they reflect but continue to diverge yielding a low-count rate at the detector. Adapted from Thermo Fisher Scientific[121].

Since the analyzer crystal sends X-rays emitted at one specific wavelength towards the detector, the latter can measure X-rays emitted from only one element at a time. To measure the X-rays corresponding to other elements in the sample, the analyzer crystal and detector should both systematically adjust their position to diffract and detect X-rays emitted at wavelengths characteristics of these elements. The adjustment in position is not random but follow a precise engineering. The latter requires conventional WD spectrometers to be designed based on a Rowland circle geometry; this means that the sample, analyzer crystal, and detector are all constrained to lie on the same circle of radius R, known as the Rowland circle. The latter is a "focusing" circle on which the analyzer crystal focuses the diffracted X-rays regardless of their wavelengths. The position adjustment required to detect a new wavelength in this geometry is as follows: First, the curved analyzer should rotate to change θ, the angle at which the X-rays hit the detector, so it can diffract X-rays with another value of wavelength. Second, as the analyzer crystal rotate, the diffracted X-rays are no longer focused on the Rowland circle. To fix this, the analyzer

crystal moves along a straight line (away from the sample or towards it depending on the targeted wavelength if it is longer or shorter) to restore the focusing point at the circle. Finally, the detector adjusts its position on the circle towards the new focus point of the diffracted X-rays. This process is schematized in Figure 69. Based on the working principle of the WD spectrometer, it is clear that it requires a prior knowledge of the elements present in the analyzed material. This is why WDS and EDS are two complementary techniques: EDS analysis is run first to identify the elements present in the sample followed by WDS analysis to perform a rigorous chemical quantification.

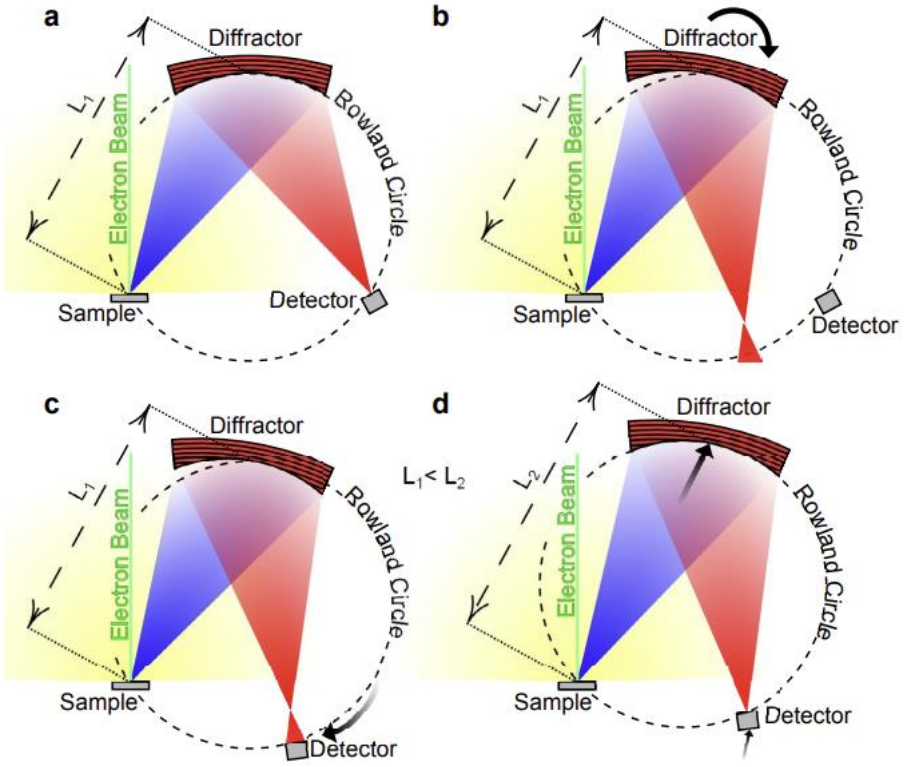

Figure 69: Schematic diagrams of the movement required by the components of a Rowland circle WDS spectrometer for the detection of lower energy X-rays (i.e., the X-rays measured in d are of lower energy than would be measured in a). The yellow area represents all X-rays emitted from the sample by the interaction of the electron beam with the sample. The blue area represents the subset of X-rays that will collide with the diffractor (diffractor size is greatly exaggerated). The red area represents the X-rays that are reflected by the diffractor. From a to b, the diffractor rotates, changing the angle, θ, at which X-rays intersect the diffractor. The X-rays reflected off the diffractor (red) are focused at a different location. From b to c, the detector moves along the Rowland circle; however, the X-rays are not focused on the Rowland circle and are therefore not focused on the detector. From c to d, the diffractor moves away from the sample, and the detector must change position to stay on the Rowland circle focusing the diffracted X-rays on the detector. Adapted from Thermo Fisher Scientific[121].

A consequence of the Rowland circle geometry is that the distance L between the sample and the analyzer crystal varies and is directly proportional to the wavelength: X-rays with longer wavelengths require longer L, while X-rays with shorter wavelengths require shorter L (see Figure 70). As L increases, the diffractor solid angle (Ω), proportional to $1/L^2$, decreases. As a result, the collection of X-rays with a long wavelength is less efficient relative to X-rays with short wavelength when using a conventional WDS spectrometer.

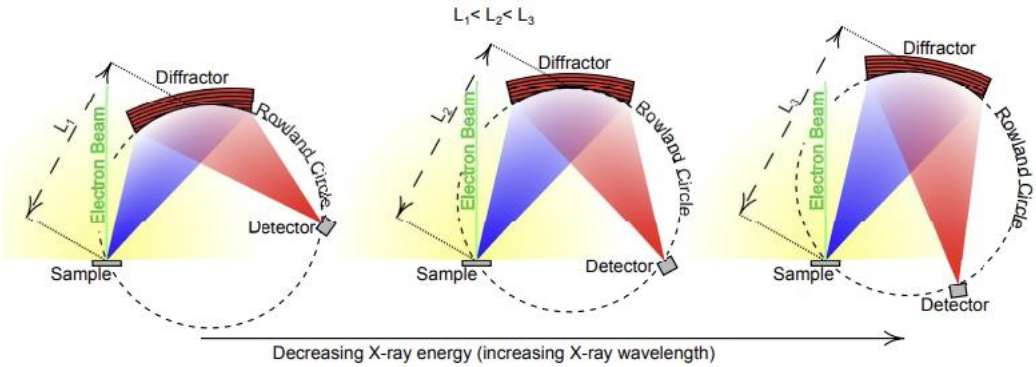

Figure 70: Schematic diagrams of conventional WDS based on the Rowland circle geometry (diffractor size is greatly exaggerated). The yellow area represents all X-rays emitted from the sample by the interaction of the electron beam with the sample. The blue area represents the subset of X-rays that will collide with the diffractor. The red area represents the X-rays that are reflected by the diffractor and are focused on the detector. From left to right, the spectrometer orientation changes to detect X-rays of lower energy. This change in orientation results in an increasing distance (L) between the sample (the X-ray source) and the diffractor. By increasing L, the X-ray intensity at the diffractor decreases because the X-ray intensity is proportional to $1/L^2$. The result of the Rowland circle orientation is that the collection of low energy X-rays (e.g., O Kα) is less efficient relative to high energy X-rays (e.g., Fe Kα). Adapted from Thermo Fisher Scientific[121].

The last thing to note regarding conventional WD spectrometer is that it includes several analyzer crystals (each with a different d-spacing) and not only one. This is for enabling the spectrometer to scan the wavelength range of almost all the elements of the periodic table as each analyzer crystal has a limited range of elements covered (i.e., a limited set of wavelengths that the crystal can diffract). The range limit is imposed by the interplanar spacing of the analyzer crystal (d) itself and the geometry of the WD spectrometer.

Recently, second generation WD spectrometers based on a parallel beam approach have enabled to perform WDS readily and easily in SEMs. Compared to the first generation WD spectrometers, they are composed of four main components: an optic, several flat analyzer crystals, a detector, and a detector electronics. The optic is a non-magnetic distortion free placed near the sample and used to capture the X-rays emitted from the sample to turn them into a collimated parallel beam (see Figure 71). Consequently, a parallel X-ray beam is sent towards the analyzer crystal instead of a divergent one (hence the term parallel beam approach). The advantage of a parallel X-ray beam is that the analyzer crystal can be flat and placed away from the sample (i.e., long distance L) without losing X-rays signal, thus solving the problem of low collection efficiency of X-rays with a long wavelength (low energy) encountered when using a conventional WD spectrometer. Another advantage of the parallel X-ray beam is that the Rowland circle geometry is not required anymore, instead second generation WD spectrometers use a simple θ-2θ scanning system in which the analyzer crystal rotates by θ without changing its distance with respect to the sample, and the detector rotates by 2θ to detect the X-rays (similar to the X-ray diffraction technique).

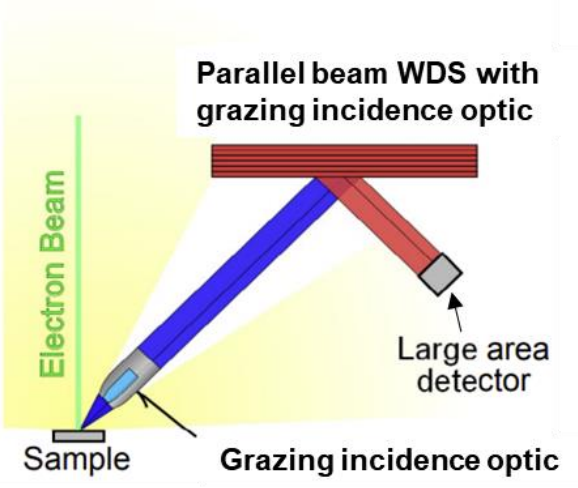

Figure 71: Schematic diagram showing the working principle of a parallel beam WDS with a grazing incidence optic: The yellow area represents all X-rays emitted from the sample by the interaction of the electron beam with the sample. The blue area represents the subset of X-rays that will collide with the diffractor. The grazing incidence optic is used to transform the divergent X-rays (yellow) into a parallel X-ray beam (blue). The blue parallel X-ray beam reflects off the flat diffractor. The red area represents the X-rays that are reflected by the diffractor to the detector. Adapted from Thermo Fisher Scientific[121].

In this study, we performed WDS analysis using XSense spectrometer which is a parallel beam WD spectrometer with a grazing incidence collimating optic (a type of optic designed specifically to improve the efficiency of collimating **long** wavelength X-rays) designed and released by Bruker in 2013. It can be attached to a port of the SEM's sample chamber (in our case, it was mounted on an Ultra 55 SEM from ZEISS) and has 6 different analyzer crystals, covering the energy range from 70 eV to 3.6 keV, and activated according to the user choice. The analyzer crystals are listed in Table 13.

Table 13: Analyzer crystals present in the XSense WD spectrometer (values taken from the technical note provided by Bruker).

Peak intensity

Crystal designation	Crystal name	2d-spacing (Å)	Analyzing range (eV)
BRML 200	-	200	66-298
BRML 80	-	80	165-745
BRML 60	-	60	220-994
BRML 30	-	30	440-1988
TIAP	Thallium hydrogen phthalate $TlHC_8H_4O_4$	25.76	509-2302
PET	Pentaerythritol $C(CH_2OH)_4$	8.74	1510-3600

Resolution

The analyzer crystals are arranged in Table 13 according to their interplanar spacing, from largest to smallest. The larger the interplanar spacing, the higher the peak intensity; hence the analyzer crystals with larger interplanar spacing are better options to use when analyzing minor elements or low intensity peaks, and to reduce the peak acquisition time of any element in general. On the other

hand, the smaller the interplanar spacing, the better the peak resolution; hence the analyzer crystals with smaller interplanar spacing are better options to use in the case of overlapping peaks. As we can see from Table 13, sometimes there is an overlapping in the analyzing range of the crystals which means that 2 analyzer crystals can be used to measure the same X-ray peak. In this case, the choice between one crystal or another depends mainly on whether the X-ray peak is overlapped. If yes, the analyzer crystal with the smaller interplanar spacing should be used; otherwise, the analyzer crystal with a larger interplanar spacing is better to use especially if the X-ray correspond to a minor element or a low intensity peak. In Table 14, we list the analyzer crystals chosen to measure the X-rays peaks characteristic of the elements present in the Dy-GBD processed NdFeB magnet. We also report other experimental conditions required to perform the measurement.

Table 14: WDS acquisition settings that we defined to measure the peaks of the elements present in the Dy-GBDP NdFeB magnets.

Element	Measured peak	Lower background energy (eV)	Peak energy (eV)	Upper background energy (eV)	Peak measure time (s)	Analyzer crystal
Boron	Kα	173.0	183.3	200.0	60	BRML 80
Oxygen	Kα	514.0	524.9	540.0	60	TIAP
Aluminum	Kα	1400.0	1487.2	1580.0	60	TIAP
Iron	Lα	675.0	704.8	737.0	60	TIAP
	Lβ	675.0	717.9	737.0	90	TIAP
	Ll	600.0	615.5	640.0	90	TIAP
Cobalt	Lα	767.0	775.1	800.0	60	TIAP
Copper	Lα	890.1	927.7	1050.0	120	TIAP
Neodymium	Mα	965.0	978.9	1025.0	120	TIAP
	Mβ	965.0	1001.8	1025.0	120	TIAP
	Mg	1160.0	1176.5	1195.0	120	TIAP
	Mz_1	737.0	753.0	767.0	120	TIAP
	Mz_2	737.0	753.0	767.0	120	TIAP
Dysprosium	Mα	1230.0	1299.0	1400.0	90	TIAP
	Mβ	1230.0	1326.0	1400.0	120	TIAP
	Mg	1400.0	1519.0	1575.0	120	TIAP
	Mz_1	900.0	1000.7	1070.0	120	TIAP

All the WD spectra were acquired at an acceleration voltage of 10 kV and with an aperture size of 120 μm to maximize the current used for X-rays generation. A full WD spectrum took around 30 min to acquire. Figure 72 shows the difference between an EDS and a WDS spectra acquired on the same region from the Dy-GBD processed NdFeB sample. In (a) the gaussian-like curves do not allow a proper deconvolution of the peaks which is problematic for the determination of Fe and Co, Nd and Dy. In (b) sharp peaks are measured allowing to access the intensity corresponding to each element.

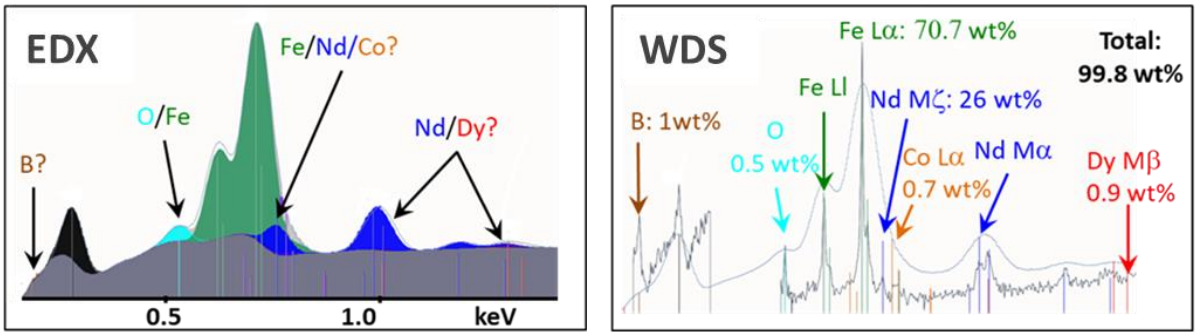

Figure 72: Comparison between EDS and WDS spectra acquired on the same region of a GBD processed NdFeB sample. WDS spectrum clearly separates the different peaks and overcome the problem of superimposition of the peaks on the continuous Bremsstrahlung background.

It should be noted that in this work, the WDS technique was mainly to evaluate the EDS quantification results. This is because the XSense WD spectrometer was purchased during my last year of PhD, and I had a limited access to it (tests were being conducted at the time). In addition, the acquisition time is considerably longer than the EDS technique which make it tedious to use for statistical routine.

2.3.2.4 Electron backscatter diffraction (EBSD)

EBSD is a microstructural crystallographic technique used to study polycrystalline materials. It provides several information such as phase identification, grain orientation and texture. To perform EBSD analysis, particular attention must be paid to sample preparation as it affects the quality of the diffraction pattern, i.e., the confidence of indexing. The sample should have a perfect surface state (very flat and well-polished). In our case, sample preparation of NdFeB for EBSD analysis was found to be very challenging due to the rapid oxidation of the sample surface. Only one EBSD experiment was successful in this work.

Inside the SEM, the sample is first tilted at T = 70° from the horizontal so it is facing the EBSD detector. The latter is an insertable detector that is attached to a port in the SEM chamber and is nearly orthogonal with respect to the pole piece. This is illustrated in Figure 73.

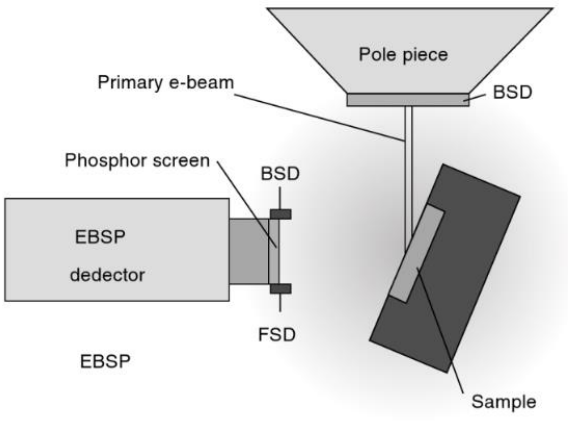

Figure 73: Schematic diagram showing the experimental setup for EBSD analysis. Adapted from Zhou et Wang[122].

To obtain an EBSD map, the electron beam scans in a raster pattern the surface of the sample. As the BSE electrons exit the sample, they interact with the crystal lattice and diffract according to Bragg's law before reaching the EBSD detector forming Kikuchi patterns. Finally, the Kikuchi patterns are indexed using an automatic software, and the EBSD map can be analyzed for the desired information.

In this work, EBSD investigations were carried out using a MERLIN field-emission gun scanning electron microscope (SEM). Kikuchi patterns were recorded at an acceleration voltage of 20 kV with an Oxford high-speed EBSD camera and analyzed using the Esprit 2.2 software.

2.3.3 Transmission electron microscopy (TEM)

Max knoll and Ernest Ruska developed the first TEM in Germany in 1931, which was later made commercially available by Siemens in 1939. Ever since, technological improvements have been made primarily to achieve higher resolution. In this regard, the discovery of FEG gun and the development of aberration correctors and monochromators were milestones that revolutionized the TEM. Nowadays, state of art TEM use FEG gun and are equipped with a monochromator and one or two aberration correctors: Cs probe corrector and Cs image corrector. They can achieve a resolution of 50 pm, revealing the atomic columns of a material.

TEM is mainly operated in two modes: Conventional TEM and Scanning (S)TEM. The former uses a parallel beam to illuminate the sample while the latter uses a convergent beam. Within these modes, various techniques such as imaging, diffraction, and spectroscopies can be performed. In this work, (S)TEM mode was used in which we performed high resolution HAADF-STEM imaging, precession electron diffraction (PED), and EDS techniques to analyze the atomic structure and chemical composition of the FIB lamellae prepared from NdFeB magnets. The experiments were conducted in a "FEI Titan Themis" microscope, which uses a Schottky FEG (X-FEG) gun and is equipped with a Cs probe corrector. In addition, the microscope is equipped with a Super X system developed by FEI for EDS analysis. The Super X system is composed of four windowless silicon drift EDS detectors (SDD), placed at a 90° angle of each other, achieving a detection solid angle of 0.64±0.06 sr. A single tilt sample holder designed for vacuum transfer by Gatan was used to prevent the oxidation of the TEM lamellae during their transfer. All TEM characterization were carried out at 200 keV.

In the following section, each of the used techniques is explained.

2.3.3.1 Electron beam-sample interaction

Similarly to SEM, TEM relies on the interaction between highly accelerated electrons and atoms in a sample. When the sample is sufficiently thin (ideally less than 100 nm), most of the electrons are transmitted through it. The transmitted electrons can be either elastically or inelastically scattered.

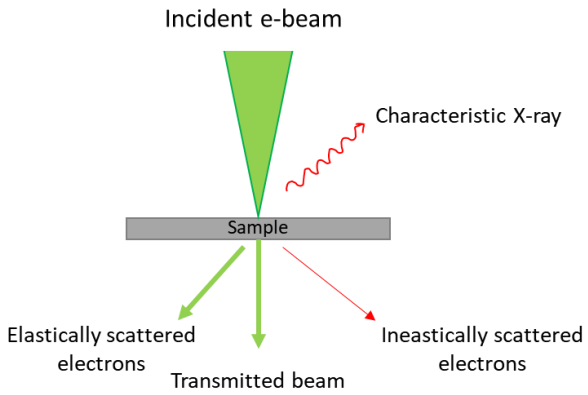

Figure 74: Electron beam-sample interaction and the variety of outcoming signals

Elastically scattered electrons can be used for various TEM imaging techniques, depending on their angle of scattering: at low angles ($\theta < 10$ mrad) they are used for Bright Field (BF) imaging, at moderate angles ($10 \text{ mrad} < \theta < 50$ mrad) they are used for Annular Dark Field (ADF) imaging, and at high angles ($\theta > 50$ mrad) they are used for High-Angle Annular Dark Field (HAADF) imaging. Each imaging technique reveals different type of information about the sample.

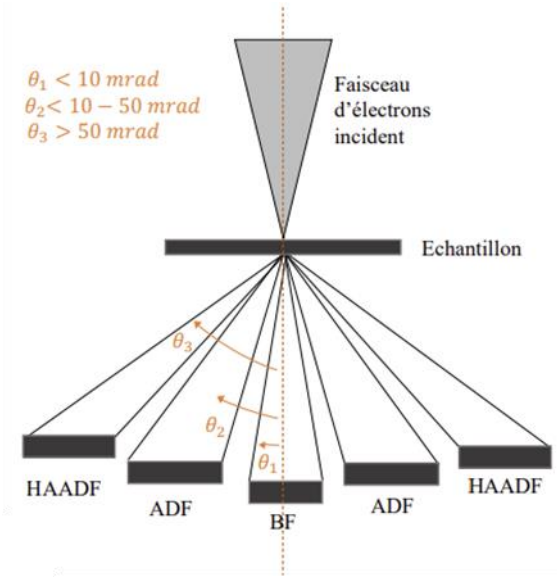

Figure 75: Setup of STEM imaging showing the three possible imaging techniques. Adapted from Henry[123].

On the other hand, inelastically scattered electrons lose some or all their energies to the atoms of the sample, yielding different types of signals such as X-rays, Auger electrons, Cathodoluminescence. Of particular interest are the X-rays which can be exploited by means of EDS to reveal information regarding the chemical composition of the sample.

2.3.3.2 High-Angle Annular Dark Field (HAADF-STEM) imaging

As already mentioned, electrons scattered at high angles ($\theta > 50$ mrad) are used for HAADF-STEM imaging. These electrons are collected using a special annual detector that discriminates electrons according to their deviation from the optical axis. Since these electrons are strongly deviated, they

lose their coherency, and form an image with no contrast reversals. Consequently, the formed high-resolution image is directly interpretable, and the bright spots can be readily linked to the positions of the atomic columns. This can be seen in Figure 76, that shows a comparison of HR-TEM image (equivalent to BF-STEM) and HAADF-STEM images acquired on the same Al_3ZrSc precipitate surrounded by an Al matrix. In the HR-TEM image, we see strong contrast variations due to changes in the local thickness of the sample, making the image less interpretable. However, in the HAADF-STEM image we can clearly distinguish the atomic columns. For this reason, HAADF-STEM imaging is usually a preferred choice for high resolution imaging of crystalline materials.

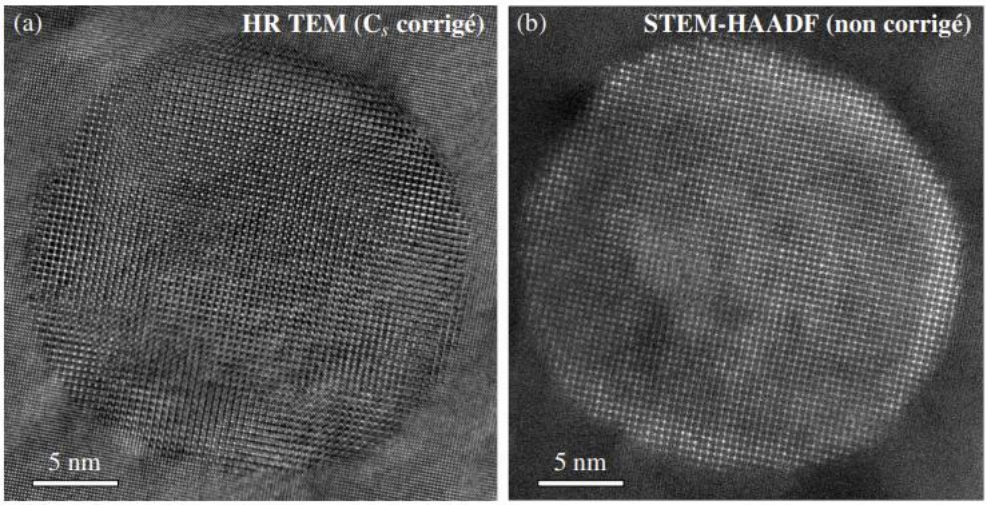

Figure 76: Comparison of images of the same Al_3ZrSc precipitate in an Al matrix obtained (a) in conventional TEM (equivalent to a BF-STEM) and (b) in uncorrected STEM-HAADF. Adapted from Esnouf[124].

The number of electrons resulting from incoherent scattering (i.e., the intensity of HAADF-STEM image) is proportional to the atomic number Z^n ($1.6 < n < 1.9$)[125,126] of the atomic columns scanned by the electron probe and the thickness of the sample. It follows that, the intensity can be used to discriminate the atomic columns based on their chemical nature: bright atomic columns are associated with heavier atoms while dark atomic columns are linked to lighter atoms. For instance, in the HAADF-STEM image of Figure 76, we can see an increase in the intensity around the edges of the precipitate, that corresponds to Zr enrichment in this region. This is why HAADF-STEM imaging is known as a Z contrast imaging technique.

2.3.3.3 Nanobeam Precession Electron Diffraction (NPED)

Nanobeam Precession electron diffraction (NPED) is an advanced diffraction technique used in STEM to improve the accuracy and quality of electron diffraction patterns. The main advantage of NPED is that it reduces the influence of dynamical diffraction effects, so that diffraction images can be analyzed using a kinematical approach. For these reasons, the technique is particularly interesting when analyzing complex or thick samples. NPED uses a small STEM probe (formed by a 10 μm aperture) to scan the sample. Then, the beam is focused onto the sample and its pivot point is placed precisely on the sample plane during alignment. Afterwards, using deflecting coils located above the sample, the beam is tilted away from the optical axis by an angle called the precession angle (of some tenths of degrees). When the beam is in a tilted position, an off-axis

diffraction pattern will form, shifted away from the non-tilted beam configuration. For that, deflecting coils located below the sample are used to tilt the diffracted beams back in so that the direct beam falls in the center of the diffraction pattern. Finally, the beam is precessed around the optical axis and diffraction patterns are collected. In the end, we obtain a diffraction pattern that is the summation of the full series of slightly tilted diffraction patterns is obtained, in which the diffraction spots are numerous, and their intensity is more uniform. A typical example is shown in Figure 77.

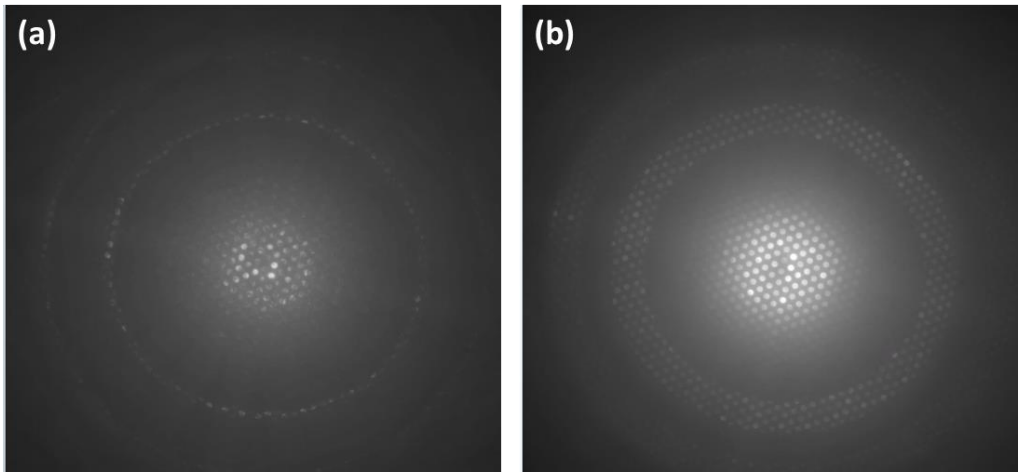

Figure 77: Comparison between a diffraction pattern acquired on 2:14:1 phase (a) without PED and (b) with PED. It is clear that the diffraction spots seen in the PED pattern are numerous and have homogenous contrast (the effect of dynamical diffraction is suppressed).

2.3.3.4 EDS-STEM

The principle of EDS is already introduced in section 2.3.2.2. Here we emphasize some relevant points to consider in the case of EDS-STEM:

- STEM uses a convergent probe and interacts with thin samples, hence there is no beam broadening (as in SEM), and the spatial resolution is considerably improved.
- Due to the lower beam current in STEM (compared to SEM), the X-rays count rate is low and data (spectra/line-scans/EDS maps) acquisition time is high.
- It is important to consider the material of the grid on which the sample is deposited/glued during EDS-STEM analyses. The material should be different from the elements present in the sample. Otherwise, the grid will produce X-rays that will overlap with the sample signal, making quantification impossible. In our case, and as indicated in section 2.2.2, we chose Mo grid instead of Cu grid since our samples contain Cu.

Elemental quantification is also possible using EDS-STEM. For that, special quantitative methods known as the k-factors and ζ-factors have been developed. In the following, we present each technique, and we finish by a general recommendation on how to select the appropriate quantitative method.

Cliff-Lorimer (k-factors)

Since the samples analyzed by TEM are extremely thin, the interaction volume in which X-rays are generated is extremely small compared to SEM. This is particularly interesting since we can assume, as a first approximation, that absorption and fluorescence matrix effects are negligeable. This means that the X-ray intensity generated by the electron beam is equal to the emitted intensity exiting the sample surface. Based on this approximation, Cliff and Lorimer[127] proposed an equation that relate the concentration of the elements present in the sample to the measured X-ray intensities. It reads as follows:

$$\frac{C_A}{C_B} = k_{AB}\frac{I_A}{I_B}, \tag{2.10}$$

where C_A and C_B are the weight percentages of elements A and B respectively ($C_A + C_B = 100$ wt.%), I_A and I_B are the measured X-ray intensities of elements A and B respectively, and k_{AB} is the Cliff-Lorimer factor or more commonly k-factor, which can be determined both theoretically and experimentally. This factor is **not constant** but varies with the beam energy, microscope, and detector system. Its theoretical expression is given by Goldstein et al.[128]:

$$k_{AB} = \frac{M_A}{(Q\omega a\varepsilon)_A}\frac{(Q\omega a\varepsilon)_B}{M_B}, \tag{2.11}$$

where M is the atomic weight, Q is the total ionization cross-section for a given shell, ω is the fluorescence yield (proportion of ionization events resulting in X-ray emission and not Auger electrons for example), a is the relative transition probability (i.e., relative intensity of a particular X-ray line), and ε is the attenuation of the X-ray beam before detection (detector efficiency).

The theoretical calculation of the k-factors is fast and easy but, in some cases, it can produce significant systematic errors (15-20%)[129,130]. For these cases, it is important to determine the k-factors experimentally. These authors[131,132] showed that k-factors can be determined experimentally with relative errors of approximately 1%, significantly enhancing the accuracy of EDS quantification. The process requires using multi-element homogenous thin standards of known composition. Unfortunately, such standards are usually not available.

Another problem encountered with the Cliff-Lorimer method is X-ray absorption. In fact, even in thin samples, absorption still occurs. Figure 78 shows the critical thickness at which 5% of X-ray absorption occurs in pure element samples. For K and L X-ray lines, absorption can be neglected if the sample thickness is 30 nm. For M-lines, the thickness should be even smaller. A thickness of 30 nm is rarely achievable in cross-section preparation, where a thickness of 100 nm is more commonly achieved (for our samples the thickness was even higher due to the complications explained in the FIB section). Clearly, X-ray absorption cannot be neglected at such thicknesses.

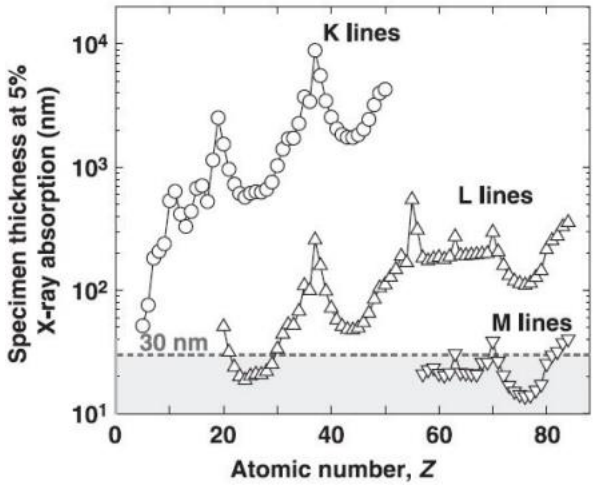

Figure 78: The critical specimen thickness at 5% X-ray absorption in the pure element thin films. The shadowed area indicates the specimen thickness range below 30 nm. Adapted from Watanabe and Williams[133].

If absorption takes place, the detected X-ray intensity is lower than the generated X-ray intensity, making C_A not proportional to I_A as proposed by Cliff and Lorimer. Therefore, it is necessary to correct the absorption effect so that it can be considered in the quantification procedure. X-ray absorption correction factor for a single X-ray line from a thin sample is derived from the expression proposed by Philibert. It is given by:

$$A_A = \frac{(\mu/\rho)_i^{sample} \operatorname{cosec} \psi \, (\rho z)}{1 - \exp^{-\left[(\mu/\rho)_i^{sample} \operatorname{cosec} \psi \, (\rho z)\right]}}, \tag{2.12}$$

where $(\mu/\rho)_i^{sample}$ is the mass absorption coefficient of the characteristic X-ray line of element i in the sample and ψ is the take-off angle.

As clearly seen from Eq. (2.12), prior knowledge of the sample thickness and density is required to be able to compute the absorption correction factor. This imposes an intrinsic problem because while sample thickness can be evaluated by other experimental techniques such as EELS, the density of the sample depends on its composition which is exactly the information we are looking to determine by EDS. To address these problems, ζ-factors method is proposed.

ζ-factors

Instead of the Cliff-Lorimer ratio method, Watanabe and Williams[133] proposed in 2006 another approach for EDS-STEM quantification, termed the ζ-factors method. They started by postulating that, if absorption and fluorescence effects are negligible (thin-sample approximation), the measured characteristic X-ray intensity I_A, emitted from an element A, is proportional to the mass-thickness ρz of the sample and the concentration C_A of element A. Accordingly, they gave the following expression:

$$I_A \zeta_A = D_e \rho z C_A, \tag{2.13}$$

where D_e is the total electron dose during acquisition and ζ_A is a proportional factor connecting I_A to C_A and whose expression is given by:

$$\zeta_A = \frac{M_A}{N_V Q_A \omega_A a_A \varepsilon_A \left(\frac{\Omega}{4\pi}\right)}, \tag{2.14}$$

where M_A is the atomic weight, N_V is the Avogadro's number, Q_A is the total ionization cross-section for a given shell, ω_A is the fluorescence yield, a_A is the relative transition probability, ε_A is the detector efficiency, and $\left(\frac{\Omega}{4\pi}\right)$ is the detector collection-angle in the hole 4π space. We draw the reader's attention to the fact that Eq. (2.13) implies that the ζ-factor can be determined experimentally from a pure-element standard if its thickness and composition are known. This is a major difference from the k-factor where at least a two-element standard of known thickness and composition is needed.

By applying Eq. (2.13) to a binary system composed of elements A and B, each emitting X-rays of intensities I_A and I_B, the following expressions of C_A, C_B, and more importantly ρz can be given (assuming $C_A + C_B = 1$):

$$\rho z = \frac{\zeta_A I_A + \zeta_B I_B}{D_e}, C_A = \frac{\zeta_A I_A}{\zeta_A I_A + \zeta_B I_B}, C_B = \frac{\zeta_B I_B}{\zeta_A I_A + \zeta_B I_B}, \tag{2.15}$$

These equations show that C_A, C_B, and ρz can be determined simultaneously from measured X-ray intensities provided that the ζ-factor of each element and D_e are known. As pointed out above, the ζ-factors can be experimentally determined from **pure-element** standards if their thicknesses and compositions are well known. D_e can be determined by measuring in-situ the probe current using a Faraday cup.

Since ρz can be calculated (which was not possible using the k-factors method), we can now incorporate the absorption correction factor A given in (2.12) into the ζ-factors and account for the absorption matrix effect. The general expressions for a material composed of N elements are then given by:

$$\rho z = \frac{\sum_A^N \zeta_A I_A A_A}{D_e}, C_A = \frac{\zeta_A I_A}{\sum_A^N \zeta_A I_A A_A}, \ldots, C_N = \frac{\zeta_N I_N}{\sum_A^N \zeta_A I_A A_A}, \tag{2.16}$$

Since A depends on ρz, an iterative loop is performed first on the calculations of mass-thickness and concentrations, then on the calculations of the absorption coefficient. Typically, the convergence rate is very fast.

It is up to the analyst to determine which EDS-STEM quantification method is best suited to his specific needs (semi-quantitative analysis, accurate quantitative analysis) and the complexity of his own samples. Cliff-Lorimer method is a suitable choice for samples for which the specimen-thin criterion assuming negligeable absorption holds. Practically, this corresponds to cases where the sample is thin enough and the analyzed X-rays are higher than 2 keV. For these cases, k-factors computed theoretically by the commercial EDS software are sufficient for quantitative analysis

(this option is referred to as a standardless Cliff-Lorimer in the EDS software). If not, and in absence of multielement standards suited for experimental determination of k-factors, the analyst, seeking accurate quantitative analysis, has no choice but to use the ζ-factors method. The latter requires a prior calibration of the ζ-factors (which is possible from pure element standards of known composition) and to measure the probe current during the analysis (using a Faraday cup).

We recall that, in our specific study, the samples we seek to analyze by EDS-STEM are FIB lamellae (with thickness > 100 nm), prepared from NdFeB magnets (which are a 7-component system). Giving these conditions, the best quantitative method to choose is the method of ζ-factors. However, we didn't have the necessary standards (neither multi-element nor pure element standards) to use this method. Although pure element standards for Fe or Cu (present in our samples) can be relatively easily found and prepared, the same does not apply for other elements such as Nd and Dy, for example. For that, the semi-quantitative standardless Cliff-Lorimer method was used to analyze the EDS-STEM spectra. Naturally, the high-energy peaks were selected for the EDS-STEM analysis, as opposed to the low-energy peaks taken in EDS-SEM.

3. Chapter III: Characterization of sintered NdFeB magnet before the GBDP

In this chapter, sintered NdFeB magnets are characterized prior to diffusing Dy via the grain boundary diffusion process (GBDP). The aim of this characterization is to gain a good understanding of the microstructure to be able to determine its evolution post GBDP. We recall that the NdFeB magnets have a global composition of $(Nd,Pr,Dy)_{31}Fe_{67.1}Co_{0.5}Cu_{0.1}Al_{0.3}B_1$ (wt.%) with 0.5 wt.% of Dy, and are fabricated on the pilot line at CEA/LITEN using traditional powder metallurgy technique (see section 2.1.1). After sintering, the NdFeB magnets underwent different annealing treatments to improve their magnetic properties. In the first part of this chapter, the magnetic properties of the samples annealed at different temperatures are measured in order to identify the optimum annealing temperature. Following the magnetic characterization, the microstructure of the NdFeB magnets in the as-sintered and optimally annealed states is investigated using different electron microscopy techniques. Using scanning electron microscopy (SEM), the various phases present in the alloy were precisely analyzed by determining their chemical compositions using energy dispersive X-ray spectroscopy (EDS) and their surface fractions. The compositions obtained by EDS are compared with those obtained by wavelength dispersive X-ray spectroscopy (WDS). Furthermore, transmission electron microscopy (TEM) was used to study the distribution of the Nd-rich phase along the grain boundaries in the optimally annealed sample since these phases are not visible by SEM. At the end of this chapter, a summary of the main results that highlight the microstructural features associated with magnetic properties enhancement via annealing is given. This summary serves as a benchmark to track microstructural changes induced by GBDP.

3.1 Magnetic properties of the NdFeB magnets before and after different annealing treatment

3.1.1 Determination of the optimal annealing temperature

As already stated in section 1.2.3, post-sinter annealing (PSA) is an effective method to improve the magnetic properties of the as-sintered NdFeB magnets. It is worth recalling that thermal annealing comprises two steps: a first high temperature annealing around 800°C for 2h, and the final annealing around 500°C for 2h (for reference, the thermal cycle used for annealing is given in

Figure 46). It has been reported that the coercivity could be optimized after tuning the temperature of the final annealing[69]. The optimal annealing temperature depends mainly on the chemical composition of the magnet which in the framework of this study is given by $(Nd,Pr,Dy)_{31}Fe_{67.1}Co_{0.5}Cu_{0.1}Al_{0.3}B_1$ (wt.%) with 0.5 wt.% of Dy, and especially the content of Cu used as an additive element[134]. To determine the optimal temperature for our composition, the dependence of magnetic properties on the temperature applied for the final annealing was measured. Figure 79 shows the second quadrant demagnetization curves of NdFeB magnets that underwent annealing for 2h at various temperatures spreading between 500 and 550°C. The high temperature annealing was performed at the same temperature of 800°C for 2h. The demagnetization curve of the as-sintered NdFeB magnet is shown in gray for reference.

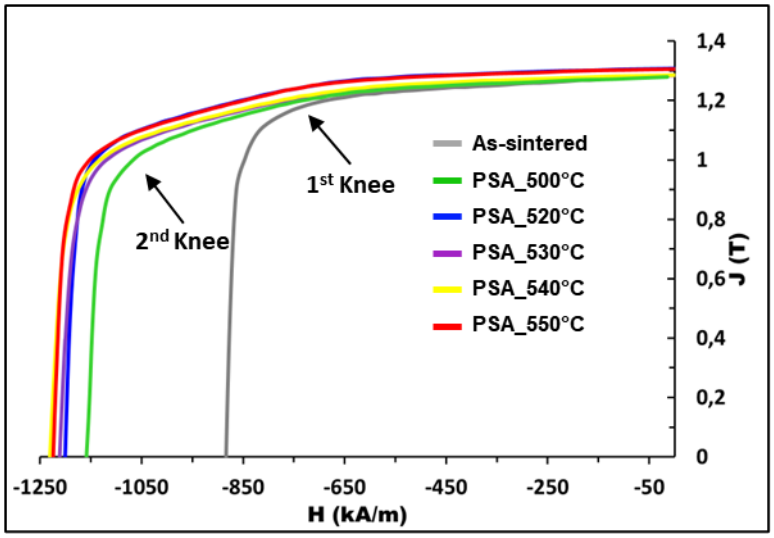

Figure 79: Second quadrant demagnetization curves of the NdFeB magnets in the as-sintered and PSA states. For the PSA state, the first annealing step is kept the same for all the magnets (800°C for 2h), only the temperature of the second annealing step is modified (500°C, 520°C, 530°C, 540°C, and 550°C for 2h).

The above demagnetization curves show that while the remanence remains nearly constant, the coercivity of the NdFeB magnets increases after annealing. The average magnetic properties of these samples are summarized in Table 15.

Table 15: Magnetic properties of the NdFeB magnet after different annealing treatments.

State of NdFeB	Coercivity H_{cJ} (kA/m)	Remanence B_R (T)	Squareness $\frac{H_{knee}}{H_{cJ}}$	$(BH)_{max}$
As-sintered	814.0 ± 13.4	1.290 ± 0.017	0.86 ± 0.02	304.72 ± 9.68
PSA at 500°C	1144.4 ± 9.8	1.295 ± 0.010	0.75 ± 0.02	316.56 ± 5.08
PSA at 520°C	1199.8 ± 1.6	1.291 ± 0.025	0.75 ± 0.01	318.11 ± 13.16
PSA at 530°C	1208.4 ± 4.7	1.288 ± 0.004	0.73 ± 0.01	314.25 ± 2.12
PSA at 540°C	1224.4 ± 8.6	1.292 ± 0.008	0.72 ± 0.01	317.89 ± 4.45
PSA at 550°C	1218.4 ± 7.6	1.309 ± 0.006	0.75 ± 0.01	328.52 ± 3.85

As seen from Table 15, the optimal annealing temperature is found to be 540°C where the increase in coercivity is about 50% (+ 410 kA/m) with respect to the as-sintered state. Below and above this temperature, the coercivity of the magnet becomes to decrease. The optimal temperature is close to the value obtained by Vial et al.[69] (520°C) for the composition

$Nd_{27.4}Pr_{3.0}Fe_{68.4}Co_{0.1}Cu_{0.1}Al_{0.1}B_{1.0}$ (wt.%) and the final coercivity is slightly higher (1220 kA/m vs 1100 kA/m).

3.1.2 Evolution of the squareness in J-H curves after annealing

The "squareness factor" (SF) of J-H curves is defined as the ratio of the knee field H_k, that corresponds to reduction of the polarization J to 90% of its initial value (i.e., the remanence J_r), and the coercive field H_{cJ} for which J = 0. The less the value of SF is, the more the magnet is prone to irreversible demagnetization for low applied fields H, which is detrimental in applications. The squareness is found to be substantially degraded in our samples (SF = 0.75), especially after annealing, compared to the values obtained in the literature (e.g., SF = 0.98 in ref[1]). An explanation of this difference requires a more detailed description of the J-H curves. Actually, the demagnetization curves reported in Figure 79 exhibit two "knees" (as indicated by the arrows in the Figure) whereas the as-sintered sample curve displays one knee occurring around an applied field H =-650 kA/m. This field value also corresponds to the first slope change noticed on the J-H curves after annealing. This observation leads us to assume that a residual population of low coercive grains, already present in the as-sintered state, has remained active after annealing and may influence the overall magnet performance.

This hypothesis is consistent with a coercivity driven by the nucleation and the propagation of reversed domains. For NdFeB, it is largely accepted that magnetization reversal starts from defects acting at GBs as nucleation sites (see section 1.1.5). When the grains are (magnetically) exchange-coupled, the reversed domains propagate easily to the adjacent grains. This results in an expansion without any barrier of the demagnetization leading to the abrupt fall in the J-H curve. In that case, the position of the knee would correspond to the weakest nucleation sites. Upon annealing, the nature of NdFeB magnets evolves from an exchange-coupled to an exchange-decoupled one, owing to a better distribution of some grain boundary phases[69,135]. Moreover, the strongest defects are expected to be "cleaned" as the GB phase spreads, shifting the switching fields to higher values[134]. In our case, it can be deduced that a part of these low coercive grains still acts as nucleation sites. However, as the grain decoupling has been improved after annealing, the first reversed domains did not propagate easily, compared to the as-sintered state, which could be a possible explanation for the two stepped J-H curves and the low squareness factor.

In the following, the microstructure of the samples before and after annealing (540 °C) is analyzed. This characterization aims at precisely investigating the microstructure of our magnets prior Dy-GBDP so we can track its evolution in chapter Ⅳ. In addition, we seek to understand the link between the microstructure and the magnetic properties post-annealing, namely the low value of SF.

3.2 Microstructural analysis

3.2.1 As-sintered sample

Figure 80 shows the polycrystalline microstructure of the as-sintered NdFeB sample. According to the ternary phase diagram and the selected composition (with an excess of rare earth with respect to the rare earth content of $Nd_2Fe_{14}B$), it is known that three main phases can be observed in such samples. Based on previous analyses[135], these 3 phases can be unambiguously identified in Figure 80: $Nd_2Fe_{14}B$ phase which is the matrix phase observed in uniform gray contrast, Nd-rich phases which are the secondary phase located at the triple/multiple junctions (i.e. grain boundary junctions) and observed in contrast ranging from white to light gray, and $NdFe_4B_4$ (Nd-boride) phase which is present in minor fraction inside the magnet and observed in dark gray contrast. Considering the composition of the sample equivalent to the ternary Nd 30.82 %, Fe 68.19 % and B 0.99 % in mass, the ternary diagram equilibrium at 20°C predicts the following distribution of the three phases in wt.%: $Nd_2Fe_{14}B$ 93.9 %, Nd 5.6 % and $NdFe_4B_4$ 0.5 %

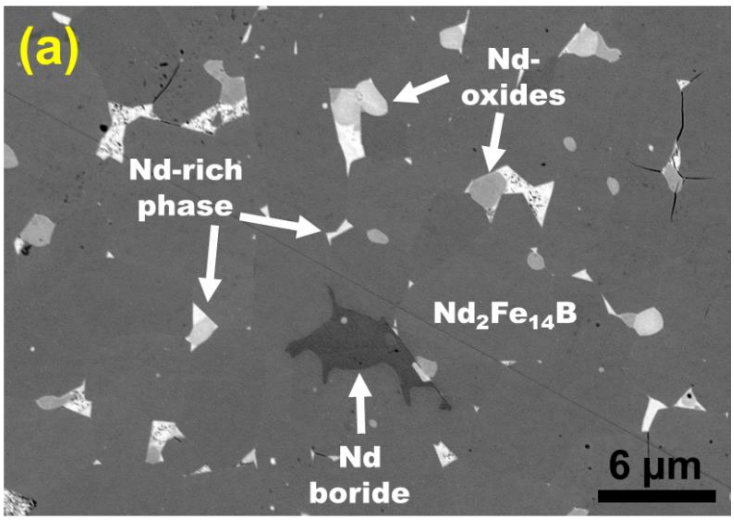

Figure 80: BSE-SEM image showing the typical microstructure of the as-sintered NdFeB magnet.

Due to the high reactivity with Nd and oxygen, the Nd-metallic phase tends to be partly oxidized during magnet manufacturing. This leads to the coexistence of Nd-oxides and metallic Nd-rich phases. In our samples, the Nd-rich phases can be separated owing to the shape difference clearly seen in the BSE-SEM image. The Nd-oxides are somewhat of a round shaped, whereas the metallic Nd-rich phases have more a triangular-liked shaped. The latter exist either separately or attached to the corners (i.e., sharp edges) of the Nd-oxides and Nd borides. A lamellar-like phase with a contrast that is slightly darker than the bright Nd-rich phases is sometimes found to be embedded inside the Nd-rich metallic phase. This phase can be clearly seen in Figure 81.

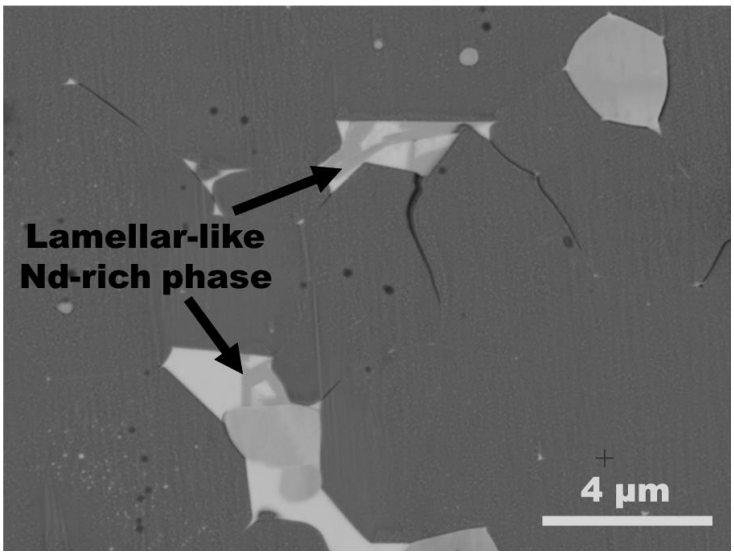

Figure 81: High magnification BSE-SEM image showing the lamellar-like Nd-rich phase.

In the following, the as-sintered NdFeB magnet is analyzed by evaluating 3 sets of parameters: $Nd_2Fe_{14}B$ and Nd-rich phase surface fraction measured on the SEM images, $Nd_2Fe_{14}B$ average grain size measured on the SEM images, and the chemical composition of all the phases present in the microstructure determined by EDS and WDS analyses. To begin, the surface fractions of the $Nd_2Fe_{14}B$ main phase and secondary Nd-rich phases are measured (Nd borides are not accounted since they are rarely detected in the microstructure). For that, ImageJ software is used to apply a threshold to the BSE-SEM images that differentiates each phase by generating a binary image as illustrated in Figure 82 (a) and (b).

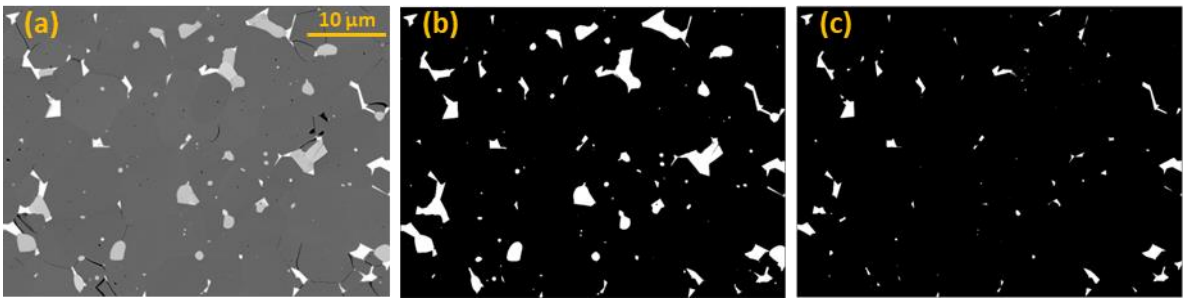

Figure 82: (a) BSE-SEM image of the as-sintered NdFeB magnet, (b) Binary image generated by applying a threshold on (a) that differentiates the $Nd_2Fe_{14}B$ phase and the Nd-rich phases, and (c) Binary image generated by applying a threshold on (a) that differentiates the metallic Nd-rich phases and Nd-oxides (in white are the metallic Nd-rich phases).

The results indicate that the surface fraction of the secondary Nd-rich phases ranges between 6-8% (range determined from analyzing four different SEM images) and the rest represents the surface fraction of the $Nd_2Fe_{14}B$ phase. This value is consistent with the mass fraction of the Nd-rich phase calculated using the ternary diagram (5.6%). We can determine the surface fraction of the Nd-oxides by applying a threshold that differentiates them from the metallic Nd-rich phases as displayed in Figure 82 (c). Among the 6-8% Nd-rich phases, there are 3-4% of Nd-oxides. This means that about half of the Nd-rich phases are oxidized during the fabrication process. A consequence of the partial oxidation of the Nd-rich phase would be lack of liquid phase formed

during the subsequent GBDP that could result in a non-percolating network of the liquid phase at GBs[136].

After having determined the $Nd_2Fe_{14}B$ and Nd-rich surface fractions, the $Nd_2Fe_{14}B$ average grain size is evaluated. For that, the lengths of 100 $Nd_2Fe_{14}B$ grains are measured manually using ImageJ software. The grain size distribution is shown in Figure 83. The $Nd_2Fe_{14}B$ average grain size is determined to be 4.3 μm.

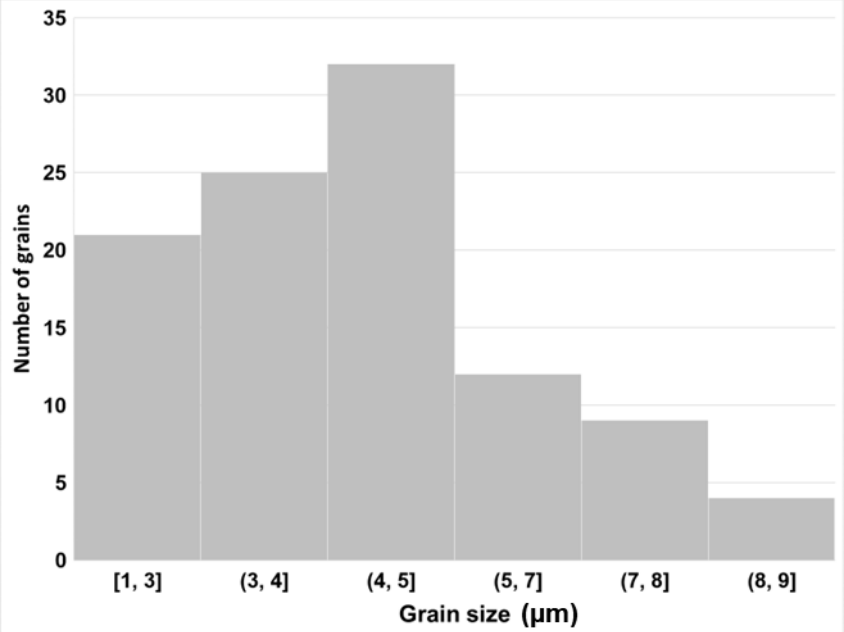

Figure 83: $Nd_2Fe_{14}B$ grain size distribution evaluated by measuring the length of 100 $Nd_2Fe_{14}B$ grains using ImageJ software.

Finally, the chemical composition of each phase present in the alloy is determined by means of EDS-SEM. All the EDS-SEM spectra are acquired under the same conditions as the EDS-SEM spectra of the standards (see section 2.3.2.2C). Figure 84 displays a typical EDS-SEM spectrum taken from the $Nd_2Fe_{14}B$ grain.

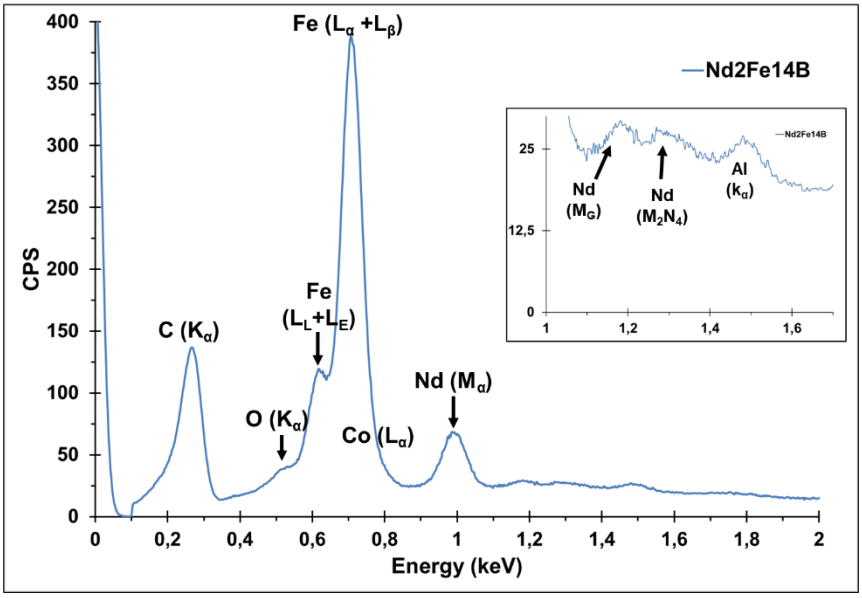

Figure 84: EDS-SEM point spectrum acquired at 5kV from the $Nd_2Fe_{14}B$ phase.

First and foremost, the Fe Lα and Nd Mα peaks are clearly visible is the EDS spectrum. This goes along with the fact that these elements are the main constituents of the $Nd_2Fe_{14}B$ phase. In contrast, the B Kα peak of energy 0.183 keV is not detected. This is mainly because of the minor concentration level of boron in the $Nd_2Fe_{14}B$ phase (for comparison, the B Kα peak is seen in the EDS spectrum of the Nd-borides). Moreover, O Kα and Al Kα peaks are visible in the EDS spectrum of the $Nd_2Fe_{14}B$ phase. The former indicates the surface oxidation of the $Nd_2Fe_{14}B$ phase during SEM sample preparation, while the latter indicates a partial substitution of Fe by Al. Indeed, as seen in section 1.2.2.1C, Bao-Min Ma et al.[137] showed that Al can penetrate the $Nd_2Fe_{14}B$ phase and substitute the Fe leading to an increase in the overall coercivity of the NdFeB magnet. Lastly, it is worth to note that the C Kα peak seen in the EDS spectrum is not intrinsic to the $Nd_2Fe_{14}B$ phase but is rather attributed to the carbon layer deposited on the surface of the sample during SEM sample preparation. The energy of each detected peak is given in Table 16.

Table 16: Energy of the characteristic X-ray peaks of the elements identified in the EDS-SEM spectrum of the $Nd_2Fe_{14}B$ phase.

Element	Peak	Energy of the peak (keV)
C	Kα	0.277
O	Kα	0.525
Fe	Ll	0.616
Fe	L_E	0.629
Fe	Lα	0.705
Fe	Lβ	0.718
Nd	$M\zeta_1$	0.753
Co	Lα	0.775
Cu	Lα	0.927
Nd	Mα	0.979
Nd	Mg	1.176
Nd	M_2N_4	1.285
Dy	Mα	1.293
Al	Kα	1.487

Using IZAC code and the standards database created for peak reference, the above spectrum is quantified. The chemical composition of the $Nd_2Fe_{14}B$ phase is determined as follows: $Fe_{81.2}Nd_{12.9}Al_{0.7}O_{5.1}$ (at. %) (boron is excluded). According to the identified chemical composition, the ratio Fe/Nd is 6.3 which is slightly lower than the Fe/Nd ratio (7) of the stoichiometric $Nd_2Fe_{14}B$ phase.

Based on the identified chemical composition, the $Nd_2Fe_{14}B$ phase does not contain Dy, Cu and Co initially present in the magnet starting composition. The absence of Cu is expected since it has a low solubility with the $Nd_2Fe_{14}B$ phase[49]. However, and as explained in chapter I, Dy and Co can penetrate the $Nd_2Fe_{14}B$ phase and substitute Nd and Fe respectively. For an acceleration voltage of 5 keV, a possible presence of Dy and/or Co inside the $Nd_2Fe_{14}B$ phase should be attested by the appearance of Dy Mα and Co Lα peaks (this is because only these peaks are excited when using an accelerating voltage of 5 keV; higher level peaks require a higher acceleration voltage). However, the energies of the Dy Mα and Co Lα peaks are 1.293 keV and 0.775 keV respectively. As a result, they overlap with the Nd M_2N_4 and Fe Lα peaks of energy 1.285 keV and 0.705 keV respectively. Therefore, we cannot conclude whether there is a minor presence of Dy and/or Co inside the $Nd_2Fe_{14}B$ phase by means of EDS.

To overcome this problem, wavelength energy dispersive X-ray spectroscopy (WDS). Compared to EDS, and as explained in section 2.3.2.3 of chapter II, the latter has a higher spectral resolution and detection limit which allow to accurately measure the concentration of the minor elements whose peaks overlap with major concentration elements. In addition, WDS has a higher sensitivity to light elements which allow us to measure the boron concentration inside the $Nd_2Fe_{14}B$ phase. We performed WDS measurements at an accelerating voltage of 10 kV and an aperture of 120 μm. These conditions were chosen to increase the number of emitted X-rays, which is necessary to obtain a sufficient WDS signal. We used the following peaks to measure the concentration of each element: Fe Lα, Co Lα, Nd $M\tau_1$, Dy Mα, Al Kα, O Kα, Cu Lα and B Kα. The chemical composition was found to be $Fe_{80.0}Nd_{11.0}Dy_{0.3}Co_{0.6}Al_{0.6}O_{1.6}B_{5.8}$ which is in excellent agreement with the stoichiometry of the $Nd_2Fe_{14}B$ phase ((Fe+Co)/(Nd+Dy) ratio is 7.1). Like the EDS result, WDS measurements confirm that Cu did not penetrate the $Nd_2Fe_{14}B$ phase. However, contrary to the EDS result, WDS measurements show that Dy and Co are present inside the $Nd_2Fe_{14}B$ phase. The composition determined by WDS will be used as a reference to compare any change in the composition of the $Nd_2Fe_{14}B$ phase post grain boundary diffusion process (GBDP) in chapter IV.

In addition, the chemical compositions of the different Nd-rich phases have been determined. A first order identification of the Nd-rich phases can be obtained by EDS mapping. Figure 85 (a) shows a region representative of the microstructure containing the different Nd-rich phases. The corresponding Nd, Cu and O EDS-SEM elemental maps are shown in Figure 85b-d.

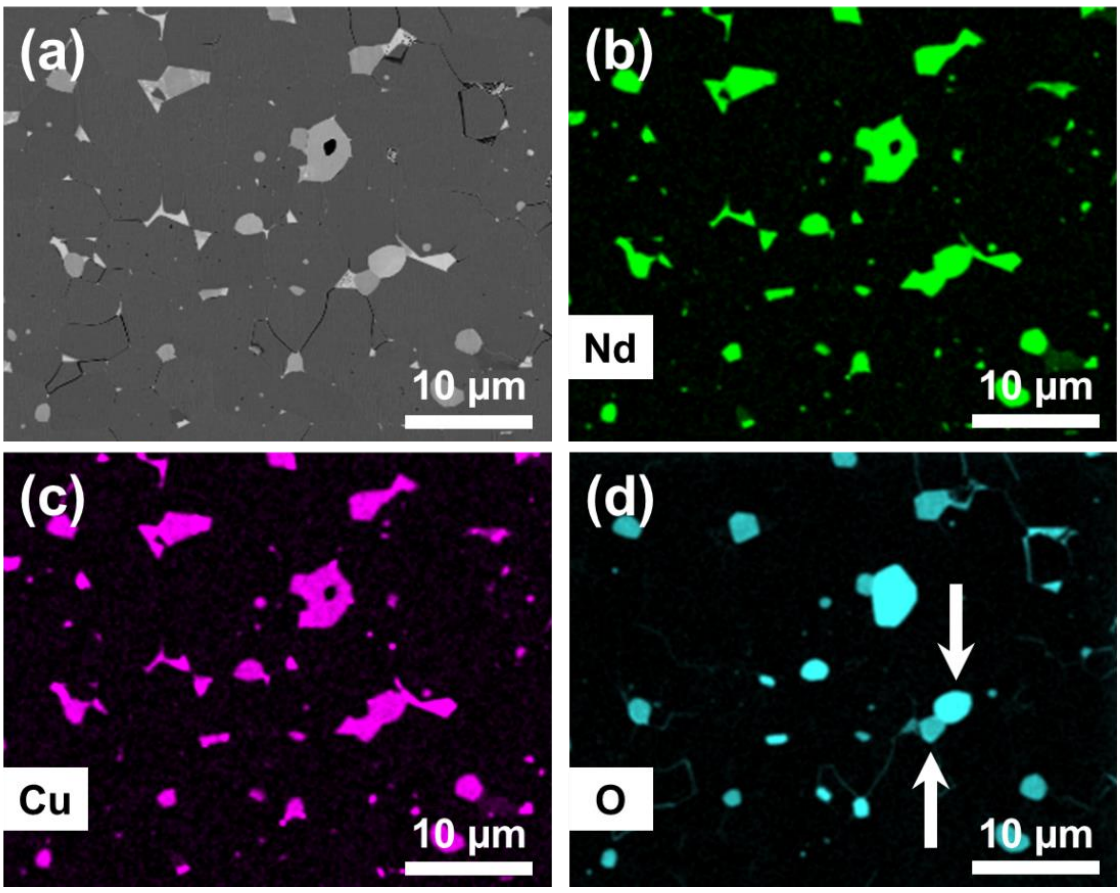

Figure 85: (a) BSE-SEM image showing the various Nd-rich phases found within the NdFeB microstructure and its corresponding (b) Nd (c) Cu (d) O EDS-SEM elemental maps acquired at an accelerating voltage of 5 kV.

While the Nd and Cu elemental maps show that all the phases at the triple/multiple junctions contain Nd and Cu, the O elemental map shows that only some of these phases are rich in O. This confirms the existence of both metallic Nd phases and Nd-oxides. It is also important to note that based on the intensity of the O elemental map, it seems that two distinct types of Nd-oxides are present within the NdFeB microstructure as indicated by the white arrows in Figure 85 (d).

To unambiguously identify the chemical composition of each type of the Nd-rich phases, an EDS-SEM spectrum from each phase was recorded. Figure 86 shows the typical spectra of each phase. The energy of each peak is previously reported in Table 16.

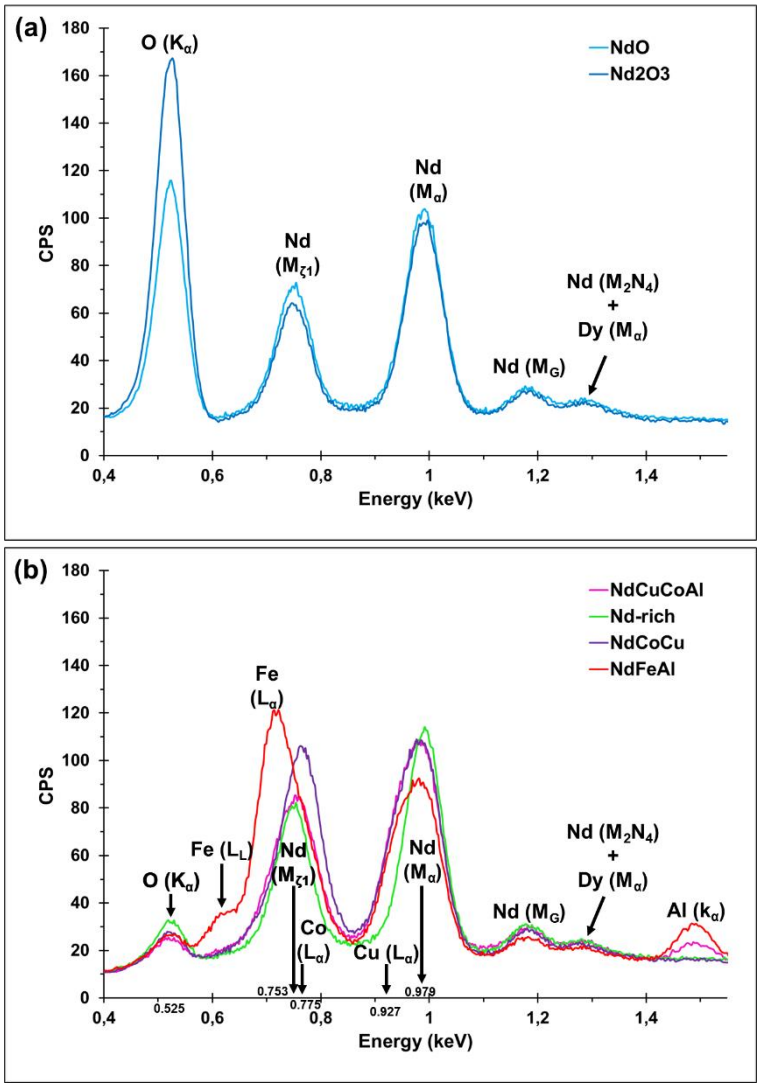

Figure 86: EDS-SEM spectra of (a) Nd-oxides and (b) metallic Nd-rich phases.

According to the shape of these spectra, a total of six different types of Nd-rich phases can be distinguished. Among these phases, the Nd-oxides are easily differentiated from the metallic Nd phases since the intensity of the O peak of the former is considerably higher than the latter as clearly seen when comparing Figure 86 (a) and (b). The low intensity O peak seen in the metallic Nd-rich phases can be attributed to surface oxidation during SEM sample preparation.

The EDS spectra displayed in Figure 86 (a) confirm the presence of 2 different types of Nd-oxides with one having a higher intensity O peak than the other. These Nd-oxides are denoted Oxide 1 (low intensity O peak) and Oxide 2 (high intensity O peak).

Figure 86 (b) represents the spectra of four different types of metallic Nd phases. Firstly, the spectrum in green indicates a phase rich in Nd with little to no additive elements (Cu, Co or Al). This phase is denoted by Nd-rich phase. Secondly, for the spectrum in purple, the gaussians around the peaks Nd $M\zeta_1$ and Nd Mα are shifted towards the higher and lower energies respectively when compared to the spectrum in green. This shift is due to the presence of Co Lα and Cu Lα peaks. For that, the phase associated to the spectrum in purple is designated by NdCoCu. Thirdly, the spectrum in pink also shows a shift of the gaussian around the Nd Mα peak towards the lower

energies as a result of the presence of Cu Lα peak. However, the gaussian around the Nd Mζ$_1$ peak is only slightly shifted toward the higher energies compared to the spectrum in green. This indicates that this phase has more Co than the Nd-rich phase but less than the NdCoCu phase. In addition, the presence of the Al Kα peak at 1.487 keV indicates the presence of Al in the phase associated to this spectrum. For that, this phase is referred to as NdCuCoAl. Lastly, the spectrum in red is easily distinguished from the other metallic Nd-rich phases due to the presence of a high intensity Fe Lα peak. This infers that the associated phase is particularly rich in Fe. Here again, the gaussian around the Nd Mα peak is shifted towards the lower energies indicating the presence of Cu. The Al Kα peak evidence the presence of Al in the associated phase. This phase will be denoted by NdFeAl phase. We note that neither the shape nor the contrast of the Nd-rich phase, NdCoCu phase and NdCuCoAl phase are particularly different in the BSE-SEM image. They all display a bright contrast and are located at the triple/multiple junctions either solely or at the corners of the Nd-oxides. However, the NdFeAl phase is the lamellar-like phase seen in Figure 81.

Hereafter, the chemical composition of each of the above-described Nd-rich phases is determined. For that, 10 spectra/phase were recorded at an accelerating voltage of 5 kV and current of 1.5 nA and then quantified using the IZAC code. The results are displayed in Table 17. A type is assigned to each phase to simplify the distinction between them and track their evolution later in chapter IV.

Table 17: Chemical composition of the various Nd-rich phases found within the as-sintered NdFeB microstructure in at. %

Phase	Type	Chemical composition (at. %) (Determined using standards and IZAC code)
Nd-rich	IA	$Nd_{69.1}O_{12.9}Fe_{13.1}Co_{3.6}Cu_{1.1}Dy_{0.1}Al_{0.1}$
NdCoCu	IB	$Nd_{53.9}O_{7.1}Fe_{10.4}Co_{21.0}Cu_{7.4}Dy_{0.0}Al_{0.1}$
NdCuCoAl	IC	$Nd_{46.5}O_{6.0}Fe_{20.7}Co_{9.1}Cu_{13.4}Dy_{0.1}Al_{4.2}$
NdFeAl	ID	$Nd_{31.0}O_{12.3}Fe_{45.2}Co_{4.8}Cu_{4.1}Dy_{0.0}Al_{2.6}$
Oxide 1	IIA	$Nd_{42.4}O_{47.5}Fe_{6.9}Co_{1.7}Cu_{0.9}Dy_{0.4}Al_{0.1}$
Oxide 2	IIB	$Nd_{34.2}O_{58.3}Fe_{5.2}Co_{1.3}Cu_{0.7}Dy_{0.3}Al_{0.1}$

First, **IA** has a chemical composition of $Nd_{69.1}O_{12.9}Fe_{13.1}Co_{3.6}Cu_{1.1}Dy_{0.1}Al_{0.1}$ (at.%) as reported in Table 17. Compared to the other metallic Nd-rich phases, this phase contains the highest amount of Nd and a very little amount of additive elements. Additionally, this phase contains about 13 at.% of Fe. However, regarding the 13 at.% of O found in its chemical composition, it is not clear whether it is intrinsic to the phase itself or the result of partial/total oxidation during SEM sample preparation. The same applies to the other metallic Nd-rich phases.

Second, **IB** has a chemical composition of $Nd_{53.9}O_{7.1}Fe_{10.4}Co_{21.0}Cu_{7.4}Al_{0.1}$ (at.%). Consequently, this phase is the richest phase in Co (20 at.% vs less than 10 at.% for the other phases). It also contains considerable amount of Fe and Cu. Although this phase contains the highest amount of Co, its stoichiometry doesn't match neither $Nd_3(Fe,Co)$ nor $Nd(Fe,Co)_2$ reported in literature to occur when adding Co (see Table 9). For this reason, this phase is considered to be the Cu^{low} Nd-rich

phase reported by Kim et al. Its Cu content (≈7 at.%) falls within the range given by Kim et al. (5-15 at% of Cu) for the Cu^{low} Nd-rich phase.

Third, **IC** has a chemical composition of $Nd_{46.5}O_{6.0}Fe_{20.7}Co_{9.1}Cu_{13.4}Dy_{0.1}Al_{4.2}$ (at.%). This phase contains the highest amount of Cu and considerable amounts of Co and Al. It also has higher amount of Fe than the above Nd-rich phase. Since this phase has the highest amount of Cu, it might be identified as the Cu^{high} Nd-rich phase reported by Kim et al. (see Table 9). It should be noted however that the amount of Cu found in this phase (≈13 at.%) is lower than the range given by Kim et al. (30-45 at% of Cu) for the Cu^{high} Nd-rich phase.

Finally, **ID** has a chemical composition of $Nd_{31.0}O_{12.3}Fe_{45.2}Co_{4.8}Cu_{4.1}Al_{2.6}$ (at.%). This phase is therefore the richest phase in Fe. It also contains considerable amount of Co, Cu and Al. Since this phase has the highest amount of Fe, and based on its stoichiometry, it can be identified as the ferromagnetic $Nd(Fe,Co,Al)_2$ phase (see Table 9). The presence of a ferromagnetic phase at the triple/multiple junctions is detrimental to the coercivity.

Regarding the Nd-oxides **IIA** and **IIB**, their chemical compositions are found to be $Nd_{42.4}O_{47.5}Fe_{6.9}Co_{1.7}Cu_{0.9}Dy_{0.4}Al_{0.1}$ (at.%) and $Nd_{34.2}O_{58.3}Fe_{5.2}Co_{1.3}Cu_{0.7}Dy_{0.3}Al_{0.1}$ (at.%) respectively. This suggests that the former can be identified as the NdO phase while the latter can be identified as the Nd_2O_3. Both of the Nd-oxides contain minor amount of additive elements (Cu, Co and Al), however it is interesting to note that the Dy added to the NdFeB starting composition is found to be mainly in these oxides.

In summary, the microstructural analysis of the as-sintered NdFeB sample mainly shows that it has an average grain size of 4.3 μm and is composed of 94-96% of $Nd_2Fe_{14}B$ and 6-8% of secondary Nd-rich phases. These surface fractions are consistent with the mass fractions calculated using the Nd-Fe-B ternary diagram. About half of the Nd-rich phases were found to be in oxide form, while the remainder were found to be metallic. The oxidation of metallic Nd-rich phases most probably occurs during the fabrication process, and results in wasting metallic Nd-rich phases since Nd-oxides have a high melting temperature and do not infiltrate into the grain boundaries (GBs) during annealing. The chemical compositions of all secondary Nd-rich phases were determined and a total of six different phases were identified: four metallic phases (IA, IB, IC, and ID) and two Nd-oxides (IIA and IIB). Among these phases, only ID is known to be ferromagnetic. Finally, it is worth noting that the Dy initially present in the NdFeB sample was found to be present in the Nd-oxides but not in the metallic Nd-rich phases.

In the following section, the microstructure of the optimally annealed sample is characterized.

3.2.2 Optimally post-sinter annealed (PSA) sample

During annealing some intergranular phases should melt and redistribute along the GBs. The aim of this section is to characterize these GB phases. The microstructure of the optimally PSA sample is displayed in Figure 87.

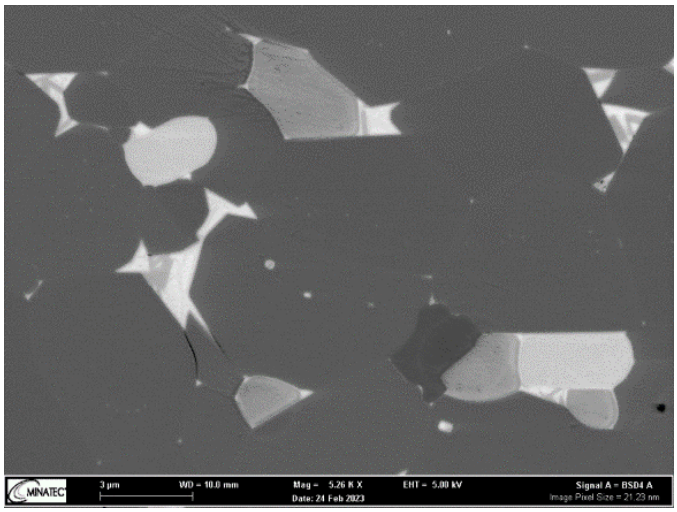

Figure 87: BSE-SEM image showing the microstructure of the optimally PSA NdFeB magnet.

When comparing the as-sintered (Figure 80) and PSA samples, no obvious difference is detectable by SEM. First, the GB phase expected to form in the PSA sample is not visible in the SEM image (see Figure 87). Furthermore, the Nd-rich secondary phases present at the triple/multiple junctions in the annealed sample were analyzed by EDS-SEM, and their chemical compositions were identified following the same protocol described in the case of the as-sintered sample (i.e., 10 EDS/SEM spectra per phase were recorded and quantified). No evolution of the secondary phases was evidenced (they were found to be the same phases identified in the as-sintered sample and reported in Table 17**Erreur ! Source du renvoi introuvable.**). The fraction of secondary phases is also found to be similar (92-94% of $Nd_2Fe_{14}B$ phase, 6-8% of Nd-rich phases).

Evolutions of the Nd-oxide phases after PSA have been reported in literature. However, the low contrast between the Nd-oxide phases did not allow to separate accurately in this study the proportion of each one and to evidence an evolution during the final annealing. Nishio et al.[134] reported the following evolution of the oxide phases during the thermal treatments:

- during the high temperature annealing (first step), the fcc-NdO oxide phase precipitates along the $Nd_2Fe_{14}B$ grains while the remaining liquid phase (Nd-rich), containing alloying elements, remains at the center of triple junctions (TJs).

- during the final annealing two changes occur: (i) the liquid phase at TJs decomposes into dhcp-Nd and hcp-Nd_2O_3 without any direct contact with $Nd_2Fe_{14}B$ grains, and (ii) the fcc-NdO layer turns into a thin amorphous Nd-Cu-O layer surrounding the $Nd_2Fe_{14}B$ grains thanks to the higher solubility of oxygen in the Nd-rich phase with Cu addition.

This amorphous phase is expected to "clean" the GBs from defects (oxides) that act as nucleation sites and, owing to its non-ferromagnetic nature, to prevent from magnetic coupling. On the other hand, the lattice mismatch between fcc-NdO oxides and the $Nd_2Fe_{14}B$ phase is known the create large distortions in the hard ferromagnetic phase, lowering the magneto-crystalline anisotropy which, in turn, leads to the nucleation of the magnetization reversal. The possible transformation of fcc-NdO oxides into hcp-Nd_2O_3 during annealing is also reported as being beneficial due to the

lower mismatch of this oxide with the $Nd_2Fe_{14}B$ lattice. For this reason, residual fcc-NdO oxides due to an insufficient control of the oxygen pick-up during the magnet manufacturing is detrimental for the magnetic performances.

Although it is known from literature that a thin continuous GB phase should be formed after annealing[64], it is difficult to detect a contrast of this phase by scanning electron microscopy (SEM). Therefore, the aim of the following section is to evidence this phase in the PSA sample by means of transmission electron microscopy (TEM). To do so, TEM lamellae were prepared using focus ion beam (FIB) technique.

3.2.2.1 $Nd_2Fe_{14}B$ phase

First, the $Nd_2Fe_{14}B$ main phase is examined. As seen in Chapter I, this phase has a complex tetragonal structure. The complexity rises from the fact that the tetragonal unit cell contains four $Nd_2Fe_{14}B$ units which is equivalent to 68 atoms. This makes understanding the $Nd_2Fe_{14}B$ projections and the corresponding diffraction patterns complicated. The easiest projection of the $Nd_2Fe_{14}B$ structure is along its c-axis (i.e., the electron beam is parallel to the c-axis). This projection is presented in Figure 88 (a) and (b) which are the bright-field (BF) and high-angle annular dark-field (HAADF) STEM images respectively. In Figure 88 (b) the Nd atoms are seen in a bright contrast laying on two perpendicular diagonals while the Fe atoms are seen in a dark contrast and forming hexagons. An enlarged image of the structure is shown in Figure 88 (c), and the inset is the schematic of the projected structure oriented accordingly. The diffraction pattern taken along this projection is shown in (d). This precession electron diffraction pattern can be indexed according to the simulation done using JEMS software to simulate the diffraction pattern of the $Nd_2Fe_{14}B$ phase along the c-axis.

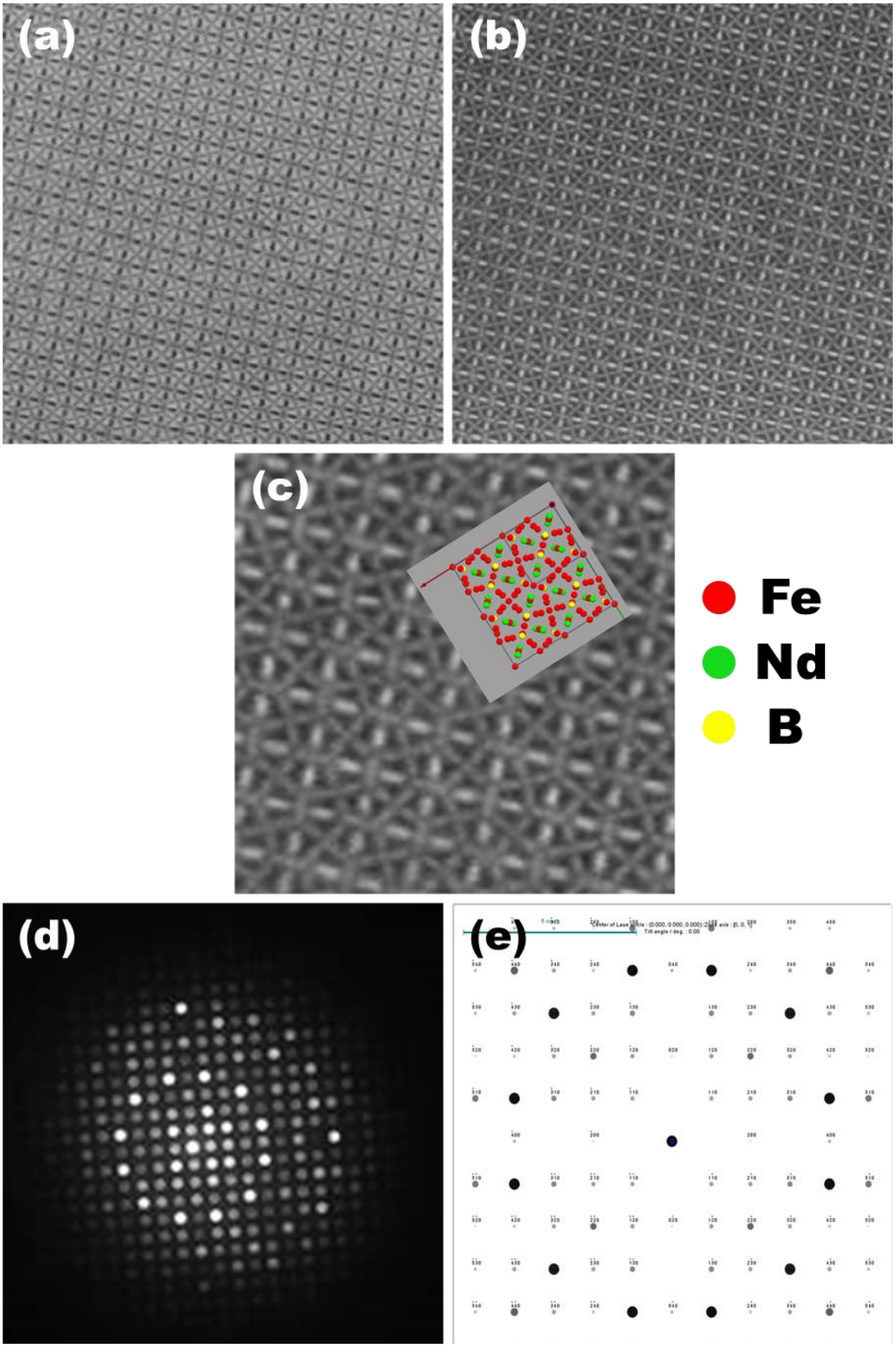

Figure 88: (a) BF-STEM image of the $Nd_2Fe_{14}B$ crystal structure along the c-axis, (b) HAADF-STEM image of the $Nd_2Fe_{14}B$ crystal structure along the c-axis, (c) enlarged view of the of the $Nd_2Fe_{14}B$ crystal structure along the c-axis taken from (b) and the inset is the projected structure, (d) selected are diffraction patterns along the c-axis and (e) simulated diffraction pattern of the of the $Nd_2Fe_{14}B$ crystal structure along the c-axis using JEMS software.

3.2.2.2 Nd-Cu rich precipitates

Nd-rich precipitates were frequently observed inside the $Nd_2Fe_{14}B$ phase. Figure 89(a) shows the presence of spherical precipitates of a size of several tens to hundreds of nanometers within the upper $Nd_2Fe_{14}B$ grains. These precipitates are found in both as-sintered and PSA sample. Figure 89(b) is a high magnification image of one of the precipitates. The corresponding EDS elemental maps show that this precipitate is rich in Nd with Cu-rich corners while no particular enrichment in O is detected. The presence of precipitates inside the $Nd_2Fe_{14}B$ grains was previously reported by Shinba et al.[43]. In their study, they have also observed these precipitates in both as-sintered and PSA samples. Using Lorentz TEM, they showed that these precipitates disturb the magnetic domains. This was attributed to the lattice mismatch between these precipitates and the $Nd_2Fe_{14}B$ grains which resulted in a strain field that can be clearly seen in their BF-TEM image. We note that while the precipitates found in this study are rich in Cu and lean in O, Shinba reported that the Nd precipitates are rich in O. In their study, the starting material did not contain Cu therefore no Cu is expected to be found inside the precipitates as is in our case.

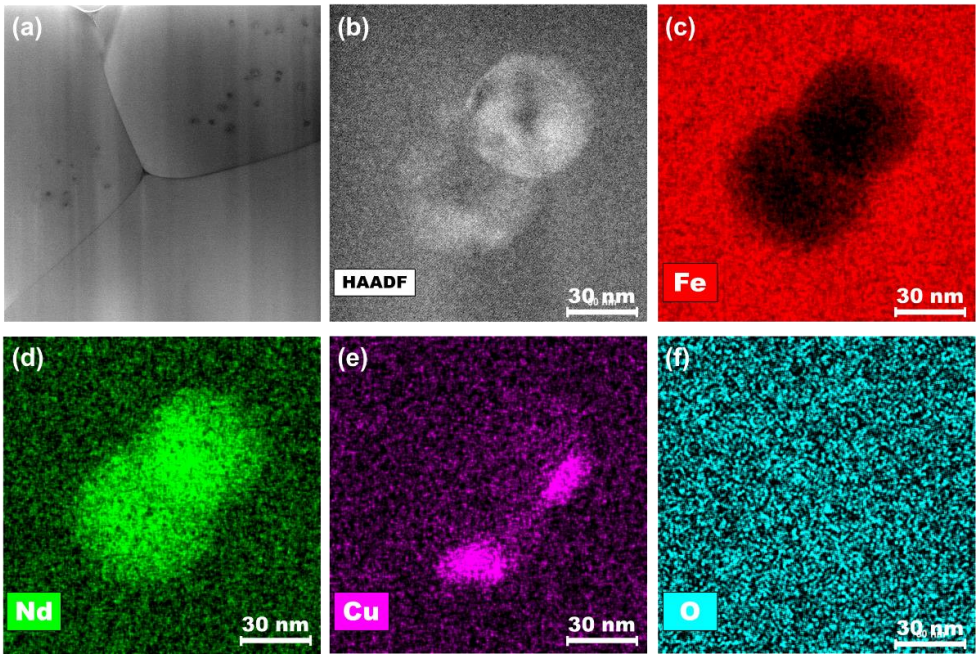

Figure 89: (a) low magnification HAADF-STEM image showing spherical precipitates distributed inhomogenously inside the upper $Nd_2Fe_{14}B$ grains, (b) High magnification HAADF-STEM image showing the precipitate, (c-f) Fe, Nd, Cu and O EDS elemental maps of the precipitate.

3.2.2.3 Nd-rich phase and its distribution along the GBs

The dimensions of the TEM lamellae prepared to study the Nd-rich phase distribution along the grain boundaries are 15×3 μm^2. Since the average $Nd_2Fe_{14}B$ grain size is about 4 μm, this means that only 2 or 3 grain boundaries per lamellae can be studied. Hence the lack of statistical analysis should be noted. In the following, the common features observed from the analyzed grain boundaries are presented.

Figure 90 displays two triangular shaped metallic Nd-rich phases located at the triple junctions of $Nd_2Fe_{14}B$ grains. The dislocations inside the Nd-rich phase seen in (a) are frequently observed within the Nd-rich phase. In contrast, no dislocations are observed in the NdFeB phase. It is probable that only the more ductile Nd-rich phase can release some of the internal stresses present in the alloy, these internal stresses being also probably at the origin of the numerous cracks along grain boundaries. Additionally, we see in this image a cracked grain boundary. This might be due to the FIB sample preparation, but could also be inherited from the sample itself since cracks at the level of the grain boundaries were frequently observed in SEM.

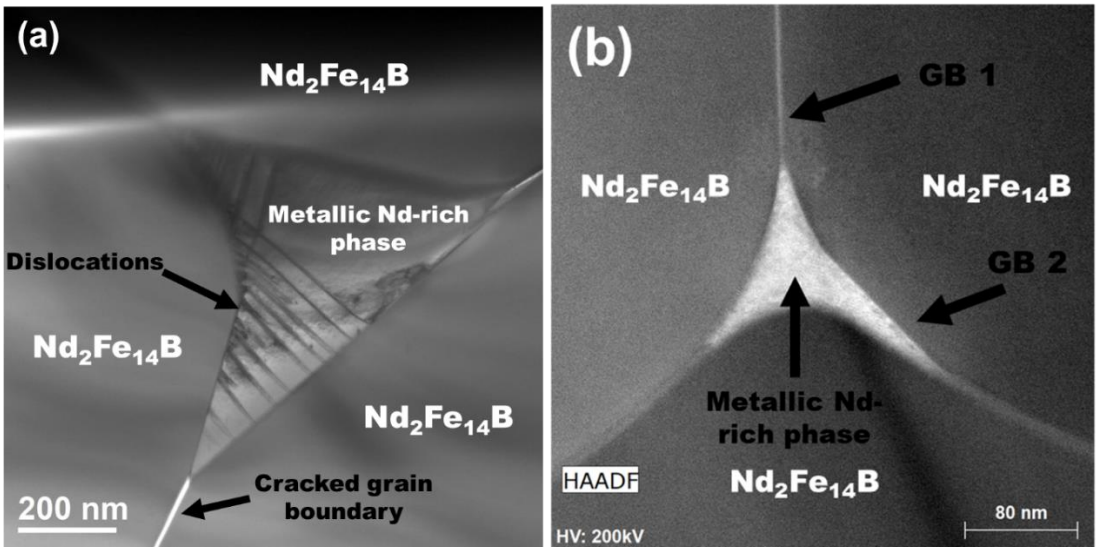

Figure 90: Low magnification BF and HAADF-STEM image of the Nd-rich phase in the PSA sample showing in: (a) dislocation contrast and (b) the difference in Nd distribution along the grain boundaries.

Figure 90 (b) is also a triangular shaped metallic Nd-rich phase observed in another lamellae. It is interesting to see in this image the difference in the Nd-rich distribution between grain boundary 1 (GB 1) and grain boundary 2 (GB 2). A thin Nd-rich phase is observed along GB 1 whereas a thick Nd-rich phase can be seen at the starting of the GB 2 (i.e., the part that is the closest to the Nd-rich triple junction). The Nd-rich phase at GB 2 becomes thinner as it moves far from the triple junction phase and eventually disappear. It is worth to note that for some grain boundaries no Nd-rich phase was detected. This shows that the distribution of Nd-rich phase along the GBs is inhomogeneous and discontinuous.

It is interesting to have a look over the Nd-rich/$Nd_2Fe_{14}B$ interface. Figure 91 (b) is a high magnification HAADF-STEM image taken from Figure 90(a) and showing the $Nd_2Fe_{14}B$/Nd-rich interface.

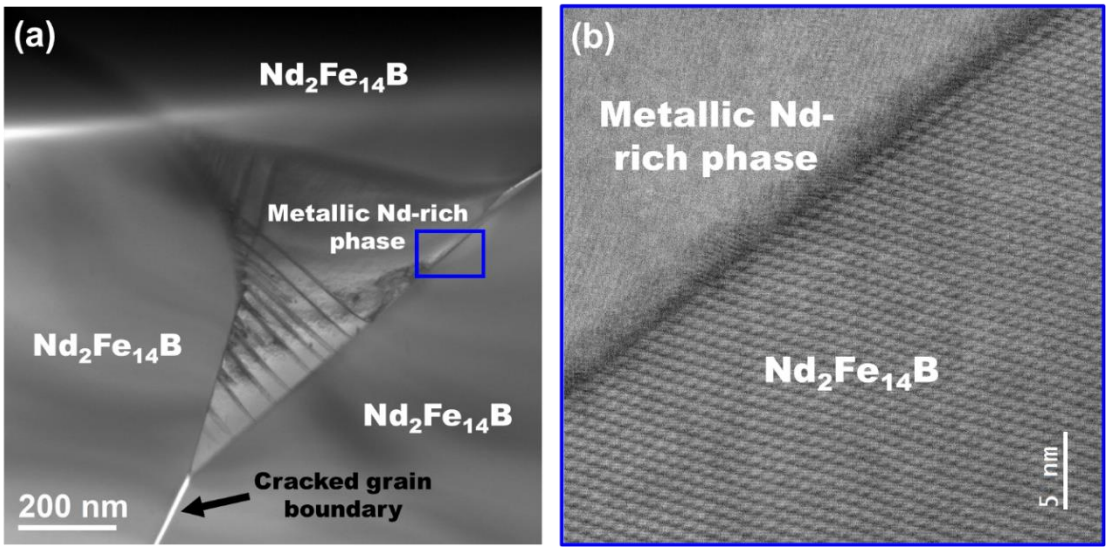

Figure 91: Microstructure of optimally post-sinter annealed sample: (a) Low magnification BF-STEM image showing a triangular shaped metallic Nd-rich phase at the triple junctions of three $Nd_2Fe_{14}B$ grains and (b) High magnification HAADF-STEM image taken at the Nd-rich/$Nd_2Fe_{14}B$ interface corresponding to the blue rectangle shown in (a).

The above image show that both $Nd_2Fe_{14}B$ and Nd-rich phase are in direct contact with each other. The $Nd_2Fe_{14}B$/Nd-rich interface is rectilinear and follows a crystallographic plane of the $Nd_2Fe_{14}B$. This atomically smooth $Nd_2Fe_{14}B$/Nd-rich interface was reported by Liu et al.[138] who suggested that interface rearrangement occurs during annealing, minimizing the interfacial energy and consequently leading to coercivity enhancement. The corresponding EDS elemental maps and the line-scan profile extracted from the elemental maps are shown in Figure 92 (b-d).

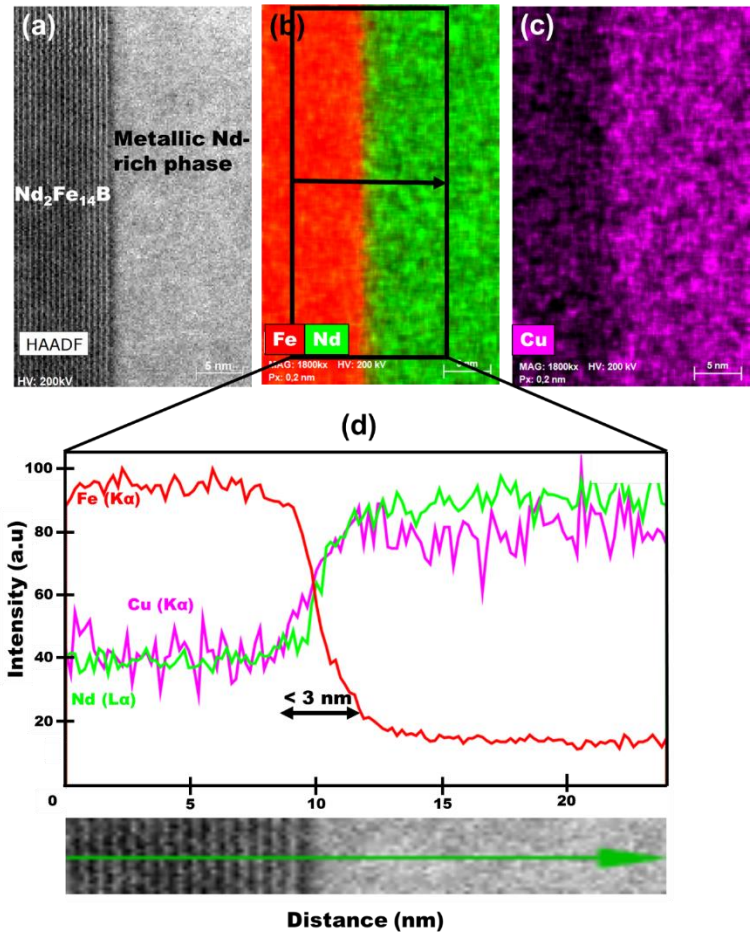

Figure 92: (a) HR-STEM image showing the $Nd_2Fe_{14}B$/Nd-rich interface (b) Fe and Nd EDS elemental maps, (c) Cu EDS elemental map and (d) Line-scan profile taken across the $Nd_2Fe_{14}B$/Nd-rich interface as indicated by the black arrow in (b).

The line-scan surprisingly doesn't show an abrupt interface but a gradient of composition between the two phases is extended over about 3 nm. Since we know from literature that Cu doesn't penetrate the $Nd_2Fe_{14}B$ phase, this chemical composition gradient is most probably due to the beam broadening in the thick FIB lamellae which limits the EDS resolution.

Sepehri-Amin et al.[64] also studied the $Nd_2Fe_{14}B$/Nd-rich interface using atom probe tomography (APT) technique (see Figure 93). They reported an enrichment of 0.6 at.% of Cu at the $Nd_2Fe_{14}B$/Nd-rich interface (Cu increased from 2.2 at.% in the metallic Nd-rich phase to 2.8 at.% at the interface), which they suggested, could accommodate the strain in the $Nd_2Fe_{14}B$ phase near the $Nd_2Fe_{14}B$/Nd-rich interface and reduce the distortion of the $Nd_2Fe_{14}B$ lattice, leading to coercivity improvement as explained in chapter I. However, in our case, the line-scan doesn't show a Cu enrichment at the $Nd_2Fe_{14}B$/Nd-rich interface.

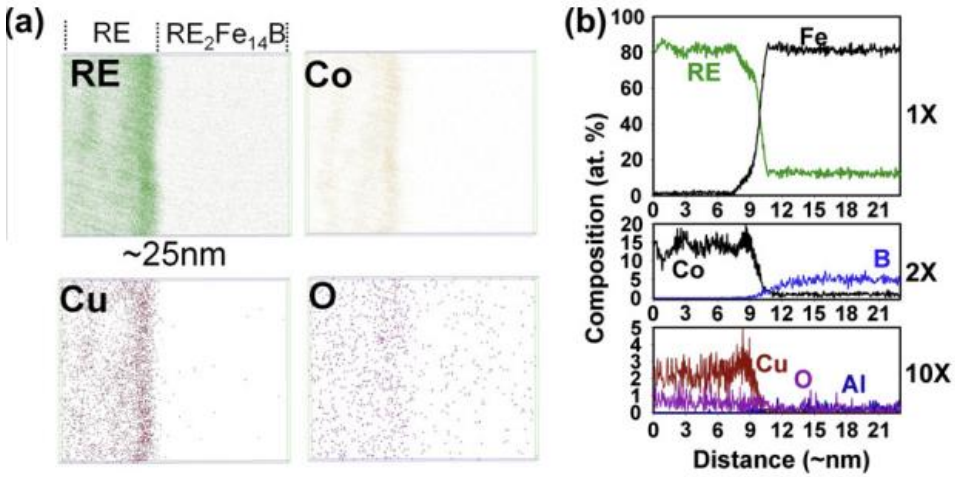

Figure 93: (a) Atom probe maps of RE = (Nd + Pr), Co, Cu, and O taken at the $Nd_2Fe_{14}B$/Nd-rich interface in the annealed sample; (b) concentration depth profiles for Fe, RE, Co, B, Cu, O, and Al determined from the 3DAP analysis shown in (a). Adapted from Sepehri-Amin[64].

In addition to the triple junction phase, the grain boundary (GB) phase was also examined. Figure 94 (b) is a high magnification HAADF-STEM image taken from Figure 94 (a) at the interface between two $Nd_2Fe_{14}B$ grains. The image shows the presence of a thin phase (less than 3 nm) at the grain boundaries. The thickness of this phase cannot be determined accurately since a Moiré pattern is seen in the GB, indicating that the latter is not parallel to the electron beam (the observation was performed using a vacuum transfer single tilt sample holder making the orientation of the GB parallel to the electron beam not possible).

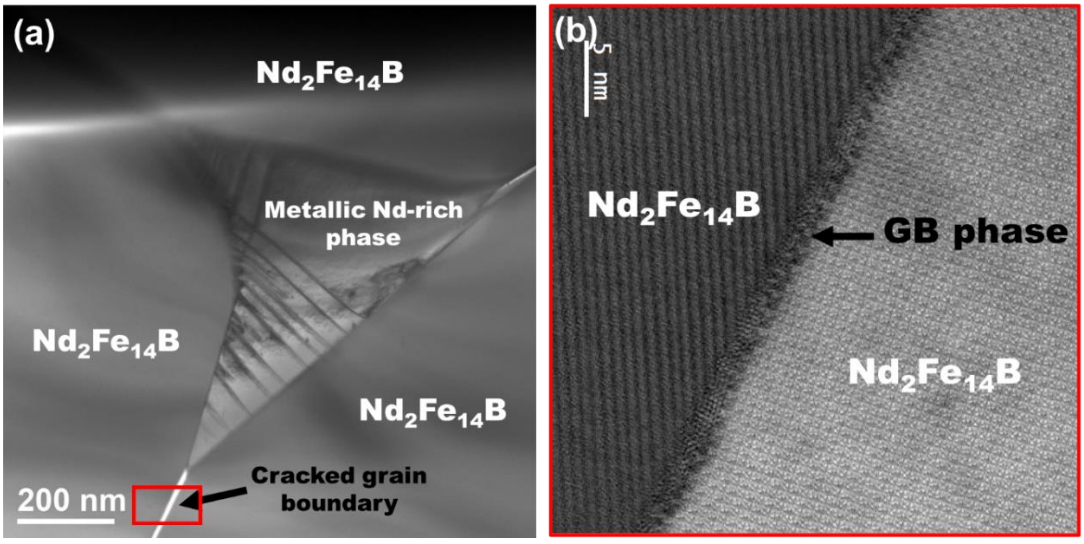

Figure 94: Microstructure of optimally post-sinter annealed sample: (a) Low magnification BF-STEM image showing a triangular shaped metallic Nd-rich phase at the triple junctions of three $Nd_2Fe_{14}B$ grains and (b) High magnification HAADF-STEM image taken along [001] zone axis of the right $Nd_2Fe_{14}B$ grain at the cracked grain boundary as indicated by the red rectangle (the exact image is taken in the lower part of the cracked grain boundary which is not visible in (a), the red rectangle is to guide the reader on the region of interest).

Figure 95 (a) is a higher magnification HAADF-STEM image of the GB seen in Figure 94 (b). The corresponding Nd and Fe EDS elemental maps are shown in Figure 95 (b). The line-scan profile across the GB displayed in Figure 95 (c) is extracted from the EDS maps. It is obvious that the thin phase at the GB is rich in Nd and Cu and depleted in Fe. The formation of this phase after annealing is expected as it has been frequently reported in literature. Sepehri-Amin et al.[64] explained that this GB phase is formed due to the Nd/NdCu eutectic reaction. They explained that when heating up to the PSA temperature, the metallic Nd-rich phases located at the triple junctions, and containing Cu, melt and infiltrate into the GBs by capillary motion. This is because the presence of Cu improves the wetting behavior of the liquid Nd-rich phase which allows its infiltration into the GBs. The presence of this phase in the intergranular region serves to decouple the $Nd_2Fe_{14}B$ grains leading to the coercivity enhancement.

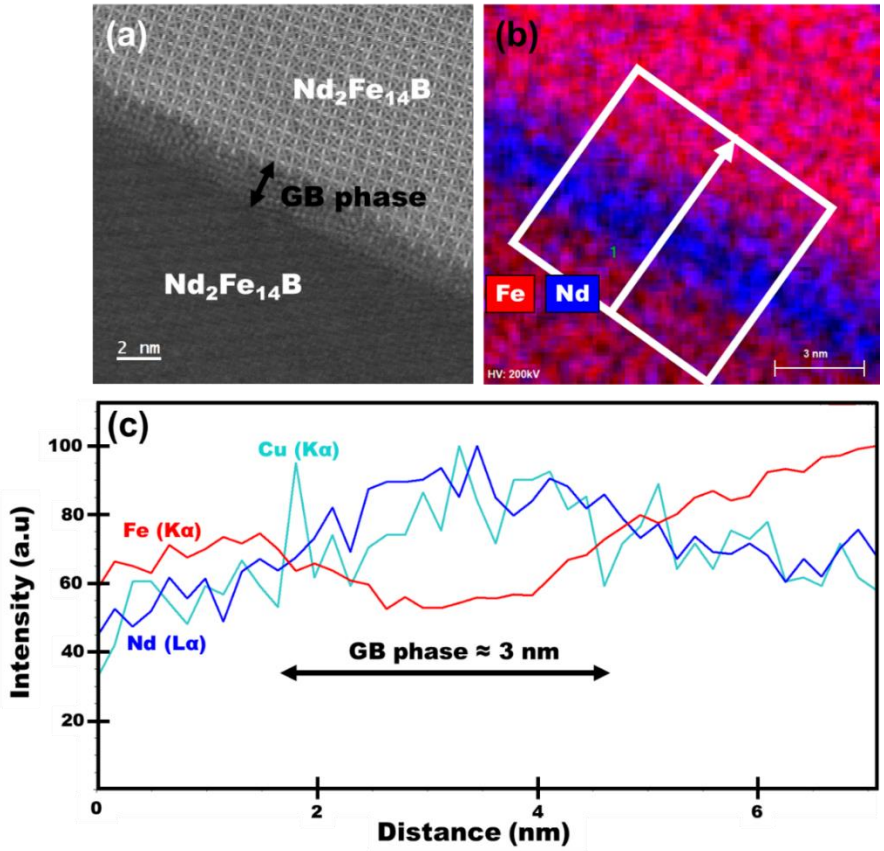

Figure 95: (a) High magnification HAADF-STEM image showing two $Nd_2Fe_{14}B$ grains and a GB phase in the optimally PSA sample, (b) Fe and Nd EDS elemental maps and (c) Line-scan profile across the GB as indicated by the white arrow in (b).

Another GB that we observed is the GB 1 presented in Figure 90 (b). Figure 96 and Figure 97 show at two different magnifications the image of the triangular-shaped Nd-rich phase and the associated Fe, Nd and Cu EDS elemental maps confirming that the metallic Nd-rich phase located at the triple junction is rich in Nd and Cu.

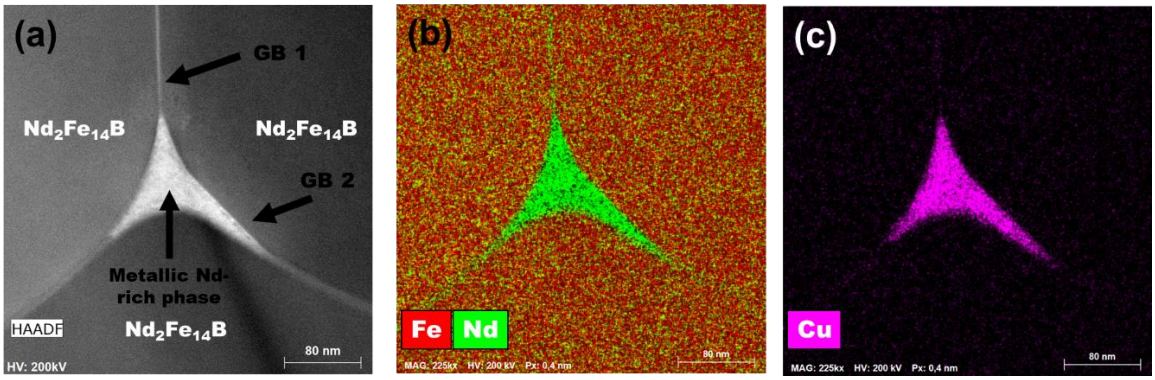

Figure 96: Low magnification HAADF-STEM image showing a triangular shaped metallic Nd-rich phase at the triple junctions of three $Nd_2Fe_{14}B$ grains, (b) Fe and Nd EDS-STEM elemental maps and (c) Cu EDS-STEM elemental map.

The higher magnification EDS elemental maps taken for the GB 1 are displayed in Figure 97 (b) and (c). The line-scan across GB 1 is extracted from the EDS maps. The position of the GB corresponds to Fe deficiency together with Nd and Cu peaks which confirm the presence of a NdCu phase at the GBs. The thickness of the GB phase was found to be ≈ 8 nm. It should be noted that this thickness is not very accurate since the GB might be tilted inside the sample. In addition, the GB phase is found to be thick in the vicinity of the triple junction and becomes thinner away from it until it disappears.

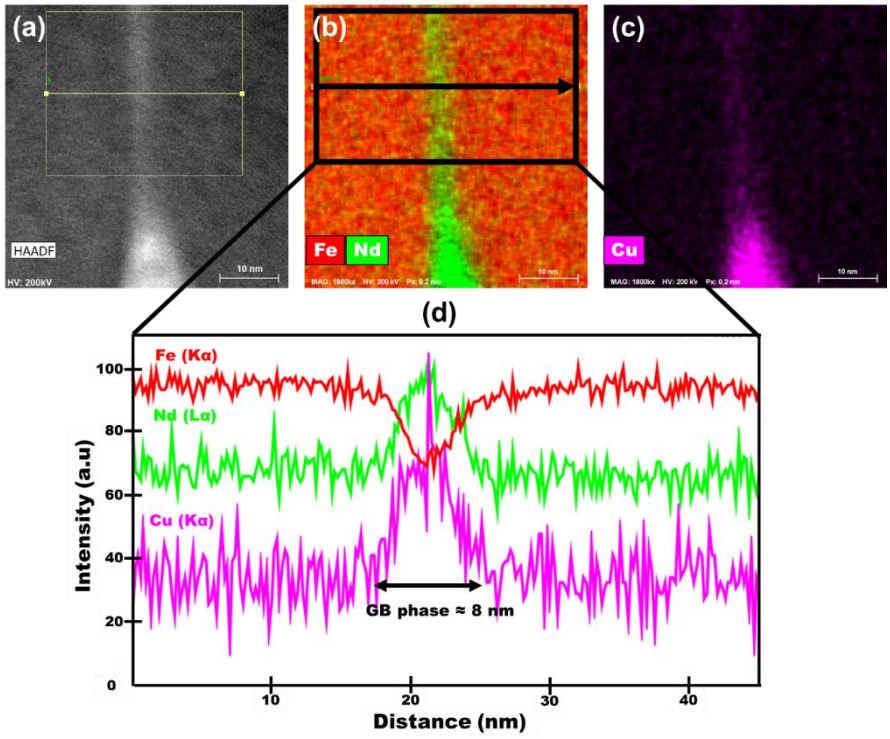

Figure 97: High magnification HAADF-STEM image of the GB 1 taken from Figure 96 (a), (b) Fe and Nd EDS-STEM elemental maps, (c) Cu EDS-STEM elemental map and (d) Line-scan profile taken across the GB as indicated by the black arrow in (b).

In summary, in this section, the Nd-rich phase and its distribution along the GBs in the annealed NdFeB sample was studied. First, the $Nd_2Fe_{14}B$/Nd-rich interface was examined. It was found to be rectilinear and atomically smooth. However, no Cu enrichment at the interface was detected In

contrary to what is reported in the literature. Then, the $Nd_2Fe_{14}B/Nd_2Fe_{14}B$ interface was investigated. As expected from the literature, the presence of a very thin (several nm) phase at the GBs was detected. This phase was found to be rich in Nd and Cu with a thickness of several nm. The exact composition of this thin GB phase is very challenging to determine, as it requires a very thin lamellae (which was technically challenging) and to make sure that the GB is oriented parallel to the electron beam. Due to the lack of time, this study was not conducted. The presence of a NdCu GB phase is at the origin of the increase in coercivity after annealing. However, it is important to note that the GB phase was rarely found to be continuous. In fact, it was found to be thick at the vicinity of the triple junction thinning as it moved away from it until it disappeared. In some cases, no phase was detected at the GBs, or the GB was simply cracked. This is not ideal since a continuous GB phase is crucial to magnetically decouple the $Nd_2Fe_{14}B$ grains so that the NdFeB magnet reaches its highest possible coercivity.

3.3 Conclusion

In this chapter, the NdFeB magnets in the as-sintered and post-sinter annealed states prior to the Dy-GBDP were characterized. As expected from the literature, the main difference between these samples is the formation of a NdCu GB phase in the annealed sample as revealed by TEM. This phase account for the +50% increase in coercivity obtained after annealing since it ensures magnetic isolation between $Nd_2Fe_{14}B$ neighboring grains. However, the thickness of the GB phase was not uniform all along the GBs. Instead, the GB phase was found to be thick in the vicinity of the triple junction and thin away from it until it disappears. This situation is not ideal since it leads to a poor decoupling of the $Nd_2Fe_{14}B$ grains as the GB phase thins out, and even a direct contact between the $Nd_2Fe_{14}B$ grains when the GB phase disappears.

In addition, the secondary Nd-rich phases located at the triple/multiple junctions were examined. Half of the metallic Nd-rich phases were found to be oxidized during the magnet manufacturing. The oxidation of metallic Nd-rich phases negatively impacts the coercivity; this is because the melting temperature of Nd-oxides is significantly higher than the annealing temperature which prevents their infiltration into the GB. Furthermore, and according to the type of Nd-oxide that is formed, it is possible to produce large distortions at the $Nd_2Fe_{14}B$/Nd-oxide interface, giving rise to numerous nucleation sites at the interface. EDS-SEM quantitative analysis enabled the identification of the six different Nd-rich phases: four metallic Nd-rich phases (IA, IB, IC, and ID) and two Nd-oxides (IIA and IIB). These phases were present in both the as-sintered and annealed samples. Among these phases, only the Nd-oxides contain Dy, initially present in the composition of the magnet. Metallic phase ID is a ferromagnetic phase, hence it is probably the most harmful phase for coercivity enhancement.

Finally, the high amount of Nd-oxides (50% of the total Nd-rich phases), the formation of ferromagnetic secondary phase (ID) and the non-uniform thickness of the GB phase are all factors that contribute to the low "squareness" (SF = 0.75) noticed in the demagnetization curves after annealing.

4. Chapter Ⅳ: Characterization of DyCo-GBDP sintered NdFeB magnet

The aim of this chapter is to investigate the Dy grain boundary diffusion process (GBDP) that is a promising method to increase the coercivity of the NdFeB magnets. In our study, as described in chapter II, both upper and lower surfaces of the sintered cylindrical NdFeB magnets analyzed in the chapter III were coated by $Dy_{63}Co_{37}$ (at.%) intermetallic powder. A heat treatment at 920°C for 2h was then performed to enable GBDP followed by a post-diffusion annealing treatment (PDA) at 540°C for 3h.

In the first part of this chapter, the evolutions of the magnetic properties of the magnet after the GBDP is presented, while in the second part the evolution of the microstructure is studied by SEM and TEM. In this second part, an overview of the microstructure is given followed by the detailed investigations of the microstructures observed at different depths in the magnet (near the surface, in the first tens and then hundreds of micrometers, and finally at larger depths). Finally, in the third part, a parametric study is performed to investigate the effect of varying the GBDP time and temperature on the microstructure and the magnetic properties of the NdFeB magnets.

4.1 Magnetic properties

Figure 98 shows the demagnetization curves of NdFeB sintered magnets in its different thermal states (as-sintered state, post-sinter annealing (PSA) state, GBDP state and post-diffusion annealing (PDA) state). All measurements were performed at 20°C using the hysteresigraph system.

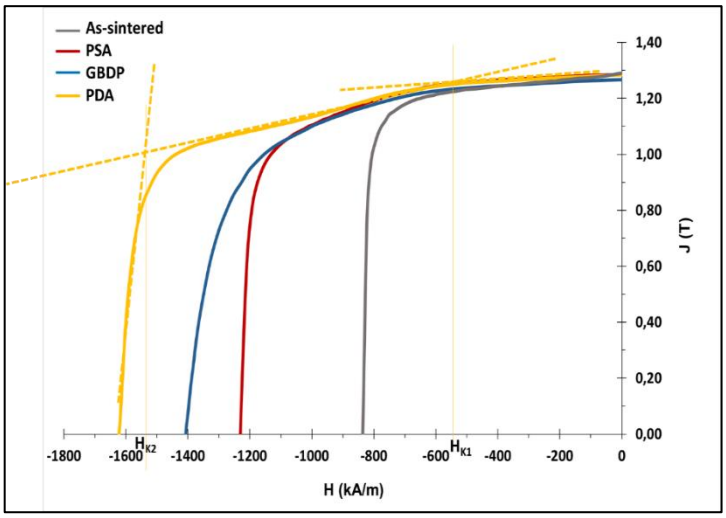

Figure 98: Demagnetization curves of the NdFeB magnet measured in the as-sintered state, annealed state PSA, GBDP state and post diffusion annealed state PDA.

It is clear that the maximum coercivity is obtained in the case of PDA state, where the gain in coercivity is 31.9% compared to the optimally PSA state (coercivity increases from 1230.4 kA/m to 1622.6 kA/m). It is interesting to compare the gain in coercivity reported in the present work to what other groups have published (see Table 18).

Table 18: Summary of the reported coercivity enhancement at RT of GBD processed sintered NdFeB magnets using DyCo alloys as diffusion sources. REE stands for rare-earth elements and e stands for magnet thickness.

Magnet chemical composition (wt.%)	**∑REE (wt.%)**	**e (mm)**	**Diffusion source**	**Amount of deposited diffusion source (wt.%)**	**$t_{Diffusion}$ (h)**	**ΔH_{cJ} (%)**	**$\frac{H_{knee}}{H_{cJ}}$**
$(Nd,Pr,Dy)_{31}Fe_{67.1}Co_{0.5}Cu_{0.1}Al_{0.3}B_1$ (This work)	31.0	5	$Dy_{63}Co_{37}$	0.7	3	31.9	0.57
$Pr_{0.08}Nd_{30.21}Fe_{68.73}B_{bal}$ (Ming et al., 2022)[139]	30.28	4	$Dy_{86.49}Co_{10.11}O_{1.9}Bal_{1.42}$	0.27	5	25.7	-
$Nd_{22.83}Pr_{7.60}Fe_{67.69}B_{0.98}Co_{0.80}Cu_{0.10}$ (Chen et al., 2018) [140]	30.44	4	$Dy_{60}Co_{40}$	Not reported	3	26.2	-
$Nd_{29.00}Dy_{3.00}Fe_{bal}B_{0.97}M_{2.39}$ (with M = Cu, Al, Co and Nb) (Jang et al., 2017)[141]	32.00	5	DyCo	Not reported	8	18.8	0.93*
$(Nd,Pr,Dy)_{31}Fe_{67.1}Co_{0.5}Cu_{0.1}Al_{0.3}B_1$ (Fliegans et al., 2019)[105]	31.0	5	$Dy_{66}Co_{34}$	0.7	3	27.5	0.64*
$(Nd,Pr,Dy)_{31}Fe_{67.1}Co_{0.5}Cu_{0.1}Al_{0.3}B_1$ (Fliegans et al., 2019)[105]	31.0	5	$Dy_{63}Co_{37}$	0.7	3	32.5	0.68

*Values estimated from demagnetization curves.

Unfortunately, the amount of coated DyCo is not always reported in literature, which consequently complicates an accurate comparison of the results. However, and taking into account the variation in magnets thickness (increasing the magnet thickness lowers the effect of GBDP to improve coercivity[142]), we can see that the increase in coercivity reported in this work falls within the range and even slightly better than the gain in coercivity reported by researchers that have used DyCo as a diffusion source.

The increase in coercivity is attributed to the intrinsic properties of Dy. In fact, as already stated in chapter I (section 1.1.5), the coercivity of the NdFeB magnet is controlled by the nucleation of reverse magnetic domains which generally occurs at the periphery of the $Nd_2Fe_{14}B$ grains due to the presence of defects lowering the magnetic anisotropy field of these grains. To overcome this problem, the Dy-GBDP aims to selectively position Dy at the periphery of the $Nd_2Fe_{14}B$ grains since $Dy_2Fe_{14}B$ has a higher anisotropy field than the $Nd_2Fe_{14}B$ (see chapter I, Table 5). This by consequence helps to hinder the nucleation of reverse magnetic domains and increases the coercivity of the magnet.

On the other side, the squareness of the demagnetization curve, which measures the magnetic stability of the magnet in practical applications, is significantly altered by the GBDP. This alteration is expressed by a double slope behavior in the demagnetization curve particularly apparent after the PDA (see Figure 98). This double slope is characterized by two values of the knee field H_{K1} et H_{K2}. It is worth noting that the value of H_{K1} remains the same before and after the GBDP. The same behavior has been observed by Fliegans et al.[85]

4.2 Study of the microstructure

4.2.1 Global view of the microstructure after GBDP

After diffusing the NdFeB sintered magnet, we proceeded to investigate the overall microstructural modifications. For that, the diffused magnet was cut along the diffusion direction, and the center part of the magnet was taken for cross-sectional microstructural characterization using SEM-EDS as represented in Figure 99 (a) and (b). Figure 99 (c) shows a cross-sectional EDS-SEM map of the Dy elemental distribution (in yellow) in the GBD processed NdFeB magnet. The top of the map is the surface of the magnet where the DyCo was deposited. The diffusion direction (i.e., z-axis) is indicated by an arrow on the left side of the map. One can clearly see two regions along the z-direction: the first region just below the surface and down to 30-40 μm where Dy is mainly found in the 2:14:1 grains, and a second region where Dy is concentrated at the GBs. In the second region, we observe a decrease in the Dy amount when moving further from the surface of the magnet. This is the consequence of the GBDP as reported in chapter I, the Dy initially deposited at the magnets surface, penetrates the magnets volume via the grain boundaries.

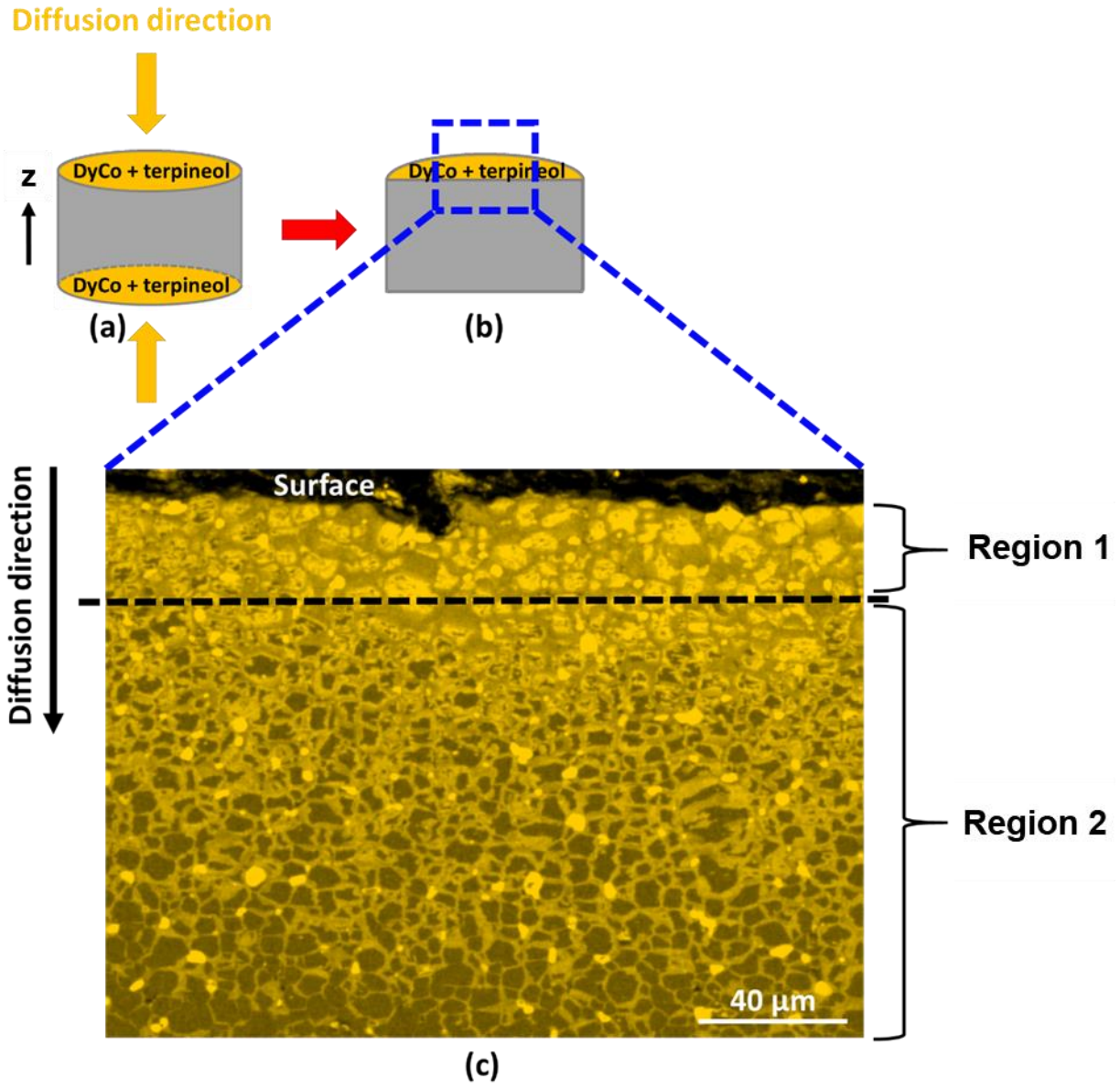

Figure 99: (a) Schematic representation of the GBD processed sintered NdFeB magnet, (b) the center part of the cut GBD processed sintered NdFeB magnet and (c) Cross-sectional EDS-SEM map of Dy elemental distribution within the GBD processed sintered magnet.

In the first region, Dy is found to be more enriched in the core of the $Nd_2Fe_{14}B$ grain as illustrated in Figure 100 below. This region will be defined as the anti-core-shell region and will be presented later in section 4.2.4.

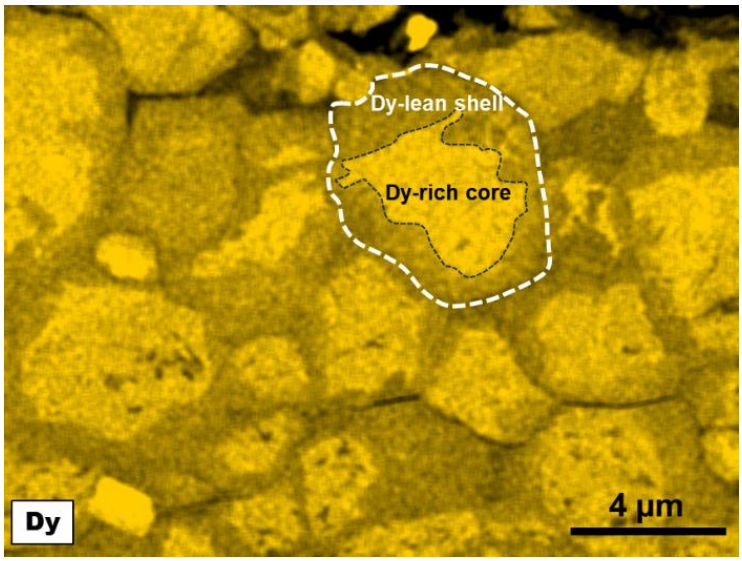

Figure 100: High magnification EDS-SEM map of Dy elemental distribution showing the anti-core-shell microstructure.

In the second region, and as pointed in chapter I, the Dy penetrates a limited outer layer of the $Nd_2Fe_{14}B$ grains from the grain boundaries to form the so-called core-shell microstructure. Core-shell microstructure is observed in our samples as shown in Figure 101 (the saturated yellow region seen in this image are explained below). The latter displays a higher magnification image of the microstructure taken at a depth of 150 µm from the magnet surface. The chemical composition of the shell and its thickness at various depths are presented in detail in section 4.2.5.1.

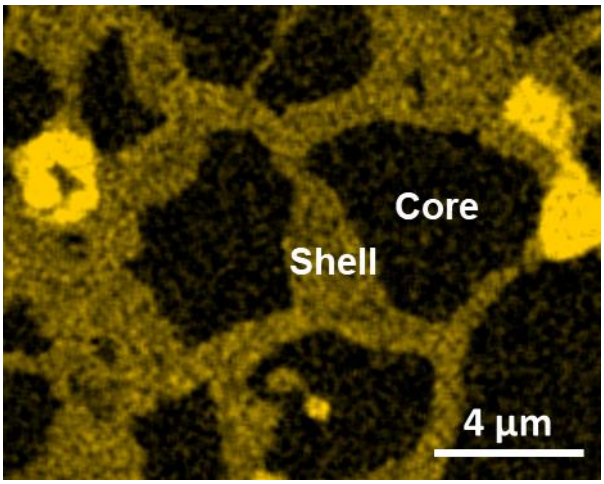

Figure 101: High magnification EDS-SEM map of Dy elemental distribution showing the core-shell microstructure at z = 150 µm.

Additionally, considerable amount of Dy was observed in the Nd-oxides. This can be clearly seen in the high magnification EDS-SEM map of Dy and O elemental distributions displayed in Figure 102 where the Nd-oxides located at the grain boundaries appear to be saturated by Dy. This will be further discussed in section 4.2.5.2.

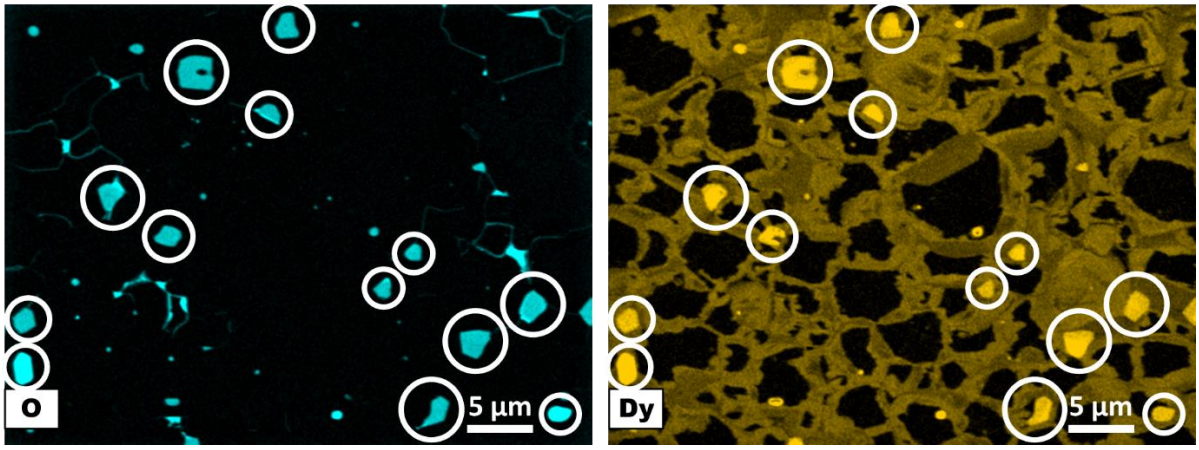

Figure 102: Dy elemental EDS map showing Nd-oxides rich in Dy (as indicated in white circles).

It is worth to recall that in this work, as explained in chapter II, the DyCo coating was deposited manually using a brush leading to a non-uniform coating thickness. This results in different areas on the surface of the magnet with different amount of Dy. Under the area with low amount of Dy deposited, we notice that region 1 (anti-core-shell microstructure) previously described is not present (see Figure 103). Instead, the region 2 (core-shell microstructure) is directly connected to the magnet surface. Taking into account the surface heterogeneities illustrated by Figure 103, we decided to examine only the parts of the magnets where regions 1 is clearly visible near the surface followed by an underneath region 2. This allows us to compare magnets treated with different experimental conditions.

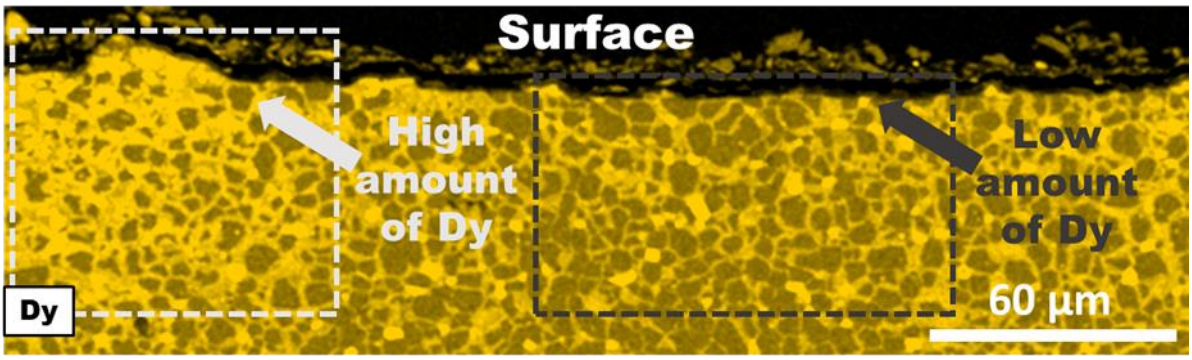

Figure 103: EDS-SEM map showing the heterogeneous Dy elemental distribution at the surface of the GBD processed NdFeB magnet.

A more detailed study of the microstructures observed in the different magnet depths is presented in the following sections (4.2.3 to 4.2.6). However, before studying these different microstructures, in order to determine the depth of penetration of Dy in our magnet and also to determine an apparent diffusion coefficient of Dy, the average concentration profile of Dy in the magnet thickness was measured by EDS.

4.2.2 Dy concentration profile along the magnet depth

In the following, the Dy concentration profile along the magnet's depth will be established and the Dy diffusion coefficient will be deduced.

EDS analyses were performed in 12 regions located at different depths from the magnet surface starting from a depth of 25 μm and ending at a depth of 400 μm. The step size between the depths was chosen to be either 25 μm or 50 μm. At each region, and to determine the average concentration of Dy over a representative area, an EDS spectrum was recorded by scanning the electron beam over 12×200 μm² areas as illustrated in Figure 104. The EDS spectra were acquired under the following conditions: accelerating voltage of 5kV, current of 1.5 nA, working distance of 10 mm, maximum pulse throughput of 30 kcps and an acquisition time (live time) of 360 sec. Afterwards, the spectra were quantified using IZAC code to extract the Dy concentration.

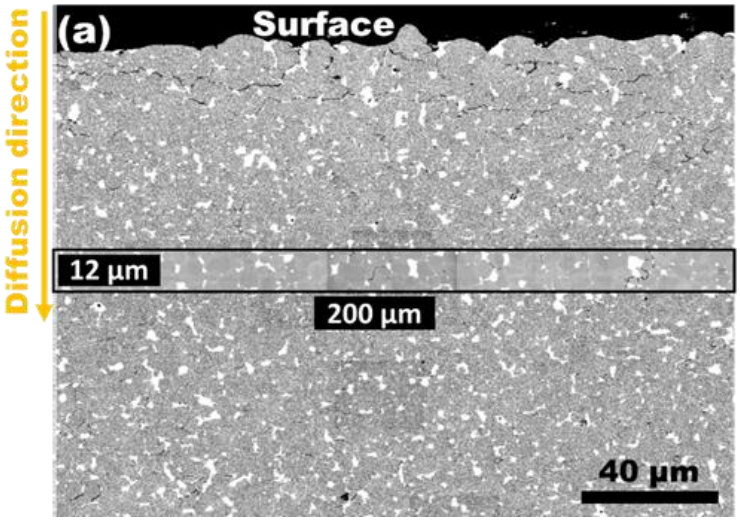

Figure 104: Cross-sectional BSE-SEM image of the GBD processed NdFeB magnet illustrating one of a region where EDS spectrums were taken.

The resulting Dy average concentration profile along the magnet depth is plotted in Figure 105.

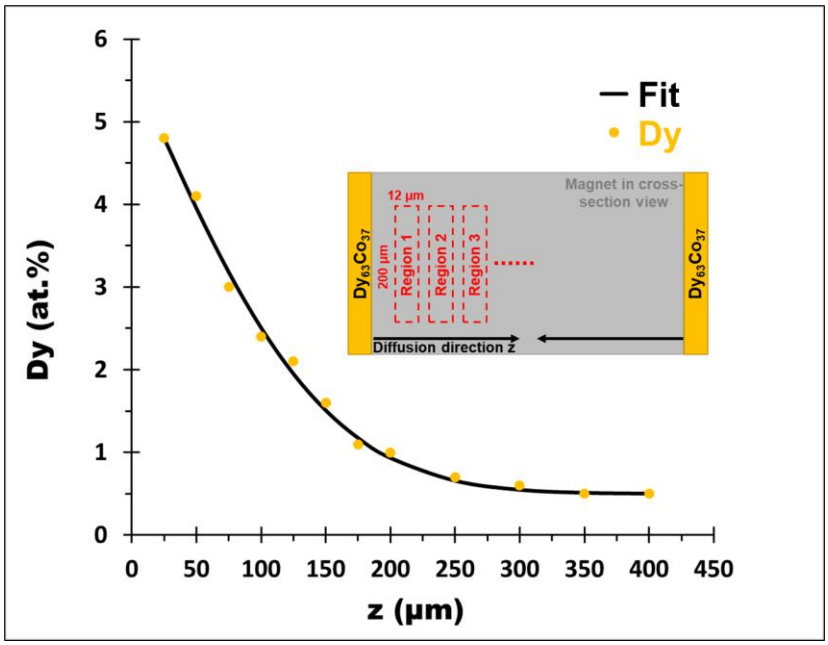

Figure 105: Average Dy concentration profile along the magnet depth. The inset is a schematic representation of the regions from which each EDS spectrum is taken.

The plotted profile shows that the Dy concentration decreases exponentially from 4.8 at. % at 25 µm to 0.4 at. % at depths deeper than 350 µm. This indicates that the total diffusion length of Dy is 350 µm. It should be noted that later on we show that Dy penetrates even deeper inside the magnet.

In order to determine the apparent Dy diffusion coefficient, the plotted Dy average concentration profile is fitted using the Grube solution to Fick's second law[143]:

$$c\,(x,t) = c_{surf} - \left(c_{surf} - c_{bulk}\right)\mathrm{erf}\left(\frac{z}{\sqrt{4Dt}}\right), \tag{4.1}$$

where c_{surf} is the surface concentration, c_{bulk} is the volume concentration, z is the distance from the coated surface, t is the diffusion time and D is the diffusion coefficient.

The fitted solution is represented in the solid black line in Figure 105. Based on the fitted data, the apparent Dy diffusion coefficient at 920°C is found to be $D_{app}^{Dy} = 6.2 \times 10^{-13}$ m²/s.

It is worth noting that the diffusion coefficient determined here, based on the profile of the average Dy concentration into the magnet, is termed an « **apparent diffusion coefficient** ». The Dy diffusion coefficient along the grain boundaries, that might better describe the GBDP, is estimated in the section 4.2.5.1.

4.2.3 Characterization of the phases present at the magnet surface after GBDP (depth z = 0 µm)

This section describes the microstructure at the surface of the magnet in order to examine the evolution of the $Dy_{63}Co_{37}$ deposit.

Figure 106 shows the surface of the NdFeB magnet before and after GBDP.

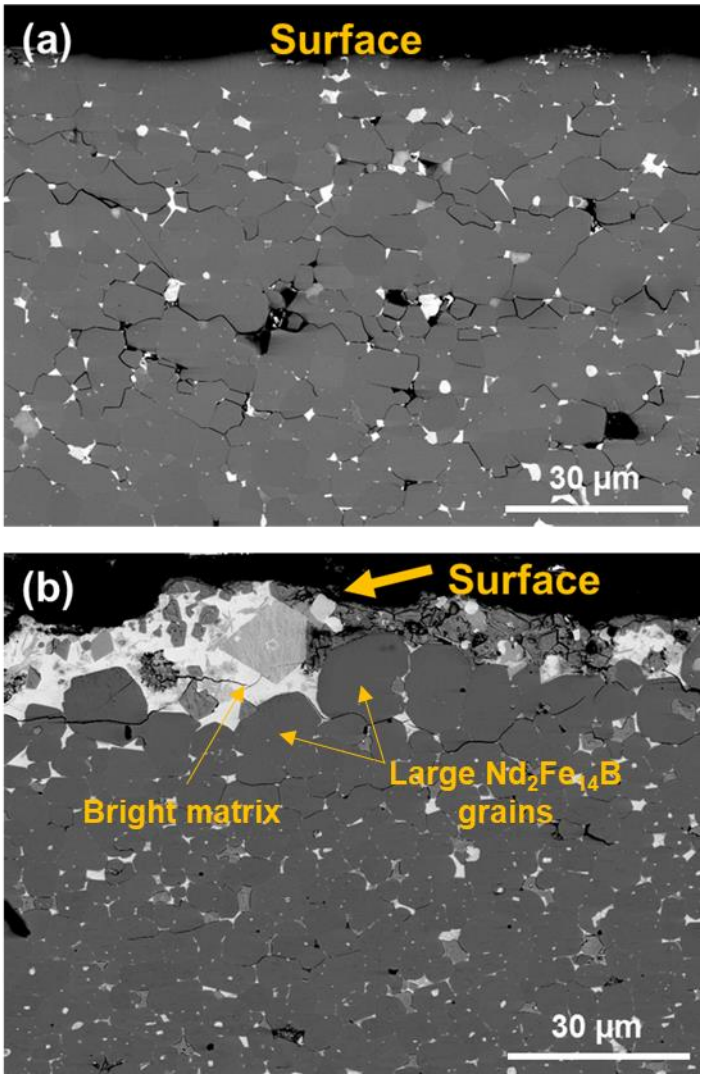

Figure 106: Cross-sectional BSE-SEM images of the surface of the NdFeB magnet: (a) post-sinter annealed PSA state and (b) PDA state.

Figure 106 reveals that different phases are formed at the surface of the magnet. These phases are of different size, shape and contrast and are found to be precipitated inside a bright matrix. The bright matrix and the precipitate form a poly-phase cluster. The bright matrix is assumed to be rich in Dy owing to its bright contrast and the fact that the DyCo was deposited at the surface. $Nd_2Fe_{14}B$ grains were also seen inside this bright matrix. However, their size is found to be considerably larger than the grains in the bulk (almost the double). This also applies to the grains that are right

below the surface. Occasionally, a thick continuous light gray phase is found at the top surface of the magnet as illustrated in Figure 107.

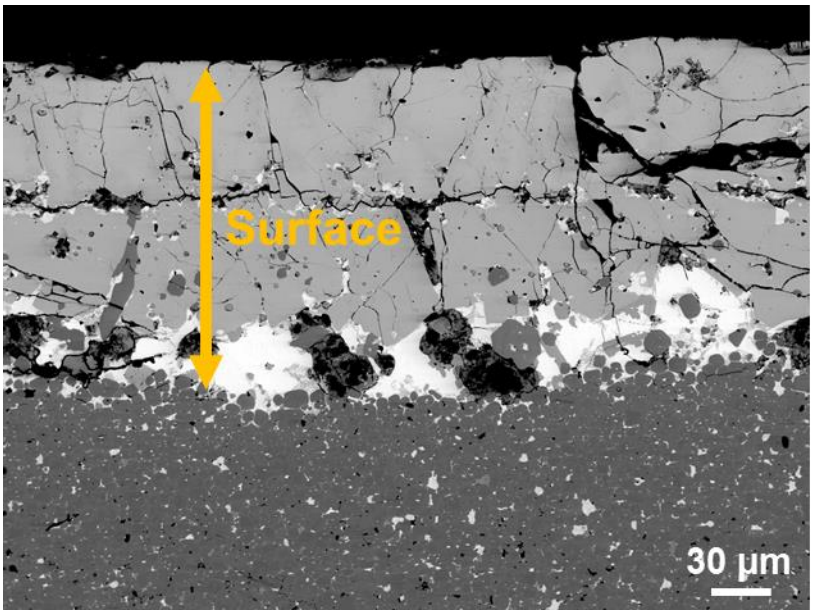

Figure 107: Cross-sectional BSE-SEM image of the GBDP NdFeB magnet showing the formation of a thick continuous layer at the top of its surface.

In what follows, the overall chemical composition of the surface of the magnet (poly-phased cluster) is first quantified. Then, the chemical compositions of the bright matrix and the various phases precipitated inside are determined. The chemical composition of the thick continuous layer seen in Figure 107 is also given.

Overall composition of the poly-phased cluster

Figure 108 shows the region of the surface of the magnet that was analyzed. To quantify its chemical composition, a spectrum was acquired from the red rectangular region as illustrated in the Figure.

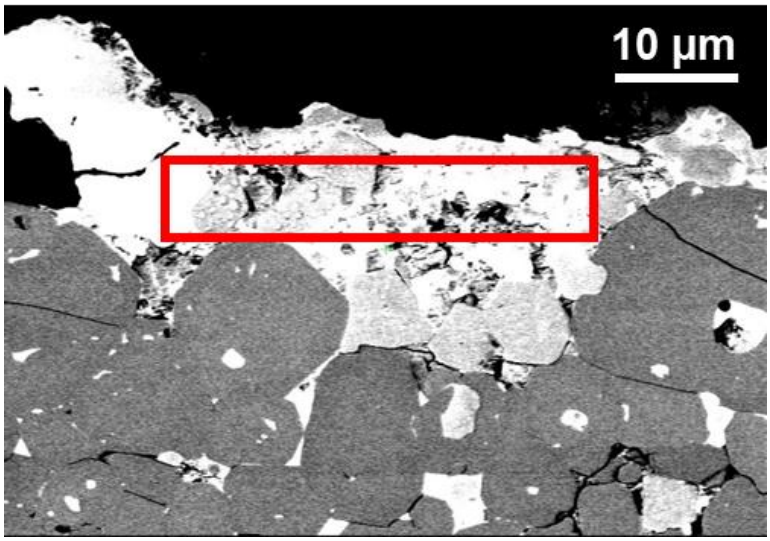

Figure 108: Cross-sectional BSE-SEM image of the surface of the GBD processed magnet. The rectangular region in red represents the part of the surface from which EDS spectrum was taken to evaluate the overall chemical composition of the surface.

The corresponding chemical composition is given in Table 19.

Table 19: Elemental concentration (in at. %) of the surface of the GBD processed NdFeB magnet showing that the amount of total rare earth elements (Nd + Dy) is 35 at.%. For reference, the amount of total REE inside the magnet is 14 at.%.

Concentration (at. %)	**Fe (L)**	**Nd (M)**	**Dy (M)**	**O (K)**	**Co (L)**	**Cu (L)**	**Al (K)**	**Nd + Dy**	$\frac{Dy}{Dy+Nd}$
Surface region of GBP processed magnet	16.8	30.4	4.8	44.5	2.3	0.8	0.4	35.2	13.6

From the table above, the determined chemical composition of the surface of the magnet is $Nd_{30.4}Dy_{4.8}O_{44.5}Fe_{16.8}Co_{2.3}Cu_{0.8}Al_{0.4}$. If we remove the O and we renormalize the element content, the latter becomes $Nd_{54.8}Dy_{8.6}Fe_{30.3}Co_{4.1}Cu_{1.4}Al_{0.7}$ in which (Nd+Dy) = 63% and (Fe + Co) = 33 % which is approximately the chemical composition of the used DyCo source. Contrary to what one could expect, the identified chemical composition shows that the surface of the magnet is mainly rich in Nd and Fe while only minor amounts of Dy and Co are present. This indicates that the source is exhausted and that Dy and Co atoms penetrated inside the magnet and replaced the Nd and Fe atoms respectively. The latter were consequently ejected toward the surface of the magnet. We note that Cu and Al were also detected at the surface of the magnet indicating that similarly to Nd and Fe, these atoms were also ejected toward the surface.

Chemical composition of the bright matrix and the precipitates:

A closer look inside the bright matrix can be seen in Figure 109. Here we can clearly see the variety of the phases precipitated inside. The latter appear to have two different morphologies: nodular and lamellar. The contrast variation between the precipitated phases is related to the variation of their chemical composition.

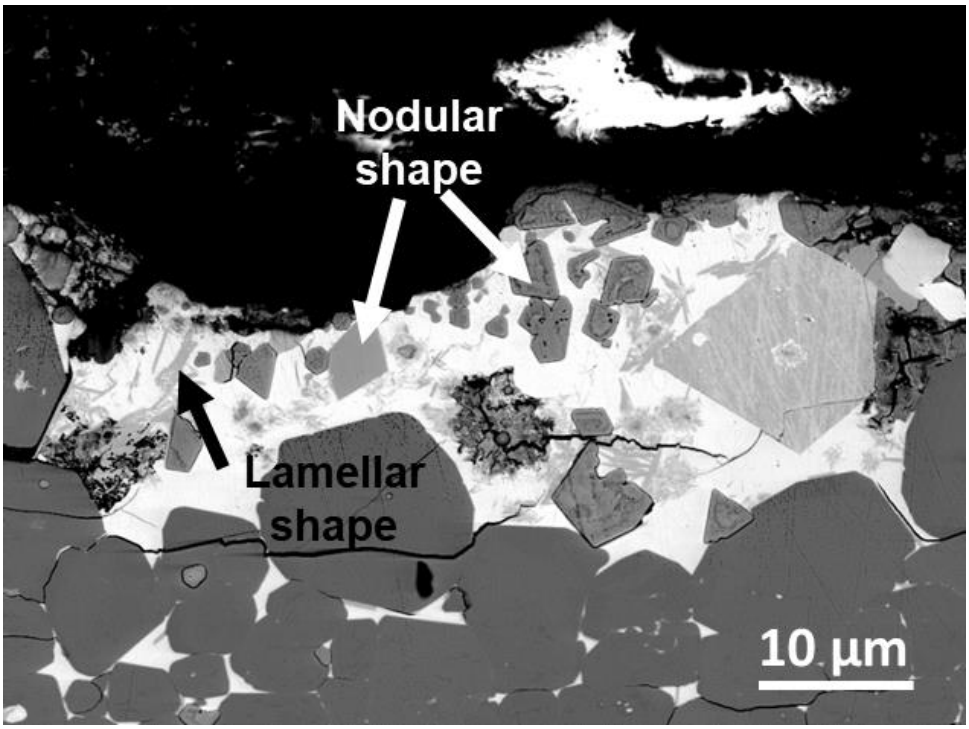

Figure 109: Low contrast cross-sectional BSE-SEM image showing the heterogeneity of the GBD processed magnet surface and the different phases inside.

The chemical compositions of the bright matrix and the above-described phases precipitated inside (see Figure 110) are listed in Table 20.

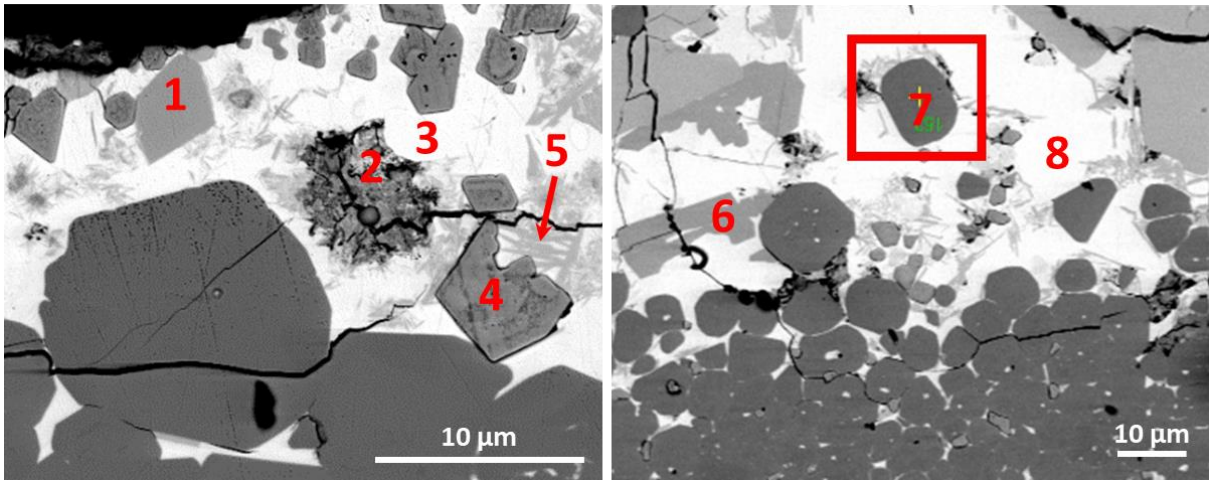

Figure 110: BSE-SEM image of the GBD processed magnet surface showing the phases where EDS point analysis was performed. Bright matrix referred as 3 and 8.

Table 20: Elemental concentration (in at.%) of the phases numbered from 1 to 8 (indicated in Figure 110) as determined by EDS.

at. %	Fe	Nd	Dy	O	Cu	Co	Al	$\frac{Dy}{Dy+Nd}$	$\frac{Fe+Co}{Nd+Dy}$	$\frac{O}{Nd+Dy}$
1	58.7	24.5	1.6	10.0	0.4	2.9	2.0	0.06	2.36	0.38
2	3.0	28.2	0.5	67.6	0.2	0.3	0.2	0.02	0.12	2.35
3	7.6	52.9	1.1	12.4	4.0	21.8	0.1	0.02	0.54	0.23
4	1.6	15.8	17.3	65.3	0.3	0.0	0.0	0.52	0.05	1.99
5	47.1	27.8	2.5	11.3	2.0	4.8	4.4	0.08	1.71	0.37
6	59.3	22.3	2.9	8.6	0.1	3.3	3.5	0.11	2.48	0.34
7	78.1	6.0	6.2	3.8	0.1	5.0	0.9	0.51	6.82	0.31
8	8.5	51.6	0.5	11.8	3.6	23.9	0.1	0.01	0.62	0.23

These phases can be classified in five types listed in Table 21.

Table 21: probable phases associated to the analyzed grains displayed in Figure 110.

Analyzed zone	Morphology	Probable phase
3 and 8 (Bright matrix)	Continuous	IB
2	Nodular	NdO_x with x = 2.35
4	Nodular	$(Nd_1, Dy_1)\ O_2$
1, 5 and 6	Nodular and lamellar	ID
7	Sphere	$(Nd_1, Dy_1)\ Fe_{14}B$

The bright matrix (zones 3 and 8) can be identified as the IB phase characterized before GBDP in chapter III. The composition of these phases is compared in Table 22. We notice that the Dy content of this phase Dy/Dy+Nd < 2% is higher and the Cu content is much lower.

The phases precipitated inside the bright matrix can be identified as follows: Nd-oxide (area 2), (Nd,Dy)-oxide (area 4), ID, (areas 1, 5 and 6) and $(Nd,Dy)_2Fe_{14}B$ (area 7). The chemical compositions of these phases are given in Table 22.

- Nd-oxide is nearly free of Dy (Dy/Dy+Nd = 2%). On the other side, the (Nd,Dy)-oxide contains a significant amount of Dy (Dy/Dy+Nd ≈ 50 %).
- ID phase was found in both nodular and lamellar shape with a similar composition with a higher content of Dy (6-11%) and a lower Cu content compared to before GBDP.

Table 22: Comparison of the chemical composition of the secondary phases before and after GBDP.

Phase	Chemical composition (at. %) (before GBDP)	Chemical composition (at. %) (after GBDP, at the surface of the magnet)
IB	$Nd_{53.9}O_{7.1}Fe_{10.4}Co_{21.0}Cu_{7.4}Dy_{0.0}Al_{0.1}$	$Nd_{52.3}O_{12.1}Fe_{8.1}Co_{22.9}Cu_{3.8}Dy_{0.8}Al_{0.1}$
Oxides	$Nd_{42.4}O_{47.5}Fe_{6.9}Co_{1.7}Cu_{0.9}Dy_{0.4}Al_{0.1}$ (O/RE = 1.1)	$Nd_{28.2}O_{67.6}Fe_{3.0}Co_{0.3}Cu_{0.2}Dy_{0.5}Al_{0.2}$ (O/RE = 2.4)
	$Nd_{34.2}O_{58.3}Fe_{5.2}Co_{1.3}Cu_{0.7}Dy_{0.3}Al_{0.1}$ (O/RE = 1.7)	$Nd_{15.8}O_{65.3}Fe_{1.6}Co_{0.0}Cu_{0.3}Dy_{17.3}Al_{0.0}$ (O/RE = 1.9)
ID	$Nd_{31.0}O_{12.3}Fe_{45.2}Co_{4.8}Cu_{4.1}Dy_{0.0}Al_{2.6}$	$Nd_{24.9}O_{10.0}Fe_{55.0}Co_{3.7}Cu_{0.8}Dy_{2.3}Al_{3.3}$

It is worth to note that $(Nd,Dy)_2Fe_{14}B$ grains were also found inside the bright matrix. Their chemical composition is given by $Nd_{6.0}O_{3.8}Fe_{78.1}Co_{5.0}Cu_{0.1}Dy_{6.2}Al_{0.9}$ and their Dy content is (Dy/Dy+Nd ≈ 50%). We note that their size was found to be 2× larger than the $Nd_2Fe_{14}B$ grains inside the magnet.

Composition of the continuous light gray phase

The chemical composition of this phase seen in Figure 107, is $Nd_{10.4}O_{6.5}Fe_{58.1}Co_{7.1}Cu_{0.3}Dy_{16.6}Al_{0.9}$, which is close to the ID phase but with a lower amount of Al and higher amount of Dy. Interestingly, the Dy content (Dy/(Dy+Nd)) inside this phase is about 60% which is the highest among all the phases formed at the surface of the magnet. The presence of such a high Dy content trapped inside this thick phase negatively impacts the efficient use of Dy since the latter cannot diffuse inside the magnet as intended.

In summary, the surface analysis mainly shows that the Dy deposited on the surface diffused into the magnet and replaced Nd that diffuses back at the surface of the sample. Probably in accordance with the phase diagram of a very Nd-rich magnet, the Nd formed an Nd-rich matrix and other Nd-rich phases with alloying elements (Cu,Al, Fe) containing little Dy. Large grains of the NdDyFeB phase then precipitated in the matrix. On the other hand, there are also a large number of oxides that trap Dy. Therefore, it seems important to avoid the formation of oxides during the process as much as possible in order to better utilize the Dy in the magnet. Finally, we note that occasionally a thick phase can be found at the surface of the magnet. This phase also traps considerable amount of Dy.

4.2.4 Anti-core-shell microstructure (0 µm< z < 25 µm)

This microstructure in this region shows two main features. First, the size of these $Nd_2Fe_{14}B$ grains was found to be in the range of 15-20 µm, i.e., 2-3 times higher than the average size of the $Nd_2Fe_{14}B$ grains inside the magnet (5 µm). Second, an interesting contrast was observed in these grains as we can see in Figure 111. This low magnification BSE-SEM image shows that the core of the grains was brighter than their outer-regions.

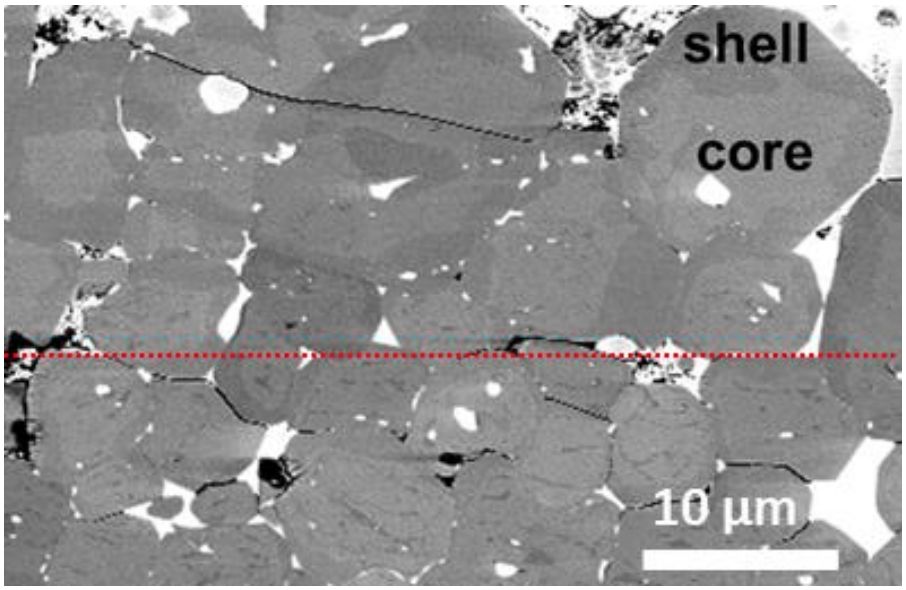

Figure 111: Low magnification BSE-SEM image showing the particularities of the anti-core-shell microstructure (grain coarsening and reversed contrast with respect to the core-shell microstructure).

To understand the origin of the BSE-SEM contrast, Dy and Nd elemental EDS maps of this microstructure were acquired. As displayed in Figure 112, the Dy elemental map shows that the core of the $Nd_2Fe_{14}B$ grains is richer in Dy than its outer region. This is consistent with the bright contrast of the core seen in the BSE-SEM image. On the other side, Nd elemental map shows that the outer region of the $Nd_2Fe_{14}B$ grains is richer in Nd than the core which suggests that Dy probably substituted Nd in the core.

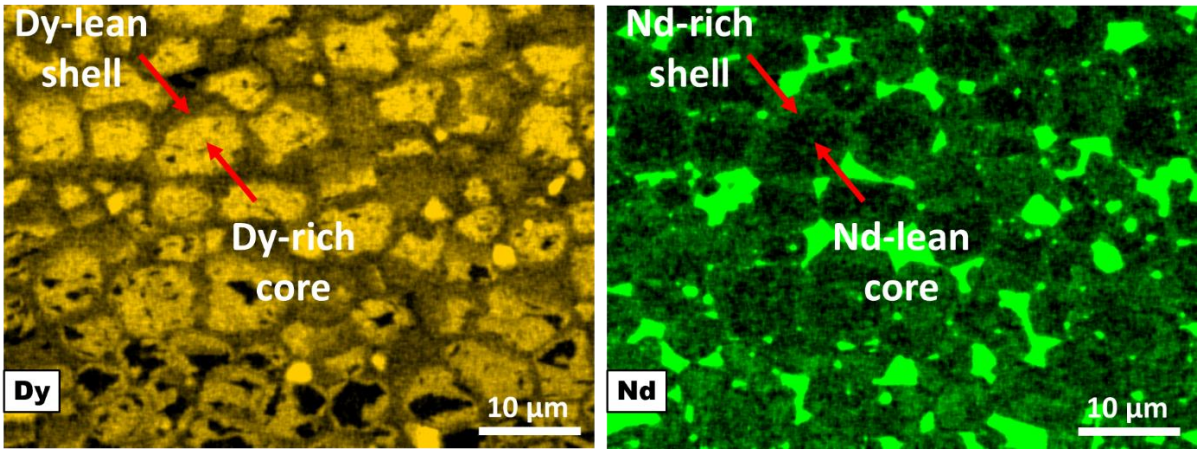

Figure 112: High magnification EDS-SEM map of Dy elemental distribution showing the anti-core-shell microstructure.

This microstructure seen just below the magnet surface is the exact opposite of the usual core-shell microstructure associated to the GBDP explained in chapter I. For that, it is called the «anti-core-shell» microstructure. It was reported for the first time by W. Li et al in 2019[144].

To identify the chemical composition of the core and the shell in this region, 3 EDS point spectra were acquired in each of them. These spectra are acquired under the same condition as the EDS spectra of the standards (i.e., an accelerating voltage of 5 kV, a current of 1.5 nA, a working distance

of 10 mm and a pulse processing time constant of 60 kcps). However, and as seen in chapter III, the overlap of the Dy (Mα) and Co (Lα) with the Nd (M_2N_4) and Fe (Lα) respectively is not properly deconvoluted during EDS quantitative analyses. In order to overcome this issue, the chemical composition of both the Dy-rich core and the Dy-lean shell was further investigated by means of wavelength dispersive X-ray spectroscopy (WDS). The WDS measurements were acquired at an accelerating voltage of 10kV, using an aperture of 120 µm (see chapter II). The comparison between the EDS and the WSD results is shown in Table 23.

Table 23: Comparison of the chemical composition of the Dy-rich core and Dy-lean shell located at a depth z = 20 µm determined using EDS and WDS. For reference, the chemical composition of the $Nd_2Fe_{14}B$ as determined by WDS in prior to the GBDP is given by $Fe_{80.4}Nd_{10.8}Dy_{0.3}Co_{0.3}Al_{0.8}O_{1.5}B_{6.0}$.

	Technique	Chemical composition	$\frac{Dy}{Dy+Nd}$	$\frac{Fe+Co}{Nd+Dy}$	$\frac{Co}{Fe+Co}$
Dy-rich core	WDS	$Fe_{79.7}Nd_{4.7}Dy_{6.4}Co_{1.5}Al_{0.6}O_{1.9}B_{5.2}$	0.58	7.3	0.02
	EDS	$Fe_{77.6}Nd_{4.6}Dy_{7.4}Co_{5.2}Cu_{0.1}Al_{0.6}O_{4.5}$	0.62	6.9	0.06
Dy-lean shell	WDS	$Fe_{79.4}Nd_{8.9}Dy_{2.7}Co_{1.0}Al_{0.8}O_{1.9}B_{5.4}$	0.23	6.9	0.01
	EDS	$Fe_{78.6}Nd_{7.4}Dy_{5.2}Co_{3.5}Cu_{0.1}Al_{0.7}O_{4.5}$	0.41	6.5	0.04
$Nd_2Fe_{14}B$ (prior GBDP)	WDS	$Fe_{80.4}Nd_{10.8}Dy_{0.3}Co_{0.3}Al_{0.8}O_{1.5}B_{6.0}$	0.03	7.3	<0.01
	EDS	$Fe_{81.2}Nd_{12.9}Al_{0.7}O_{5.1}$	0.00	6.3	0.00

The major difference between EDS and WDS techniques is mainly visible in the determination of the Co content of the Dy-rich core and the Dy-lean shell. In fact, the Co content is found to be systematically and considerably higher when identified using the EDS technique. As a result, the Co substitution rates inside the Dy-rich core and the Dy-lean shell are respectively 3× and 4× higher than what is identified by WDS. A possible way to overcome this problem is to acquire EDS spectra at higher voltage (minimum 10 kV) to excite the Co (Kα) peak of energy 6.93 keV. However, it is necessary to keep in mind that there is an overlap between this peak and the Fe (Kβ) peak which might also complicate a correct determination of the Co content. This was not investigated in the framework of this study.

Referring to the chemical composition of the 2:14:1 phase before the GBDP (see Table 23), it is clear that both Dy-rich core and Dy-lean shell contain higher amount of Dy and Co and lesser amount of Nd and Fe. This confirms that Dy and Co penetrate the 2:14:1 grain and substitute a part of the Nd and Fe respectively. The Dy-rich core contains more Dy and Co than the Dy-lean shell, which goes along with the fact that the Dy-rich core displays a brighter contrast than the Dy-lean shell as seen in Figure 111. The (Fe+Co)/(Nd+Dy) ratio in the case of WDS is in excellent agreement with the stoichiometry of the 2:14:1 phase.

In summary, the WDS and EDS analyses of the anti-core-shell microstructure revealed a core in which 60% of the Nd is replaced by Dy and a shell in which 25% (measured by WDS and 40% by EDS) of the Nd is replaced by Dy. Regarding the Co, WDS showed that in the core 2% (vs 6% by EDS) of the Fe is replaced by Co while in the shell 1% (vs 4% by EDS) of the Fe is replaced by Co. The difference between WDS and EDS is related to the overlapping between Fe La and Co La peaks and shows that the unsuitability of EDS, under the used experimental conditions, to determine the concentration of Co in our samples. It should also be kept in mind that in this zone there

has been an increase in grain size. However, in what follows, we will be mainly relying on the EDS results since the WDS detector was not accessible (the equipment was purchased in my last year of PhD, and I had a limited access).

4.2.5 Core-shell microstructure (25 µm < z < 500 µm)

In this section, the core-shell microstructure is analyzed at different depths from the magnetic surface. In the first part, we study the Dy-rich shell, and we try to quantify the evolution with the depth of different parameters such as, the shell thickness or the surface fraction of the shell, the grain size, and the shell composition. In the second part, we analyzed the evolution after the GBDP of the secondary phases that are the Nd-rich phases and Nd-oxides in terms of surface fraction and composition. In the final part, we perform crystallographic investigations by means of EBSD and TEM in the aim to understand the asymmetric behavior of the Dy-rich shell.

4.2.5.1 Dy-rich shell

Figure 113 shows several Dy elemental maps taken at various depth of the GBDP NdFeB magnet.

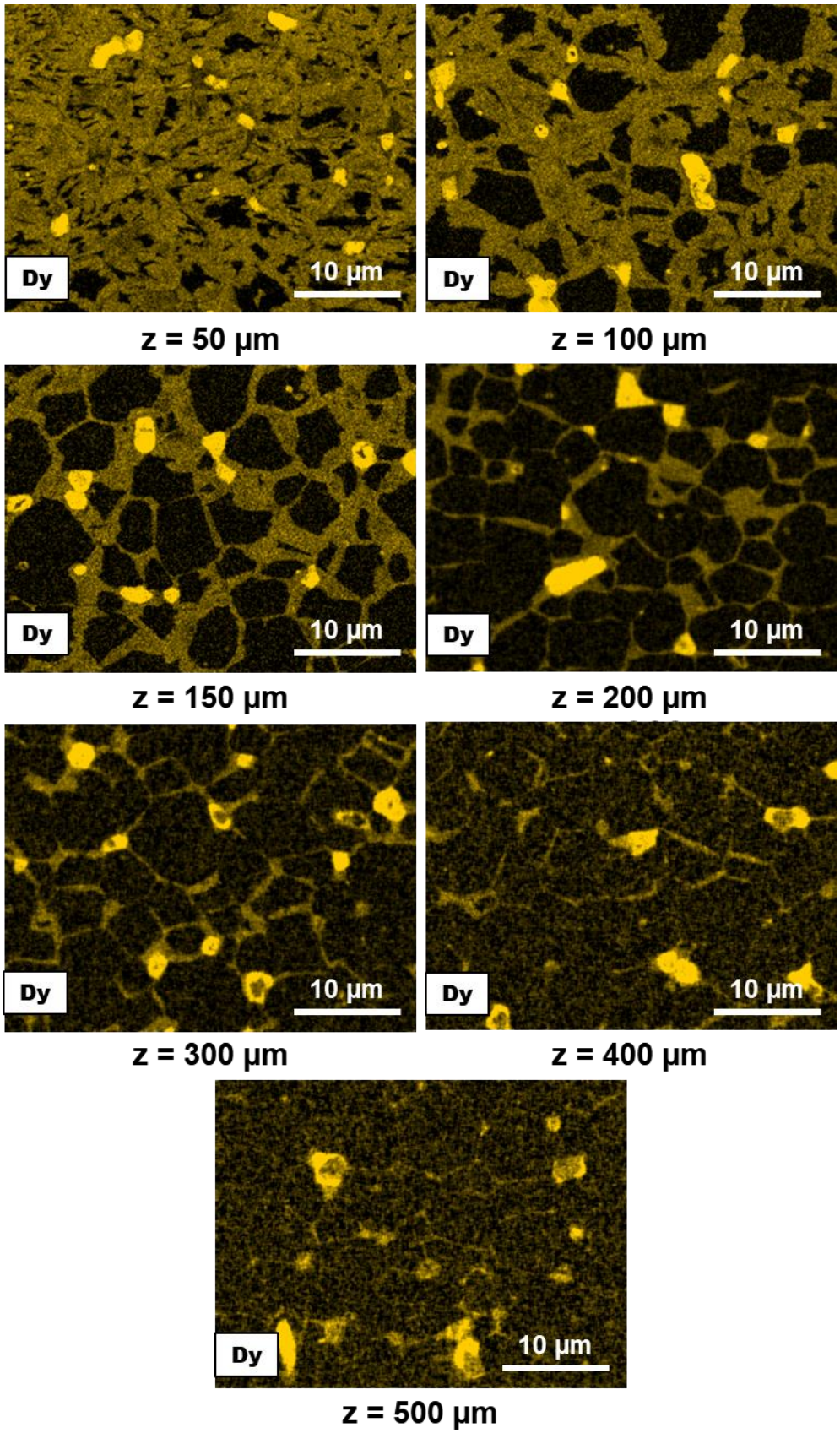

Figure 113: High magnification EDS-SEM map of Dy elemental distribution recorded at different magnet depth, showing the variation the Dy-rich shell thickness with respect to the magnet depth.

The Dy map taken at z = 50 µm shows that the Dy almost completely penetrates the 5 µm averaged $Nd_2Fe_{14}B$ grains, and no clear core-shell microstructure is visible. At z = 100 µm, the core-shell microstructure is well defined. The shell thickness is about 1-2 µm (it should be noted that this is a rough estimation since the shell thickness varies from one grain to another and within the grain itself, this will be detailed later). The shell thickness continues to decrease as moving far from the magnets surface. At z = 500 µm, the Dy-rich shell thickness ranges between hundred and tens of nanometers and is barely visible with the limited SEM resolution. Hence, the Dy EDS maps clearly show that the Dy-rich shell thickness decreases with increasing depth.

It is interesting to plot the variation of the shell thickness as a function of the magnet depth. However, since the shell thickness varies considerably between one grain and another, and since the grain boundaries are not clearly seen in the images, we first use the Dy maps to determine the evolution of the surface fraction of the Dy-rich shell as a function of magnet depth (see Figure 114 (a)), and then we calculate the corresponding shell thickness (see Figure 114 (b)). The details of this calculation are given in Appendix 1.

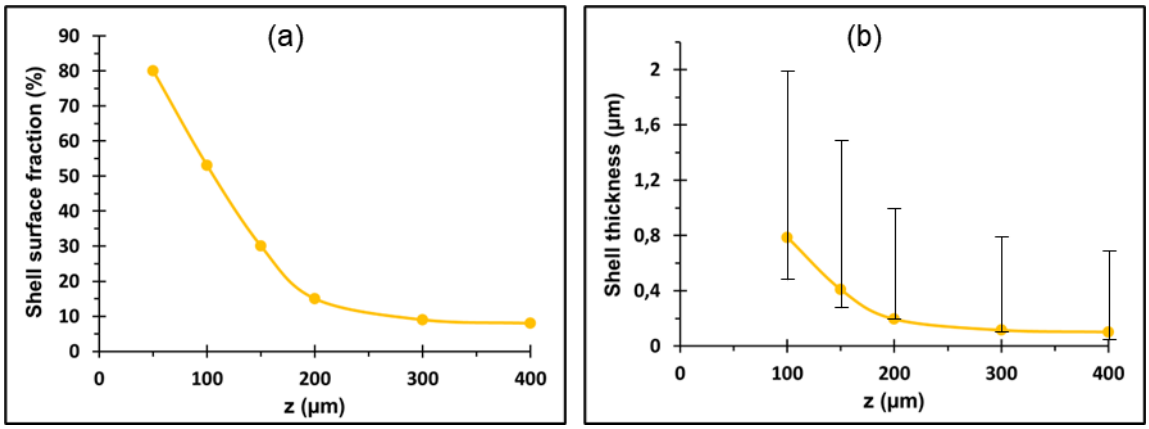

Figure 114: Variation of (a) the shell area and (b) the shell thickness with respect to the magnet depth. The shell thickness was calculated by considering a radius (r) of the 2:14:1 grain of 2.5 µm and by using the relation $r(1-\sqrt{1-f})$, where f denotes the surface fraction of the shell.

The calculation of the shell thickness based on the surface fraction give an estimated value of the shell thickness at each depth. These estimated values should be taken by precocious since they do not fully account for the experimental observations. BSE-SEM images and Dy EDS maps show that, at each depth, the shell thickness varies considerably from one grain to another. To account for this variation, the upper and lower limits of the shell thickness observed experimentally on the EDS maps and BSE-SEM images are added to the estimated values at each depth in Figure 114(b).

Hereafter, we wanted to see if there is a variation in the $Nd_2Fe_{14}B$ grain size post GBDP as reported in other studies[87]. For that, ImageJ software was used to measure the size of the $Nd_2Fe_{14}B$ grains at depths ranging from z=50 µm to z=300 µm. At each depth, the lengths of 100 $Nd_2Fe_{14}B$ grains were measured to calculate the average grain size. The average grain size was found to be constant between z=50 µm to z=300 µm with a value of is 5.1 µm. This value is bigger than the average grain size determined before GBDP (4.3 µm).

Afterwards, we proceeded to determine the chemical composition of the Dy-rich shell as well as its variation with respect to the magnet depth. For that, we acquired 10 EDS point spectra from the Dy-rich shells located between 50 μm and 450 μm. These spectra were quantified using the IZAC code and the standards database for peak reference. The average chemical composition is given in Table 24.

Table 24: Average chemical composition of the Dy-rich shells determined as a function of the magnet depth by analyzing 10 EDS spectra/depth. The chemical composition of the core is determined by EDS to be $Fe_{78.3}Nd_{12.3}Dy_{0.1}Co_{3.4}Al_{0.8}O_{5.1}$ (at. %). For reference, the chemical composition of the $Nd_2Fe_{14}B$ phase prior to the GBDP as determined by WDS is given by $Fe_{80.4}Nd_{10.8}Dy_{0.3}Co_{0.3}Al_{0.8}O_{1.5}B_{6.0}$ (at. %).

Depth	Average chemical composition of the Dy-rich shell (at. %)	$\frac{Fe+Co}{Dy+Nd}$	Dy + Nd (at. %)	$\frac{Co}{Fe+Co}$	$\frac{Dy}{Dy+Nd}$
50 μm	$Fe_{79.5}Nd_{5.9}Dy_{6.1}Co_{3.7}Cu_{0.3}Al_{0.7}O_{3.9}$	6.9	12.0 at. %	4%	51%
100 μm	$Fe_{80.1}Nd_{8.6}Dy_{3.8}Co_{3.0}Cu_{0.3}Al_{0.7}O_{3.6}$	6.7	12.4 at. %	4%	31%
150 μm	$Fe_{80.1}Nd_{9.3}Dy_{3.2}Co_{2.7}Cu_{0.3}Al_{0.8}O_{3.6}$	6.6	12.5 at. %	3%	26%
200 μm	$Fe_{80.2}Nd_{9.5}Dy_{2.9}Co_{2.8}Cu_{0.3}Al_{0.7}O_{3.7}$	6.7	12.4 at. %	3%	23%
250 μm	$Fe_{80.4}Nd_{9.6}Dy_{2.9}Co_{2.6}Cu_{0.2}Al_{0.7}O_{3.6}$	6.6	12.5 at. %	3%	23%
300 μm	$Fe_{80.4}Nd_{9.4}Dy_{3.0}Co_{2.6}Cu_{0.2}Al_{0.7}O_{3.6}$	6.7	12.4 at. %	3%	24%
350 μm	$Fe_{80.1}Nd_{9.5}Dy_{2.9}Co_{2.5}Cu_{0.3}Al_{0.8}O_{4.0}$	6.6	12.4 at. %	3%	23%
400 μm	$Fe_{80.1}Nd_{10.0}Dy_{2.4}Co_{2.4}Cu_{0.3}Al_{0.8}O_{4.0}$	6.7	12.4 at. %	3%	19%
450 μm	$Fe_{80.1}Nd_{10.1}Dy_{2.5}Co_{2.3}Cu_{0.3}Al_{0.8}O_{4.0}$	6.5	12.6 at. %	3%	20%

Compared to the chemical composition of the $Nd_2Fe_{14}B$ phase prior the GBDP, it is clear that the Dy-rich shells contain higher amount of Dy and Co and lesser amount of Nd and Fe. When the depth from the magnet surface increases, the amount of Dy and Co inside the Dy-rich shells decreases. Simultaneously, the amount of Nd and Fe inside the Dy-rich shells increases. The (Fe+Co)/(Nd+Dy) ratio in the analyzed Dy-rich shells ranges between 6.5 and 6.9 which is in good agreement with the stoichiometry of the 2:14:1 phase.

Hereafter, and as explained in chap 2, WDS measurements have been performed in order to estimate the accuracy of EDS measurements. The WDS measurements were acquired under an accelerating voltage of 10kV and an aperture of 120 μm to maximize the current. Since the WDS measurements are time consuming (on average, each WDS spectra took 30 min), we limited the analysis to 3 shells per depth. Also, and due to the lower spatial resolution (the acceleration voltage is 10 keV, for which the resolution is 300 nm as seen in chapter II), we limited the analysis to regions with thick Dy-rich shells. For this, 3 WDS measurements were taken from shells located at 100 μm and 150 μm (where the shell thickness ranges between 1-2 μm). The corresponding results are displayed in Table 25.

Table 25: Comparison of the chemical composition of the core and the Dy-rich shells of the $Nd_2Fe_{14}B$ grains located at a depth of z = 100 µm, z = 150 µm and z = 2mm determined by using EDS and WDS techniques. For reference, the chemical composition of the $Nd_2Fe_{14}B$ phase prior to the GBDP as determined by WDS is given by $Fe_{80.4}Nd_{10.8}Dy_{0.3}Co_{0.3}Al_{0.8}O_{1.5}B_{6.0}$.

Depth		EDS	WDS
100 µm	Dy-rich shell	$Fe_{80.1}Nd_{8.6}Dy_{3.8}Co_{3.0}Cu_{0.3}Al_{0.7}O_{3.6}$	$Fe_{78.1}Nd_{8.2}Dy_{4.0}Co_{1.3}Al_{0.7}O_{2.8}B_{5.7}$
	Core	$Fe_{78.3}Nd_{12.3}Dy_{0.1}Co_{3.4}Cu_{0.0}Al_{0.8}O_{5.1}$	$Fe_{78.5}Nd_{11.0}Dy_{0.4}Co_{1.2}Al_{0.8}O_{2.4}B_{5.8}$
150 µm	Dy-rich shell	$Fe_{80.1}Nd_{9.3}Dy_{3.2}Co_{2.7}Cu_{0.3}Al_{0.8}O_{3.6}$	$Fe_{80.3}Nd_{8.0}Dy_{3.2}Co_{0.4}Al_{0.7}O_{1.8}B_{5.7}$
	Core	$Fe_{78.3}Nd_{12.3}Dy_{0.1}Co_{3.4}Cu_{0.0}Al_{0.8}O_{5.1}$	$Fe_{79.6}Nd_{11.1}Dy_{0.3}Co_{0.7}Al_{0.7}O_{2.1}B_{5.5}$
Volume (2 mm)	Dy-rich shell	No Dy-rich shells detected at this depth	No Dy-rich shells detected at this depth
	Core	-	$Fe_{80.0}Nd_{11.0}Dy_{0.3}Co_{0.6}Al_{0.6}O_{1.6}B_{5.8}$

When comparing the EDS and WDS results, we notice that the Dy amount found in the Dy-rich shells is quite similar. However, the amount of Co is systematically overestimated using EDS. This is like what we observed in the anti-core-shell region. Similarly to EDS, WDS shows that the amount of Dy and Co in the Dy-rich shells decrease with increasing magnet depth. Although the amount of Co measured in the Dy-rich shell at z=100 µm is 1.3 at.%, it quickly drops to 0.4 at.% at z=150 µm. This value is similar to the concentration of Co inside the 2:14:1 phase prior the GBDP (0.3 at.%). Therefore, there is no significant enrichment of Co inside the Dy-rich shells. WDS measurements confirm that there is no Dy inside the core (at z=100 µm, the Dy inside the core is 0.4 at.% vs 0.3 at.% before the GBDP). However, WDS shows the presence of Co inside the core at z=100 µm (with a lesser amount than what the EDS suggests). At z=2mm, the amount of Co inside the 2:14:1 phase is found to be 0.6 at.% vs 0.3 at.% before the GBDP. However, we don't have enough statistics to evaluate the relevance of the determined value. From the above chemical compositions, we can calculate the Dy and Co substitution rates which we report in Table 26.

Table 26: Comparison of the Dy and Co substitution rates as determined by EDS and WDS at a depth of z=100 µm and z=150 µm. For reference, the Co/(Fe+Co) and Dy/(Dy+Nd) ratios in the 2:14:1 phase before GBDP are <1% and 3% respectively.

Depth		$\frac{Co}{Fe+Co}$		$\frac{Dy}{Nd+Dy}$	
		EDS	WDS	EDS	WDS
100 µm	Dy-rich shell	4%	2%	31%	33%
	Core	4%	2%	0%	4%
150 µm	Dy-rich shell	3%	0%	26%	29%
	Core	4%	0%	0%	3%

The Dy substitution rates calculated from EDS and WDS results are quite similar. This is expected since we measure a similar amount of Dy with both techniques. The Dy/(Nd+Dy) ratio inside the core is 3-4% which is similar to what we had before the GBDP (i.e., Dy does not penetrate the

core of the 2:14:1 phase). In the shell at z = 100 and 150 µm, this ratio is respectively 33% and 29%. On the other side, the Co substitution rates are considerably over-estimated by EDS and cannot be used for interpretation. The WDS is more accurate to measure the Co. Based on the WDS results at z=100 µm, the Co penetrates both the core and the shell. It is important to emphasize the different behavior between Co and Dy as Dy doesn't penetrate the core and is only confined in the shell. However, we do not measure considerable presence of Co inside the core and the shell at z=150 µm. In conclusion, the EDS spectra acquired at 5 kV and quantified using IZAC code and the standards database are reliable as per the amount of Dy present in the analyzed zones. However, we cannot rely on the amount of Co determined from the EDS spectra taken at 5 kV to draw conclusions regarding the diffusion of Co inside the NdFeB magnet.

Hereafter, we can evaluate the Dy substitution rate in the Dy-rich shells with respect to the magnets depth. For that, we calculate the ratio Dy/(Dy+Nd). The results are displayed in Figure 115. On one side, we can see that the total amount of the Nd and Dy remains constant ≈ 12.4 at. % at different depth which confirm that the Dy substitutes the Nd in the Dy-rich shells. On the other side, the Dy substitution rate decreases rapidly from 50 % at z = 50 µm to 23 % at z = 200 and appear to remain constant until z = 350 µm. Beyond this depth, the Dy substitution rate decreases slowly and reaches a level of 20 % at z = 450 µm.

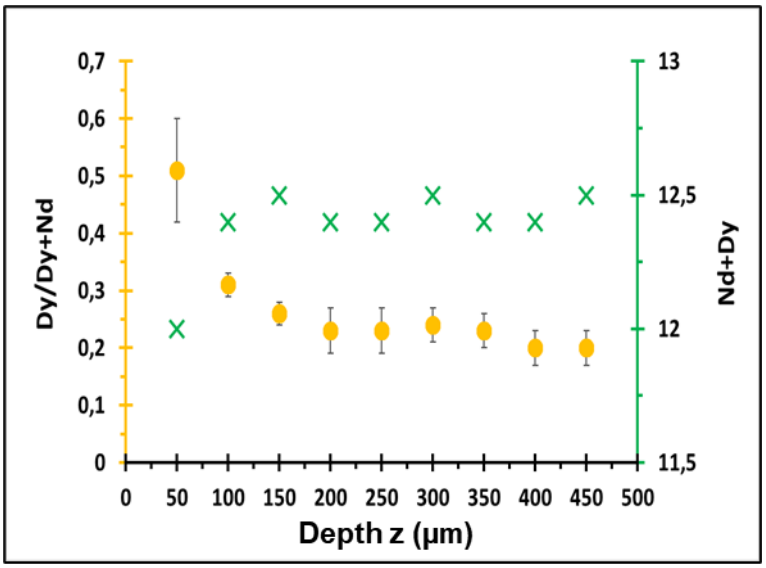

Figure 115: Variation of the Dy substitution rate (Dy/(Dy+Nd)) and the total amount of REE (Nd + Dy) within the Dy-rich shell with respect to the magnets depth. Each data point corresponds to the average of 10 EDS measurement in 10 Dy-rich shell.

In addition, we can study the local Dy gradient along the shell thickness. For that, we have acquired an EDS concentration profiles across a Dy-rich shell located at z=60 µm as indicated by the white arrow in Figure 116 (a). Figure 116 (b) shows the corresponding Nd and Dy EDS (linear) concentration profiles. Interestingly, the Dy concentration profile across the shell displays a plateau and an abrupt interface when transitioning from the core to the shell. This profile does not correspond to a classical diffusion profile which should be exponentially decreasing as seen in Figure 105. We note that the Nd and Dy concentration profiles display opposite behaviors. The measured Nd and Dy content in the core are 12.4 at. % and 0 at.% respectively. Moving forward to the shell, the Nd decreases abruptly to 7.6 at.% while the Dy increases abruptly to 4.4 at.%.

However, the total amount of Nd and Dy remains constant at 12.4 at.% which is consistent with the $(Nd,Dy)_2Fe_{14}B$ phase. This is consistent with the fact that the Dy substitutes the Nd in the Dy-rich shell.

Similar analyses performed by TEM is also shown in the following section 1.2.5.3

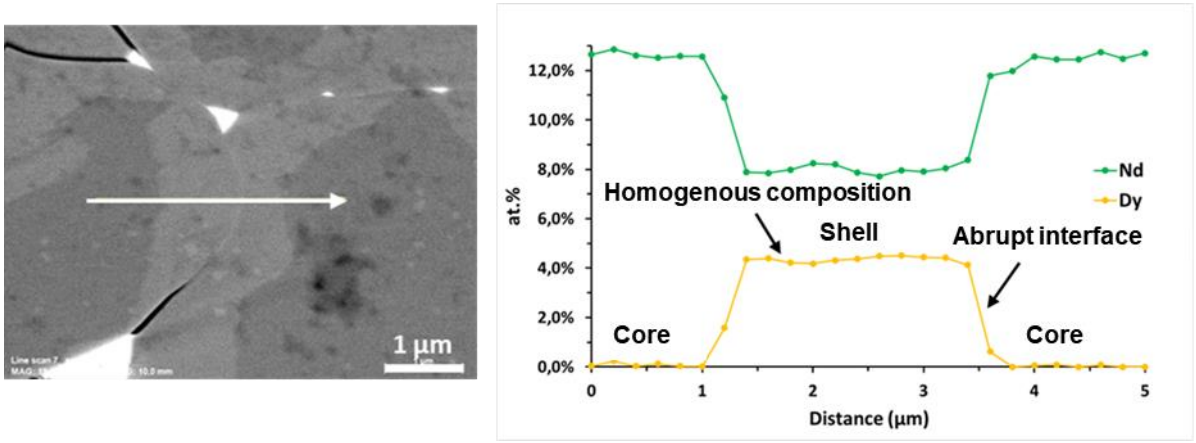

Figure 116: Variation of the Nd and Dy concentration profiles across a core-shell microstructure at z = 60 µm.

Moreover, we can study the Dy diffusion coefficient by plotting the variation of the Dy shell concentration as a function of the magnet depth. This is displayed in Figure 117.

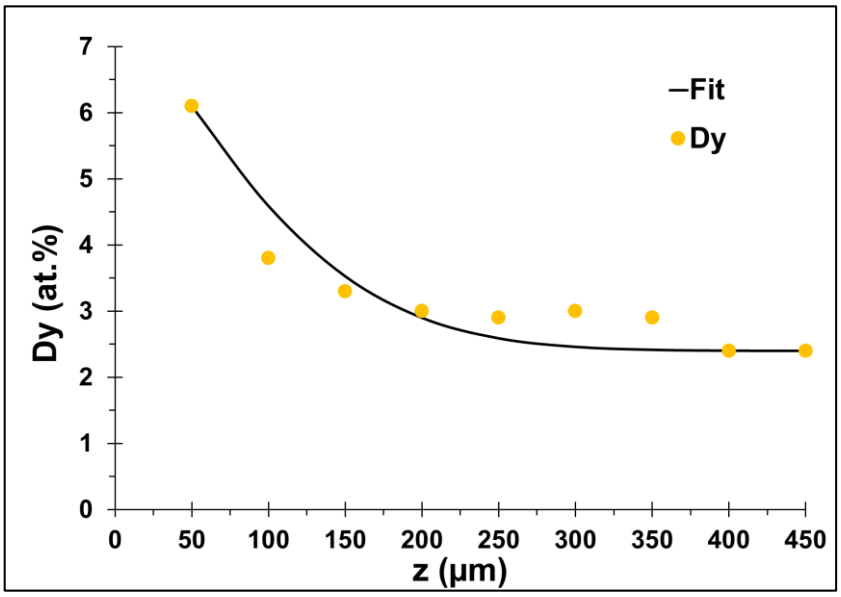

Figure 117: Variation of the Dy shell concentration profile as a function of the magnet depth. Each Dy data point is the average of 10 EDS spectra taken inside 10 different Dy-rich shells. The black solid line is the Grube solution to Fick's second law used to fit the experimental data.

Similarly to the average concentration profile plotted in Figure 104, the above plotted profile shows that the Dy shell concentration decreases exponentially from 6.1 at. % at 50 µm to 2.5 at. % at 450 µm. The Dy diffusion coefficient in the shell (D_{GB}^{Dy}), calculated by fitting the plotted Dy shell concentration profile using the Grube model, is found to be $D_{GB}^{Dy} = 6.5 \times 10^{-13}$ m²/s. This GB

diffusion coefficient is the same as the « **apparent diffusion coefficient** » determined in 4.2.2 ($D_{app}^{Dy} = 6.2 \times 10^{-13}$ m²/s). This similarity will be discussed later.

4.2.5.2 Secondary phases

After examining the Dy content in the shell, in this part we are interested in the Dy content in the secondary phases. In fact, Dy present in these phases does not contribute to the improvement of the magnetic properties, consequently, these phases could consume the Dy in an unnecessary way.

As reported in chapter III, two types of secondary phases are identified in the NdFeB sintered magnets: metallic Nd-rich phases (IA, IB, IC, and ID) and Nd-oxides (IIA and IIB). At the GBDP temperature, metallic Nd-rich phases containing Cu are in liquid state hence contributing to the diffusion channels for Dy atoms. However, Nd-oxides remain in the solid state thus acting as obstacles for Dy diffusion. In the following, we start by determining the surface fraction of the different secondary phases, their Dy content and its variation with respect to the magnet depth.

Similarly to the case of Dy-rich shell, the surface fraction of the secondary phases was determined by image processing using ImageJ software. The results are displayed in Table 27.

Table 27: Variation of the surface fraction of Nd-rich phases and Nd-oxides with respect to the magnet depth.

Depth / Phase	100 µm	200 µm	300 µm	2000 µm
Nd-rich phase	3%	4%	3%	3%
Nd-oxides	5%	4%	3%	3%

At z=50 µm, the surface fraction of the Nd-rich phases varies from 6 to 13%, depending on the analyzed images. Beyond this depth, the surface fraction of the Nd-rich phase and Nd-oxides does not appear to vary along the magnet depth. In fact, we can see that the surface fraction of these phases remained the same as prior to the GBDP (the surface fraction of the Nd-rich phases was found to be between 6-8%).

Table 28 shows the chemical composition (in at. %) of the different secondary phases found at a depth of z = 100 µm. The chemical composition was evaluated by quantifying 5 EDS spectra taken for each type of the secondary phases.

Table 28: Elemental composition (at. %) of secondary phases located at a depth of z = 100 µm, Dy substitution rate (Dy/(Dy+Nd)), (Fe+Co/(Dy+Nd)) and (O/(Dy+Nd)) within these phases determined using EDS.

Phase	Type	Chemical composition (at. %) (Determined using standards and IZAC code)	$\frac{Dy}{Dy+Nd}$	$\frac{Fe+Co}{Nd+Dy}$	$\frac{O}{Nd+Dy}$
Nd-rich	IA	$Nd_{72.1}O_{6.3}Fe_{14.9}Co_{4.1}Cu_{1.9}Dy_{0.5}Al_{0.2}$	0.01	0.26	0.09
NdCoCu	IB	$Nd_{51.9}O_{7.9}Fe_{12.7}Co_{20.0}Cu_{6.7}Dy_{0.6}Al_{0.1}$	0.01	0.62	0.15
NdFeAl	ID	$Nd_{26.7}O_{6.3}Fe_{52.7}Co_{4.5}Cu_{3.5}Dy_{1.5}Al_{4.8}$	0.05	2.03	0.22
NdO_2	IIA'	$Nd_{24.3}O_{64.5}Fe_{3.7}Co_{0.3}Cu_{0.7}Dy_{6.4}$	0.21	0.13	2
Nd_2O_3	IIB	$Nd_{27.4}O_{57.2}Fe_{4.6}Co_{0.7}Cu_{0.8}Dy_{9.4}$	0.26	0.14	1.55

The first thing to notice when analyzing the Nd-rich phases is the absence of the Nd-rich phase type IC. The latter was identified in chapter III as one of the four types of the metallic Nd-rich phases located at the triple/multiple junctions in the as-sintered NdFeB magnet with the highest Cu content. Another observation is the absence of the IIA oxide (NdO) and appearance of the IIA' (NdO_2). The remaining Nd-rich phases are found to be similar to the ones identified in chapter III with a nuance that is the presence of Dy as a result of the GBDP. To compare the amount of Dy present in each of the secondary phases, we calculate the ratio Dy/(Dy + Nd). Interestingly, the results indicate that metallic Nd-rich phases have very little amount of Dy (≤1%) while there is a lot more in the Nd-oxides (≈ 20-25%). However, we note that within the metallic Nd-rich phases, the ID phase seems to have 5x higher Dy content than the other metallic phases. Since only trace amount of Dy were found in the metallic Nd-rich phases, this shows that they act as excellent diffusion paths for Dy. On the contrary, the high amount of Dy found in Nd-oxides attests that the latter tend to trap Dy which result in impeding the Dy diffusion within the NdFeB magnet and reducing the diffusion length. This also result in wasting the Dy resource since Dy-enriched Nd-oxides do not contribute to improve the coercivity of the magnet. It is worth to note that the surface fraction of Nd-oxides remained the same prior to the GBDP. This means that the Dy introduced in the magnet probably interacted with the already existing oxides and did not form new oxides in the microstructure.

Figure 118 shows the variation of the ratio Dy/(Dy+Nd) with respect to the magnet's depth in the metallic Nd-rich phases and Nd-oxides.

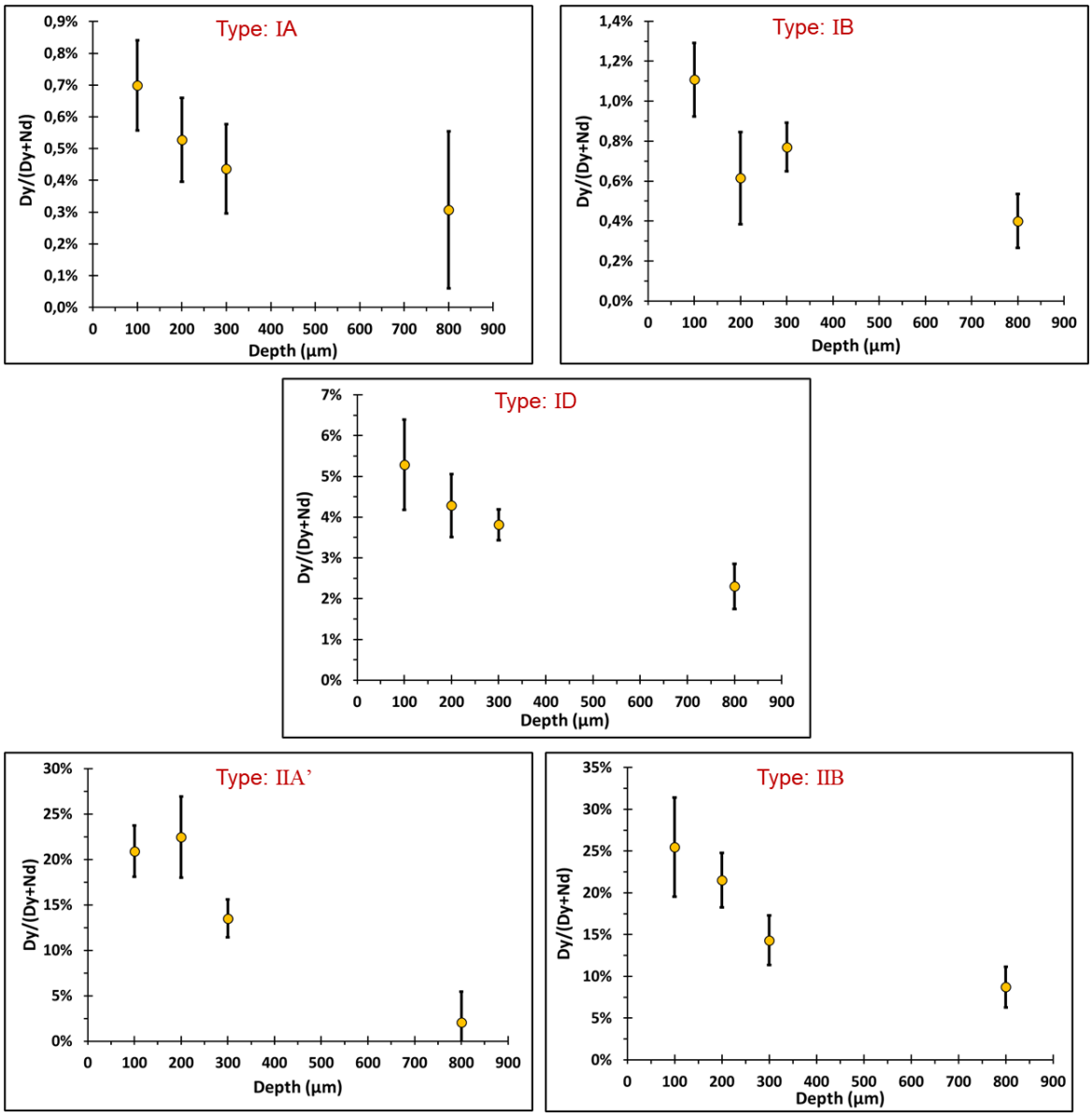

Figure 118: Variation of the Dy substitution rate (Dy/(Dy+Nd) in metallic Nd-rich phases (IA, IB, and ID) and Nd-oxides (IIA' and IIB) with respect to the magnets depth.

The Dy substitution rate inside all the phases rate was found to be decreasing when moving far from the magnets surface, and no Dy was detected in the secondary phases located at 2 mm (not shown here). It is worth to point out that Dy is detected in these phases in a region located at a depth of 800 µm from the surface where Dy could not be detected in the NdFeB grains. This result attests that the diffusion of the Dy is probably not limited to the 350 µm as suggested in section 4.2.2.

Since we know the surface fraction (A) and the composition of each phase in the GBD processed NdFeB magnet, we can use the rule of mixture to evaluate the overall Dy content at different depth and compare it to the experimental overall Dy content determined from EDS analysis. The rule of mixture is given in the following equation:

$$\left(\frac{Dy}{Dy+Nd}\right)_{overall} = \left[\left(\frac{Dy}{Dy+Nd}\right)\times A\right]_{Dy-shell} + \left[\left(\frac{Dy}{Dy+Nd}\right)\times A\right]_{NdO2} + \left[\left(\frac{Dy}{Dy+Nd}\right)\times A\right]_{Nd2O3} + \left[\left(\frac{Dy}{Dy+Nd}\right)\times A\right]_{Nd-rich} + \left[\left(\frac{Dy}{Dy+Nd}\right)\times A\right]_{NdCoCu} + \left[\left(\frac{Dy}{Dy+Nd}\right)\times A\right]_{NdFeAl} \quad (4.2)$$

Since the amount of Dy found in the metallic Nd-rich phases is negligible, we can disregard these phases. Also, and although ID phase has a higher Dy content than the rest of the metallic Nd-rich phases, the surface fraction of this phase is quite small which justifies why we are not taking it into account. However, and since it is complicated to differentiate the two types of Nd-oxides from the image, we only consider the total surface fraction of the two types of oxides. This implies that the Dy-content in NdO_2 (24.2%) and Nd_2O_3 (27.4%) should also be replaced by their average Dy-content. In result, (4.2) can be reduced to (4.3):

$$\left(\frac{Dy}{Dy+Nd}\right)_{overall} = \left[\left(\frac{Dy}{Dy+Nd}\right)\times A\right]_{Dy-shell} + \left[\left(\frac{Dy}{Dy+Nd}\right)_{average}\times A_{average}\right]_{Nd-oxides} \quad (4.3)$$

Table 29 recapitulates at different depth, the average Dy content and surface fraction of the Dy-rich phases (Dy-rich shell and Dy-rich Nd-oxides), the calculated overall Dy content evaluated using (4.3) and the experimental Dy content determined from EDS spectra taken from regions of dimensions 200 × 12 μm².

Table 29: Dy substitution rate (Dy/(Dy+Nd)) and the surface fraction of the Dy-rich shell and Nd-oxides phases at different depth, expected overall Dy content calculated using the mixture equation and the measured overall Dy content extracted from EDS spectrums taken from regions of dimensions 200 × 12 μm².

Depth		Dy-rich shells	Dy-rich oxide	calculated overall Dy content	Measured overall Dy content
z = 100μm	Average $\frac{Dy}{Dy+Nd}$	31%	24%	17%	17%
	Surface fraction	53%	4%		
z = 200μm	Average $\frac{Dy}{Dy+Nd}$	23%	23%	4%	7%
	Surface fraction	15%	4%		
z = 300μm	Average $\frac{Dy}{Dy+Nd}$	25%	14%	3%	4%
	Surface fraction	9%	4%		

We can see that both the calculated and measured Dy content are found to be quite similar with a 3% difference at 200 μm. This good agreement between calculated and measured values validates our experimental measurements taken by SEM-EDS (surface fraction and chemical composition)

It is interesting to evaluate the quantity of Dy wasted in Nd-oxides especially since their Dy content is comparable to the Dy content found in the Dy-rich shell as we can see from Table 29. Equation (4.4) is used to evaluate the Dy consumption, and the results are displayed in Table 30 for different depth.

$$\frac{\left[\left(\frac{Dy}{Dy+Nd}\right)_{average} \times A_{average}\right]_{Nd-oxides}}{\left(\frac{Dy}{Dy+Nd}\right)_{overall}} \quad (4.4)$$

Table 30: Quantity of Dy wasted in Nd-oxides at different depths.

Depth	Amount of Dy in Nd-oxides
100 µm	5.6%
200 µm	23%
300 µm	19%

In summary, the surface fractions and the compositions of the secondary phases (Nd-rich phases and Nd oxides) were analyzed at different depths of the magnet. These analyzes show that the Nd oxides are rich in Dy unlike the main Nd-rich phases. Table 30 *shows that Nd oxides can trap a large amount of Dy which can be about 5% of the total Dy present in the microstructure at 100 µm from the surface where most of the Dy is in the shell. This amount can reach 20% at 200 µm where the microstructure only shows a thin Dy-rich shell.*

4.2.5.3 Crystallographic investigations

A. EBSD study

When EDS maps or BSE-SEM images similar of the core-shell structure are analyzed in detail, the Dy-rich shell clearly appears asymmetric. This asymmetric feature is expressed by the formation of the Dy-rich shell at only one side of the GB as illustrated in Figure 119. EBSD analysis was carried out to check if this asymmetric feature can be explained by a preferential crystallographic orientation for the Dy-rich shell formation.

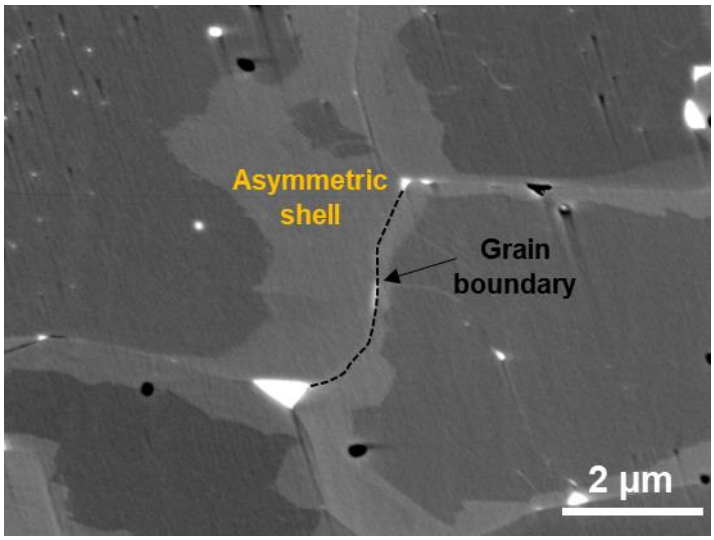

Figure 119: BSE-SEM image showing the formation of Dy-rich shell at only one side of the grain boundary.

Inside the microscope, the sample is mounted so that the axis of cylinder is parallel to the image vertical axis (y direction). Figure 120 (a) is an EBSD inverse pole figure (IPF_y) map of a core-shell microstructure located in region 2. It shows the crystallographic orientation of the $Nd_2Fe_{14}B$ grains parallel to the y direction. The color code is shown in Figure 120 (b): red color indicates that the [001] direction is parallel to the y direction, green color indicates that the [100] direction is parallel to the y direction, and blue color indicates that [110] direction is parallel to the y direction. Not surprisingly, we can see that the grains are all oriented with their c-axis almost parallel to the y-axis of the image, which is the axis of the cylinder. In this figure, the projection of the c-axis of the grains 1, 2 and 3 has been represented by an arrow. Figure 120 (c) shows the Dy-EDS elemental map for the same region as in Figure 120 (a). This map allows us to distinguish the core from the shell.

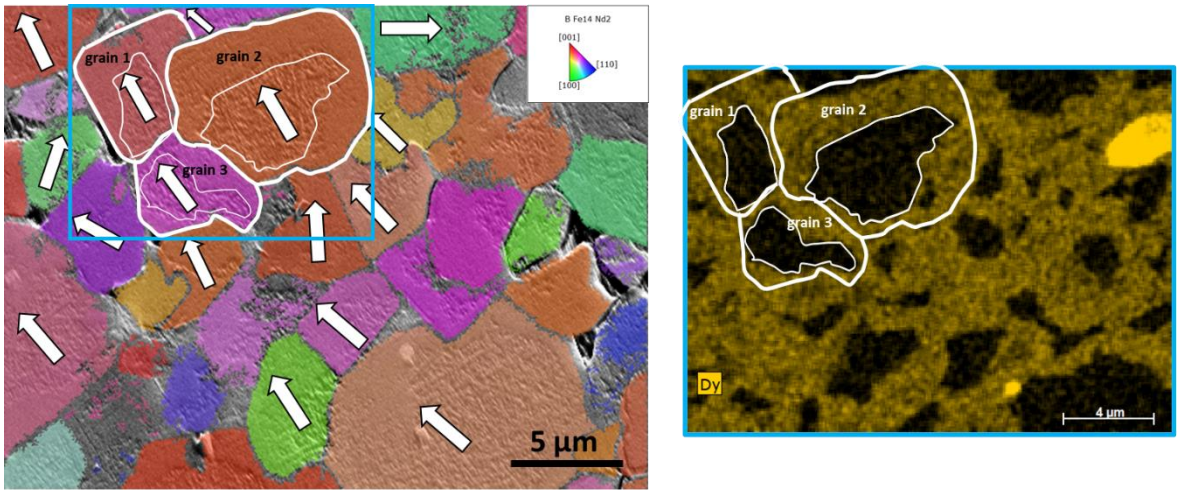

(a) (b)

Figure 120: (a) IPF_y map of a core-shell microstructure and (b) Dy-EDS elemental map for the region selected by a rectangle in (a).

The IPF_y map shows that there is no misorientation at the core/shell interface, which indicates an epitaxial grain growth of the shell as reported by Loewe et al.[79] and Seelam et al.[80]. More interestingly, we can see that, for all the 2 :14 :1 grains, the Dy-rich shell is formed in directions that are parallel and perpendicular to the c-axis. This shows that for these grains, there is no preferential orientation for the formation of the Dy-shell. However, due to the limited number of grains in the EBSD analysis, we cannot generalize this conclusion and clearly state whether there is or not a preferential direction for the formation of the Dy-rich shell.

B. (S)TEM study

The core-shell microstructure was further studied using a probe aberration corrected STEM. Figure 121 (a) shows a HAADF/STEM image of a core-shell microstructure located at a depth of 150 μm. Usually, the HAADF image is sensitive to the atomic number Z, with contrast approximately proportional to Z^2. However, probably because the atomic number of Nd (60) and Dy (66) are too close, the ratio of Z_{Dy}^2/Z_{Nd}^2 being only of 1.2, the image shows no contrast variation between the core and the shell. Moreover, when the lamella is too thick, the Kikuchi lines present at the diffraction pattern disturb the HAADF "Z-contrast". This absence of contrast variation makes it complicated to distinguish the core and the shell in the HAADF image. Moreover, and since the core and the shell have the same crystallographic structure, the interface core/shell cannot be seen using STEM. This interface can only be highlighted on the Dy and Nd elemental maps recorded by EDS. Therefore, acquiring EDS maps is indispensable to distinguish the core from the shell. Figure 121 (b) and (c) show the Nd and Dy EDS elemental maps around the grain boundaries. The grain boundaries drawn in these maps were located based on the HAADF image. Based on the Nd map, we can see a depletion of Nd in the shell compared to the core. This confirm that Dy substitutes Nd in the shell. The shell thickness ranges between 1-2 μm as previously observed in SEM and is found to be asymmetric on both grains and grain boundaries level as already seen by EBSD. Figure 121 (d) shows the Dy EDS (linear) concentration profile across the core-shell indicated by a white arrow in Figure 121 (b). We can see again that the Dy concentration profile displays a plateau and an abrupt interface when transitioning from the core to the shell, which confirms the previous observation performed by SEM.

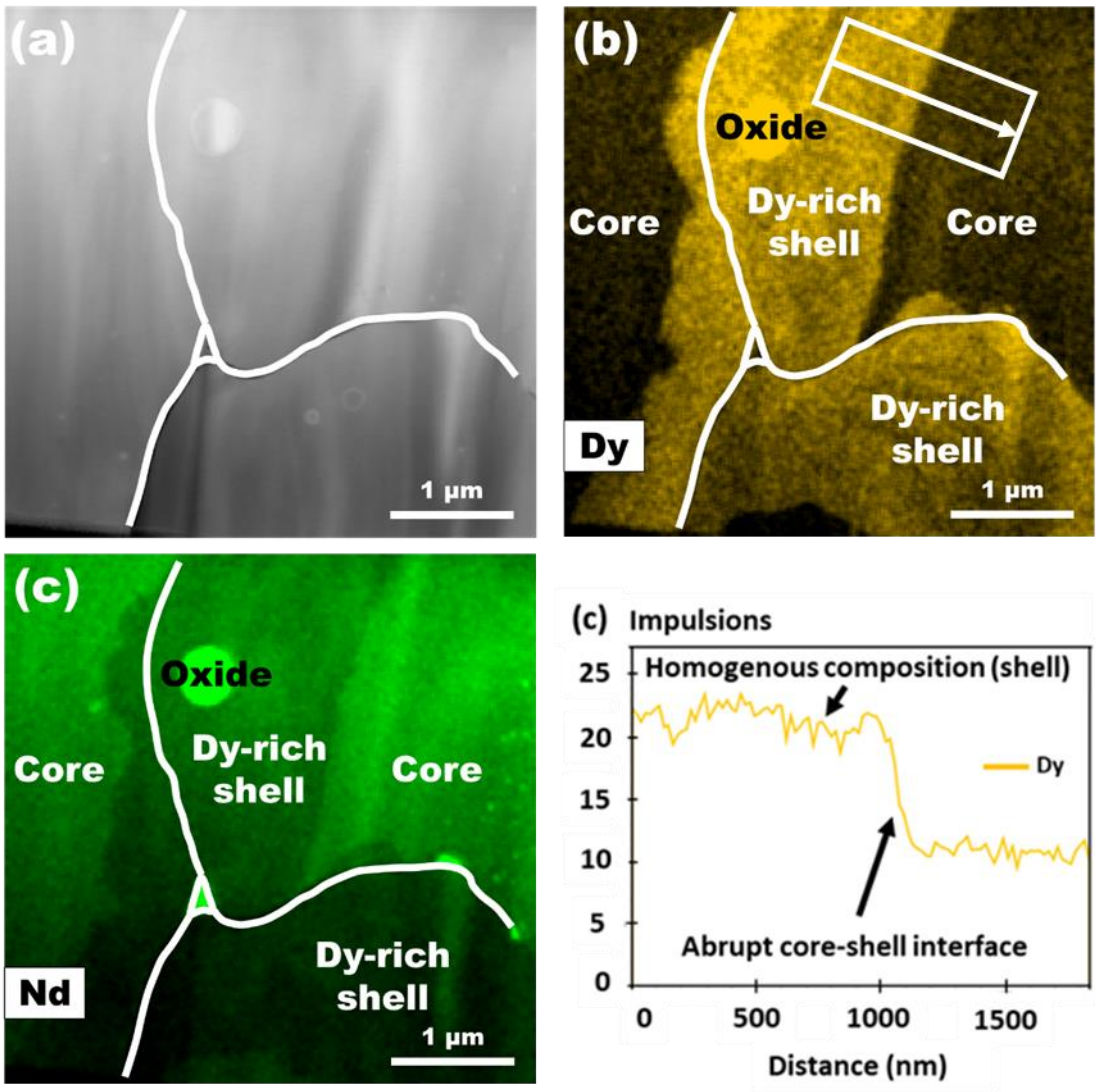

Figure 121: (a) HAADF-STEM image of a core-shell structure located at a depth of 150 µm, (b) and (c) are EDS-STEM maps of Dy and Nd elemental distribution respectively and (d) is the Dy line-scan profile extracted from the EDS map.

To quantify the shell chemical composition, several regions were taken in the EDS-map of the shell. Using the K factors method implemented in the Esprit software, the average chemical composition was found to be $Fe_{78.3}Nd_{8.7}Dy_{4.1}Co_{2.3}Cu_{0.6}B_{6.0}$. According to this chemical composition, the Dy/(Nd+Dy) and Co/(Fe+Co) ratios are 32% and 3% respectively.

As the composition of the Dy-rich shells located at a depth of 150 µm was analyzed using the three spectroscopy techniques associated to SEM or TEM (EDS/SEM, WDS/SEM and EDS/TEM), the results obtained by these 3 techniques can be compared. Table 31 recapitulates Dy/(Nd+Dy) and Co/(Fe+Co) ratios determined by these three different used spectroscopy techniques.

Table 31: Chemical composition of the Dy-rich shell located at z=150 µm determined by EDS-SEM, WDS and EDS-STEM.

Technique	Rays	Chemical composition of the Dy-rich shell (at. %)	$\frac{Dy}{Dy+Nd}$	$\frac{Co}{Co+Fe}$
EDS-SEM (5 kV)	Dy (Mα), Nd (Mα), Fe (Lα) and Co (Lα)	$Fe_{80.1}Nd_{9.3}Dy_{3.2}Co_{2.7}Cu_{0.3}Al_{0.5}O_{3.6}$	26 %	3%
WDS (10 kV)	Dy (Mα), Nd (Mτ1), Fe (Lα) and Co (Lα)	$Fe_{80.3}Nd_{8.0}Dy_{3.2}Co_{0.4}Al_{0.7}O_{1.8}B_{5.7}$	29 %	0.5%
EDS-STEM (200 kV)	Dy (Mα), Nd (Lα), Fe (Kα) and Co (Kα)	$Fe_{78.3}Nd_{8.7}Dy_{4.1}Co_{2.3}Cu_{0.6}B_{6.0}$	32%	3%

Based on the values given in the table above, we can say that the results given by EDS-TEM and EDS-SEM for the Dy/(Dy+Nd) ratio are slightly different. STEM results probably lack accuracy since the analysis is standardless and just based on the K factors that are probably not well estimated for the L and M lines of the different elements. In addition to that, we point out that when using EDS-STEM there is no sufficient X-ray counts on the detectors when compared to EDS-SEM. In consequence, we expect a higher statistical error when using EDS-STEM.

Figure 122 (a) and (b) shows BF images of another core-shell microstructure located at a depth of 150 µm where some dislocations are imaged.

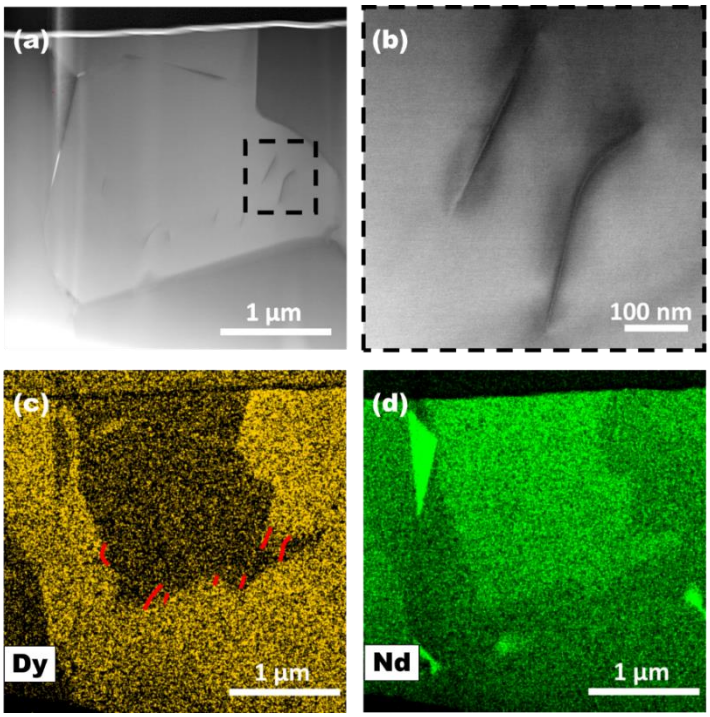

Figure 122: (a) BF-TEM image of a core-shell located at a depth of 150 µm, (b) high magnification image of the dislocations, (c) and (d) EDS-STEM maps of Dy and Nd elemental distribution respectively. The red lines in (c) correspond to the positions of dislocations.

Although dislocations are not frequently observed in the 2:14:1 phase, Figure 122 (c) shows that the dislocations are located near the core/shell interface. These dislocations can be created in the system to release the stress caused by the lattice mismatch between the core and the shell. Indeed, if we consider a Dy substitution rate of 30% inside the Dy-rich shell, the corresponding lattice parameter c given in literature is 1.215 nm compared to 1.220 nm of the NdFeB phase (the impact of Dy on lattice parameter a is lower). Therefore, we can calculate the lattice misfit between the core and the shell given by:

$$\frac{c_{core}-c_{shell}}{c_{core}} = \frac{1.220-1.215}{1.220} = 0.4\ \% \tag{4.5}$$

This lattice misfit leads to the generation at the interface of accommodation stress that can be released by the creation of misfit dislocations. We can calculate the periodicity of these misfit dislocations (i.e., the distance at which they occur for completely relaxing the interfacial stress). The number n of planes at which the misfit dislocations occur is n = 1/lattice misfit = 244. Hence, the system creates misfit dislocations every n = 244 planes. This corresponds to a distance of n × 1.220 ≈ 300 nm. This distance is in relatively good agreement with the distance between the dislocations observed on the Figure 122.

In summary, the images show that the Dy-rich shell thickness is not homogeneous either around each grain or on each side of a grain boundary. The EBSD study, which allows the knowledge of the crystallographic orientation of the grain boundary, was insufficient to deduce a relation between the heterogeneity of the shell thickness and crystallography, since the shell thickness varies greatly for grain boundaries with similar crystallographic orientation. HAADF/STEM images showed no contrast between the core and shell, making the interface difficult to observe at high resolution. This core/shell interface can only be revealed in Dy or Nd EDS elemental maps. EDS analyses performed in STEM mode confirm the abrupt Dy profil at the core/shell interface. The misfit between the shell and the core is about 0.4%. The stresses generated by this misfit do not seem to be relieved by misfit dislocations, since dislocations were observed in only one case.

4.2.6 Beyond the core-shell microstructure (z>500µm)

As already seen in Figure 113, at z=500 µm only thin Dy-rich shells are vaguely distinguished in the SEM-EDS map. Beyond this depth, we can no longer see Dy-rich shells using SEM-EDS. To check if Dy is present at the GBs beyond this depth, we switch from using a SEM to using a STEM.

To be able to perform STEM observations, we prepared a FIB lamella at a depth of z = 800 µm. Figure 123 (a) shows the region where the EDS analysis has been performed and in which A and B denote two $Nd_2Fe_{14}B$ grains. Figure 123 (b) shows the Fe-EDS elemental map, in which we can distinguish an Fe-depleted region corresponding to the position of the grain boundary (GB). Both Nd and Cu elemental maps in Figure 123 (c) and (d) show the presence of an NdCu rich phase at the GB region. This phase is known to be formed during Post diffusion annealing (PDA) and serves to decouple the adjacent $Nd_2Fe_{14}B$ grains. The Dy elemental map in Figure 123 (e) confirms the presence of Dy in the vicinity of the GB, which indicates that Dy penetrates beyond 500 µm. Fe, Nd, Cu and Dy line-scan profiles can be seen in Figure 123 (f). The position of the GB on the

linear profile corresponds to the zone of Fe depletion accompanied by the presence of Nd and Cu peaks. An enlarged image of the Dy and Cu linear profiles is shown in Figure 123 (g). Interestingly, the Dy profile shows an asymmetric diffusion behavior of the Dy that diffuses from the GB into the left hard magnetic $Nd_2Fe_{14}B$ grain denoted by A in Figure 123 (a) and not in the GB denoted by B. The Dy Diffusion distance is around 40 nm. It should also be noted that in this case, the Dy profile across the GB no longer shows an abrupt interface but decays exponentially similar to a classical diffusion profile.

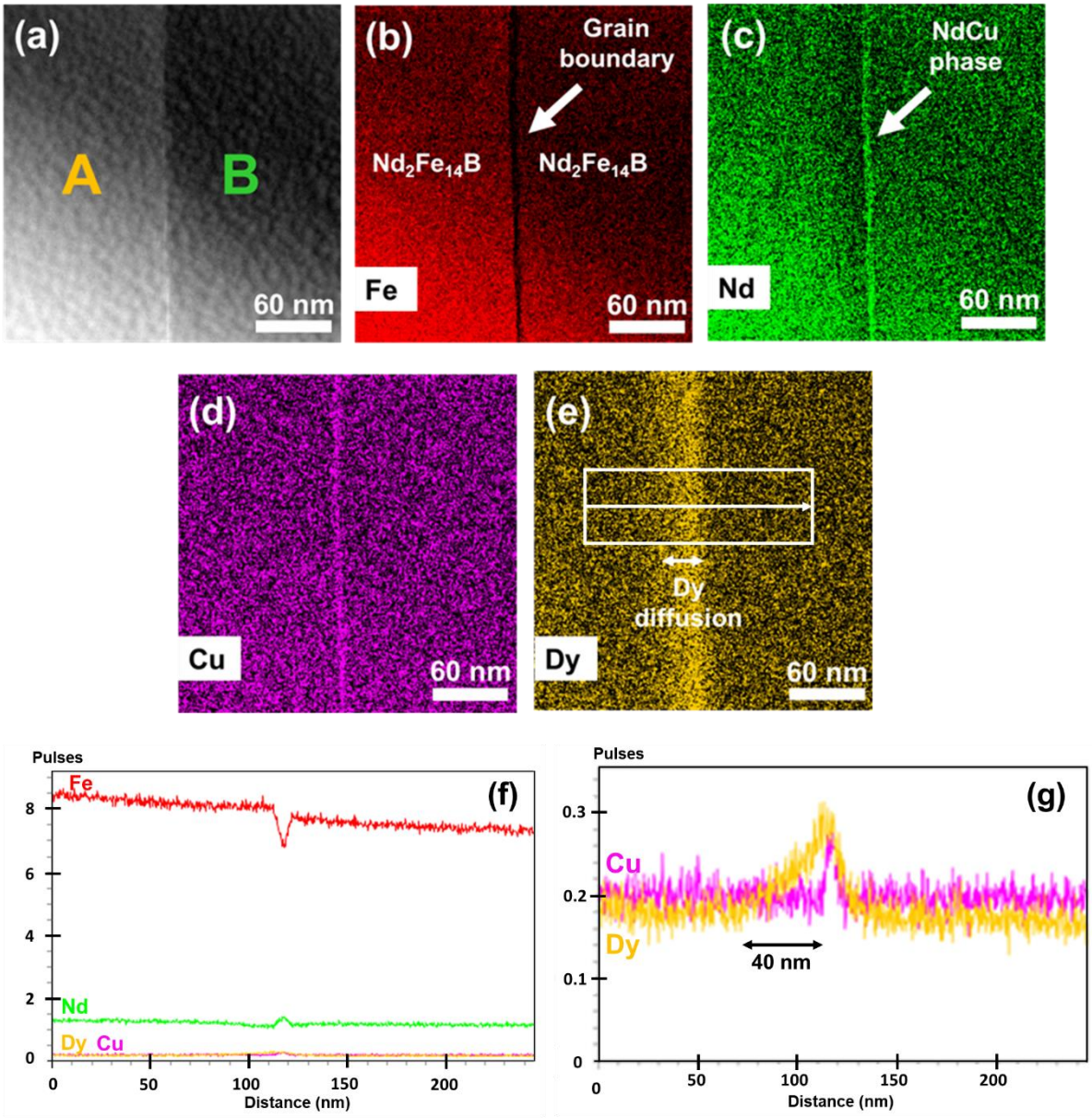

Figure 123: (a) HAADF-STEM image showing two $Nd_2Fe_{14}B$ grains denoted by A and B from the GBD processed sintered NdFeB magnet at a depth of 800 µm, (b-e) EDS-STEM maps of Fe, Nd, Dy and Cu elemental distribution in the vicinity of a grain boundary region located at 800 µm from the magnet surface and (f) Fe, Nd, Cu and Dy line-scan profiles taken across the grain boundary as indicated by the white arrow in (e) and (g) enlarged line-scan profile showing the Cu and Dy distribution.

To check whether the asymmetrical feature is related to crystallography orientation of the 2 grains with respect to the GB plane (we could expect that the diffusion is easier along the (001), we try to

determine these orientations. For this, the sample is tilted in order to orient in [001] zone axis successively the grain A and the grain B.

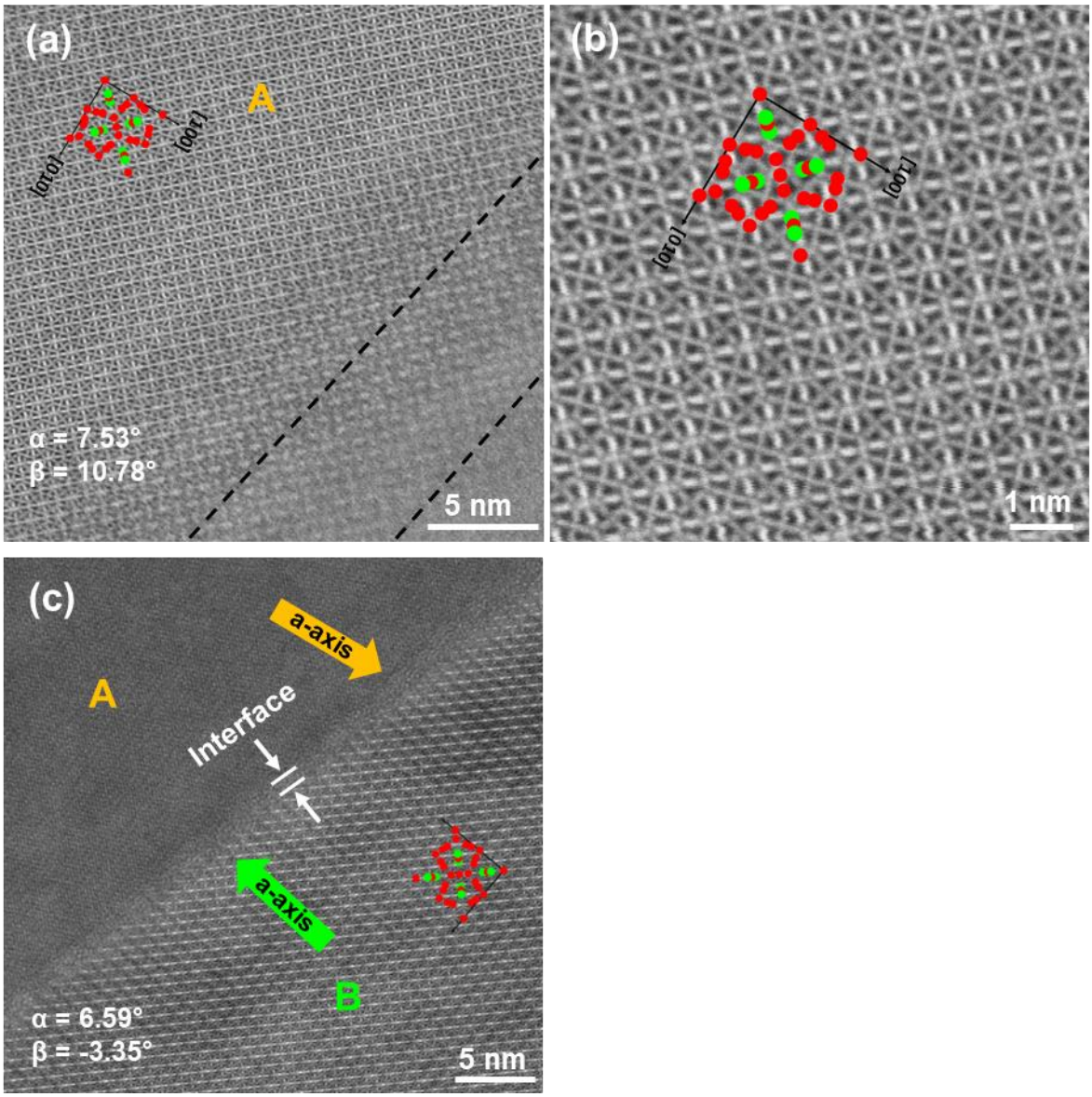

Figure 124: (a) HR-STEM image taken along the zone axis of grain A, (b) higher magnification image showing the structure of grain A and the inset is the structure oriented accordingly and (c) HR-STEM image taken along the zone axis of grain B.

We start by orienting the grain A along a low index crystallographic axis, by tilting the double tilt sample holder. In the case of Figure 124 (a), the tilt angles were equal to $\alpha = -7.53°$ and $\beta = 10.78°$ and the obtained direction of observation was the c-axis. In this figure, the GB plane is slightly visible as it is inclined in the TEM lamella, so in projection, it gives a thickness that can be seen by the two dotted lines. Figure 124 (b) is a higher magnification image showing the grain A structure projected along this c-axis. This image shows that the GB plane is nearly parallel to the a-axis [100]. Afterwards, we orient the grain B along a nearest low index zone-axis which corresponds to a tilt of $\alpha = 6.95°$ and $\beta = -3.35°$ as seen in Figure 124 (c). For this sample orientation, it is found that the GB plane in the grain B is also nearly parallel to (100). We thus see that the 2 grains are only slightly disoriented with respect to each other (the holder was tilting less than 15° between the two

grain zone axis orientations). The crystal orientation of each grain with respect to the GB plan does not seem to explain the asymmetry of the Dy-rich shell. This is in contrast to the result of Kim et al. who showed a dependence between the Dy diffusion and the crystallographic orientation of the c-axis[145].

In summary, the analyses performed at the magnet depth of 800 μm show that Dy is still detected by EDS/STEM in the vicinity of grain boundaries. This indicates that Dy diffuses deeper in the magnet as it can be detected by SEM. This low amount of Dy is certainly partly responsible of the 22% gain in coercivity. Surprisingly, the Dy seems to diffuse asymmetrically in the GBs; this is certainly due to the crystallographic orientation of the grains but we did not enough detailed grain boundary orientation studies to have a clear vision of this diffusion asymmetry. It should also be noted that for this low amount of Dy, the Dy profile across the GB no longer exhibits an abrupt interface but decays with an exponential shape representative of the common diffusion profile. A tentative model to explain all the observed mechanism will be performed in chapter V.

4.3 Parametric study of the GBDP

4.3.1 Effect of diffusion time

In this section, we aim to study the effect of the diffusion time on the magnetic and microstructural properties of the GBD processed magnets. For that, a GBDP NdFeB magnet was prepared following the same protocol described in section 2.1.2 of chapter II, except that instead of a diffusion time of 3h, we opt for a diffusion time of 1h. This magnet is designated by 1h-GBD magnet. In addition, we needed a higher diffusion time to be able to confirm certain observations. Due to the limited access to the furnace, we couldn't prepare the sample within the framework of this study. Hence, a NdFeB magnet with the same composition as our magnets, subjected to the GBDP at 920 °C for 12 h, and prepared at LMCM laboratory by Jérôme Fliegans[92] is taken for our study. This magnet is designated by 12h-GBD magnet. Hereafter, we report the magnetic and microstructural properties of the 1h-GBD and 12h-GBD magnets and compare them to the ones obtained in the case of 3h-GBD processed NdFeB magnet.

Figure 125 shows the demagnetization curves of the 1h-GBD and 3h-GBD magnets. It can be noted that there is no change in the magnetic properties. Furthermore, and on the same samples, Fliegans[92] reported that the magnetic properties after GBDP performed at 3h and 12h did not change.

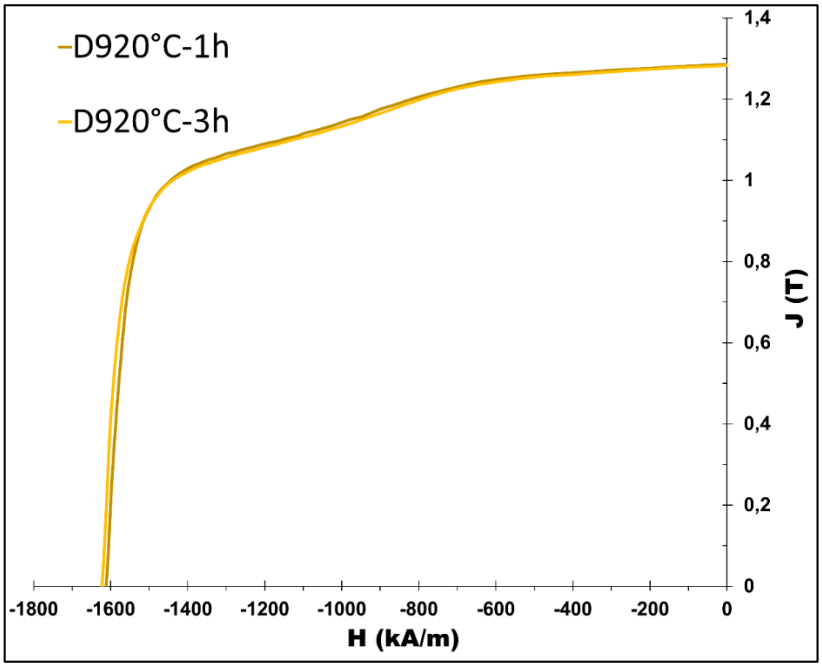

Figure 125: Demagnetization curves of the 1h and 3h GBDP magnets.

The corresponding magnetic properties are summarized in Table 32. The results show that increasing the diffusion time (t_{diff}) has no significant effect on the coercivity H_{cJ} or any of the other magnetic properties (same conclusion for the 12h-GBD magnet as reported by Fliegans[92]).

Table 32: Magnetic properties of the 1h and 3h GBD processed NdFeB magnets.

Sample	H_{cJ} (kA/m)	J_r(T)	$(BH)_{max}$ (kJ/m^3)
3h-GBD processed NdFeB magnet	1622.6 kA/m	1.284 T	313.31 kJ/m^3
1h-GBD processed NdFeB magnet	1611.9 kA/m	1.285 T	315.26 kJ/m^3

Figure 126 (b-d) display the Dy concentration-depth profiles for the 1h, 3h and 12h GBD magnets. Each profile is plotted based on quantifying the EDS spectra taken from regions of dimensions 200 × 12 μm² (following the same protocol explained in section 4.2.2.)

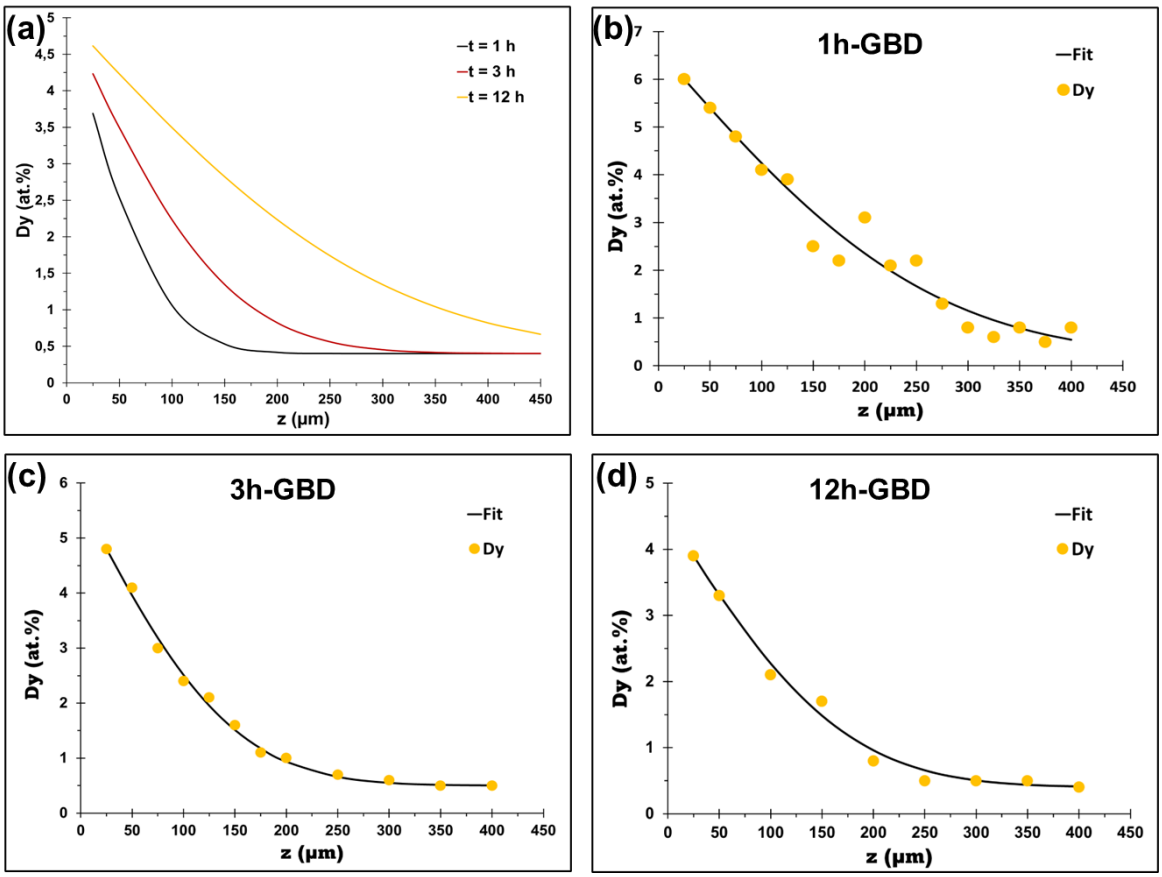

Figure 126: (a) Variation of Dy concentration for various diffusion time when the diffusion coefficient is given by D = 6,5 × 10^{-13} m²/s calculated using Grube's solution for Fick's second law. Average Dy concentration profile along the magnet depth for (b) 1h-GBDP magnet, (c) 3h-GBDP magnet (right) and (d) 12h-GBDP magnet.

Assuming that the diffusion coefficient is independent of the concentration and that the diffusion source is constant, the variation of Dy concentration is given by Grube's solution. In this case, the slope of the concentration profile is proportional to $(Dt)^{-1/2}$. Since the diffusion coefficient is expected to be the same in the 1 h, 3 h and 12 h cases (in all cases the same diffusing species, Dy, diffuse in the same host medium, NdFeB magnet, at the same diffusion temperature), the slope is governed by $t^{-1/2}$ law. Hence, when t increases (from 1 h to 12 h) the Dy concentration profile tends to flatten out. We can use the diffusion coefficient determined earlier for the of 3h-GBD magnet to plot the expected time-evolution of the Dy concentration profile. This is shown in Figure 126 (a). For t = 1 h, the concentration profile is steep, and the total diffusion length (i.e., the length at which the evolution of the concentration profile ceases) is short. As the diffusion time increases, the concentration profile is flattened, and the total diffusion length is large. However, the experimental Dy concentration profiles of the 1 h, 3 h and 12 h GBD magnets given in Figure 126 (b-d) do not follow this trend. For all the concentration profiles, the total diffusion length is found to be 400 µm. Hence, the total diffusion length does not grow with the diffusion time. All these elements clearly state that the examined Dy concentration profiles do not follow $t^{-1/2}$ law and that the diffusion model based on an infinite source does not account for our experimental observations and should be reconsidered.

It is interesting to calculate the amount of Dy present in the analyzed regions. To do so, we calculate the area under the Dy concentration profiles and divide it by the total penetration depth (400 μm). This gives the percentage of Dy present in each analyzed region. The latter is found to be 2.4%, 1.4% and 1.2% for the 1h-GBD, 3h-GBD and 12h-GBD magnets respectively. To find the equivalent mass of Dy, we proceed as follows: First, we calculate the number of Dy atoms (N_{Dy}) by multiplying the percentage of Dy found within each analyzed volume by the ratio of the volume of the analyzed area ($\pi \times 0.5 \times 0.5 \times 0.04$ cm^3) and the volume of $Nd_2Fe_{14}B$ ($12.2 \times 12.2 \times 12.2 \times 10^{-24}$ cm^3) as recapitulated by the eq. (4.6) below:

$$N_{Dy}(atoms) = \%Dy \times \frac{V_{analyzed\ area}}{V_{Nd2Fe14B}} \tag{4.6}$$

Then, the mass of Dy is calculated using the following equation:

$$m_{Dy} = \frac{N_{Dy} \times M_{Nd2Fe14B}}{N_A} \tag{4.7}$$

The results indicate the presence of 11 mg, 6 mg and 5 mg of Dy inside the 1h-GBDP, 3h-GBDP and 12h-GBDP magnets respectively. Compared to the mass of Dy initially deposited at the magnets' surfaces (11.5 mg for all samples), the calculated values seem to indicate that the Dy did not completely penetrate inside the magnets for the 3h-GBDP and 12h-GBDP magnets. However, the EDS analysis of the surface of the magnet showed that only a minor amount of Dy remains at the surface of the magnet trapped inside the RE oxides (see 4.2.3). The calculated values are most probably due to the region where the analysis is performed taking into account the heterogeneity that we previously reported at the surface of the magnets (see Figure 103).

Moving forward, we can also compare the microstructure of the GBDP magnets. Starting from the surface, we found that the surface of the 1h-GBD and 12h-GBD magnets display the same heterogeneity and phases as reported in the case of 3h-GBD magnet in section 4.2.3. Furthermore, an anti-core shell structure is detected below the surface of the 1h-GBD and 12h-GBD magnets similarly to the 3h-GBD case. The depth range of the anti-core-shell microstructure increases with increasing diffusion time: 15 μm, 30 μm and 43 μm for the 1h-GBD, 3h-GBD, and 12h-GBD respectively as displayed in Figure 127 (the Dy map of the 12h-GBD magnet is not shown here).

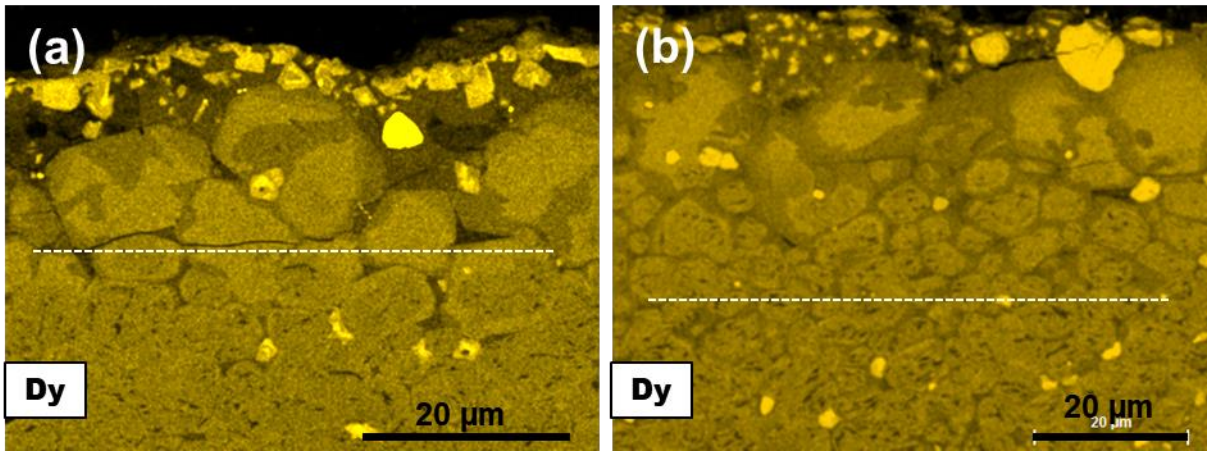

Figure 127: EDS-SEM maps of Dy elemental distribution of the anti-core-shell microstructure inside the (a) 1h-GBD processed magnet and (b) the 3h-GBD processed NdFeB magnet (the images are not at the same magnification). The white dotted line represents the end limit of the anti-core-shell region.

Underneath the anti-core-shell structured grains, the Dy penetrates almost the entire $Nd_2Fe_{14}B$ grains as we can see in Figure 128 (a). This is similar to the region located at z=50 µm in the 3h-GBD magnet seen in Figure 113. However, the depth range of this region is found to be greater in the 1h-GBDP magnet than the 3h-GBD magnet. In the former it extends up to a depth z = 75 µm while in the latter it reaches a depth of z = 50 µm.

In region 2, we start to see the core-shell structured grains displayed in Figure 128 (b-e). As seen in the case of the 3h-GBDP magnet, the core-shell structure is visible by SEM until a depth of approximately 400 µm (this depth is not shown here).

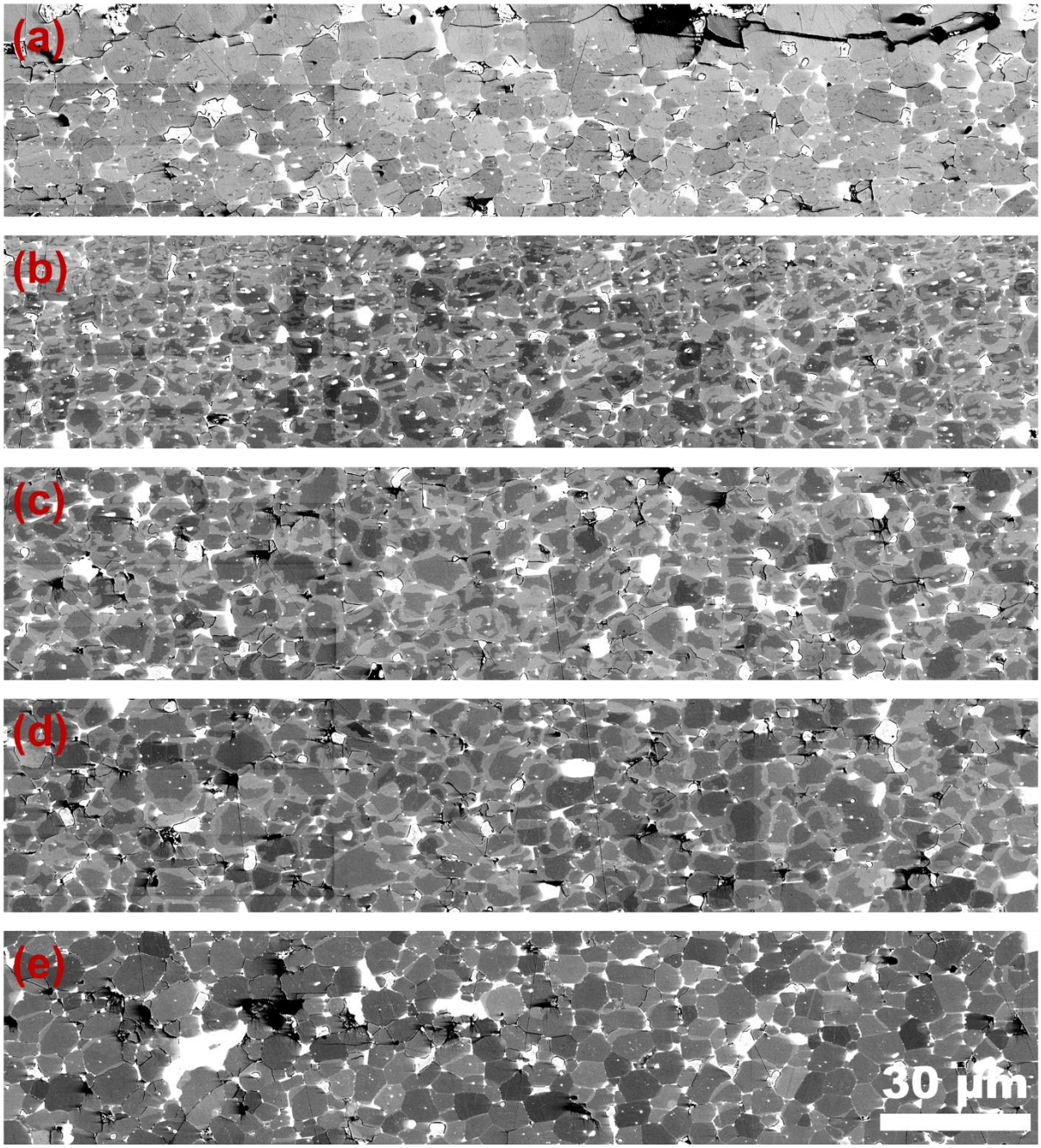

Figure 128: BSE-SEM images showing the variation of Dy-rich shell thickness along the magnet depth (a) 25 µm, (b) 100 µm, (c) 150 µm, (d) 225 µm and (e) 300 µm.

Lastly, we identify the chemical composition of the Dy-rich shells and its evolution with respect to the magnet depth. For that, 10 EDS point spectra are acquired at 5 kV and 1.5 nA from the Dy-rich shells located between 25 µm and 300 µm. These spectra were quantified using the IZAC code. Below are the results compared to the 3h-GBD magnet (Table 33). The Dy substitution rates in the Dy-rich shells in both 1h and 3h GBDP NdFeB magnets are also reported in Table 34.

Table 33: Variation of the average chemical composition of the Dy-rich shells as a function of diffusion time in the 1h-GBD and 3h-GBD magnets. At each depth, the given chemical composition corresponds to the average of 10 EDS measurements in 10 Dy-rich shells.

Depth	1h-GBD magnet (at. %)	3h-GBD magnet (at. %)
25 µm	$Fe_{78.2}Nd_{6.1}\mathbf{Dy_{6.1}}Co_{4.8}Cu_{0.1}Al_{0.7}O_{4.1}$	Anti-core-shell region
50 µm	$Fe_{78.5}Nd_{6.8}\mathbf{Dy_{5.4}}Co_{4.5}Cu_{0.1}Al_{0.7}O_{4.1}$	$Fe_{79.5}Nd_{5.9}\mathbf{Dy_{6.1}}Co_{3.7}Cu_{0.3}Al_{0.7}O_{3.9}$
100 µm	$Fe_{78.9}Nd_{7.7}Dy_{4.5}Co_{4.1}Cu_{0.0}Al_{0.7}O_{4.0}$	$Fe_{80.1}Nd_{8.6}\mathbf{Dy_{3.8}}Co_{3.0}Cu_{0.3}Al_{0.7}O_{3.6}$
150 µm	$Fe_{79.0}Nd_{8.4}\mathbf{Dy_{4.0}}Co_{4.0}Cu_{0.0}Al_{0.7}O_{3.9}$	$Fe_{80.1}Nd_{9.3}\mathbf{Dy_{3.2}}Co_{2.7}Cu_{0.3}Al_{0.8}O_{3.6}$
200 µm	$Fe_{79.0}Nd_{8.9}\mathbf{Dy_{3.4}}Co_{3.8}Cu_{0.0}Al_{0.8}O_{4.1}$	$Fe_{80.2}Nd_{9.5}\mathbf{Dy_{2.9}}Co_{2.8}Cu_{0.3}Al_{0.7}O_{3.7}$
250 µm	$Fe_{79.4}Nd_{9.0}\mathbf{Dy_{3.3}}Co_{3.5}Cu_{0.0}Al_{0.8}O_{4.0}$	$Fe_{80.4}Nd_{9.6}\mathbf{Dy_{2.9}}Co_{2.6}Cu_{0.2}Al_{0.7}O_{3.6}$
300 µm	$Fe_{79.2}Nd_{9.6}\mathbf{Dy_{2.8}}Co_{3.5}Cu_{0.0}Al_{0.8}O_{4.0}$	$Fe_{80.4}Nd_{9.4}\mathbf{Dy_{3.0}}Co_{2.6}Cu_{0.2}Al_{0.7}O_{3.6}$

Table 34: Dy/(Dy+Nd) ratios in the Dy-rich shells as a function of the depth in the 1h-GBD and 3h-GBD magnets.

Diffusion depth z	50 µm	100 µm	150 µm	200 µm	250 µm	300 µm
3h-GBD processed magnet	51 %	31 %	26 %	23 %	23 %	24 %
1h-GBD processed magnet	44 %	37 %	32 %	28 %	27 %	23 %

By examining the evolution of the chemical composition of the Dy-rich shells, we see that the Dy content decrease with increasing depth while the Nd content increases. The sum Nd + Dy remains constant (≈12.4 at. %). All these elements show that Dy substitutes Nd in the 2:14:1 phase. If we compare the 1h and 3h GBD magnets, we find that the difference in the Dy content in their shells decrease with increasing depth (from 0.7 at% at z = 100 µm to 0.2 at% at z = 300 µm). Note that the depths 25 µm and 50 µm are not taken into consideration since there is no proper formation of Dy-rich shells as revealed by SEM. It is interesting to follow the evolution of the Dy substitution rate inside the Dy-rich shells along the magnet depth. The values are reported in Table 34. Again, considering the depths after z = 50 µm, the Dy substitution rate ranges between 20% to 30%.

4.3.2 Effect of diffusion temperature

Another parameter that we investigated in this study is the GBD temperature. For that, we prepared a GBD processed NdFeB magnet following the same protocol described in the introduction, except that instead of a diffusion temperature of 920°C, we held the magnet at a diffusion temperature of 870°C for 3h. This magnet is designated by 870°C-GBD. Hereafter, we proceeded to plot the Dy concentration profile of the latter along its depth as shown in Figure 129 (a). The Dy concentration profile of the GBD processed magnet at 920°C for 3h (designated here by 920°C-GBD) is also shown for comparison.

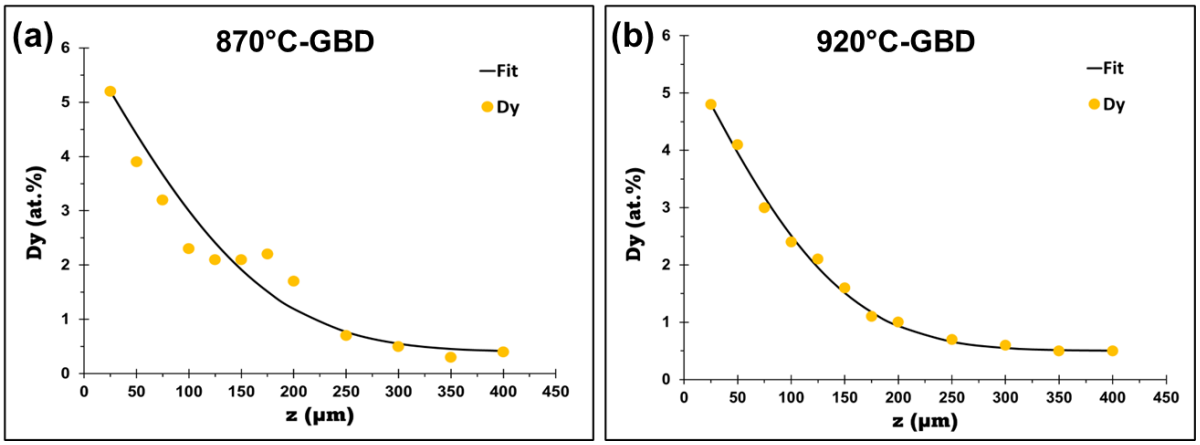

Figure 129: Average Dy concentration profile along the magnet depth for (a) 870°C-GBDP magnet and (b) 920°C-GBDP magnet. In both cases, the diffusion time was 3h.

Surprisingly, both concentration profiles are very similar. This is against what we would expect since lowering the diffusion temperature is expected to decrease the diffusion coefficient. This will be explained in chapter V considering a finite Dy diffusion source. For both cases, the total diffusion length is 400 µm. The Dy diffusion coefficients at 870°C and 920°C determined using Grube's solution are D_{app}^{Dy}(870 °C-3 h) = 8.6 × 10^{-13} m²/s and D_{app}^{Dy} (920 °C-3 h) = 6.2 × 10^{-13} m²/s respectively.

Hereafter, the chemical compositions of the Dy-rich shells at different depths are identified. For that, we acquired 10 EDS point spectra at 5 kV and 1.5 nA from the Dy-rich shells located between 25 µm and 250 µm. Higher than this depth, the Dy-rich shells were too thin to be analyzed by SEM. The spectra were quantified using the IZAC code. The results are presented in Table 35 alongside the results obtained for the 920°C-GBD magnet. The corresponding Dy substitution rates in the Dy-rich shells in both magnets are reported in Table 36.

Table 35: Variation of the average chemical composition of the Dy-rich shells as a function of the depth in the 870°C and 920°C GBD magnets (diffusion time t_{diff} = 3h).

Depth	870°C-GBD magnet (at. %)	920°C-GBD magnet (at. %)
25 µm	$Fe_{78.8}Nd_{6.4}\mathbf{Dy_{5.8}}Co_{5.3}Cu_{0.3}Al_{0.8}O_{2.7}$	Anti-core-shell region
50 µm	$Fe_{79.3}Nd_{7.5}\mathbf{Dy_{4.9}}Co_{4.5}Cu_{0.3}Al_{0.8}O_{2.8}$	$Fe_{79.5}Nd_{5.9}\mathbf{Dy_{6.1}}Co_{3.7}Cu_{0.3}Al_{0.7}O_{3.9}$
100 µm	$Fe_{79.5}Nd_{8.7}\mathbf{Dy_{3.8}}Co_{4.2}Cu_{0.2}Al_{0.9}O_{2.7}$	$Fe_{80.1}Nd_{8.6}\mathbf{Dy_{3.8}}Co_{3.0}Cu_{0.3}Al_{0.7}O_{3.6}$
150 µm	$Fe_{78.9}Nd_{8.6}\mathbf{Dy_{3.9}}Co_{4.0}Cu_{0.2}Al_{0.8}O_{2.7}$	$Fe_{80.1}Nd_{9.3}\mathbf{Dy_{3.2}}Co_{2.7}Cu_{0.3}Al_{0.8}O_{3.6}$
200 µm	$Fe_{80.0}Nd_{9.0}\mathbf{Dy_{3.5}}Co_{3.6}Cu_{0.2}Al_{0.9}O_{2.8}$	$Fe_{80.2}Nd_{9.5}\mathbf{Dy_{2.9}}Co_{2.8}Cu_{0.3}Al_{0.7}O_{3.7}$
250 µm	$Fe_{80.1}Nd_{9.6}\mathbf{Dy_{2.9}}Co_{3.7}Cu_{0.2}Al_{0.9}O_{2.7}$	$Fe_{80.4}Nd_{9.6}\mathbf{Dy_{2.9}}Co_{2.6}Cu_{0.2}Al_{0.7}O_{3.6}$

Table 36: Dy/(Dy+Nd) ratios in the Dy-rich shells as a function of the depth in the 870°C and 920°C GBD magnets. Each ratio at each depth corresponds to the average of 10 EDS measurements in 10 Dy-rich shells.

	50 µm	100 µm	150 µm	200 µm	250 µm
870°C -GBD processed magnet	40 %	30 %	31 %	28 %	23 %
920°C -GBD processed magnet	51 %	31 %	26 %	23 %	23 %

Similar to what we noted in the case of varying the diffusion time, here also we can see that the Dy content inside the Dy-rich shells decreases with increasing depth while maintaining a constant sum with Nd of about 12.4 at.%. The Dy content in the Dy-rich shells located at z=50 µm in the 920°C-GBD magnet is higher than that of the 870°C-GBD magnet. However, the Dy content in the Dy-rich shells located at greater depth shows an opposite trend. The Dy content is higher in the Dy-rich shells of the 870°C-GBD magnet. At z=250 µm, we have a similar Dy content of 2.9 at.% in the Dy-rich shells of both magnets.

When comparing the 870°C-GBD and 920°C-GBD magnets, we find that the Dy content in their Dy-rich shells is either the same or slightly different (by 0.7 at.%) (here also only depths after z = 50 µm are considered). More interestingly, the Dy substitution rate inside the Dy-rich shells ranges between 20-30% as reported earlier.

4.4 Summary

4.4.1 Effect of concentration gradient on the coercivity

In this section, we propose to review the relationship between the magnetic properties and the Dy concentration profiles. As seen in Figure 99, the Dy introduced from the surface of the magnet by the GBDP is not distributed uniformly inside the magnet. The $Nd_2Fe_{14}B$ grains near the surface contain much more Dy than the ones in the center of the magnet leading to a Dy concentration

gradient. Since Dy magnetically hardens the $Nd_2Fe_{14}B$ phase, the $Nd_2Fe_{14}B$ grains near the surface will have higher resistance to the demagnetizing field than the ones at the center. This is translated into a double slope behavior where the less coercive grains at the center of the magnet firstly reverse magnetically (H_{K1} in Figure 98), followed by the higher coercive grains near the surface (H_{K2} in Figure 98).

Another note to be made is the fact that the demagnetization curves of our samples do not vary with the duration of the GBDP (1h, 3h, 12h). Consistently, for the different GBDP durations, the total diffusion length was found to be similar (400 µm). This result is not straightforward to explain since it is widely recognized that the GBDP is driven by diffusion and consequently we expect the diffusion length to follow $t^{-1/2}$ law. Several authors examined the relationship between H_{cJ} and the diffusion time t_{diff}[142,146–148]. In Figure 130, we plot the variation of the coercivity increment (δH_{cJ} = H_{cJ} (before GBDP) - H_{cJ} (after GBDP)) with respect to the diffusion time as reported by these authors.

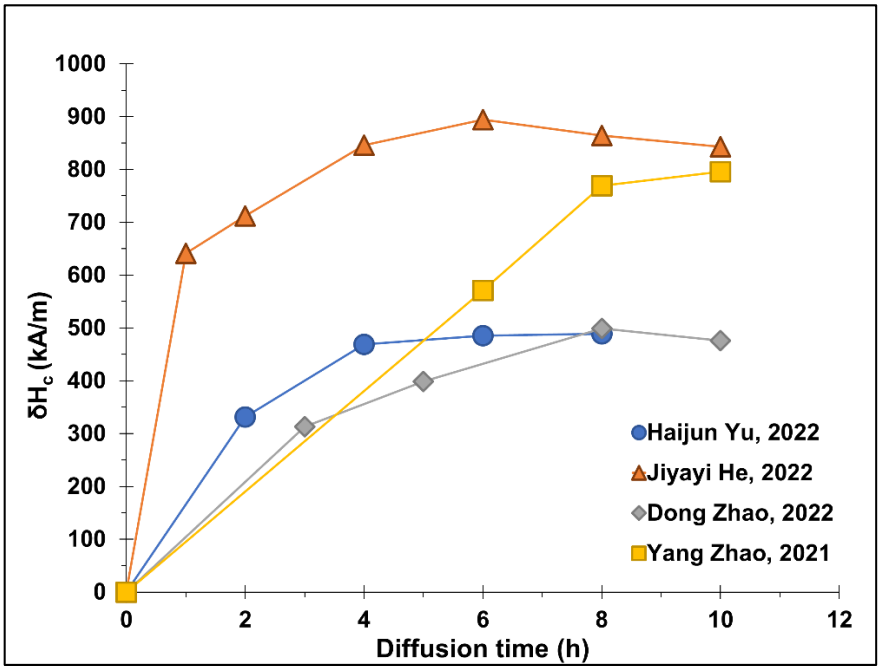

Figure 130: Coercivity increase as a function of the diffusion time as reported in[142,146–148]. All the studies are done at T = 900°C.

By comparing their results, we notice a similar trend: at the start of the GBDP, H_{cJ} quickly increases with t_{diff}. Then, it hits a maximum value beyond which the coercivity either hardly increases or slightly drops. The time at which the coercivity hits its maximum value differs from one author to another. The latter was reported to be 4 h according to Haijun Yu[146], 6h according to Jiyayi He[142], and 8 h according to Dong Zhao[147] and Yang Zhao[148]. In our case, this time is found to be 1 h which is considerably shorter compared to the above-mentioned times.

An interpretation to explain the evolution of the coercivity with respect to the diffusion time is given by Huixin Zeng[149]. It states as follows: at the beginning of the GBDP, the layers underneath the surface are "hardened" by the Dy/Tb while the inner part of the magnet isn't yet. The magnet is in an "unsaturated" state and the difference in the distribution of Dy/Tb creates a stray field that

negatively impacts the coercivity. After a certain diffusion time, the Dy/Tb are homogenously distributed within the magnet and the coercivity reaches its maximum value. Here, the magnet is in its "homogenous state". A further increase in diffusion time will oversaturate the magnet causing its grains to be enlarged and distorted. As a result, the coercivity decreases. Both "unsaturated" and "oversaturated" states are undesired for optimized magnetic properties. A schematic visualization is provided in Figure 131.

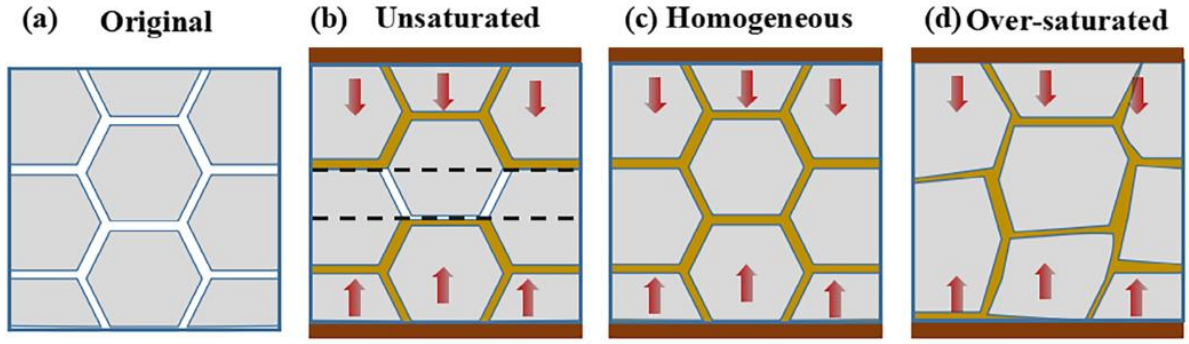

Figure 131: Schematic illustration of the (a) original magnet and three diffusion states: (b) unsaturated, (c) homogeneous, and (d) over-saturated. Adapted from[149].

4.4.2 Dy diffusion in the liquid phase along the GBs

We can compare our GB diffusion coefficient to the one found by Loewe et al.[79] who similarly studied the Dy gradient in a NdFeB magnet subjected to the GBDP at 900°C for 6h. Loewe assumed that this diffusion coefficient is representative of the diffusion of Dy in the liquid phase at 900°C, considering that the Dy-shell corresponds to the solidification of the Dy-rich liquid phase. By tracing the Dy concentration profile of the Dy-rich shells using wavelength dispersive X-ray spectroscopy (WDS) measurements, they determined a diffusion coefficient of $D_{GB}^{Dy} = (2.5 \pm 0.5) \times 10^{-13}$ m²/s. This value is at the same order of magnitude of the GB diffusion coefficient (D_{GB}^{Dy}) determined in this study. In our study, the GB diffusion coefficient was found to be similar to the apparent diffusion coefficient D_{app}^{Dy} (see 4.2.2). This result is consistent with the assumption that the diffusion in GBs is the limiting factor of the penetration of Dy into the magnet.

4.5 Conclusion

The Dy concentration map (see Figure 99) shows the presence of two regions in the GBDP NdFeB magnet: region 1 where Dy is concentrated inside the 2:14:1 grains, and region 2 where the Dy is mainly localized at the GBs.

- At the surface of the GBDP magnet, Nd is the main REE found at the surface. This shows that almost all the Dy deposited at the surface of the magnet has penetrated inside the magnet. A small amount of Dy remains trapped inside the oxides formed at the surface of the magnet. This Dy is being wasted since it doesn't contribute to the overall enhancement of coercivity via the GBDP.

- The region 1 of the GBDP magnet contains 16% of the Dy that have penetrated into the magnet. This Dy is wasted since it does not contribute to the GBDP. The grains inside this region are coarser than the ones in region 2.

- In the region 2, the penetration of Dy inside the NdFeB magnet is mainly driven by the liquid phase present et the GBs. The Dy penetrates inside this liquid phase by substituting Nd atoms that are ejected towards the surface of the magnet.

- Dy enrichment inside the Nd-rich secondary phases of type I does not modify their chemical compositions. The Nd-rich phases formed after annealing are similar with or without the GBDP.

- Nd-rich secondary phases of type II trap considerable amount of Dy (up to 20-25%). This Dy is wasted since type II does not contribute to enhance the magnetic properties.

Observations made using quantitative EDS analysis shed new light on the distribution of Dy in the microstructure. Namely, two observations can be reported:

- Almost all the Dy deposited at the surface of the magnet has penetrated inside the magnet. Hence, the diffusion source cannot be considered as an infinite source.

- In region 2, the Dy substitution rate in the shells does not exceed the 20-30% range.

These two observations must be considered to explain shell formation mechanism. This is what we propose to do in chapter V.

5. Chapter V: Discussion

In this chapter, simulations will be implemented to propose interpretations of the questions raised at the end of chapter IV.

- For the first question, concerning the finite diffusion source, a diffusion model with a finite source is used to simulate the averaged Dy concentration profiles. It is worth to note that in literature regarding Dy-GBDP in sintered NdFeB magnets, a finite diffusion source was never considered before. The goal is to evaluate the impact of a finite diffusion source on the evolution of the concentration profiles compared to the case with an infinite diffusion source. Namely, we seek to check if, by considering a finite diffusion source, we can show that the concentration profiles do not evolve according to the treatment conditions.

- For the second question, which concerns the Dy substitution rate ranging between 20-30% inside the Dy-rich shells, thermodynamic simulations are performed to see whether an approach based on phase diagrams could explain this rate.

- Concerning the Dy plateau observed at the level of the Dy-rich shells, two approaches are evoked. The first is the Chemically Induced Liquid Film Migration (CILFM) introduced in chapter I, and the second is a non-linear diffusion model that we propose in this work.

We conclude this chapter by an interpretation of the results based on the different simulations.

5.1 Simulation of the diffusion with a finite source

Several authors proposed to describe the Dy concentration profiles after GBDP considering diffusion models based on some features of the microstructure of the polycrystalline sintered materials. This approach was used to account for the evolution of the averaged concentration of Dy as a function of the depth from the magnet surface. As discussed previously, Loewe et al.[79] assumed that the evolution of the Dy content in the solid shells C_{shell}^{Dy}, as measured at RT, reflects the Dy diffusion profile along the liquid phase formed during the thermal treatment at 900°C. Accordingly, they determined, after fitting these concentration profiles, a diffusion coefficient that is representative of the diffusion of Dy along the grain boundaries, D_{GB}^{Dy}.

Fliegeans et al.[85] extended this model considering that the diffusion into the $Nd_2Fe_{14}B$ solid grains, from their surface, also occurs during GBDP. They implemented the Fisher model to estimate the penetration of Dy into the grains by solid state diffusion. For this computation, a second diffusion coefficient is required, i.e., the volume (bulk) diffusion coefficient D_v^{Dy}. It is worth noting that in this model the diffusion source was assumed to be infinite, in other words, the Dy concentration at the magnet surface (the boundary condition for the diffusion model) was supposed to be

constant. This approximation is questionable in the present work since, as seen in chapter IV, almost all of the Dy deposited on the surface of the magnet has penetrated inside. Therefore, the purpose of the next paragraph is to discuss about the impact of the finite source on the diffusion profiles.

5.1.1 Homogeneous diffusion with finite source

The aim of this section is to simulate the evolution of the Dy concentration profiles with the diffusion time when considering a finite diffusion source. It is worth noting that for the sake of simplicity we will consider here the diffusion problem for a uniform and homogeneous semi-infinite medium. Hence, the distinction between the diffusion along the liquid intergranular phase (D_{GB}^{Dy}) and within the grain (D_{v}^{Dy}) is not taken into account explicitly. Rather, the Dy concentration considered in this section refers to the averaged values measured in section 4.2.2 of chapter IV, and from which an apparent diffusion coefficient was determined $D_{app}^{Dy} = 6 \times 10^{-13}$ m²/s.

At the beginning of the GBDP, Dy is still available on the surface of the magnet. In this case, the source can be assumed infinite and the Dy concentration profile is governed by the Grube's model used in chapter IV (Eq.(4.1)). As the time increases, the diffusion source is "exhausted". Grube's model remains valid up to a time t_s that represents the time required for consuming the Dy deposited at the surface of the magnet. For $t > t_s$, Eq. (4.1) is replaced by a more complex analytical expression that takes into account the source "starvation". The concentration profile is then given under the following integral form:

$$\frac{C(z) - C_s}{C_0 - C_s} = \int_0^{\infty} \frac{\operatorname{erfc}(z'/2l)}{2\sqrt{\pi D_{app}^{Dy}(t - t_s)}} \left\{ \exp\left[\frac{-(z - z')^2}{4D_{app}^{Dy}(t - t_s)}\right] + \exp\left[\frac{-(z + z')^2}{4D_{app}^{Dy}(t - t_s)}\right] \right\} dz', \quad (5.1)$$

where l denotes the diffusion length for $t = t_s$, i.e., $l = \sqrt{D_{app}^{Dy} t_s}$.

The Eqs (4.1)-(5.1) are solved with a Scilab script for the following parameters values:

- Total amount of Dy deposited on the magnet surfaces = 0.7 % of the mass magnet
- $D_{app}^{Dy} = 6 \times 10^{-13}$ m²/s
- Magnet thickness = 5 mm
- C_s = 10 wt.% and C_0 = 0.2 wt.%
- $t_s \approx$ 3h

The resulting concentration profiles are plotted as function of the depth for the different GBDP times in Figure 132.

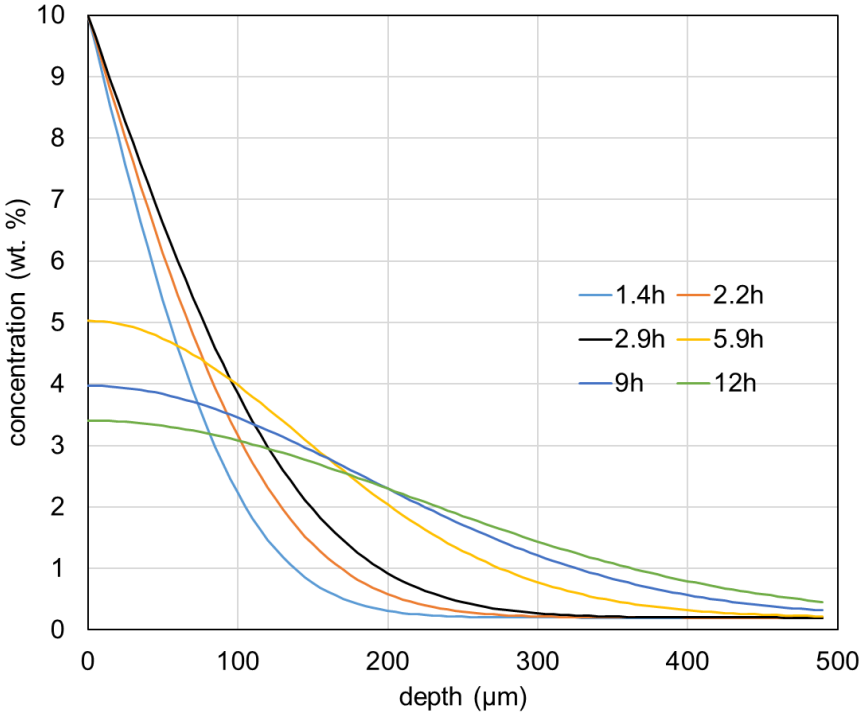

Figure 132: Evolution of the concentration profiles with time calculated with the apparent diffusion coefficient (homogeneous model) considering a finite source term.

Figure 132 shows that for $t < t_s$ (i.e., infinite diffusion source), the concentration at the magnet surface is constant and decreases exponentially with increasing magnet depth. The concentration profiles exhibit a growing diffusion length as the time rises. For $t > t_s$ (i.e., finite diffusion source), the calculated concentration values near the magnet surface (depth < 200 µm) decrease with time and the profile becomes flat while the diffusion length still rises.

This simple model shows that in case of a finite source, the external layer of the magnet (i.e., the part of the magnet just below its surface) firstly experiences a step of Dy accumulation followed by a regime for which this external layer acts as a secondary diffusion source feeding the inner regions of the magnet. However, it is worth noting that the diffusion model, based on the apparent diffusion coefficient D_{app}^{Dy}, predicts a trend toward the spreading of the Dy concentration, i.e., a continuous increase in the diffusion length, that is not confirmed by the experimental data as pointed out in chapter IV.

A possible explanation of this mismatch may lie in the fact that Dy penetrates the bulk of the magnet not as if the medium was homogeneous but rather differently via grain boundaries and the grains bulk. This assumption will be investigated in the next paragraph.

5.1.2 Heterogeneous diffusion with finite source

As explained in section 1.3.2.1, Fliegans et al.[85] used the Fisher model to simulate the Dy distribution in the GBDP magnet. The Fisher model[150] depicts the diffusion in grain volume and along grain boundaries.

The diffusion coefficients in both media, grain boundary and grain volume, are assumed to be independent of the concentration. For the GB medium, Fliegans[85] used the GB diffusion coefficient determined by Loewe et al.[151] (D_{GB}^{Dy} = 1.1 × 10^{-10} m^2/s); for the volume medium, he used an expression given by De Campos et al.[152] to calculate the volume diffusion coefficient as a function of the GBDP temperature (D_v^{Dy}= 1.3 × 10^{-17} m^2/s at 920°C). The Fick's laws are solved in each media with a continuity condition at the interface.

In this work, further improvements of the Fisher model have been considered here: (i) a more precise solution to the diffusion problem taking into account the time derivative of the concentration due to Whipple[153] and (ii) a solution accounting for a finite amount of material used as diffusion source due to Suzuoka[154]. The analytical solutions express the concentration as a function of two spatial coordinates: the depth from the surface (y) and the lateral distance from the grain boundary center (x).

The constant (infinite) source solution is given as:

$$C_c(x,y,t) = C_s\left[\operatorname{erfc}\left(\frac{\eta}{2}\right) + \frac{\eta}{2\sqrt{\pi}}\int_1^{\Delta}\exp\left(-\frac{\eta^2}{4\sigma}\right)\operatorname{erfc}\left\{\sqrt{\frac{\Delta-1}{\Delta-\sigma}}\left(\frac{\xi}{2}+\frac{\sigma-1}{2\beta}\right)\right\}\frac{d\sigma}{\sigma^{3/2}}\right]. \quad (5.2)$$

The instantaneous (finite) source solution is expressed as:

$$C_f(x,y,t) = \frac{K}{\sqrt{\pi D_v t}}\left[\exp\left(-\frac{\eta^2}{4\sigma}\right) + \frac{1}{4}\int_1^{\Delta}\left(\frac{\eta^2}{\sigma}-2\right)\exp\left(-\frac{\eta^2}{4\sigma}\right)\operatorname{erfc}\left\{\sqrt{\frac{\Delta-1}{\Delta-\sigma}}\left(\frac{\xi}{2}+\frac{\sigma-1}{2\beta}\right)\right\}\frac{d\sigma}{\sigma^{3/2}}\right]. \quad (5.3)$$

The reduced variables are defined as (with a being the half width of the GB):

$\eta = y/\sqrt{D_v t}$, $\xi = (x-a)/\sqrt{D_v t}$, $\Delta = D_{GB}/D_v$, and $\beta = (\Delta-1)a/\sqrt{D_v t}$.

The variables η and ξ represent dimensionless coordinates perpendicular and parallel to the GB respectively. The parameters Δ and β are measures of the magnitude of the GB diffusivity relative to the volume diffusivity.

In (5.2) C_s denotes the constant concentration at the magnet surface and K in (5.3) represents the total amount of Dy deposited at the surface divided by the area (surface concentration).

Figure 133 extracted from the work of Suzuoka compares the calculated concentration profiles obtained with constant and finite diffusion sources.

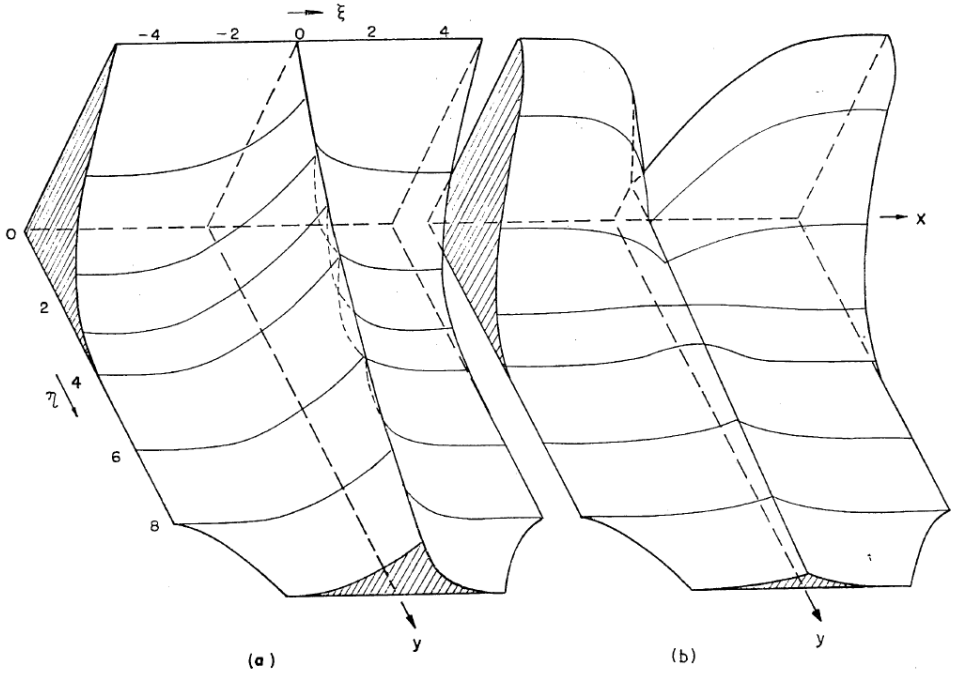

Figure 133: Concentration profiles at different depths of a bi-crystal model calculated with the Whipple solution (left) and the Suzuoka solution (right) for reduced time β = 50. The grain boundary center line is located at x=0, and the magnet surface corresponds to y=0. Adapted from Suzuoka[154].

Interestingly, it can be seen that, when a finite source is considered, a depletion of the concentration could appear near the grain boundary for grains located near the magnet surface. As a result, the direction of diffusion is reversed, from the grains to the grain boundaries. This behavior reflects the fact that these grains become, after a given time, the new diffusion source for the deeper layers once the deposited material has been consumed. This observation is interesting since it might explain the occurrence of the anti-core-shell microstructure seen in our samples in chapter IV (section 4.2.4). In the following, we will check whether this is indeed the case.

Firstly, the averaged concentration profiles along the magnet depth for infinite and finite diffusion sources are plotted on Figure 134.

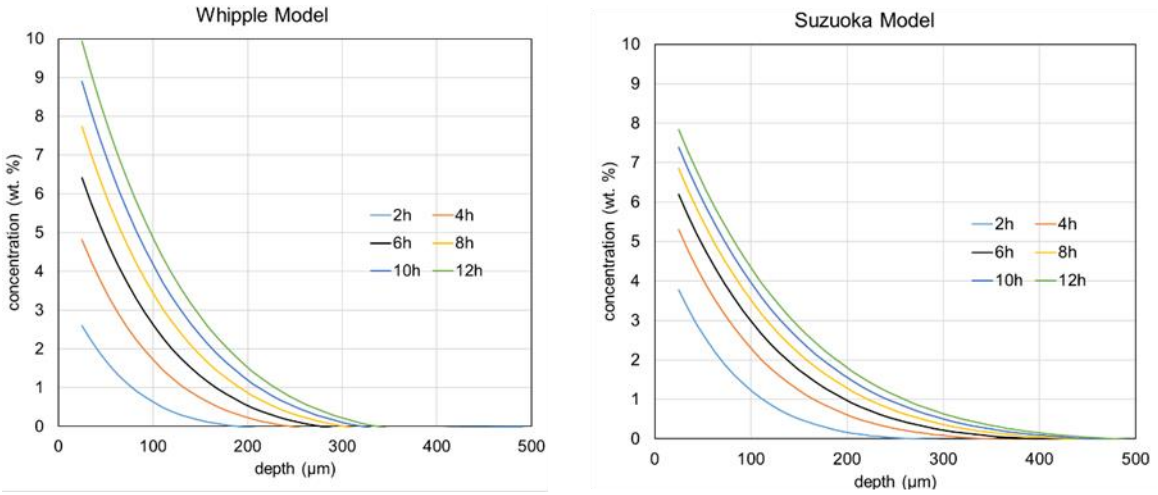

Figure 134: Evolution with time of the averaged concentration profiles calculated for the bi-crystal model with relations (5.6) for the constant source and (5.7) for the finite source for diffusion coefficient evaluated at 920°C.

The profiles are computed using equations (A.2.1) for the infinite source and (A.2.2) for the finite source derived by Suzuoka and reported in Appendix 2. These equations are analytical expressions giving, for a given depth value (y), the concentration averaged along the lateral direction (x). The calculation has been performed with a Scilab subroutine. The diffusion coefficient values D_v^{Dy} and D_{GB}^{Dy} taken here are 1.3×10^{-17} m²/s and 6×10^{-13} m²/s respectively. It is worth noting that, with such values, the reduced parameter β is comprised between 10^4 and 10^5, considerably higher than $\beta = 50$ in the case of Suzuoka. The value of a is 10 nm.

Figure 134 shows that the profiles decrease monotonically from the surface in both cases. For a finite source, the average concentration, for a given depth value, rises slower compared to the constant source case. The evolution calculated in 5.1.1 for a finite source with an apparent (homogeneous) diffusion coefficient (see Figure 132) is not reproduced here, notably the decrease in the concentration with time calculated near the surface due to the source consumption. In order to reproduce the same behavior, the diffusion coefficient in the grain bulk (D_v^{Dy}) should be larger. Figure 135 shows the results obtained with a value of D_v^{Dy} artificially multiplicated by a factor 10^4 leading to β values comprised between 6 and 200.

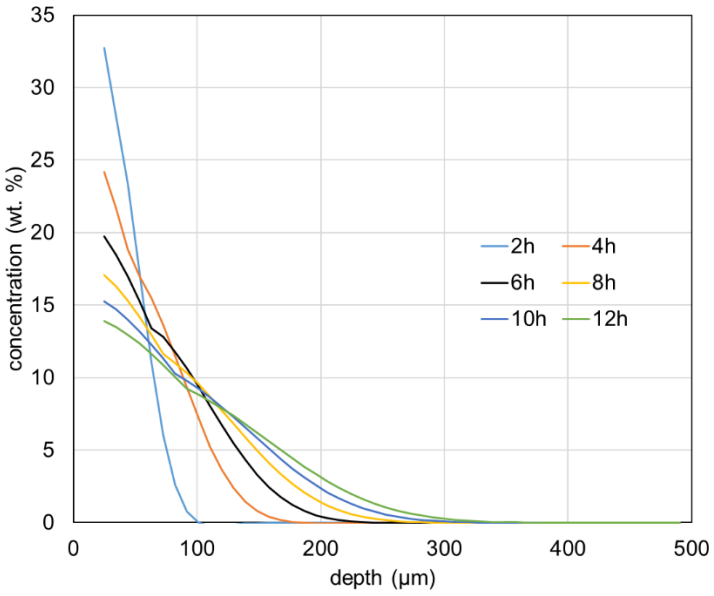

Figure 135: Evolution with time of the averaged concentration profiles calculated for the bi-crystal model with the relation of Suzuoka (5.7) for the finite source for a diffusion coefficient $\mathbf{D_v^{Dy}}$ augmented by a factor 10^4 compared to the case of Figure 134.

Finally, Figure 136 shows the time evolution of intragranular concentration profiles for grains at depths of 100 and 200 µm calculated with a finite source. It can be noticed that the concentration near the grain surface (x = 0) decreases with time for y = 100 µm whereas it increases with time toward an asymptotic for y=200 µm.

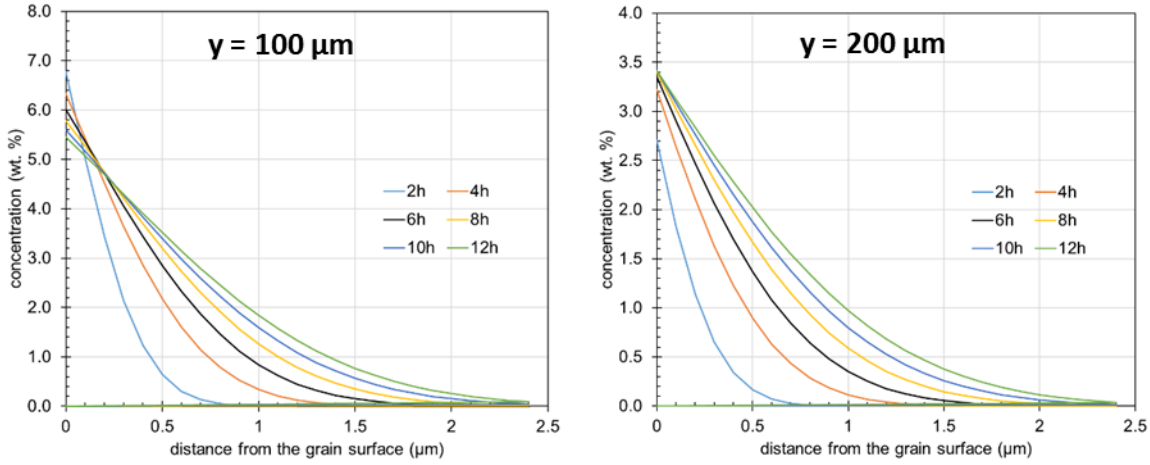

Figure 136: Intragranular Dy concentration profile calculated for the $Nd_2Fe_{14}B$ grains located at two depths 100 µm (left) and 200 µm (right) in the case of a finite source.

Figure 137 displays the evolution with time of the concentration at grain surface for several depths.

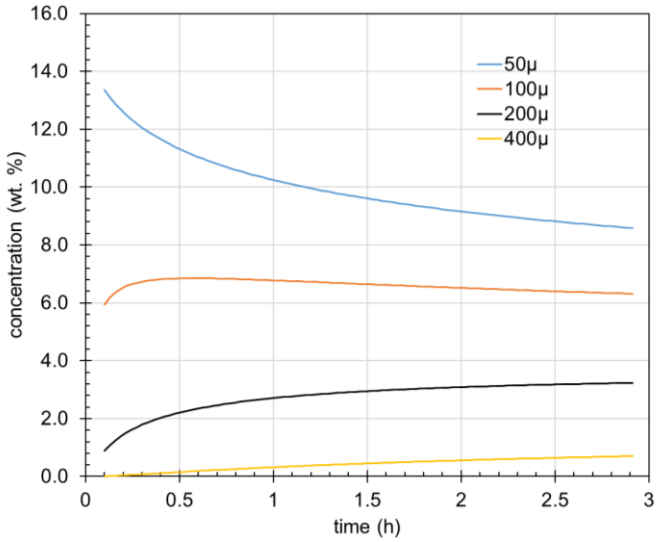

Figure 137: Evolution with time of the intragranular Dy concentration profile calculated for the $Nd_2Fe_{14}B$ grains located at different depths in the case of finite source.

This figure highlights two different behaviors: for depth values lower than 100 µm, the concentration decreases with time whereas the concentration rises for deeper regions. Furthermore, it can be noticed that the concentration at grain surface evolves very slowly for time higher than 3h.

5.1.3 Synthesis on diffusion models

The diffusion model based on a finite diffusion source shows that the diffusion length still grows with the diffusion time but at a lower speed compared to the case of an infinite diffusion source. Hence, this model does not explain the departure of the averaged concentration profiles from a $t^{-1/2}$ law. In addition, the model does not show the occurrence of the anti-core-shell microstructure clearly observed in chapter IV near the magnet surface. A diffusion model based on finite diffusion source does not explain the observed experimental microstructure.

5.2 Simulation of the Dy-shell formation

The aim of this section is to understand the Dy concentration profiles at the level of the Dy-rich shell. For that, the two mechanisms evoked in literature, namely the solidification of the liquid phase and the chemically induced liquid film migration (CILFM) (see section 1.3.2 of chapter I) are first investigated. Finally, an improvement of the diffusion model is proposed to account for the formation of the Dy-rich shells.

5.2.1 Partial melting of grains

5.2.1.1 Liquid phase fraction without Dy in the GB phase

The amount and composition of the liquid phase present at the GBs at 900°C (GBDP temperature) can be determined based on thermodynamic calculations. Figure 138 displays the isopleth at 80 wt.% Fe extracted from the ternary phase diagram Nd-Fe-B.

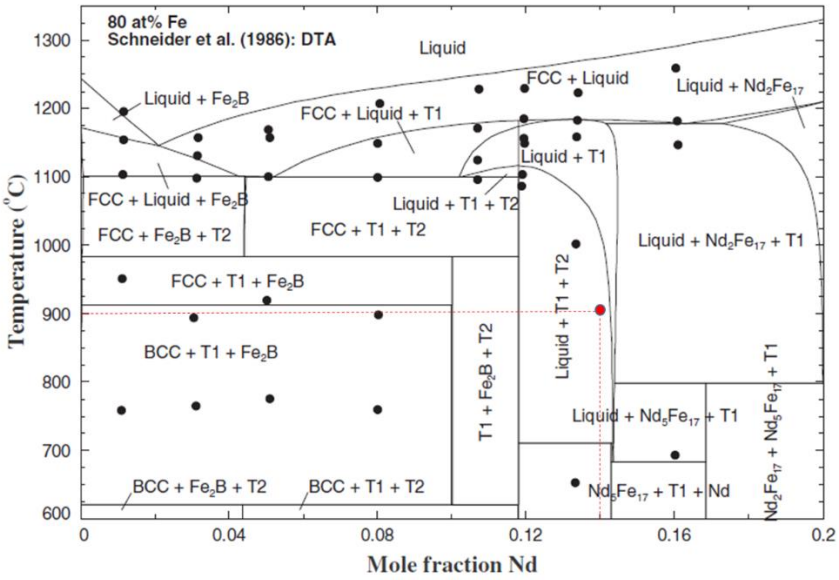

Figure 138: Isopleth at 80 at% Fe extracted from Nd-Fe-B ternary phase diagram. Adapted from Van Ende[30].

The red point plotted in the diagram stands for the ternary $Nd_{14}Fe_{80}B_6$, which corresponds to the mass composition ($Nd_{30.82}Fe_{68.19}B_{0.99}$), i.e., close to the content of the majority elements in the studied samples: $(Nd,Pr,Dy)_{31}Fe_{67.1}Co_{0.5}Cu_{0.1}Al_{0.3}B_1$ (wt.%). For the ternary $Nd_{14}Fe_{80}B_6$, the phases formed at 20°C are $Nd_2Fe_{14}B$ (T1), $Nd_{1.11}Fe_4B_4$ (T2) and α-Nd, whereas at 900°C the phases T1 and T2 coexist with a liquid phase made of Nd, Fe and B as seen from Figure 138.

Since 3 phases are present at 900°C, the lever rule cannot be applied to determine their amount. Hence, the amount of each phase has been calculated using the Calphad software based on the standard minimization of the Gibbs free energy. In addition, the chemical composition of the liquid phase is determined. The results are given in the Table 37.

Table 37: Phase fraction (wt.%) of the phases formed at 20°C and 900°C inside the magnet of composition $Nd_{30.82}Fe_{68.19}B_{0.99}$ (wt.%).

Temperature	**$Nd_2Fe_{14}B$ (T1)**	**$Nd_{1.11}Fe_4B_4$ (T2)**	**α–Nd**	**Nd-rich liquid**	
				Mass fraction	Composition
20°C	93.93 %	0.51 %	5.57 %	-	-
900°C	91.53 %	0.32 %	-	8.15 %	$Nd_{77.05}Fe_{22.43}B_{0.52}$ (wt.%) or $Nd_{54.28}Fe_{40.74}B_{4.97}$ (at.%)

As seen from Table 37, when the temperature increases from 20°C to 900°C, α-Nd melts and transform into a liquid phase. The solid phases T1 and T2 partially melt leading to an enrichment with Fe and B of the liquid phase. Hence, the latter has a composition of $Nd_{77.05}Fe_{22.43}B_{0.52}$ (wt.%) and represents a mass fraction of 8.15%. This liquid phase is located at grain boundaries and surrounds the grains of the T1 phase at 900°C. During the GBDP, the liquid will be enriched by Dy owing to the grain boundary diffusion.

During the cooling down, a part of the liquid phase will solidify into α-Nd, while the other part will solidify in the form of 2:14:1 phase enriched with Dy. The amount of 2:14:1 phase that will solidify around the grains is given by the difference of the mass fractions of T1 at 20°C (93.9 %) and 900°C (91.5 %). For the studied composition, the fraction of this solidified shell is expected to be equal to 2.4 %. This value is much lower than the measured fraction of Dy-rich shell (e.g., at a depth of 150 μm, the measured fraction of Dy-rich shells is 30%).

A possible explanation proposed by Seelam et al.[80] would involve a higher content of rare earth elements evidenced by the authors in regions close to the magnet surface (at a depth of ≈ 50 μm). The authors showed that the surface fraction of the α-Nd phases increases from 5-6% before GBDP to 8-11% after the GBDP in regions near the magnet surface. As a result, the amount of liquid phase at 900°C increases with the content of Nd at the expense of T1 and T2 phases as illustrated by the isopleth at 6 at.% B (Figure 139).

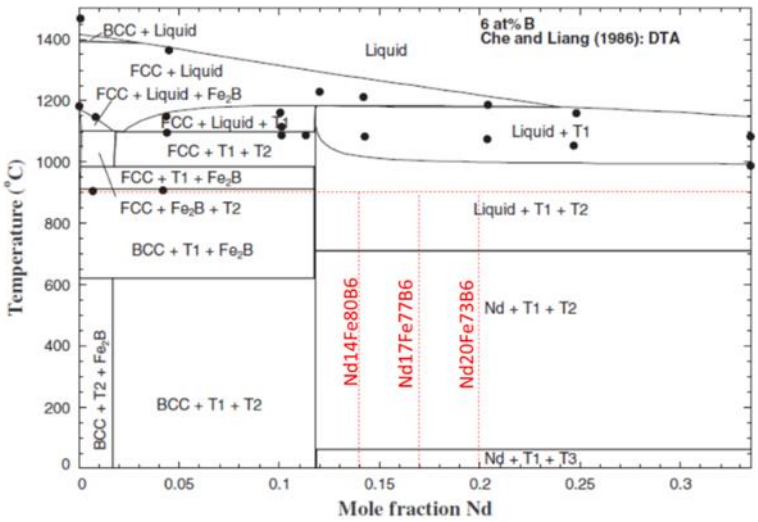

Figure 139: Isopleth at 6 at% B extracted from Nd-Fe-B ternary phase diagram. Adapted from Van Ende[30].

For the compositions $Nd_{17}Fe_{77}B_6$ and $Nd_{20}Fe_{73}B_6$ the fraction of the shell would rise to 5.7 % and to 9.1 % respectively. However, in this study, such Nd enrichment was only observed at the surface of the magnet surface and up to a depth of 50 μm (i.e., region 1). In region 2, where the core-shell microstructure is formed, this Nd enrichment was not evidenced here.

In the following, another way to explain the increase in the amount of liquid phase is proposed by considering the effect of the partial substitution of Nd by Dy in the liquid phase.

5.2.1.2 Liquid phase fraction with Dy in the GB phase

Further thermodynamic calculations have been made to estimate the evolution of the fraction of the liquid phase formed at 900°C taking into account a partial substitution of the Nd by Dy atoms. The Dy atoms are supposed to be supplied by the diffusion of the heavy rare earth from the magnet surface along the GBs. It is worth noting that the total amount of REEs has been considered to be constant and equal to the nominal value 30.82 wt.%. In other terms, the approach considered here is different than the one suggested by Seelam[80] where Dy is considered to increase the total amount of REE. Instead, we consider that Dy atoms penetrate the magnet and partially substitute Nd atoms that exit the magnet towards the surface, such that the total amount of REEs remains unchanged (30.82 wt.%). The thermodynamic parameters required for the calculation of the Gibbs energy into the liquid with a mixture of Nd and Dy have been extracted from the work of Dai et al.[155]. For the solid, it has been assumed that Nd and Dy have the same properties. Four cases with different overall Dy content were examined: $Nd_{29.82}Dy_{1.0}Fe_{68.19}B_{0.99}$, $Nd_{28.82}Dy_{2.0}Fe_{68.19}B_{0.99}$, $Nd_{27.82}Dy_{3.0}Fe_{68.19}B_{0.99}$, and $Nd_{26.82}Dy_{4.0}Fe_{68.19}B_{0.99}$ which correspond to an overall added Dy of 1 wt.%, 2 wt.%, 3 wt.%, and 4 wt.% respectively. The results are reported in Table 38.

Table 38: Evolution of the mass fraction of the phases present at equilibrium in the NdFeB system at 900°C with respect to the overall amount of Dy.

Overall Dy content (wt.%)	**$Nd_2Fe_{14}B$**	**$NdFe_4B_4$**	**Liquid**			**Fraction of Dy-rich shells**
			Mass fraction	Composition (wt.%)	$\frac{Dy}{Nd+Dy}$	$Nd_2Fe_{14}B$ (RT) - $Nd_2Fe_{14}B$ (900°C)
Without Dy	91.53 %	0.32 %	8.15 %	$Nd_{77.05}Fe_{22.43}B_{0.52}$	0	2.4%
+ 1 wt.%	90.30 %	0.07 %	9.64 %	$Nd_{59.16}Dy_{10.38}Fe_{29.63}B_{0.83}$	15%	3.63%
+ 2 wt.%	88.99 %	0 %	11.01 %	$Nd_{46.10}Dy_{18.17}Fe_{34.83}B_{0.91}$	28%	4.94%
+ 4 wt.%	85.99 %	0 %	14.01 %	$Nd_{27.66}Dy_{28.54}Fe_{42.87}B_{0.93}$	50%	7.94%
+ 6 wt.%	82.47 %	0 %	17.53 %	$Nd_{16.06}Dy_{34.23}Fe_{48.77}B_{0.94}$	68%	11.46%

Table 38 shows that by increasing the Dy/(Nd+Dy) ratio in the liquid phase, a higher amount of the 2:14:1 solid phase melt, resulting in an increase in the amount of the liquid phase. As part of the 2:14:1 phase is dissolving in the liquid phase, the iron and boron contents of the liquid increase. The evolution of the amount of liquid phase and the Fe content in it are plotted in Figure 140.

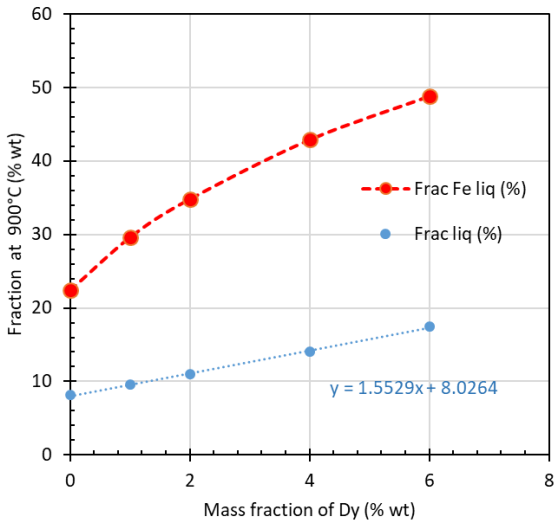

Figure 140: Evolution of liquid phase fraction and the iron content of the liquid phase with the total amount of Dy.

At a depth of 150 µm, the average Dy concentration (i.e., overall Dy content) measured in chapter IV is 1.6 at.% (see Figure 105) which is equivalent to 1.8 wt.%. The closest value to 1.8 wt.% is 2 wt.% in Table 38. For this value, the fraction of the liquid phase rises from about 8 (without Dy) to 11 % and the composition of the liquid phase becomes: $Nd_{46.10}Dy_{18.17}Fe_{34.83}B_{0.91}$ (wt.%). It is worth noting that, in the liquid phase, the ratio (Dy/Dy+Nd) is 0.28. This value is consistent with the Dy substitution rate inside the Dy-rich shells ranging between 20-30% as seen in chapter IV.

The fraction of the Dy-rich shells increases from 2.4% (without Dy) to 4.94%. This value is still lower that the measured one at 150 µm (30%). Accordingly, the Dy enrichment of the liquid phase could not entirely explain the formation of large shells. However, the rise in the amount of the liquid phase could have a positive effect on the diffusivities along the GBs, allowing a percolating network to be more developed as the Dy attains the GBs.

5.2.1.3 Synthesis

In this section, thermodynamic calculations were used to consider the effect of the partial substitution of Nd by Dy in the GB liquid phase on the quantity of the $Nd_2Fe_{14}B$ phase that melts at 900 °C. We showed that, compared to Nd, Dy further melts the $Nd_2Fe_{14}B$ grains hence increasing the fraction of the liquid phase formed at this temperature. However, the Dy enrichment of the liquid phase could not entirely explain the formation of large shells.

5.2.2 Liquid film migration driven by grain coarsening.

Using thermodynamic calculations, we showed that Dy increases the amount of liquid phase present at the GBDP temperature. However, the quantity of this liquid phase remains considerably lower than that required to explain the surface fractions of Dy-rich shells by solidification. That said, this liquid phase might be involved in a liquid film migration process that can explain the surface fraction of the Dy-rich shells. In this process, a driving force can move the wetted grain boundary into one of the parent grains. As the GB is moving, it leaves behind a new solid solution.

Kim et al.[87] proposed the liquid film migration mechanism to explain the formation of the shells based on the microstructure features observed in their study. Namely, they observed grain coarsening near the magnet surface, and showed that it was correlated with the surface fraction of the shells (see Figure 141). Consequently, they proposed that the LFM is driven by grain coarsening.

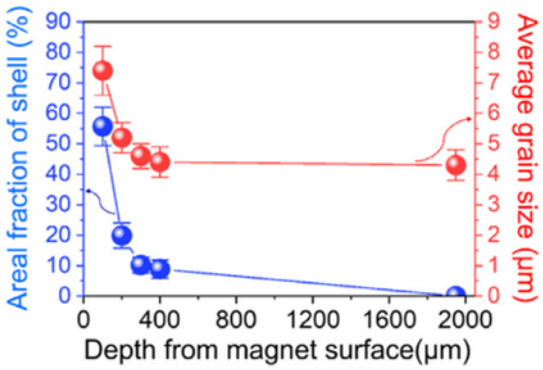

Figure 141: Variations of the areal fraction of the shell and the average grain size as a function of the depth from the sample surface. Adapted from Tae-Hoon Kim et al.[87]

To validate this hypothesis, the authors performed a two-dimensional phase field simulation and showed that the shells are formed when the small grains vanish during grain coarsening, hence supporting the hypothesis.

To check if this mechanism can be applied to this work, the evolution of the shell surface fraction and the average grain size as a function of the magnet depth were plotted in Figure 142.

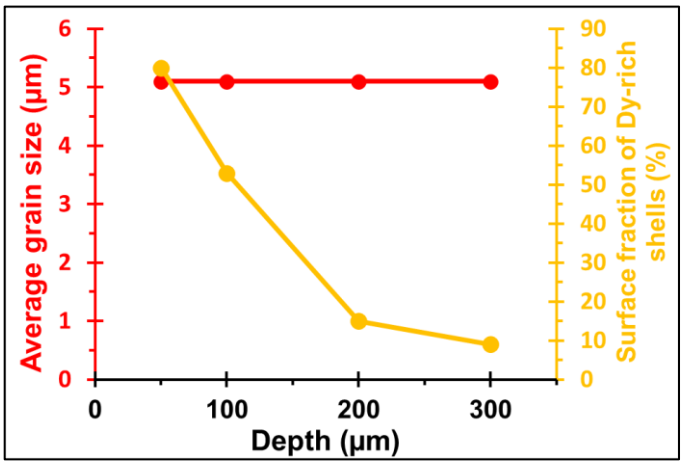

Figure 142: Variations of the areal fraction of the shell and the average grain size as a function of the depth from the sample surface.

Compared to the results of Kim et al.[87], no correlation between the grain size and the fraction of the Dy-rich shells was found here. Our experimental results do not support the grain coarsening as a driving force for the CILFM. Hence, this model is less likely to explain the formation of the Dy-rich shells in this study.

5.2.3 Non-linear Diffusion: concentration-dependent diffusion coefficient

The previous modelling results in section 5.1.2 have been obtained considering that the diffusion coefficient was independent of the concentration. As a result, the intragranular concentration profiles have been found to be decreasing when moving away from the grain surface (see Figure 136). The shape of the modelled intragranular concentration profiles strongly differs from the concentration profile taken across the shell characterized by a plateau accompanied by an abrupt interface when transitioning from the core to the shell as illustrated in Figure 143.

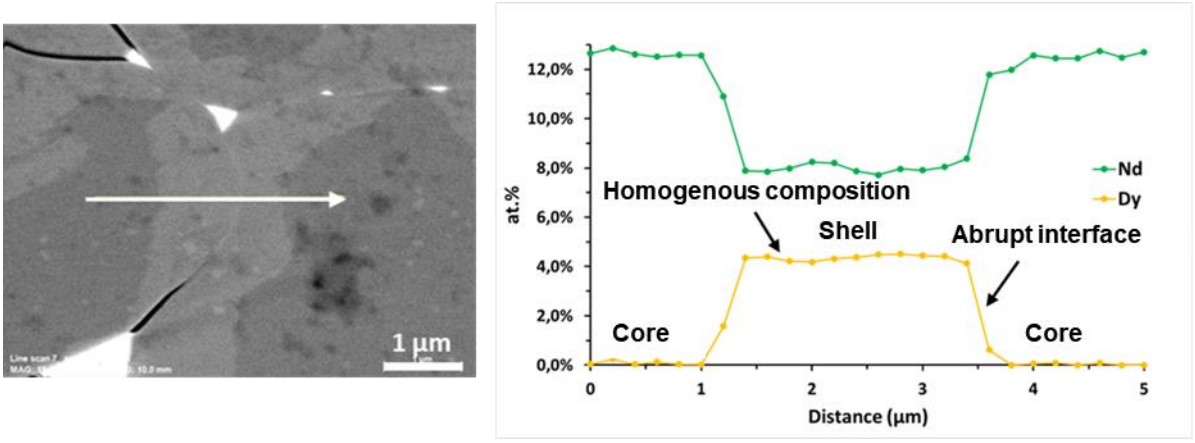

Figure 143: Variation of the Nd and Dy concentration profiles across a core-shell microstructure at z = 60 µm.

Since the diffusion coefficients taken for modeling were considered to be independent from the concentration, the simulated profiles had inherently an exponentially decreasing shape, which is why they strongly differ from the experimentally observed plateau. In fact, a linear diffusion model in which the diffusion coefficient is considered to be independent from the concentration cannot describe the experimentally observed plateau.

Moreover, if we examine closely the shape of the Dy concentration profile given by Cook et al.[156] in their study of the diffusion coefficients (see Figure 144), we can notice that it displays a succession of abrupt falls. This is consistent with a concentration dependent diffusion coefficient and consequently raises a question about the validity of the concentration independent assumption that the authors made in order to determine the Dy diffusion coefficient in $Nd_2Fe_{14}B$ phase.

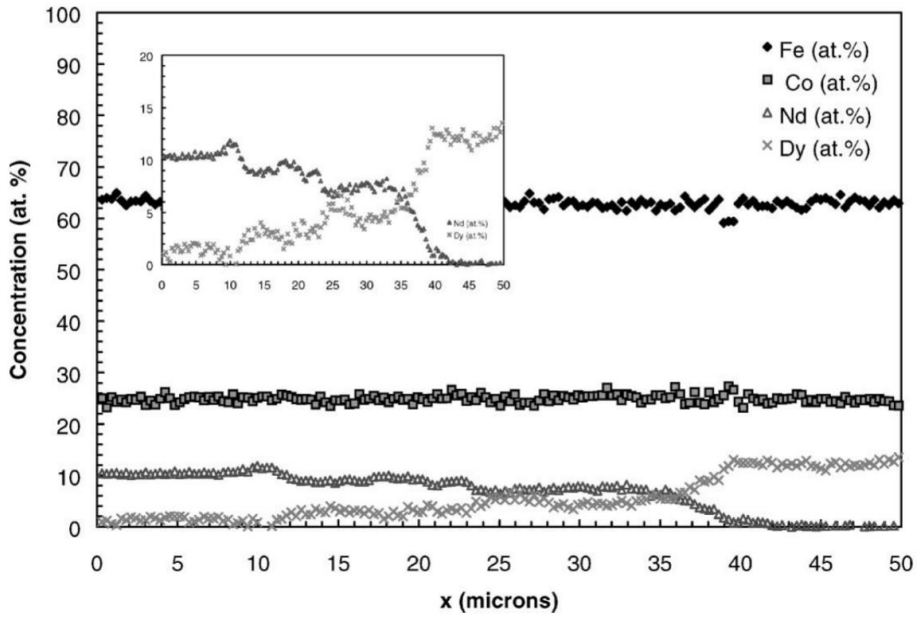

Figure 144: Compositional profiles resulting from bonding of $Nd_2Fe_{10}Co_4B$ and $Dy_2Fe_{10}Co_4B$ at 1323 K for 18000 s (structural details of the rare earth composition curves are shown in the insert). Adapted from Cook[156].

Several diffusion systems exhibiting anomalous diffusion profiles have been studied: for instance, the diffusion of Cd in InSb[157], the diffusion of B-P-As in Si[158] and the diffusion of Ga in single crystals ZnO[159]. In this latest work, the authors performed an implantation of ^{71}Ga atoms in ZnO and measured the Ga profile by SIMS after annealing at 900 °C. Their results are plotted in Figure 145 and revealed a Ga profile featuring a plateau followed by an abrupt decrease in the Ga concentration. The authors fitted the profiles by a diffusion model with a concentration-dependent coefficient. In these three cases, the concentration-dependent diffusion coefficient was physically justified by the transport mechanisms involving different charge states of diffusing vacancies and substitutional species.

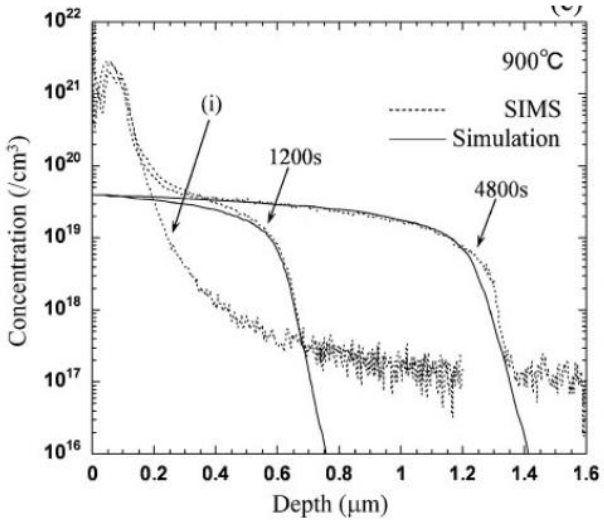

Figure 145: ^{71}Ga concentration profiles in single crystal ZnO and the fitting by the simulation. Profile (i) indicates the implanted standard. The annealing time is shown in the figure. Adapted from Nakagawa[159].

In the case of the diffusion mechanism for Dy in $Nd_2Fe_{14}B$ phase, a concentration dependent diffusion coefficient can be explained by the fact that the Dy diffusing atoms can be 'trapped' into energetically favorable sites (namely, the 4f site with smaller Weigner-Seitz atomic cell volume)[160,161]. This results in a low effective diffusion coefficient for low concentration values. Once the sites would be saturated (for C ~ 8 wt.% determined by taking into account the Dy substitution rate range 20-30%), the effective diffusion coefficient would rise allowing more atoms to fill the diffusing layer. This case of concentration dependent coefficient diffusion in polycrystals is solved in the following section by a numerical approach.

5.3 Finite Element simulation of diffusion in the sintered microstructure

The Finite Element (FE) method allows taking into account transient conditions for the diffusion in 2D/3D heterogeneous media. Owing to the FE approach, the intragranular diffusion profiles in grain are calculated for a finite source of Dy in the case of concentration-dependent diffusion coefficient.

5.3.1 Geometry and boundary conditions

For the simulation performed in this work, the polycrystalline microstructure of the sintered magnet is described as an array of 2D squared grains separated by an intergranular phase. Both media, the grain and intergranular phase, are assumed to be homogeneous and, for each, a diffusion coefficient is ascribed: D_{GB}^{Dy} for the intergranular phase and D_{v}^{Dy} for the grain. The size of grain and the thickness of the intergranular phase are the geometrical parameters of the model. The Dy coating is described as a homogeneous layer with a given initial concentration of Dy (C_0). The thickness of this layer is adjusted to account for the total amount of Dy used for GBDP experiment (0.7 wt.%). The initial Dy concentration in the magnet is assumed to be null.

For the numerical resolution, the sample is discretized into small regular elements (see Figure 146) with a size refinement close to the grain boundary adjusted in order to describe accurately the diffusion gradient in this area. Each grain is spatially discretized into 600 elements, the smallest having a size of 20 nm at GB. Forty rows of grains are considered in the magnet thickness from the magnet surface, each having a size of 5 μm, leading to representation of the polycrystalline media up to 200 μm from the surface. Below 200 μm, the magnet is described as a homogeneous media covering a total depth of 2.5 mm. This approach allows limiting the size of the numerical model. All the boundary lines of this 2D model are ascribed to have a flux equal to 0, meaning that no Dy enters or escapes the represented domain. This boundary conditions account for symmetrical conditions in the periodic array of grains, allowing only a half grain and grain boundary to be represented for each raw. Figure 146 displays the geometrical representation of the sample and the meshing used in the simulation. The diffusion problem is solved by the Finite Element method with the Cast3m software.

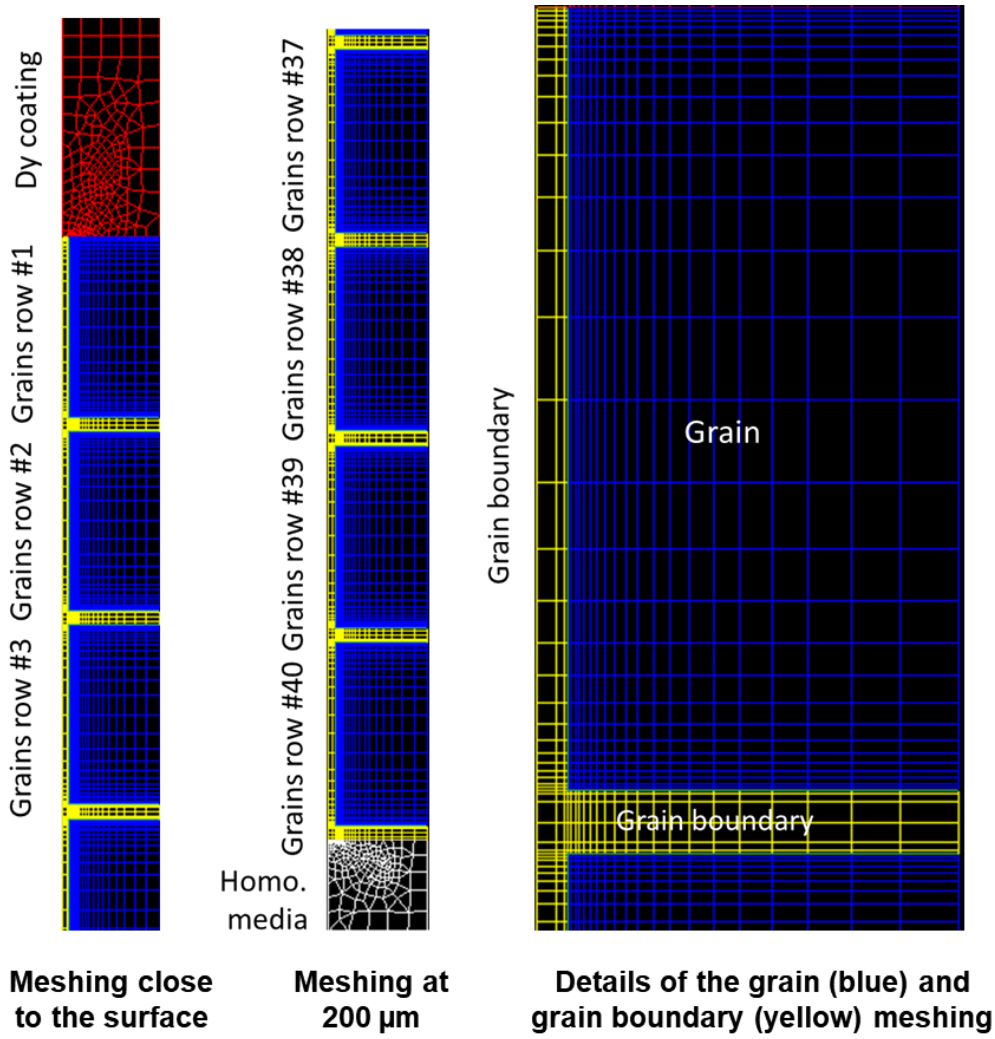

Figure 146: Representation of the sintered microstructure for the Finite Element simulation of the GBDP (the size of the grain is 5 µm and the thickness of grain boundary is 200 nm in this example)

5.3.2 Sets of parameters and results with the reference case

The values of the physical parameters considered are given in the Table 39. The reference case corresponds to the set of parameters already used in the previous semi-analytical calculations (section 5.1.2).

Table 39: Sets of parameters considered for the FE simulation.

	Reference case	Nonlinear diffusion in grains	Enhanced diffusion at GBs
Initial Dy concentration in the coating (C_0) [wt. %]	30	30	30
Grain size [µm]	5	5	5
Grain boundary thickness (2δ) [nm]	10	10	10
Grain boundary diffusion coefficient ($D^0_{GB}.\delta$) [$m^3.s^{-2}$]	$5.5\ 10^{-19}$	$5.5\ 10^{-19}$	$5.5\ 10^{-18}$
Grain diffusion coefficient (D^0_V) [$m^2.s^{-2}$]	$1.3\ 10^{-17}$	$1.3\ 10^{-17} \times f(C)$	$1.3\ 10^{-17} \times f(C)$

Figure 147 shows the average concentration profiles along the depth obtained with the reference set of parameters (linear case) for different times (left) and the intragranular concentration profiles for a grain located at 25 µm (right).

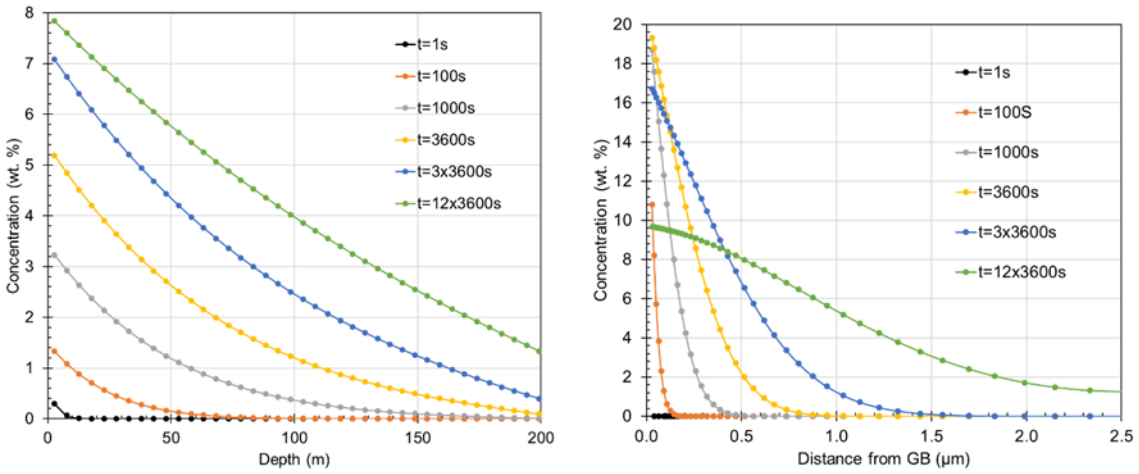

Figure 147: Evolution of the concentration profiles for different time values obtained with the FE approach for the reference set of parameters (left: averaged concentration, right: intragranular concentration at 25 µm)

The evolution of the concentration profiles is consistent with the analytical solution obtained with the Suzuoka approach (see Figure 134 and Figure 136). It is worth noting that for durations greater that 3h, the Finite Element approach accounts for the consumption of the finite source of Dy with a decrease in the intergranular concentration close to the GB.

5.3.3 Results with the non-linear diffusion case

In addition to the reference case, two further cases have been selected for the parametric study. In the first one, a concentration-dependent diffusion coefficient is considered for the intergranular diffusion according to the law: $D_V(C) = D_V^0 \times f(C)$ where the function f(C) is a stepped function plotted in Figure 148. For a concentration of 8 wt.% the value of f changes abruptly from 1 to 10.

This behavior accounts for the assumption of a saturation of the number of sites in the $Nd_2Fe_{14}B$ lattice for a preferential substitution of Nd by Dy.

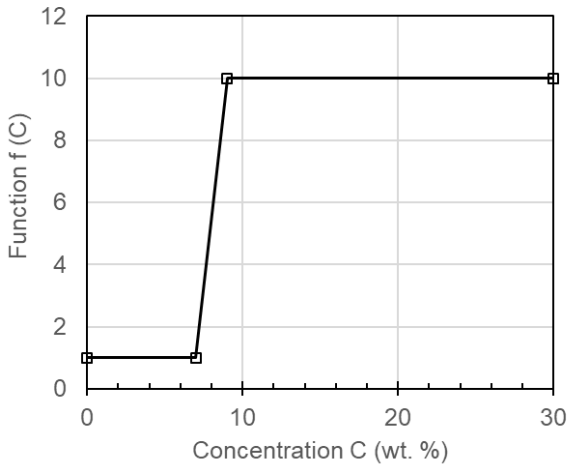

Figure 148: Threshold function implemented for the evolution of the diffusion coefficient with the concentration in the non-linear cases.

The concentration profiles calculated with the non-linear intergranular coefficient given in the second column of Table 39 are reported in Figure 149.

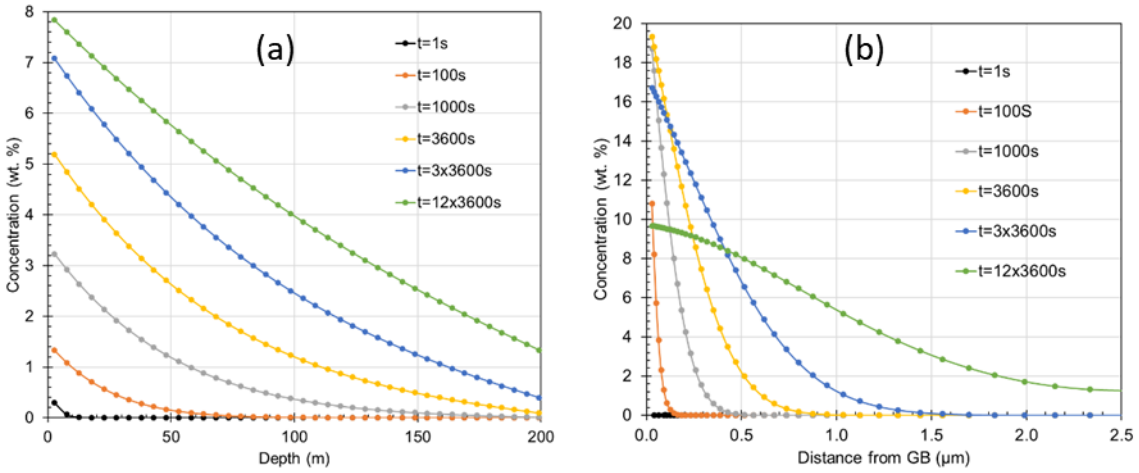

Figure 149: Evolution of the (a) averaged concentration profiles and (b) the intragranular concentration for a grain located at a depth of 50 µm for different time values obtained with the FE approach with a concentration dependent volume diffusion coefficient.

This case provides interesting results:

- Figure 149 (a) shows that, up to 3 hours, the averaged concentration profile along the depth exhibits two parts (characterized by different slopes). Basically, the penetration of the Dy in the magnet is less than with the constant diffusion coefficient. The first part extends until a distance from the surface of about 60- 80 µm and is characterize by a strong retention of the diffusing atoms.

- Figure 149 (b) shows that the intragranular profile at 50 µm displays a sharp diffusion front that progress toward the center of the grain with time. This intragranular profile is very

different from the classical diffusion profile and corresponds well to the experimentally observed plateau.

- Figure 150 shows the evolution of the Dy-rich shells with respect to the magnet depth. The size of the shell decreases with the depth until the connection with the second part of the curve. In this first part, more Dy atoms are incorporated in the grains compared to the constant coefficient diffusion case. In the second part of the averaged profile (>100 µm), the concentration (both averaged and in grains) follow the classical diffusion model with less capture of the diffusing atoms in the grains.

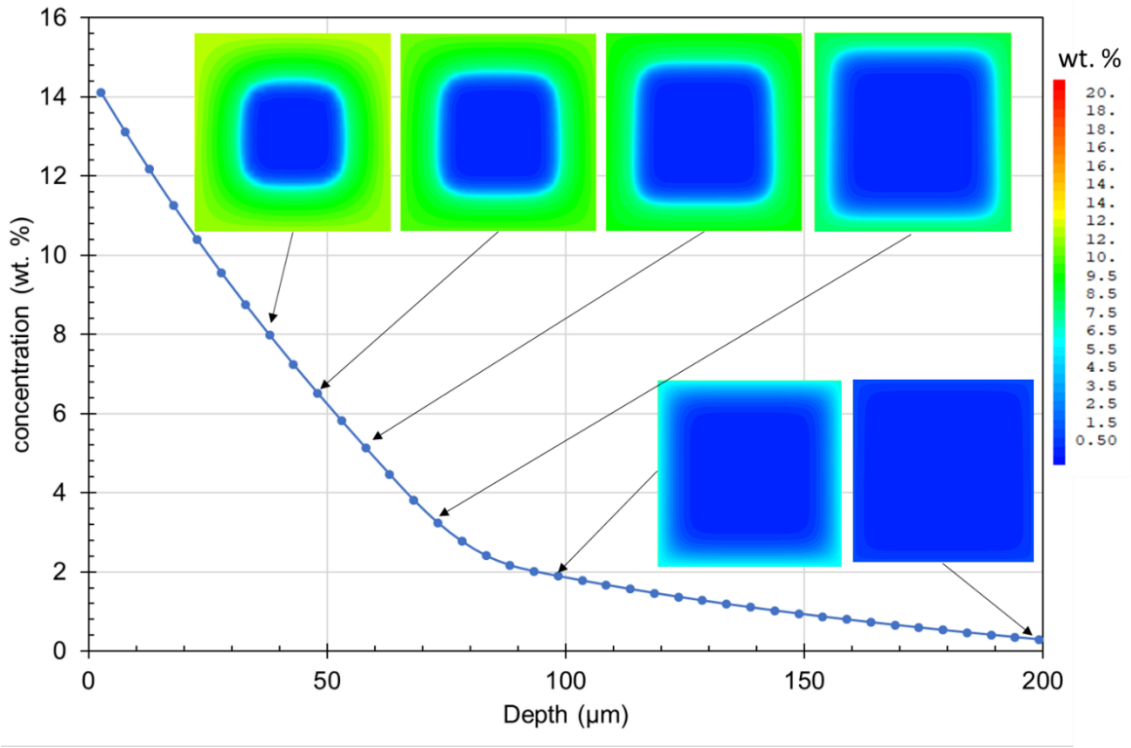

Figure 150: Evolution of the concentration profiles in selected grains at t =3h obtained with the FE approach for the non-linear case with concentration dependent intragranular diffusion coefficient.

Finally, Figure 151 shows the time evolution of the concentration in a grain located at a depth of 10 µm. After 3h, the averaged concentration near the surface is decreasing which corresponds to the consumption of the initial Dy in the coating. This situation leads to the inversion of the gradient of the concentration profile in the grain that could explain the anti-core-shell structures observed near the surface. The averaged concentration profile at 12h displays a second slope change leading to an irregular profile.

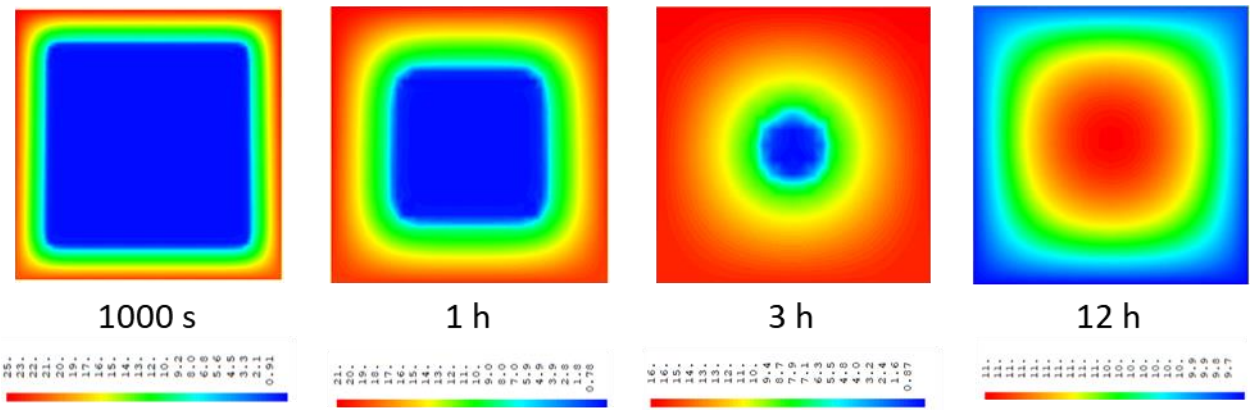

Figure 151: Evolution of the concentration maps with time in the grain located at 10 µm from the surface, in the case of nonlinear intragranular diffusion (concentration in wt. %)

5.3.4 Results with the enhanced grain boundary diffusion

The rise in the diffusion coefficient at GBs, associated to, leads to an increase in the penetration of the diffusing specie into the polycrystalline medium up to 200µm. The averaged concentration profile at 3h is plotted on the Figure 152 using the same scale than for the previous case.

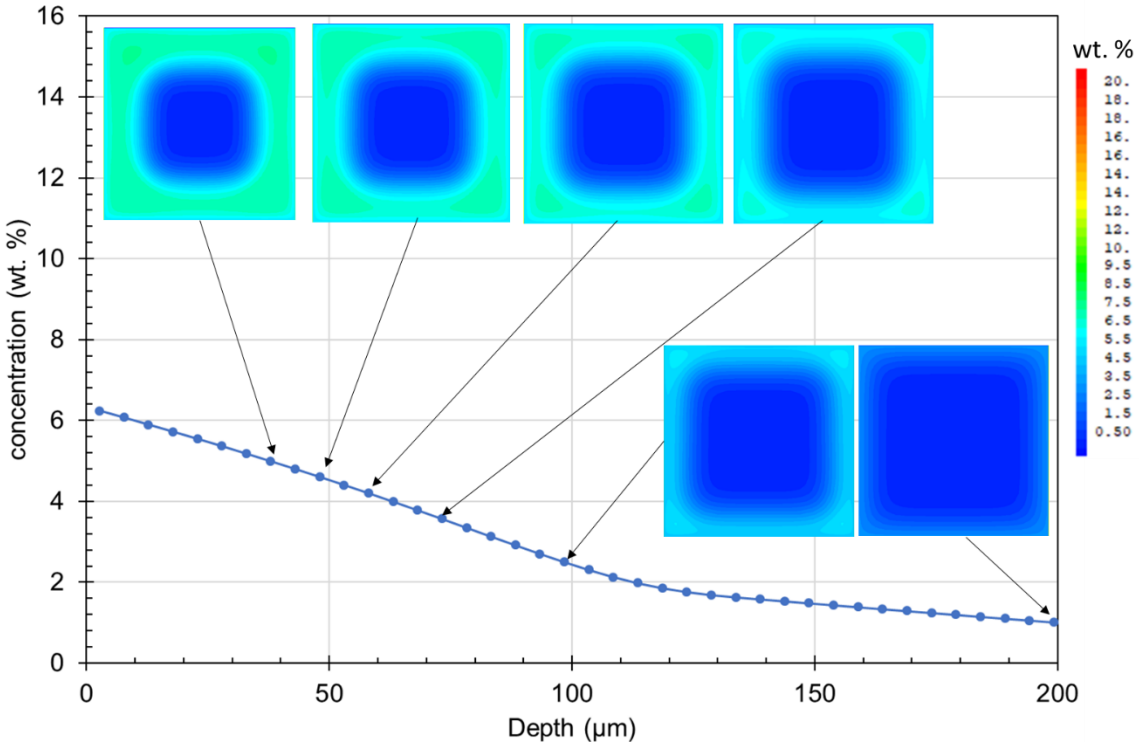

Figure 152: Evolution of the concentration profiles in selected grains at t=3h obtained with the FE approach for the non-linear case with concentration dependent intragranular diffusion coefficient and enhanced diffusion at GBs.

The concentration tends to be more homogeneous due to the faster diffusion at GBs. The stepped intergranular profile is still obtained within the range 50-100 µm but it appears to be less pronounced than the previous case. The concentration maps for a grain located at 10 µm are displayed in Figure 153.

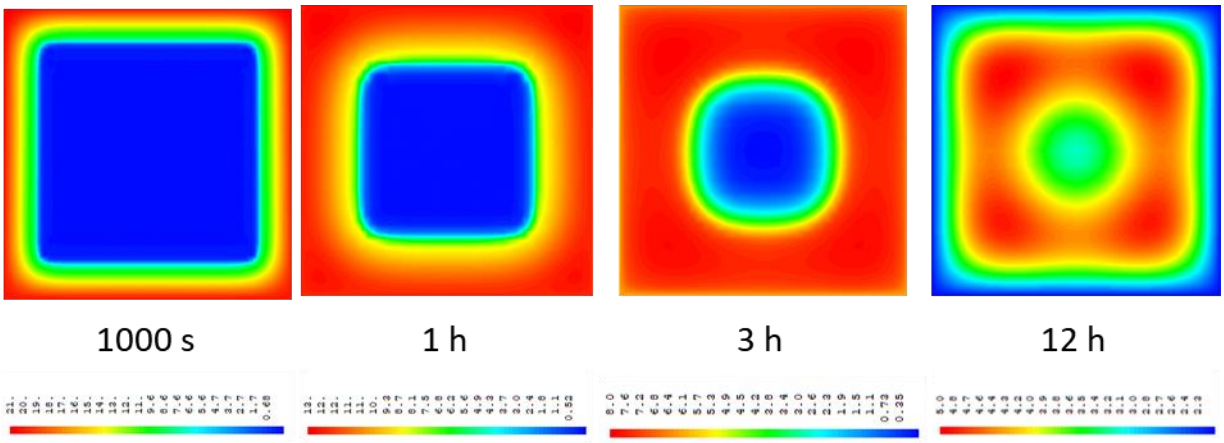

Figure 153: Evolution of the concentration maps with time in the grain located at 10 µm from the surface, in the case of nonlinear intragranular diffusion and enhanced diffusion at GBs (concentration in wt. %)

These maps show that the core-shell distribution appears in the early stage (1h) with a diffusion front that progress inward until the complete 'filling' of this grain that occurs between 3 and 12h. At 12h, the inverse concentration profile is achieved.

5.4 Conclusion

The simulations performed in this chapter enabled to highlight the following elements:

- The formation of a liquid phase at the GBs is crucial for the GBDP. This liquid phase plays a major role in transporting the Dy inside the magnet. However, this liquid phase should be connected so it forms a percolating network to allow the Dy to penetrate and reach all the 2:14:1 grains. It is important to note that this quantity of liquid alone does not explain the thickness of the shell.

- By considering a finite diffusion source, the formation of anti-core shells can be depicted. However, the finite diffusion source shows that the diffusion length grows with the diffusion time. Hence, it does not explain why the experimental concentration profiles do not evolve according to the GBD processing conditions studied in this work.

- FE simulations using a concentration-dependent diffusion coefficient can account for Dy-shell formation by volume diffusion in the grain. However, this coefficient lacks experimental validation. Hence, measurements of diffusion coefficients are required to establish such a relation. This mechanism of shell formation is independent of the quantity of liquid forming at the GBs.

However, these models taken separately, cannot explain with satisfaction the experimental results. Instead, the combination of thermodynamic, diffusion and percolation approaches could better account for our results. For that, and enhanced concentration-dependent diffusion coefficient.

Based on these findings, we propose that it is the percolation that limits the penetration of Dy into the magnet. By diffusing Dy inside the magnet, it will increase the quantity of liquid phase, as shown in the thermodynamic calculations, and will enable crossing the penetration threshold[136].

From the above elements, we can conclude that the following approaches should improve the efficiency of the GBDP:

- Prevent the formation of oxides that trap Dy and block the liquid diffusion channels.
- Increase the liquid quantity by means of eutectics, which form a liquid phase at low temperature.

6. General conclusion and perspectives

The aim of this thesis is to study the Dy-GBDP in polycrystalline sintered NdFeB magnets in order to better understand the distribution of Dy inside the magnets. As stated in the introduction, Dy is a critical material to which geopolitical and environmental challenges are associated. Hence, understanding Dy distribution is crucial to optimize the GBDP by proposing levers allowing to efficiently use the Dy so that it could be used in a lesser amount. In particular, there is a need to clarify the role of the liquid phase formed at the GBs during the GBDP. So far, the role of this phase remains a subject of debate in literature.

To conduct this study, cylindrical shaped (ϕ10 x 5 mm²) sintered NdFeB magnets of nominal composition $(Nd,Pr,Dy)_{31}Fe_{67.1}Co_{0.5}Cu_{0.1}Al_{0.3}B_1$ (wt.%) were prepared on the pilot line of the CEA/LITEN. Hereafter, the magnets were annealed at 540°C to optimize their microstructure. The first part of this work focused on precisely characterizing the microstructure of the magnets prior to the GBDP by analyzing all the phases present in the magnet (main and secondary Nd-rich phases). For that purpose, different electron microscopy techniques (SEM, EDS, WDS, and TEM) were combined. In particular, quantitative EDS was implemented to precisely determine the chemical compositions of the different phases and to track their evolution later on. Four different types of metallic Nd-rich phases (IA, IB, IC and ID) and two types of Nd-oxides (IIA and IIB) were identified. TEM observations confirmed the presence of a NdCu GB phase in accordance with several previous reports. During annealing (here 540°C), low melting metallic Nd-rich phases are in liquid state. The liquid infiltrates along the grain boundaries driven by capillary pressure and surface tension, and the NdCu phase is formed. This phase is non-magnetic and serves to magnetically decouple the $Nd_2Fe_{14}B$ grains leading to a considerable increase in the coercivity (in this study +50%). It is worth to note that the thickness of the GB phase was found to be discontinuous (i.e., thick at the vicinity of the triple junctions and then thins out). In addition, some GBs were lacking this phase. An ideal microstructure requires a continuous GB phase distributed along all the GBs inside the magnet to decouple all the $Nd_2Fe_{14}B$ grains and ensure an optimum coercivity for the magnet.

The second part of this work concerned the evolution of the microstructure of the magnet due to the GBDP. For that purpose, the magnets were coated with DyCo and underwent an annealing treatment at 920°C. Hereafter, the magnets were annealed at 540°C to be able to compare them with the annealed state prior to the GBDP. SEM observations showed the presence of three different regions inside the magnet. First, the surface of the magnet was found to be mainly rich in Nd and O. Minor amount of Dy was also detected but was found to be mainly trapped inside the rare-earth (RE) oxides. This showed that the diffusion source was exhausted and that almost all Dy penetrated inside the magnet. Second, a distinct region 1 underneath the surface of the magnet and up to a depth of ≈ 50 μm was identified. This region is characterized by a high amount of Dy (≈16%) present inside the $Nd_2Fe_{14}B$ grains. This Dy is considered a waste of the heavy rare earth

source since it prevents it from being used deeper inside the magnet. Third, a region 2 (50 μm < z < 400 μm) was identified. In this region, the Dy is mainly localized at the GBs and the outer-layer of the $Nd_2Fe_{14}B$ grains forming a core-shell microstructure. The thickness of the Dy-rich shells was found to be decreasing with increasing magnet depth from 2 μm down to tens of nanometers. Interestingly, the Dy substitution rate (Dy/Dy+Nd) inside the Dy-rich shells was found to be ranging between 20-30% and the Dy concentration profile along the Dy-rich shells displayed a plateau and not a classic diffusion profile. Beyond this depth, TEM observations showed the presence of Dy at the GBs at a depth of z = 800 μm, confirming that Dy diffuses deeper than 400 μm inside the volume of the magnet. Regarding the evolution of the secondary Nd-rich phases, EDS chemical analysis showed the presence of the metallic Nd-rich phases IA, IB and ID identified prior to the GBDP with a trace amount of Dy. This shows that Dy (and Co) does not change the chemical composition of these phases. We note that the phase IC containing the highest amount of Cu was not detected. On the other hand, secondary oxide phases of type II were found to trap considerable amount of Dy (up to 20-25%). This Dy is wasted since oxides does not contribute to enhance the magnetic properties.

A parametric experimental study was conducted by varying the diffusion time (1h, 3h, and 12h) and GBDP temperature (920°C – 870°C). Surprisingly, the microstructural characterization showed that neither the average Dy concentration profiles nor the composition and thickness of the Dy-rich shells evolved within the range of the tested experimental conditions. These results were hardly consistent with a simple Dy diffusion model in the magnet (considered as a semi-infinite homogenous medium) for which the concentration profiles should vary with the previous experimental conditions.

In order to elucidate these features, numerical simulations with more advanced models have been performed to allow a better description of the penetration of Dy into the polycrystalline material. The simulations took into account the migration of Dy in the heterogeneous medium with distinct diffusion coefficient along GBs and into the grains. Phase diagram equilibrium was considered to estimate the amount of liquid phase forms as a function of the Dy concentration. The simulation took into account the finite diffusion source at the surface and the results were compared to some features that emerged from the microstructural characterizations: (i) the fact that the average Dy concentration profile from the surface is established after 1h and remains unchanged after 12 h of thermal treatment , (ii) the Dy-rich shells that exhibit a substitution rate ranging within a short range and a constant Dy concentration over the shell thickness.

When considering a finite diffusion source into a diffusion model, the diffusion length still grows with the GBDP time but at a lower speed compared to the case with an infinite diffusion source. However, this model was not able to depict the formation of the anti-core-shell microstructure when the value of the volume diffusion coefficient reported in the literature is used as input parameter. The simulation and experiment would match together only if one considered a value of volume diffusion coefficient 10^4 times higher. Thus, even if the anti-core shell structure is clearly correlated to the exhaust of the Dy source at the surface of the magnet, this result indicated that the amount of Dy captured by the grains is higher than the amount predicted by the solid-state intragranular diffusion model. This was a motivation to investigate if the Nd substitution by Dy

could *per se* change the diffusional properties along the liquid phase along GB or possibly in the volume of grains.

Thermodynamics stated that the liquid phase formed at GBs during the thermal treatment around 900°C, owing to the eutectic reaction, would turn into an Dy rich shell by the solidification occurring during the cooling down. The drawback of the partial melting/solidification approach is that it severely underestimates the surface fraction of the Dy-rich shell (e.g., at 150 μm, the surface fraction is 30% vs 2.4% from the phase diagram). However, thermodynamic calculations performed in this work showed that the introduction of Dy into the liquid phase increases the amount of liquid. The liquid volume fraction increase from 2% to 4% when the Dy concentration in the liquid is 28% (value corresponding to a substitution rate of 28% compatible with what is detected in the Dy-rich shells). This result alone doesn't explain the thickness of the shells, but it does suggest that the melting of the DyCo alloy increased the fraction of liquid phase around the grains. This would lead to local equilibrium conditions that are reached early in the process and account for the steady average concentration profile observed.

Finally, we proposed to describe the formation of the flat Dy concentration profile observed over the shells by a Fick's model for which the diffusion coefficient depends on the Dy content. This hypothesis is based on experimental results reported in literature for different materials for which abrupt diffusional fronts have been evidenced. Numerical simulations involving Finite Element Analysis were performed to solve the diffusion in a polycrystalline medium according to this assumption. By doing so, we noticed that the experimental results can be better taken into account. Namely, the formation of the anti-core-shell microstructure, the shell thicknesses and the Dy concentration plateau over the shell were well depicted.

Analyzing the simulation results led to a discussion aiming at clarifying the mechanisms that may pilot the Dy penetration inside the magnet and prevent the formation of the ideal microstructure post GBDP. The ideal microstructure would be achieved with a more homogeneous distribution of Dy all along the magnet depth, ideally forming at the grain scale a core-shell structure with Dy-rich shell of about 10-100 nm. Actually, owing to the magneto-crystalline anisotropy energy improvement induced by the Nd substitution by Dy in the region where the magnetization reversal nucleates, the switching field of such grains is improved even for very thin shells. However, since the coercivity depends on the weakest region of the magnet, all the grains in the bulk material should be affected and hardened by the Dy.

In the GBDP experiments reported in this work, the Dy average concentration profile rapidly decreases from the surface and thus induces a magnetic hardening of the magnet only over a limited thickness (400 μm). Despite a gain in the coercive field measured after GBDP, this translates into a stepped demagnetization J-H curves characterized by low values of the "squarenness" factor that is detrimental for the application

This work suggests that the GBDP process should be controlled by the quantity and the distribution of the liquid phase at the GBs rather than a pure diffusional mechanism. The results point out that a sufficient amount of liquid phase would be required to form a percolating network leading to an efficient use of the Dy.

Some perspectives of this study can be proposed. We consider that an effort for an improvement and validation of the percolation-driven diffusion model is still required. We think that it could be interesting to perform Dy diffusion experiments in magnets containing different amounts of rare earth elements in their initial composition. By doing so, it would be possible to change the amount of the liquid phase formed during the thermal treatment owing to the eutectic reaction of the Nd-Fe-B system. A quantitative microstructural analysis, as the one implemented in this work, will allow stating if the extension and time-evolution of the Dy concentration profile is actually related to the connection of a liquid phase network at GBs.

Independently, further works at the crystal level are required to obtain a better description of the diffusional mechanism in the $Nd_2Fe_{14}B$ structure. Beside diffusion experiment performed with single crystals, molecular dynamic approach could be implemented to investigate the possible dependence of the diffusion coefficient on the Dy substitution rate as well as on the crystallographic orientation.

Bibliography

(1) *Executive summary – Global EV Outlook 2023 – Analysis*. IEA. https://www.iea.org/reports/global-ev-outlook-2023/executive-summary (accessed 2023-10-20).

(2) Severson, M. H.; Nguyen, R. T.; Ormerod, J.; Williams, S. An Integrated Supply Chain Analysis for Cobalt and Rare Earth Elements under Global Electrification and Constrained Resources. *Resources, Conservation and Recycling* **2023**, *189*, 106761. https://doi.org/10.1016/j.resconrec.2022.106761.

(3) Gutfleisch, O.; Willard, M. A.; Brück, E.; Chen, C. H.; Sankar, S. G.; Liu, J. P. Magnetic Materials and Devices for the 21st Century: Stronger, Lighter, and More Energy Efficient. *Adv. Mater.* **2011**, *23* (7), 821–842. https://doi.org/10.1002/adma.201002180.

(4) Directorate-General for Internal Market, I.; Grohol, M.; Veeh, C. *Study on the Critical Raw Materials for the EU 2023: Final Report*; Publications Office of the European Union: LU, 2023.

(5) Doe-Critical-Material-Assessment_07312023.Pdf. https://www.energy.gov/sites/default/files/2023-07/doe-critical-material-assessment_07312023.pdf (accessed 2023-09-24).

(6) Sepehri-Amin, H.; Hirosawa, S.; Hono, K. Chapter 4 - Advances in Nd-Fe-B Based Permanent Magnets. In *Handbook of Magnetic Materials*; Brück, E., Ed.; Elsevier, 2018; Vol. 27, pp 269–372. https://doi.org/10.1016/bs.hmm.2018.08.003.

(7) du Trémolet de Lacheisserie, E. *Magnétisme, Tome 1: Les Fondements*, Université Grenoble Alpes.; 2000.

(8) DEGAUQUE, J. Matériaux à Propriétés Magnétiques Dures : Notions de Base. *Tech. ing., Matér. mét* **2001**, *MB4* (M4600), M4600.1-M4600.15.

(9) Eriksson, O.; Johansson, B.; Albers, R. C.; Boring, A. M.; Brooks, M. S. S. Orbital Magnetism in Fe, Co, and Ni. *Phys. Rev. B* **1990**, *42* (4), 2707–2710. https://doi.org/10.1103/PhysRevB.42.2707.

(10) O, M. Landolt - Bornstein: Numerical Data and Functional Relationships in Science and Technology. *New series group III* **1987**, *22*, 63,117.

(11) Stefanita, C.-G. *Magnetism: Basics and Applications*; Springer: Berlin, Heidelberg, 2012. https://doi.org/10.1007/978-3-642-22977-0.

(12) Miyazaki, T.; Jin, H. *The Physics of Ferromagnetism*; Springer Science & Business Media, 2012.

(13) Coey, J. M. D. *Magnetism and Magnetic Materials*; Cambridge University Press, 2010.

(14) Oudet, X.; Lochak, G. Total Angular Momentum and Atomic Magnetic Moments. *Journal of Magnetism and Magnetic Materials* **1987**, *65* (1), 99–122. https://doi.org/10.1016/0304-8853(87)90315-5.

(15) Herbst, J. F.; Croat, J. J.; Pinkerton, F. E.; Yelon, W. B. Relationships between Crystal Structure and Magnetic Properties in Nd 2 Fe 14 B. *Phys. Rev. B* **1984**, *29* (7), 4176–4178. https://doi.org/10.1103/PhysRevB.29.4176.

(16) Herbst, J. F. R 2 Fe 14 B Materials: Intrinsic Properties and Technological Aspects. *Rev. Mod. Phys.* **1991**, *63* (4), 819–898. https://doi.org/10.1103/RevModPhys.63.819.

(17) Givord, D.; Li, H. S.; Moreau, J. M. Magnetic Properties and Crystal Structure of Nd2Fe14B. *Solid State Communications* **1984**, *50* (6), 497–499. https://doi.org/10.1016/0038-1098(84)90315-6.

(18) Sagawa, M.; Fujimura, S.; Yamamoto, H.; Matsuura, Y.; Hiraga, K. Permanent Magnet Materials Based on the Rare Earth-Iron-Boron Tetragonal Compounds. *IEEE Transactions on Magnetics* **1984**, *20* (5), 1584–1589. https://doi.org/10.1109/TMAG.1984.1063214.

(19) Isnard, O.; Fruchart, D. Magnetism in Fe-Based Intermetallics: Relationships between Local Environments and Local Magnetic Moments. *Journal of Alloys and Compounds* **1994**, *205* (1), 1–15. https://doi.org/10.1016/0925-8388(94)90757-9.
(20) Ching, W. Y.; Gu, Z. Electronic Structure of Nd2Fe14B. *Journal of Applied Physics* **1987**, *61* (8), 3718–3720. https://doi.org/10.1063/1.338671.
(21) Givord, D.; Li, H. S.; Tasset, F. Polarized Neutron Study of the Compounds Y2Fe14B and Nd2Fe14B. *Journal of Applied Physics* **1985**, *57* (8), 4100–4102. https://doi.org/10.1063/1.334631.
(22) Boust, J. Magnetic and Optical Properties of Correlated Rare-Earth Compounds from First Principles. phdthesis, Institut Polytechnique de Paris, 2022. https://theses.hal.science/tel-04107496 (accessed 2023-10-22).
(23) Stoner, E. C.; Wohlfarth, E. P. A Mechanism of Magnetic Hysteresis in Heterogeneous Alloys. *IEEE Transactions on Magnetics* **1991**, *27* (4), 3475–3518. https://doi.org/10.1109/TMAG.1991.1183750.
(24) Ciuta, G. Une étude expérimentale de la coercivité des aimants NdFeB. 137.
(25) Hugonnet, B. Frittage et évolution de la microstructure au cours des traitements thermiques d'aimants NdFeB: influence sur les propriétés magnétiques. 164.
(26) Zickler, G. A.; Toson, P.; Asali, A.; Fidler, J. Nanoanalytical TEM Studies and Micromagnetic Modelling of Nd-Fe-B Magnets. *Physics Procedia* **2015**, *75*, 1442–1449. https://doi.org/10.1016/j.phpro.2015.12.164.
(27) Kronmüller, H.; Durst, K.-D.; Sagawa, M. Analysis of the Magnetic Hardening Mechanism in RE-FeB Permanent Magnets. *Journal of Magnetism and Magnetic Materials* **1988**, *74* (3), 291–302. https://doi.org/10.1016/0304-8853(88)90202-8.
(28) Sepehri-Amin, H.; Ohkubo, T.; Gruber, M.; Schrefl, T.; Hono, K. Micromagnetic Simulations on the Grain Size Dependence of Coercivity in Anisotropic Nd–Fe–B Sintered Magnets. *Scripta Materialia* **2014**, *89*, 29–32. https://doi.org/10.1016/j.scriptamat.2014.06.020.
(29) Sasaki, T. T.; Ohkubo, T.; Hono, K. Structure and Chemical Compositions of the Grain Boundary Phase in Nd-Fe-B Sintered Magnets. *Acta Materialia* **2016**, *115*, 269–277. https://doi.org/10.1016/j.actamat.2016.05.035.
(30) Van Ende, M.-A.; Jung, I.-H. Critical Thermodynamic Evaluation and Optimization of the Fe–B, Fe–Nd, B–Nd and Nd–Fe–B Systems. *Journal of Alloys and Compounds* **2013**, *548*, 133–154. https://doi.org/10.1016/j.jallcom.2012.08.127.
(31) Gschneidner, K. A. Pressure Dependence of the Intra Rare Earth Generalized Binary Phase Diagram. *Journal of the Less Common Metals* **1985**, *110* (1–2), 1–10. https://doi.org/10.1016/0022-5088(85)90301-7.
(32) Goo, E.; Thomas, G.; Ramesh, R.; Okada, M.; Homma, M.; Krishnan, K. M. Microstructure of Fe-Didymium-B Magnets. *Journal of Magnetism and Magnetic Materials* **1986**, *54–57*, 563–566. https://doi.org/10.1016/0304-8853(86)90710-9.
(33) Ramesh, R.; Chen, J. K.; Thomas, G. On the Grain-boundary Phase in Iron Rare-earth Boron Magnets. *Journal of Applied Physics* **1987**, *61* (8), 2993–2998. https://doi.org/10.1063/1.337849.
(34) Tang, W.; Zhou, S.; Wang, R. On the Neodymium-Rich Phases in Nd□ Fe□ B Magnets. *Journal of the Less Common Metals* **1988**, *141* (2), 217–223. https://doi.org/10.1016/0022-5088(88)90407-9.
(35) Tang, W.; Zhou, S.; Wang, R.; Graham, C. D. An Investigation of the Nd-rich Phases in the Nd-Fe-B System. *Journal of Applied Physics* **1988**, *64* (10), 5516–5518. https://doi.org/10.1063/1.342321.
(36) Lemarchand, D.; Vigier, P.; Labulle, B. On the Oxygen Stabilized Nd-Rich Phase in the Nd-Fe-B (-O) Permanent Magnet System. *IEEE Transactions on Magnetics* **1990**, *26* (5), 2649–2651. https://doi.org/10.1109/20.104826.

(37) Yin, X. J.; Hall, M. G.; Jones, I. P.; Faria, R. N.; Harris, I. R. The Microstructural Characterisation of Nd-Fe-B Alloys. I: Light Element Microanalysis. *Journal of Magnetism and Magnetic Materials* **1993**, *125* (1), 78–90. https://doi.org/10.1016/0304-8853(93)90821-I.

(38) Stadelmaier, H. H.; El-Masry, N. A. UNDERSTANDING RARE EARTH PERMANENT MAGNET ALLOYS: CRYSTAL CHEMISTRY AND PROBLEMS INHERENT IN PHASE CONSTITUTION.; 1985; pp 613–633.

(39) Abe, T.; Chen, Y.; Saengdeejimg, A.; Kobayashi, Y. Computational Phase Diagrams for the Nd-Based Magnets Based on the Combined Ab Initio/CALPHAD Approach. *Scripta Materialia* **2018**, *154*, 305–310. https://doi.org/10.1016/j.scriptamat.2018.01.030.

(40) Fidler, J.; Knoch, K. G. Electron Microscopy of Nd-Fe-B Based Magnets. *Journal of Magnetism and Magnetic Materials* **1989**, *80* (1), 48–56. https://doi.org/10.1016/0304-8853(89)90323-5.

(41) Fidler, J. Analytical Microscope Studies of Sintered Nd-Fe-B Magnets. *IEEE Transactions on Magnetics* **1985**, *21* (5), 1955–1957. https://doi.org/10.1109/TMAG.1985.1063992.

(42) Pi, S. H.; Choi, J. M.; Kim, Y. G. Effects of Heat Treatments on Coercivity and Microstructure in Nd15Fe77B8 Sintered Magnets. *Materials Science and Engineering: B* **1995**, *32* (1–2), 89–91. https://doi.org/10.1016/0921-5107(94)01168-0.

(43) Shinba, Y.; Konno, T. J.; Ishikawa, K.; Hiraga, K.; Sagawa, M. Transmission Electron Microscopy Study on Nd-Rich Phase and Grain Boundary Structure of Nd–Fe–B Sintered Magnets. *Journal of Applied Physics* **2005**, *97* (5), 053504. https://doi.org/10.1063/1.1851017.

(44) Mo, W.; Zhang, L.; Liu, Q.; Shan, A.; Wu, J.; Komuro, M. Dependence of the Crystal Structure of the Nd-Rich Phase on Oxygen Content in an Nd–Fe–B Sintered Magnet. *Scripta Materialia* **2008**, *59* (2), 179–182. https://doi.org/10.1016/j.scriptamat.2008.03.004.

(45) Fidler, J.; Knoch, K. G.; Kronmüller, H.; Schneider, G. Analytical TEM Study of Al-Doped, "Two-Phase" Nd–Fe–B Sintered Magnets. *J. Mater. Res.* **1989**, *4* (4), 806–814. https://doi.org/10.1557/JMR.1989.0806.

(46) Fukagawa, T.; Hirosawa, S. Coercivity Generation of Surface Nd2Fe14B Grains and Mechanism of Fcc-Phase Formation at the Nd/Nd2Fe14B Interface in Nd-Sputtered Nd–Fe–B Sintered Magnets. *Journal of Applied Physics* **2008**, *104* (1), 013911. https://doi.org/10.1063/1.2952556.

(47) Makita, K.; Yamashita, O. Phase Boundary Structure in Nd–Fe–B Sintered Magnets. *Appl. Phys. Lett.* **1999**, *74* (14), 2056–2058. https://doi.org/10.1063/1.123755.

(48) Chen, Y.; Saengdeejing, A.; Matsuura, M.; Sugimoto, S. Formation of the Face-Centered Cubic (FCC)-NdOxPhase at Nd/Nd-Fe-B Interface: A First-Principles Modeling. *JOM* **2014**, *66* (7), 1133–1137. https://doi.org/10.1007/s11837-014-1004-1.

(49) Liu, X. B.; Altounian, Z. The Role of Cu in Sintered Nd-Fe-B Magnets: Ab Initio Study. *IEEE Transactions on Magnetics* **2012**, *48* (11), 3144–3146. https://doi.org/10.1109/TMAG.2012.2202380.

(50) Kim, T.-H.; Lee, S.-R.; Lee, M.-W.; Jang, T.-S.; Kim, J. W.; Kim, Y. D.; Kim, H.-J. Dependence of Magnetic, Phase-Transformation and Microstructural Characteristics on the Cu Content of Nd–Fe–B Sintered Magnet. *Acta Materialia* **2014**, *66*, 12–21. https://doi.org/10.1016/j.actamat.2013.11.063.

(51) Matsuura, M.; Sugimoto, S.; Fukada, T.; Goto, R.; Tezuka, N. Effect of Cu Addition on Coercivity and Interfacial State of Nd-Fe-B/Nd-Rich Thin Films. *J. Phys.: Conf. Ser.* **2010**, *200* (8), 082019. https://doi.org/10.1088/1742-6596/200/8/082019.

(52) Kim, T.-H.; Lee, S.-R.; Namkumg, S.; Jang, T.-S. A Study on the Nd-Rich Phase Evolution in the Nd–Fe–B Sintered Magnet and Its Mechanism during Post-Sintering Annealing. *Journal of Alloys and Compounds* **2012**, *537*, 261–268. https://doi.org/10.1016/j.jallcom.2012.05.075.

(53) Kim, T.-H.; Lee, S.-R.; Bae, K.-H.; Kim, H.-J.; Lee, M.-W.; Jang, T.-S. Effects of Al/Cu Co-Doping on Crystal Structure and Chemical Composition of Nd-Rich Phases in Nd-Fe-B Sintered Magnet. *Acta Materialia* **2017**, *133*, 200–207. https://doi.org/10.1016/j.actamat.2017.05.046.

(54) Mottram, R. S.; Williams, A. J.; Harris, I. R. BlendingmaidlldeidtiopnoswodferaltuompinroiudmuceansdincteorbeadltmtaogNnedt s Fe B. *Journal of Magnetism and Magnetic Materials* **2000**.

(55) Rodewald, W.; Fernengel, W. Properties of Sintered Nd-Fe-TM-B Magnets. *IEEE Transactions on Magnetics* **1988**, *24* (2), 1638–1640. https://doi.org/10.1109/20.11555.

(56) Knoch, K. G.; Schneider, G.; Fidler, J.; Henig, E. T.; Kronmuller, H. Al-Doped Nd-Fe-B Permanent Magnets: Wetting and Microstructural Investigations. *IEEE Transactions on Magnetics* **1989**, *25* (5), 3426–3428. https://doi.org/10.1109/20.42323.

(57) Grieb, B.; Knoch, K. G.; Henig, E.-Th.; Petzow, G. Influence of Al-Based Additions on Coercivity and Microstructure in Fe-Nd-B Magnets. *Journal of Magnetism and Magnetic Materials* **1989**, *80* (1), 75–79. https://doi.org/10.1016/0304-8853(89)90328-4.

(58) Grieb, B.; Henig, E.-T.; Martinek, G.; Stadelmaier, H. H.; Petzow, G. Phase Relations and Magnetic Properties of New Phases in the Fe-Nd-Al and Fe-Nd-C Systems and Their Influence on Magnets. *IEEE Transactions on Magnetics* **1990**, *26* (5), 1367–1369. https://doi.org/10.1109/20.104380.

(59) Legras, L.; Delamare, J.; Lemarchand, D.; Dinh, J. V.; Vigier, P. Characterization of the Nd-Fe-Al p., Phase in the Microstructure of an Aluminium- and Vanadium-Substituted Nd-Fe-B Magnet. **1995**.

(60) Mottram, R. S.; Williams, A. J.; Harris, I. R. Blending Additionsporof dcoubcealstintoteNredd m Faeg n eBts Milled Powder To. *Journal of Magnetism and Magnetic Materials* **2000**.

(61) Arai, S.; Shibata, T. Highly Heat-Resistant Nd-Fe-Co-B System Permanent Magnets. *IEEE Transactions on Magnetics* **1985**, *21* (5), 1952–1954. https://doi.org/10.1109/TMAG.1985.1064033.

(62) Davies, B. E.; Mottram, R. S.; Harris, I. R. Recent Developments in the Sintering of NdFeB. *Materials Chemistry and Physics* **2001**, *67* (1–3), 272–281. https://doi.org/10.1016/S0254-0584(00)00450-8.

(63) Ma, B.-M.; Narasimhan, K. S. V. L. Temperature Dependence of Magnetic Properties of Nd-Fe-B Magnets. *Journal of Magnetism and Magnetic Materials* **1986**, *54–57*, 559–562. https://doi.org/10.1016/0304-8853(86)90709-2.

(64) Sepehri-Amin, H.; Ohkubo, T.; Shima, T.; Hono, K. Grain Boundary and Interface Chemistry of an Nd–Fe–B-Based Sintered Magnet. *Acta Materialia* **2012**, *60* (3), 819–830. https://doi.org/10.1016/j.actamat.2011.10.043.

(65) Kim, A. S.; Camp, F. E. High Performance NdFeB Magnets (Invited). *Journal of Applied Physics* **1996**, *79* (8), 5035–5039. https://doi.org/10.1063/1.361566.

(66) Hussain, A.; Van Ende, M.-A.; Kim, J.; Jung, I.-H. Critical Thermodynamic Evaluation and Optimization of the Co–Nd, Cu–Nd and Nd–Ni Systems. *Calphad* **2013**, *41*, 26–41. https://doi.org/10.1016/j.calphad.2012.12.003.

(67) Meyer, C.; Hartmann-Boutron, F.; Gros, Y.; Berthier, Y.; Buevoz, J. L. Detailed Study of NdFe2 and Additional Results Relative to PrFe 2 and YbFe2. Comparison with Other R.E. Fe2 Compounds. *J. Phys. France* **1981**, *42* (4), 605–620. https://doi.org/10.1051/jphys:01981004204060500.

(68) Mottram, R. S.; Williams, A. J.; Harris, I. R. The Effects of Blending Additions of Copper and Cobalt to Nd16Fe76B8 Milled Powder to Produce Sintered Magnets. *Journal of Magnetism and Magnetic Materials* **2001**, *234* (1), 80–89. https://doi.org/10.1016/S0304-8853(01)00067-1.

(69) Vial, F.; Joly, F.; Nevalainen, E.; Sagawa, M.; Hiraga, K.; Park, K. T. Improvement of Coercivity of Sintered NdFeB Permanent Magnets by Heat Treatment. *Journal of Magnetism*

and Magnetic Materials **2002**, *242–245*, 1329–1334. https://doi.org/10.1016/S0304-8853(01)00967-2.

(70) Sagawa, M.; Fujimura, S.; Togawa, N.; Yamamoto, H.; Matsuura, Y. New Material for Permanent Magnets on a Base of Nd and Fe (Invited). *Journal of Applied Physics* **1984**, *55* (6), 2083–2087. https://doi.org/10.1063/1.333572.

(71) Sakuma, A.; Suzuki, T.; Furuuchi, T.; Shima, T.; Hono, K. Magnetism of Nd–Fe Films as a Model of Grain Boundary Phase in Nd–Fe–B Permanent Magnets. *Appl. Phys. Express* **2016**, *9* (1), 013002. https://doi.org/10.7567/APEX.9.013002.

(72) Soderžnik, M.; Sepehri-Amin, H.; Sasaki, T. T.; Ohkubo, T.; Takada, Y.; Sato, T.; Kaneko, Y.; Kato, A.; Schrefl, T.; Hono, K. Magnetization Reversal of Exchange-Coupled and Exchange-Decoupled Nd-Fe-B Magnets Observed by Magneto-Optical Kerr Effect Microscopy. *Acta Materialia* **2017**, *135*, 68–76. https://doi.org/10.1016/j.actamat.2017.05.006.

(73) Hrkac, G.; Woodcock, T. G.; Butler, K. T.; Saharan, L.; Bryan, M. T.; Schrefl, T.; Gutfleisch, O. Impact of Different Nd-Rich Crystal-Phases on the Coercivity of Nd–Fe–B Grain Ensembles. *Scripta Materialia* **2014**, *70*, 35–38. https://doi.org/10.1016/j.scriptamat.2013.08.029.

(74) Mazilkin, A.; Straumal, B. B.; Protasova, S. G.; Gorji, S.; Straumal, A. B.; Katter, M.; Schütz, G.; Barezky, B. Grain Boundary Oxide Layers in NdFeB-Based Permanent Magnets. *Materials & Design* **2021**, *199*, 109417. https://doi.org/10.1016/j.matdes.2020.109417.

(75) Sagawa, M.; Une, Y. Chapter 5 - The Status of Sintered NdFeB Magnets. In *Modern Permanent Magnets*; Croat, J., Ormerod, J., Eds.; Woodhead Publishing Series in Electronic and Optical Materials; Woodhead Publishing, 2022; pp 135–168. https://doi.org/10.1016/B978-0-323-88658-1.00010-8.

(76) Hirota, K.; Nakamura, H.; Minowa, T.; Honshima, M. Coercivity Enhancement by the Grain Boundary Diffusion Process to Nd–Fe–B Sintered Magnets. *IEEE Transactions on Magnetics* **2006**, *42* (10), 2909–2911. https://doi.org/10.1109/TMAG.2006.879906.

(77) Sepehri-Amin, H.; Ohkubo, T.; Hono, K. The Mechanism of Coercivity Enhancement by the Grain Boundary Diffusion Process of Nd–Fe–B Sintered Magnets. *Acta Materialia* **2013**, *61* (6), 1982–1990. https://doi.org/10.1016/j.actamat.2012.12.018.

(78) He, J.; Cao, J.; Yu, Z.; Song, W.; Yu, H.; Hussain, M.; Liu, Z. Grain Boundary Diffusion Sources and Their Coating Methods for Nd-Fe-B Permanent Magnets. *Metals* **2021**, *11* (9), 1434. https://doi.org/10.3390/met11091434.

(79) Löewe, K.; Brombacher, C.; Katter, M.; Gutfleisch, O. Temperature-Dependent Dy Diffusion Processes in Nd–Fe–B Permanent Magnets. *Acta Materialia* **2015**, *83*, 248–255. https://doi.org/10.1016/j.actamat.2014.09.039.

(80) Seelam, U. M. R.; Ohkubo, T.; Abe, T.; Hirosawa, S.; Hono, K. Faceted Shell Structure in Grain Boundary Diffusion-Processed Sintered Nd–Fe–B Magnets. *Journal of Alloys and Compounds* **2014**, *617*, 884–892. https://doi.org/10.1016/j.jallcom.2014.07.166.

(81) Soderžnik, K. Ž.; Rožman, K. Ž.; Komelj, M.; Kovács, A.; Diehle, P.; Denneulin, T.; Savenko, A.; Soderžnik, M.; Kobe, S.; Dunin-Borkowski, R. E.; Mayer, J.; Markoli, B.; Šturm, S. Microstructural Insights into the Coercivity Enhancement of Grain-Boundary-Diffusion-Processed Tb-Treated Nd-Fe-B Sintered Magnets beyond the Core-Shell Formation Mechanism. *Journal of Alloys and Compounds* **2021**, *864*, 158915. https://doi.org/10.1016/j.jallcom.2021.158915.

(82) Liu, Z.; He, J.; Ramanujan, R. V. Significant Progress of Grain Boundary Diffusion Process for Cost-Effective Rare Earth Permanent Magnets: A Review. *Materials & Design* **2021**, *209*, 110004. https://doi.org/10.1016/j.matdes.2021.110004.

(83) Suss, D.; Schrefl, T.; Fidler, J. Micromagnetics Simulation of High Energy Density Permanent Magnets. *IEEE Transactions on Magnetics* **2000**, *36* (5), 3282–3284. https://doi.org/10.1109/20.908770.

(84) Zhou, L.; Li, J.; Cheng, X.; Liu, T.; Yu, X.; Li, B. Dy Gradient and Coercivity in Grain Boundary Diffusion Processed Nd-Fe-B Magnet. *Journal of Rare Earths* **2017**, *35* (6), 559–566. https://doi.org/10.1016/S1002-0721(17)60948-7.

(85) Fliegans, J.; Rado, C.; Soulas, R.; Guetaz, L.; Tosoni, O.; Dempsey, N. M.; Delette, G. Revisiting the Demagnetization Curves of Dy-Diffused Nd-Fe-B Sintered Magnets. *Journal of Magnetism and Magnetic Materials* **2021**, *520*, 167280. https://doi.org/10.1016/j.jmmm.2020.167280.

(86) Martin, G.; Perraillon, B. DIFFUSION INTERGRANULAIRE.LA DIFFUSION INTERGRANULAIRE. *J. Phys. Colloques* **1975**, *36* (C4), C4-165-C4-190. https://doi.org/10.1051/jphyscol:1975418.

(87) Kim, T.-H.; Sasaki, T. T.; Koyama, T.; Fujikawa, Y.; Miwa, M.; Enokido, Y.; Ohkubo, T.; Hono, K. Formation Mechanism of Tb-Rich Shell in Grain Boundary Diffusion Processed Nd–Fe–B Sintered Magnets. *Scripta Materialia* **2020**, *178*, 433–437. https://doi.org/10.1016/j.scriptamat.2019.12.002.

(88) Fang, H.; Lippmann, S.; Zhang, Q.; Zhu, M.; Rettenmayr, M. Modelling of Liquid Film Migration in Al-Cu Alloys. *Philosophical Transactions of the Royal Society A* **2022**. https://doi.org/10.1098/rsta.2020.0328.

(89) Baik, Y.-J.; Yoon, D. N. Chemically Induced Migration of Liquid Films and Grain Boundaries in Mo□ Ni□ (Fe) Alloy. *Acta Metallurgica* **1986**, *34* (10), 2039–2044. https://doi.org/10.1016/0001-6160(86)90262-2.

(90) Song, Y.-D.; Yoon, D. N. The Driving Force for Chemically Induced Migration of Molten Ni Films between w Grains. *Metall Trans A* **1984**, *15* (7), 1503–1505. https://doi.org/10.1007/BF02648584.

(91) Hugonnet, B. Frittage et évolution de la microstructure au cours des traitements thermiques d'aimants NdFeB : influence sur les propriétés magnétiques. phdthesis, Université Grenoble Alpes, 2016. https://theses.hal.science/tel-01689768 (accessed 2023-10-23).

(92) Fliegans, J. Coercivity of NdFeB-Based Sintered Permanent Magnets – Experimental and Numerical Approaches. 37.

(93) Sarriegui-Estupiñan, G. C. (Gabriela C. Study of Grain Growth in Nd-Fe-B Powders Obtained by Gas Atomization. *Thesis* **2022**.

(94) Yamamoto, K.; Matsuura, M.; Sugimoto, S. Microstructure Formation in Strip-Cast RE-Fe-B Alloys for Magnets. *Metall Mater Trans A* **2017**, *48* (7), 3482–3489. https://doi.org/10.1007/s11661-017-4124-8.

(95) Moosa, I. S.; Nutting, J. Hydrogen Decrepitation of a Permanent Magnet Nd-Fe-B Alloy. *Journal of the Less Common Metals* **1988**, *144* (2), 221–225. https://doi.org/10.1016/0022-5088(88)90135-X.

(96) McGuiness, P. J.; Harris, I. R.; Scholz, U. D.; Nagel, H. Hydrogen Absorption and Desorption in NdFeB Alloys*. *Zeitschrift für Physikalische Chemie* **1989**, *163* (2), 687–692. https://doi.org/10.1524/zpch.1989.163.Part_2.0687.

(97) McGuiness, P. J.; Harris, I. R. The Use of Hydrogen in the Production and Characterization of NdFeB Magnets. *Journal of Applied Physics* **1988**, *64* (10), 5308–5310. https://doi.org/10.1063/1.342401.

(98) Verdier, M.; Morros, J.; Pere, D.; Shell, N.; Harris, I. R. Stability of Nd-Fe-B Powders Obtained by Hydrogen Decrepitation. *IEEE Transactions on Magnetics* **1994**, *30* (2), 657–659. https://doi.org/10.1109/20.312367.

(99) Williams, A. J.; McGuiness, P. J.; Harris, I. R. Mass Spectrometer Hydrogen Desorption Studies on Some Hydrided NdFeB-Type Alloys. *Journal of the Less Common Metals* **1991**, *171* (1), 149–155. https://doi.org/10.1016/0022-5088(91)90271-5.

(100) Uestuener, K.; Katter, M.; Rodewald, W. Dependence of the Mean Grain Size and Coercivity of Sintered Nd–Fe–B Magnets on the Initial Powder Particle Size. *IEEE Trans. Magn.* **2006**, *42* (10), 2897–2899. https://doi.org/10.1109/TMAG.2006.879889.

(101) Sepehri-Amin, H.; Une, Y.; Ohkubo, T.; Hono, K.; Sagawa, M. Microstructure of Fine-Grained Nd–Fe–B Sintered Magnets with High Coercivity. *Scripta Materialia* **2011**, *65* (5), 396–399. https://doi.org/10.1016/j.scriptamat.2011.05.006.
(102) Kaneko, Y. Highest Performance of Nd-Fe-B Magnet over 55 MGOe. *IEEE Transactions on Magnetics* **2000**, *36* (5), 3275–3278. https://doi.org/10.1109/20.908767.
(103) Brown, D.; Ma, B.-M.; Chen, Z. Developments in the Processing and Properties of NdFeb-Type Permanent Magnets. *Journal of Magnetism and Magnetic Materials* **2002**, *248* (3), 432–440. https://doi.org/10.1016/S0304-8853(02)00334-7.
(104) Straumal, B. B.; Kucheev, Yu. O.; Yatskovskaya, I. L.; Mogilnikova, I. V.; Schütz, G.; Nekrasov, A. N.; Baretzky, B. Grain Boundary Wetting in the NdFeB-Based Hard Magnetic Alloys. *J Mater Sci* **2012**, *47* (24), 8352–8359. https://doi.org/10.1007/s10853-012-6618-5.
(105) Fliegans, J. Coercivity of NdFeB-Based Sintered Permanent Magnets: Experimental and Numerical Approaches.
(106) Chen, C. H.; Graham, C. D.; Strnat, R. M.; Pugh, B. K.; Wangler, A.; Higgins, A. K. Verification by Finite Element Modeling for the Origin of the Apparent Image Effect in Closed-Circuit Magnetic Measurements. *Journal of Magnetism and Magnetic Materials* **2011**, *323* (1), 108–114. https://doi.org/10.1016/j.jmmm.2010.08.042.
(107) Chauhan, A. Deformation and Damage Mechanisms of ODS Steels under High-Temperature Cyclic Loading, 2018. https://doi.org/10.5445/IR/1000080339.
(108) Gaudenzi de faria, M. Robust Control for Manipulation inside a Scanning Electron Microscope. These de doctorat, Besançon, 2016. https://www.theses.fr/2016BESA2068 (accessed 2023-08-03).
(109) Agnese, F. Advanced Transmission Electron Microscopy Studies of Semiconductor Nanocrystals Synthesized by Colloidal Methods. phdthesis, Université Grenoble Alpes, 2018. https://theses.hal.science/tel-02274608 (accessed 2023-09-20).
(110) Williams, D. B.; Carter, C. B. The Transmission Electron Microscope. In *Transmission Electron Microscopy: A Textbook for Materials Science*; Williams, D. B., Carter, C. B., Eds.; Springer US: Boston, MA, 1996; pp 3–17. https://doi.org/10.1007/978-1-4757-2519-3_1.
(111) Goldstein, J. I.; Newbury, D. E.; Michael, J. R.; Ritchie, N. W. M.; Scott, J. H. J.; Joy, D. C. *Scanning Electron Microscopy and X-Ray Microanalysis*; Springer, 2017.
(112) R, C. Application Des Sondes Electroniques a Une Methode d'analyse Ponctuelle Chimique et Cristallographique. *These Universite de Paris 1951* **1952**.
(113) Robin, E. Procédé d'étude d'une Zone d'un Objet Pour En Déterminer Une Épaisseur Massique et Une Composition En Utilisant Un Faisceau d'électrons et Des Mesures d'intensité d'un Rayonnement XMethode Zur Bestimmung Der Massendicke Und Der Zusammensetzung Einer Zone Eines Objektes Mittels Eines Elektronenstrahls Und Messungen Der Rönt genintensitätenMethod for the Determination of the Mass Thickness and the Composition of a Zone of an Object Using an Electron Beam and Measurements of X-Ray Intensities. EP3032244B1, August 2017. https://hal.science/hal-02072427 (accessed 2023-10-23).
(114) Wittry, D. B. Methods of Quantitative Electron Probe Analysis*. *Advances in X-Ray Analysis* **1963**, *7*, 395–418. https://doi.org/10.1154/S037603080000269X.
(115) Pattee, H. H.; Cosslett, V. E.; Engström, A. *X-Ray Optics and X-Ray Microanalysis*; Elsevier, 2013.
(116) Duncumb, P.; Shields, P. K. The Electron Microprobe. **1966**, No. 7, 490.
(117) Heinrich, K. F. J. National Bureau of Standards Technical Note 521, 1969.
(118) Packwood, R. H.; Brown, J. D. A Gaussian Expression to Describe ϕ(Pz) Curves for Quantitative Electron Probe Microanalysis. *X-Ray Spectrometry* **1981**, *10* (3), 138–146. https://doi.org/10.1002/xrs.1300100311.
(119) Robin, E. Method for Studying a Zone of an Object so as to Determine a Mass-Thickness and a Composition Thereof by Using an Electron Beam and Measurements of X-Ray

Radiation Intensity. US10240918B2, March 26, 2019. https://patents.google.com/patent/US10240918B2/en (accessed 2023-10-25).
(120) Love, G.; Sewell, D. A.; Scott, V. D. AN IMPROVED ABSORPTION CORRECTION FOR QUANTITTATIVE ANALYSIS. *J. Phys. Colloques* **1984**, *45* (C2), C2-24. https://doi.org/10.1051/jphyscol:1984205.
(121) Thermo Fisher Scientific. Principles and Applications of Parallel Beam Wavelength DispersiveX-Ray Spectroscopy.
(122) Zhou, W.; Wang, Z. L. *Scanning Microscopy for Nanotechnology: Techniques and Applications*; Springer Science & Business Media, 2007.
(123) Henry, L. Développement d'une technique de caractérisation pour la mesure de déformation et de composition chimique à l'échelle nanométrique appliquée aux dispositifs avancés de la microélectronique. phdthesis, Université Grenoble Alpes [2020-....], 2021. https://theses.hal.science/tel-03425148 (accessed 2023-10-24).
(124) Esnouf, C. *Caractérisation microstructurale des matériaux: analyse par les rayonnements X et électronique*; PPUR Presses polytechniques, 2011.
(125) Hartel, P.; Rose, H.; Dinges, C. Conditions and Reasons for Incoherent Imaging in STEM. *Ultramicroscopy* **1996**, *63* (2), 93–114. https://doi.org/10.1016/0304-3991(96)00020-4.
(126) Rafferty, B.; Nellist, D.; Pennycook, J. On the Origin of Transverse Incoherence in Z-Contrast STEM. *Microscopy* **2001**, *50* (3), 227–233. https://doi.org/10.1093/jmicro/50.3.227.
(127) Cliff, G.; Lorimer, G. W. The Quantitative Analysis of Thin Specimens. *Journal of Microscopy* **1975**, *103* (2), 203–207. https://doi.org/10.1111/j.1365-2818.1975.tb03895.x.
(128) Metcalfe, E.; Broomfield, J. P. DETERMINATION OF CLIFF-LORIMER k FACTORS FOR A HITACHI H700H 200 kV SCANNING TRANSMISSION ELECTRON MICROSCOPE. *J. Phys. Colloques* **1984**, *45* (C2), C2-407-C2-410. https://doi.org/10.1051/jphyscol:1984292.
(129) Newbury, D. E.; Williams, D. B.; Goldstein, J. I.; Fiori, C. E. Observation on the Calculation of kAB Factors for Analytical Electron Microscopy. *Anal Electron Microsc* **1984**, *2*, 276–278.
(130) Maher, D. M.; Joy, D. C.; Ellington, M. B.; Zaluzec, N. J.; Mochel, P. E. Relative Accuracy of K-Factor Calculations for Thin-Film X-Ray Analysis. *Analytical Electron Microscopy*. 1981, pp 33–38.
(131) Wood, J. E.; Williams, D. B.; Goldstein, J. I. Experimental and Theoretical Determination of kAFe Factors for Quantitative X-Ray Microanalysis in the Analytical Electron Microscope. *Journal of Microscopy* **1984**, *133* (3), 255–274. https://doi.org/10.1111/j.1365-2818.1984.tb00490.x.
(132) Sheridan, P. J. Determination of Experimental and Theoretical kASi Factors for a 200-kV Analytical Electron Microscope. *Journal of Electron Microscopy Technique* **1989**, *11* (1), 41–61. https://doi.org/10.1002/jemt.1060110107.
(133) Watanabe, M.; Williams, D. B. The Quantitative Analysis of Thin Specimens: A Review of Progress from the Cliff-Lorimer to the New ζ-Factor Methods. *Journal of Microscopy* **2006**, *221* (2), 89–109. https://doi.org/10.1111/j.1365-2818.2006.01549.x.
(134) Nishio, S.; Sugimoto, S.; Goto, R.; Matsuura, M.; Tezuka, N. Effect of Cu Addition on the Phase Equilibria in Nd-Fe-B Sintered Magnets. *Mater. Trans.* **2009**, *50* (4), 723–726. https://doi.org/10.2320/matertrans.MBW200824.
(135) Hono, K.; Sepehri-Amin, H. Strategy for High-Coercivity Nd–Fe–B Magnets. *Scripta Materialia* **2012**, *67* (6), 530–535. https://doi.org/10.1016/j.scriptamat.2012.06.038.
(136) Ghanbarzadeh, S.; Prodanović, M.; Hesse, M. A. Percolation and Grain Boundary Wetting in Anisotropic Texturally Equilibrated Pore Networks. *Phys. Rev. Lett.* **2014**, *113* (4), 048001. https://doi.org/10.1103/PhysRevLett.113.048001.

(137) Ma, B.-M.; Narasimhan, K. NdFeB Magnets with Higher Curie Temperature. *IEEE Transactions on Magnetics* **1986**, *22* (5), 916–918. https://doi.org/10.1109/TMAG.1986.1064527.
(138) Liu, Q.; Xu, F.; Wang, J.; Dong, X.; Zhang, L.; Yang, J. An Investigation of the Microstructure in the Grain Boundary Region of Nd–Fe–B Sintered Magnet during Post-Sintering Annealing. *Scripta Materialia* **2013**, *68* (9), 687–690. https://doi.org/10.1016/j.scriptamat.2013.01.019.
(139) Ming, X.; Han, X.; Yang, M.; Yan, G. Enhanced Magnetic Performance of Sintered Nd-Fe-B Magnets by Dy-Co Film Grain Boundary Diffusion. *Journal of Magnetism and Magnetic Materials* **2022**, *550*, 169064. https://doi.org/10.1016/j.jmmm.2022.169064.
(140) Chen, F.; Zhang, L.; Jin, Y.; Cheng, Y. Simultaneous Enhancement of the Coercivity and Remanence at High Temperatures in a Sintered Nd-Fe-B Magnet after Grain Boundary Diffusion with Dy60Co40 Alloy. *Materials Characterization* **2018**, *144*, 547–553. https://doi.org/10.1016/j.matchar.2018.08.012.
(141) Jang, T.-S.; Lee, S.-R.; Kim, H.-J.; Bae, K.-H.; Lee, M.-W. Microstructure and Magnetic Properties of NdFeB Sintered Magnets Diffusion-Treated with Cu/Al Mixed Dyco Alloy-Powder. *Archives of Metallurgy and Materials; 2017; vol. 62; No 2* **2017**.
(142) He, J.; Song, W.; Liu, X.; Yu, H.; Zhong, X.; Liu, Z. High-Efficient Selected Area Grain Boundary Diffusion for Enhancing the Coercivity of Thick Nd-Fe-B Magnets. *Applied Physics Letters* **2022**, *120* (4), 042405. https://doi.org/10.1063/5.0080935.
(143) Mehrer, H. *Diffusion in Solids: Fundamentals, Methods, Materials, Diffusion-Controlled Processes*; Springer Science & Business Media, 2007.
(144) Li, W.; Zhang, Q.; Zhu, Q.; Xiao, S.; Xu, C.; Yang, L.; Zheng, B.; Mao, S.; Song, Z. Formation of Anti-Shell/Core Structure of Heavy Rare Earth Elements (Tb, Dy) in Sintered Nd-Fe-B Magnet after Grain Boundary Diffusion Process. *Scripta Materialia* **2019**, *163*, 40–43. https://doi.org/10.1016/j.scriptamat.2018.12.034.
(145) Kim, T.-H.; Lee, S.-R.; Yun, S. J.; Lim, S. H.; Kim, H.-J.; Lee, M.-W.; Jang, T.-S. Anisotropic Diffusion Mechanism in Grain Boundary Diffusion Processed Nd–Fe–B Sintered Magnet. *Acta Materialia* **2016**, *112*, 59–66. https://doi.org/10.1016/j.actamat.2016.04.019.
(146) Yu, H.; Bao, X.; Li, J.; Gao, X. Microstructure Optimization and Coercivity Enhancement of Nd-Fe-B Magnet by Double-Step Diffusion with Pr60Cu20Al20 Alloy and Tb Metal. *Journal of Magnetism and Magnetic Materials* **2022**, *562*, 169743. https://doi.org/10.1016/j.jmmm.2022.169743.
(147) Zhao, D.; Liu, F.; Gao, Y.; Jiang, P.; Liu, L.; Zhao, M.; Ren, S.; Pei, W. Dy Evolution and Coercivity Improvement Mechanism of Sintered NdFeB Magnets in Thermal Diffusion Process. *Journal of Magnetism and Magnetic Materials* **2022**, *563*, 169943. https://doi.org/10.1016/j.jmmm.2022.169943.
(148) Zhao, Y.; Feng, H.; Li, A.; Li, W. Diffusion Temperature Dependent Microstructure and Magnetic Properties of TbH_x Grain Boundary Diffused Nd–Fe–B Magnets. *AIP Advances* **2021**, *11* (2), 025208. https://doi.org/10.1063/5.0026389.
(149) Zeng, H.; Liu, Z.; Li, W.; Zhang, J.; Zhao, L.; Zhong, X.; Yu, H.; Guo, B. Significantly Enhancing the Coercivity of NdFeB Magnets by Ternary Pr-Al-Cu Alloys Diffusion and Understanding the Elements Diffusion Behavior. *Journal of Magnetism and Magnetic Materials* **2019**, *471*, 97–104. https://doi.org/10.1016/j.jmmm.2018.09.080.
(150) Fisher, J. C. Calculation of Diffusion Penetration Curves for Surface and Grain Boundary Diffusion. *Journal of Applied Physics* **1951**, *22* (1), 74–77. https://doi.org/10.1063/1.1699825.
(151) Loewe, K.; Benke, D.; Kübel, C.; Lienig, T.; Skokov, K. P.; Gutfleisch, O. Grain Boundary Diffusion of Different Rare Earth Elements in Nd-Fe-B Sintered Magnets by Experiment and FEM Simulation. *Acta Materialia* **2017**, *124*, 421–429. https://doi.org/10.1016/j.actamat.2016.11.034.

(152) Campos, M. F. de. Diffusion Coefficients of Interest for the Simulation of Heat Treatment in Rare-Earth Transition Metal Magnets. *Materials Science Forum* **2012**, *727–728*, 163–168. https://doi.org/10.4028/www.scientific.net/MSF.727-728.163.
(153) Whipple, R. T. P. CXXXVIII. Concentration Contours in Grain Boundary Diffusion. *The London, Edinburgh, and Dublin Philosophical Magazine and Journal of Science* **1954**, *45* (371), 1225–1236. https://doi.org/10.1080/14786441208561131.
(154) Suzuoka, T. Exact Solutions of Two Ideal Cases in Grain Boundary Diffusion Problem and the Application to Sectioning Method. *Journal of the Physical Society of Japan* **1964**, *19* (6), 839–851. https://doi.org/10.1143/JPSJ.19.839.
(155) Dai, Z.; Li, K.; Wang, Z.; Liu, W.; Zhang, Z. Magnetic-Property Assessment on Dy–Nd–Fe–B Permanent Magnet by Thermodynamic Calculation and Micromagnetic Simulation. *Materials* **2022**, *15* (21), 7648. https://doi.org/10.3390/ma15217648.
(156) Cook, B. A.; Harringa, J. L.; Laabs, F. C.; Dennis, K. W.; Russell, A. M.; McCallum, R. W. Diffusion of Fe, Co, Nd, and Dy in R2(Fe1−xCox)14B Where R=Nd or Dy. *Journal of Magnetism and Magnetic Materials* **2001**, *233* (3), 136–141. https://doi.org/10.1016/S0304-8853(01)00378-X.
(157) Kolodny, A.; Shappir, J. Diffusion Properties of Cadmium in Indium Antimonide. *J. Electrochem. Soc.* **1978**, *125* (9), 1530. https://doi.org/10.1149/1.2131710.
(158) Uematsu, M. Simulation of Boron, Phosphorus, and Arsenic Diffusion in Silicon Based on an Integrated Diffusion Model, and the Anomalous Phosphorus Diffusion Mechanism. *Journal of Applied Physics* **1997**, *82* (5), 2228–2246. https://doi.org/10.1063/1.366030.
(159) Nakagawa, T.; Sakaguchi, I.; Uematsu, M.; Sato, Y.; Ohashi, N.; Haneda, H.; Ikuhara, Y. Diffusion Model of Gallium in Single-Crystal ZnO Proposed from Analysis of Concentration-Dependent Profiles Based on the Fermi-Level Effect. *Jpn. J. Appl. Phys.* **2007**, *46* (7R), 4099. https://doi.org/10.1143/JJAP.46.4099.
(160) Saito, K.; Doi, S.; Abe, T.; Ono, K. Quantitative Evaluation of Site Preference in Dy-Substituted Nd2Fe14B. *Journal of Alloys and Compounds* **2017**, *721*, 476–481. https://doi.org/10.1016/j.jallcom.2017.04.155.
(161) Haider, S. K.; Kang, M.-C.; Hong, J.; Kang, Y. S.; Yang, C.-W.; Kim, D. Determination of Dy Substitution Site in Nd2−xDyxFe14B by HAADF-STEM and Illustration of Magnetic Anisotropy of "g" and "f" Sites, before and after Substitution. *Sci Rep* **2021**, *11* (1), 6347. https://doi.org/10.1038/s41598-021-85713-5.

List of figures

List of tables

Aucune entrée de table d'illustration n'a été trouvée.

Appendix 1: Determination of the surface fraction of Dy-rich shells

EDS-SEM maps of Dy, Nd and O taken at several depth (from 50 µm until 400 µm) were treated using imageJ software. Each SEM-EDS map at each depth was taken at a magnification of 3000× which represents a surface of dimensions 39 × 29 µm². Using imageJ, we first started by converting the RGB EDS-SEM map into an 8-bit image. Then, a threshold was applied to select the shell and convert the grayscale image into a binary image. From these binary images, ImageJ can measure the surface fraction of the Dy-rich shells. The process is summarized in Figure A.1 in which we show how the area of the Dy-rich shells and that of the other phases present in GBD processed NdFeB magnet are quantified.

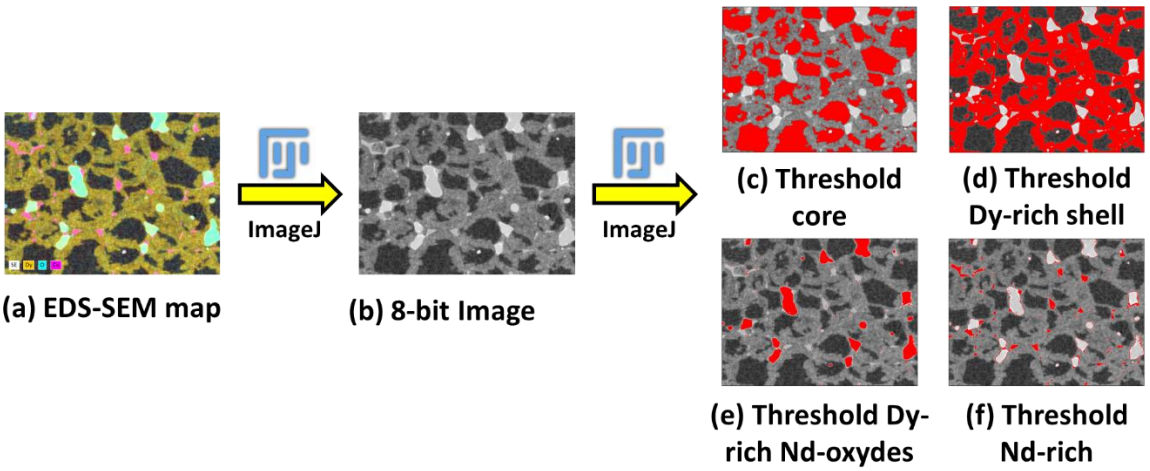

Figure A.1: steps of determining the relative surface fraction of the different phases present in GBD processed sintered NdFeB magnet using ImageJ software.

The evolution of the surface fraction of the Dy-rich shells between 50 µm and 400 µm is reported in Table A.1. We can see that the Dy-rich shell surface fraction decreases from 80% at z = 50 µm to 8% at z = 400 µm.

Table A.1: Surface fraction evolution of the Dy-rich shell with respect to the magnet depth.

Depth	50 µm	100 µm	150 µm	200 µm	300 µm	400 µm
Surface fraction of the Dy-rich shells	80%	53%	30%	15%	9%	8%

Appendix 2: Suzuoka's equations for averaged concentration

The analytical expressions used to plot the averaged concentration profiles in Figure 134 are given by Suzuoka in the following form:

$$\overline{C_c}(y,t) = C_s\,[\mathrm{erfc}(\eta/2) + C_I/n], \tag{A.2.1}$$

$$\overline{C_f}(y,t) = K/\sqrt{\pi D_v t}\;[\exp(-\eta^2/4) + C_{II}/n], \tag{A.2.2}$$

where the terms C_I and C_{II} are given by:

$$C_I(y,t) = \frac{2\eta}{\sqrt{\pi}}\int_1^{\Delta} \exp\left(-\frac{\eta^2}{4\sigma}\right)\sqrt{\frac{\Delta-\sigma}{\Delta-1}}\left[\exp(-X^2)/\sqrt{\pi}) - X\mathrm{erfc}(X)\right]\frac{d\sigma}{\sigma^{3/2}}, \tag{A.2.3}$$

and

$$C_{II}(y,t) = \frac{2\eta}{\sqrt{\pi}}\int_1^{\Delta}\left(\frac{\eta^2}{\sigma}-2\right)\exp\left(-\frac{\eta^2}{4\sigma}\right)\sqrt{\frac{\Delta-\sigma}{\Delta-1}}\left[\exp(-X^2)/\sqrt{\pi}) - X\mathrm{erfc}(X)\right]\frac{d\sigma}{\sigma^{3/2}}, \tag{A.2.4}$$

with:

$$X = \sqrt{\frac{\Delta-1}{\Delta-\sigma}}\frac{\sigma-1}{2\beta}$$

It is worth noting that the expressions (A.2.1) and (A.2.2) account for the grain size via the parameter n which is a function of the grain size d_g:

$$n = \frac{d_g}{2\sqrt{D_v t}}$$

Table of contents